ENERGY LABORATORY

MASSACHUSETTS INSTITUTE OF TECHNOLOGY

BUOYANT JET BEHAVIOR IN CONFINED REGIONS

by

David J. Fry and E. Eric Adams

Energy Laboratory Report No. MIT-EL 81-050

September 1981

BUOYANT JET BEHAVIOR IN CONFINED REGIONS

by

David J. Fry

and

E. Eric Adams

Energy Laboratory
and
Ralph M. Parsons Laboratory
for
Water Resources and Hydrodynamics
Department of Civil Engineering

Massachusetts Institute of Technology
Cambridge, Mass. 02139

September 1981

ABSTRACT

Previous confined jet studies have emphasized the behavior of non-buoyant jets inside ducts or near plane boundaries (Coanda effect). Buoyancy, however, is a major factor in the confined jet behavior experienced in many environmental fluid mechanics problems and, in particular, in the external fluid mechanics associated with an operating Ocean Thermal Energy Conversion (OTEC) plant. In many of these cases confinement and buoyancy offer opposing influences on jet trajectory and diffusion.

An experimental set-up was designed, similar to some encountered in OTEC, but simple enough to facilitate accurate measurements and to allow the results to be interpreted through dimensional analysis. The particular experimental situation chosen was a submerged, negatively buoyant, horizontal, radial jet discharging into ambient water which was initially uniform in temperature and density. A near-surface intake was included in some experiments and not in others. Two distinct flow regimes were possible depending on the relative importance of buoyancy and confinement.

The first flow regime (buoyancy-dominated) is termed a detached jet. The ambient region above the jet is an irrotational flow consisting entirely of original ambient fluid. The flow magnitude is determined by the entrainment requirements of the upper boundary of the jet and the intake flow, if any. The ambient region below the jet is made up of fluid pulled from the jet as it nears a vertical trajectory. The flow here is rotational and at a lower temperature than the original ambient fluid.

The second flow regime (confinement-dominated) is termed an attached jet. Low pressures in the circulating region above the jet pull the jet to the surface. After impact the jet flow splits and no longer can be characterized as a jet. The portion of jet flow downstream from the impact point is negatively buoyant with respect to the original ambient fluid and therefore sinks - some returning as entrainment for the underside of the jet. In this case neither the top nor the bottom ambient region has the temperature of the original ambient water.

Seventeen experiments yielded temperature and trajectory data on the radial jet in both of the flow regimes. Velocity data also were collected in the upper ambient region for the detached jet. Finally discharge conditions that caused transition from one flow regime to the other were determined. A hysterisis effect was noted as the conditions for "attaching" a detached jet were different from those needed to "detach" an attached jet.

2

Dimensional analysis yielded a single dimensionless number that was fairly successful at predicting the transition points between regimes. However, three dimensionless numbers were apparently needed to completely characterize the experimental behavior. The dimensional analysis was also helpful in formulating an analytical jet model.

An integral jet model (based on a spreading assumption) was successfully adapted to include effects of velocity and pressure fields in ambient regions. The model predicts jet trajectories, velocities, and temperatures, and transitions of experiments between flow regimes. The model can be applied to plane jets as well and buoyant and non-buoyant confined plane jet data from other studies were also compared with model predictions.

ACKNOWLEDGEMENTS

Table of Contents

7

<div align="center">8</div>

I. Introduction

1.1 Occurrence of Confined Jets

A velocity discontinuity between two fluids causes strong shearing
and often generates free turbulence with its characteristic diffusion
of momentum and mass. When one fluid emerges from an orifice the
resulting phenomena is referred to as "turbulent jet diffusion." The
width of the highly turbulent zone increases in the direction of flow as
forward velocities decrease and more outside, non-turbulent water is
pulled (entrained) into the turbulent zone. The widening is gradual enough
to allow the phenomena to be classified as a boundary layer flow.

In many jet problems the "ambient" fluid region can be considered
as a motionless source of fluid that is entrained by the jet. The region
is so large that the actual motion required to continually supply the jet
entrainment has no significant effect on jet diffusion or trajectory.
These cases are termed "unconfined jets."

However the proximity of boundaries to the turbulent jet zone can
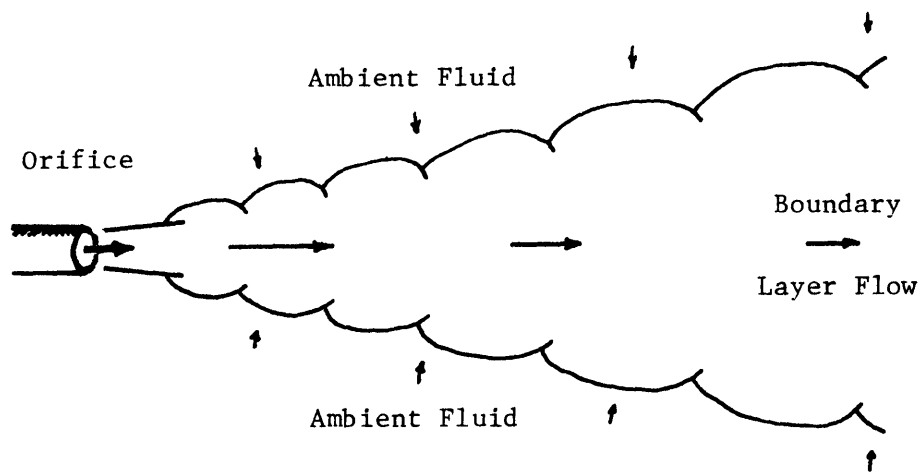
Figure 1-1 Turbulent Jet Diffusion

10

cause significant flow in the ambient fluid region. In such cases,
pressure and velocity fields created in the ambient fluid can dramatically
affect jet diffusion and trajectory. When these effects are significant,
the jet is termed "confined".

The earliest study of confined jets related to the "Coanda" effect.
A non-buoyant, two-dimensional, plane jet was issued in the vicinity of
a solid boundary. The solid boundary was observed to deflect the jet
causing the jet to impact the boundary. The ambient fluid region between
the jet and boundary develops a significant low pressure zone because a
return flow of jet water is needed to supply entrainment for the initial
portion of the jet. Two common geometries are illustrated in Figure 1-2.
Modern fluid switching devices employ the same phenomenon. The jet path
can be switched by temporarily changing the pressure in an ambient fluid
region. Once a direction of deflection is established it is maintained
until another pressure change causes switching.

Another confined jet problem of practical importance occurs in jet
pump and furnace design. Here a non-buoyant jet is completely surrounded
by the walls of a duct that has a coincident axis. Geometries which are
often analysed include a circular jet within a cylindrical tube or a
plane jet centered between two plane boundaries. The ambient fluid region
(Figure 1-3) may or may not be flowing at the jet orifice. In either
case, the confinement creates flow and pressure fields forward of this
point. Under their influence the jet gradually expands until it reaches
the walls. A transition is then made to normal turbulent pipe flow.

Recent interest in the discharge flows of Ocean Thermal Energy

Detached   Attached

Angled Plane Boundary

Offset Plane Boundary   Fluidic Switch

Flow

No Flow
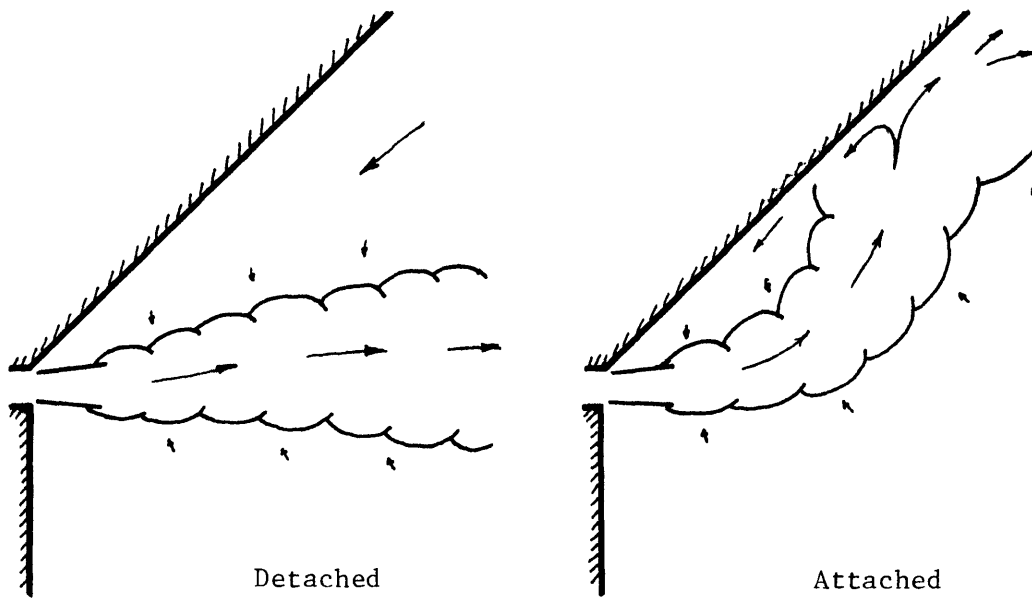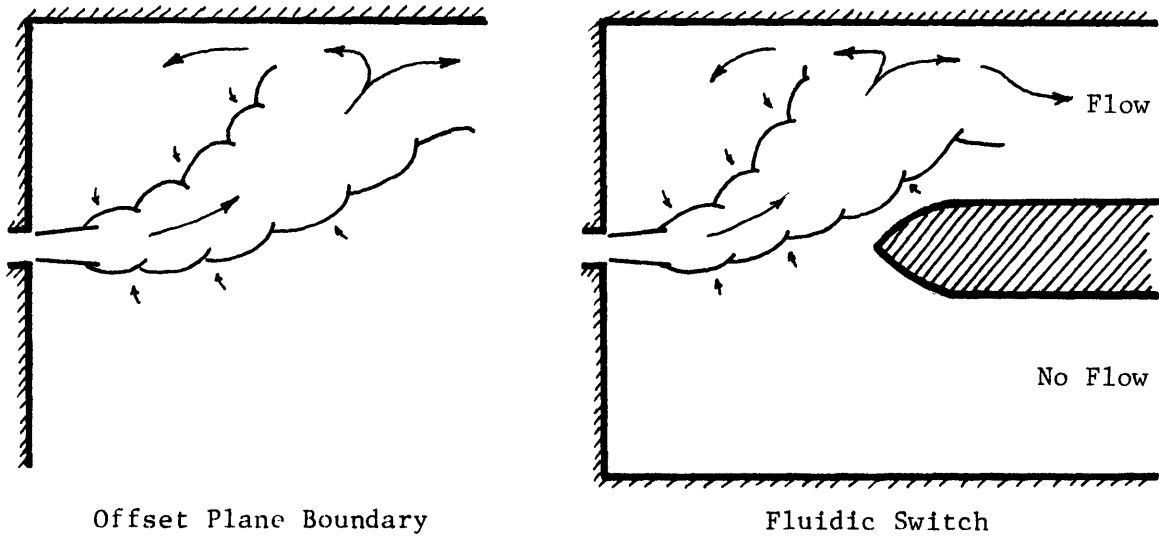
Figure 1-2   Examples of Coanda Effect

12

Duct Wall

| Flow Establishment | Established Flow | Recirculation Zone | Wall Interaction |
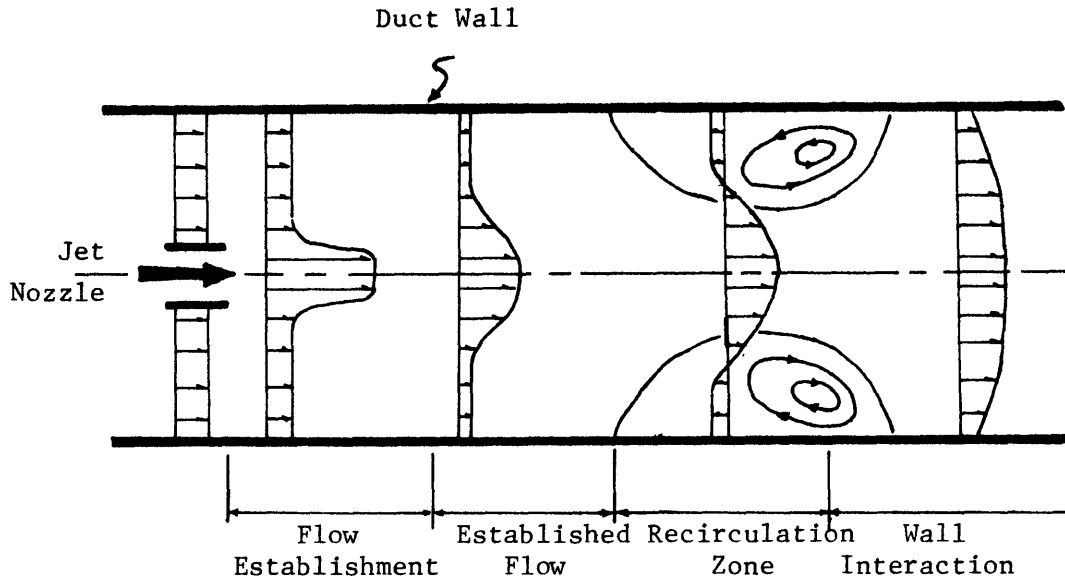
Figure 1-3 Ducted Jet Velocity Profiles

Conversion (OTEC) plants introduces additional confined jet examples. OTEC

jets will be discharged at deep tropical ocean sites. Only the large flow

rates ($\sim$ 1000 m^3/s for a 100 MWe plant) make confinement effects a reasonable

possibility. Several possible confined jet situations are discussed in

the next two sections and they provide the basic motivation for this study.

1.2 OTEC Operation

Ocean Thermal Energy Conversion (OTEC) is a method of generating

power using the difference in temperature between the upper and lower

layers of a stratified ocean. In the tropics, the water surface may reach

temperatures of 25 to 30°C due to the absorption of solar radiation. At

depths of 500 to 1000 m water is colder (typically 5-10°C) due to flow

from the polar regions that occurs as part of the global ocean circulation.

All OTEC concepts work by effecting a transfer of heat from the upper

layers to the cold underlying water. These layers are normally insulated

13

by density stratification effects (the lower water being denser than the warm upper water). From this heat transfer OTEC can extract useable forms of power (mechanical or electrical) through a heat engine of some kind.

One leading concept has OTEC plants withdrawing a large flow of warm surface water to evaporate a working fluid in a set of heat exchangers (evaporator). The vaporized working fluid spins a power turbine on its way to a second set of heat exchangers (condenser) where cold ocean water is used to condense the vapor. The condensed working fluid is then pumped back to the evaporator to repeat the cycle. The working fluid transfers heat from the warm to the cold ocean water and in the process produces power (spinning turbine). The heat transfer changes the temperature of the ocean water flows by approximately 2°C according to preliminary designs (Lockheed, 1975 and TRW, 1975). That is, the temperature of the evaporator flow will drop by 2°C (∿27°C → 25°C) and the temperature of the condensing water flow will rise by 2°C (∿8°C → 10°C) before they are discharged from the plant (Figure 1-4).

External ocean conditions are integrally related to OTEC plant operations. Maximizing the useable power output requires the largest possible temperature difference ("ΔT") be maintained between the withdrawn ocean water flows. The ΔT is basically dependent on the plant location and the depth of its cold water intake. But disturbance of the natural temperature profile or possible direct recirculation of discharge jets into plant intake also may be important. One analysis estimates 13% loss in net power production for "ΔT" of only 1°C (Lavi, 1975). For this reason there is keen interest in the effects of discharge jets on intake flows and the ocean. Environmental impact assessments also

14

$$\Delta T = 27° - 8°$$
$$= 19°C$$
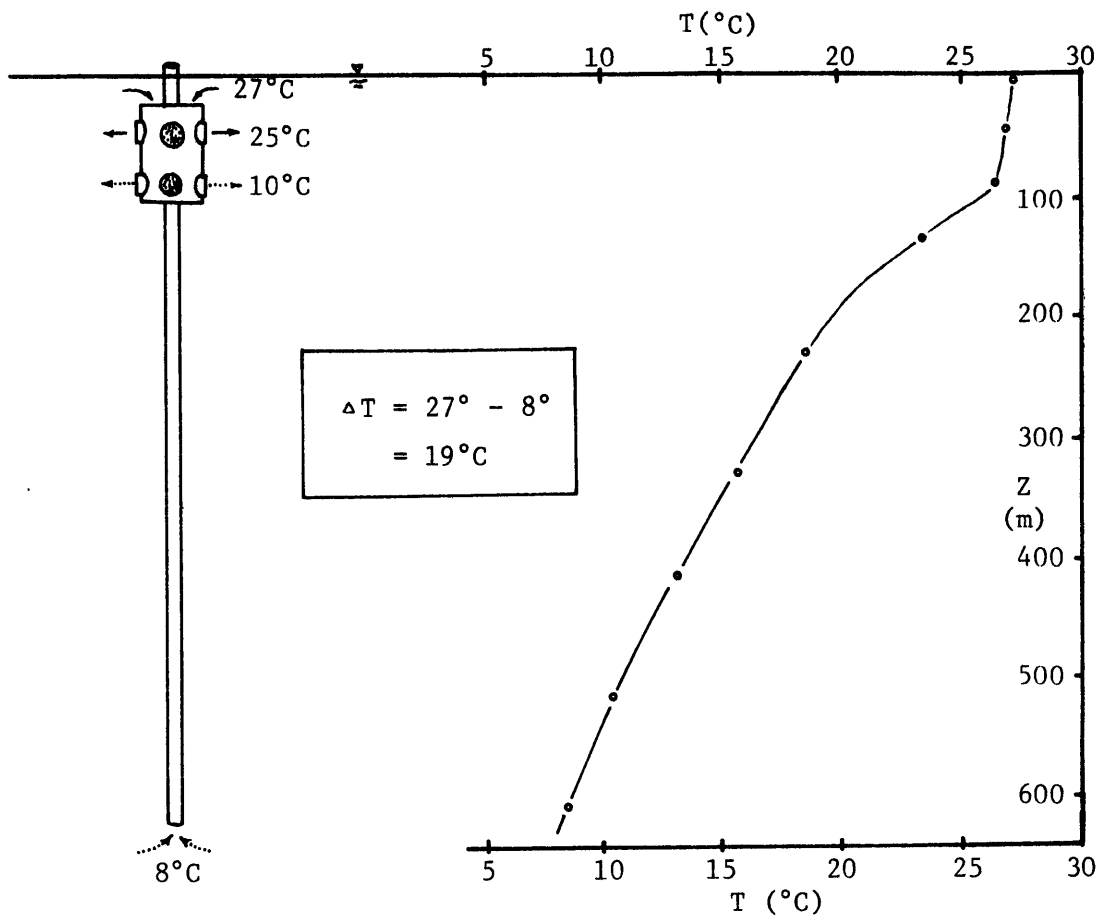
Carribean Sea Temperature Profile
[Fuglister, 1960]

Figure 1-4 Schematic of OTEC Operating Temperatures

15

require information on discharge jet behavior. The transport of constituents of the discharge such as nutrients, working fluid leaks, corrosion products and chlorine must be evaluated.

1.3 OTEC and Confined Jets

Conceptually, an OTEC plant is a vertical axis in the ocean with intakes at both ends. Because the components of the power cycles (turbine, pumps, heat exchangers, etc.) need to be accessible, they will be located closer to the surface end of the axis. The warm and cold flows will be used and discharged at nearly this same level in order to minimize piping cost. (Figure 1-5)

Given these concepts, the flow and pressure fields in ambient fluid regions may well affect discharge jet , trajectory, diffusion, and potential recirculation. The surface and the stable density stratification of the ocean restrict the size of ambient fluid regions. The intake flow field and entrainment flow fields of adjacent jets further add to the magnitude of external flow and pressure fields. Several possible flow situations are illustrated in Figure 1-6. In several cases two distinct flow fields are possible depending on whether ambient fluid regions locally are completely bounded or have an opening to the ocean at large.

1.4 Objectives of this Study

The Coanda effect and ducted jet behavior has been studied primarily with neutrally buoyant jets. Buoyancy, however, is a major factor in the confined jet behavior illustrated in Figure 1-6. In cases a,b,d and e buoyancy and confinement offer opposing influences on jet trajectory. Two distinct flow fields are possible depending on which effect dominates.

16
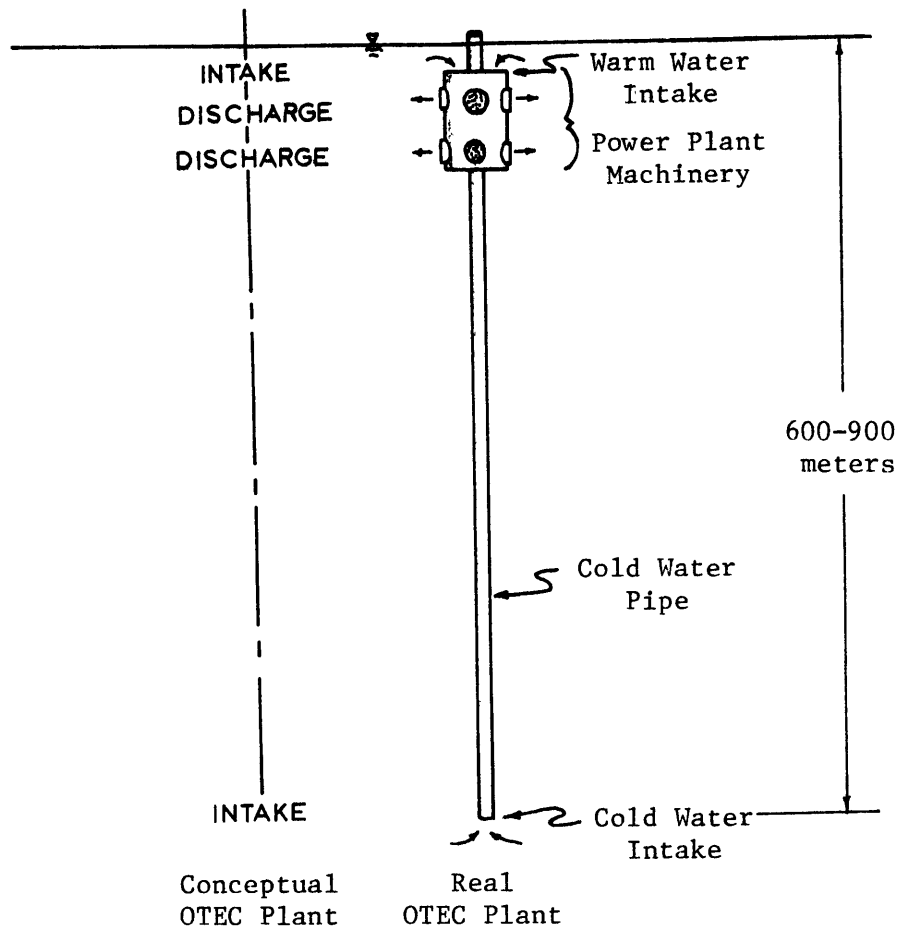
Figure 1-5 Basic OTEC Configuration

a.
Single
Radial
Port

Ocean Density
Profile

b.
Single
Radial
Port

c.
Overhead View
4 Separate Ports

d.
Double
Radial
Port

Ocean Density
Profile

e.
Double
Radial
Port
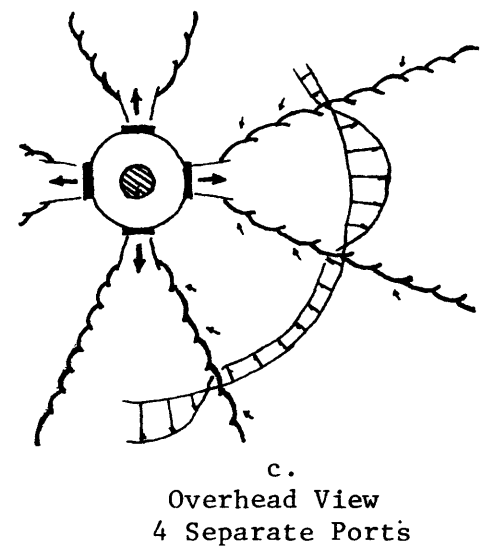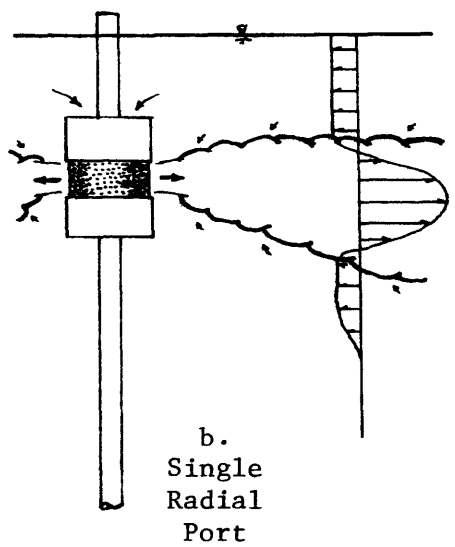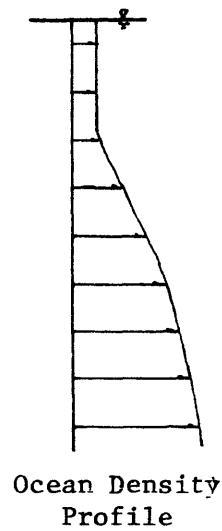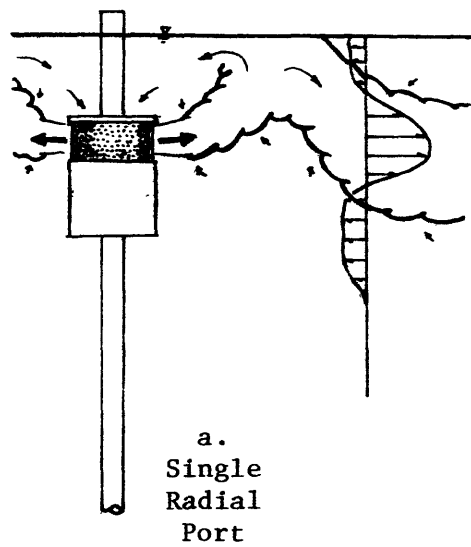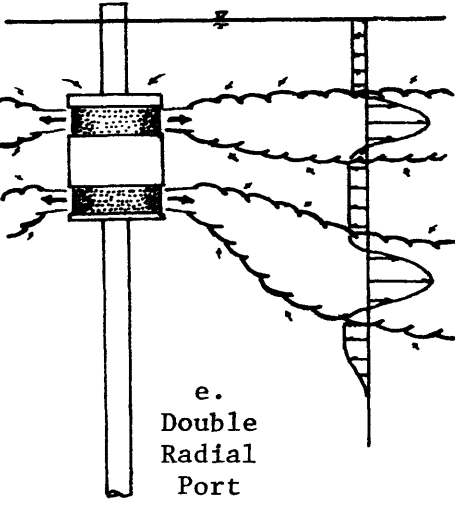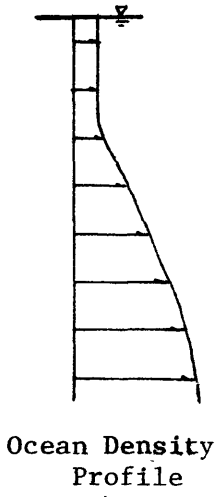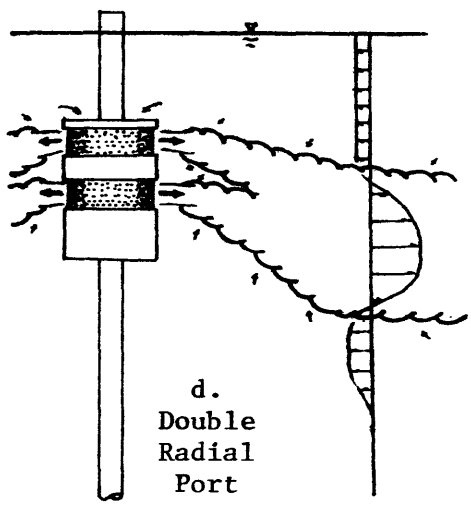
Figure 1-6   Possible Confined Flow
Fields for Ocean
Thermal Energy
Conversion

18

The objective of this study was to explore these flow fields both experimentally and analytically.

1.5 Summary of the Study

An experimental set-up was designed, similar to some encountered in OTEC, but simple enough to facilitate accurate measurements and to allow the results to be interpreted through dimensional analysis. The particular experimental situation chosen was a submerged, negatively buoyant, horizontal, radial jet discharging into ambient water which was initially uniform in temperature. (Figure 1-7) A surface intake was included in some experiments and not in others. Two distinct flow regimes were possible depending on the relative importance of buoyancy and confinement.

The first flow regime (Figure 1-7a) is termed a detached jet. The ambient region above the jet is an irrotational flow consisting entirely of original ambient fluid. The flow magnitude is determined by the entrainment requirements of the upper boundary of the jet and the intake flow,if any. The ambient region below the jet is made up of fluid pulled from the jet as it nears a vertical trajectory. The flow here is rotational and at a lower temperature than the original ambient fluid.

The second flow regime (Figure 1-7b) is termed an attached jet. Low pressures in the circulating region above the jet pull the jet to the surface. After impact the jet flow splits and no longer can be characterized as a jet. The portion of jet flow downstream from the impact point is negatively buoyant with respect to the original ambient fluid and therefore sinks - some returning as entrainment for the underside of

19
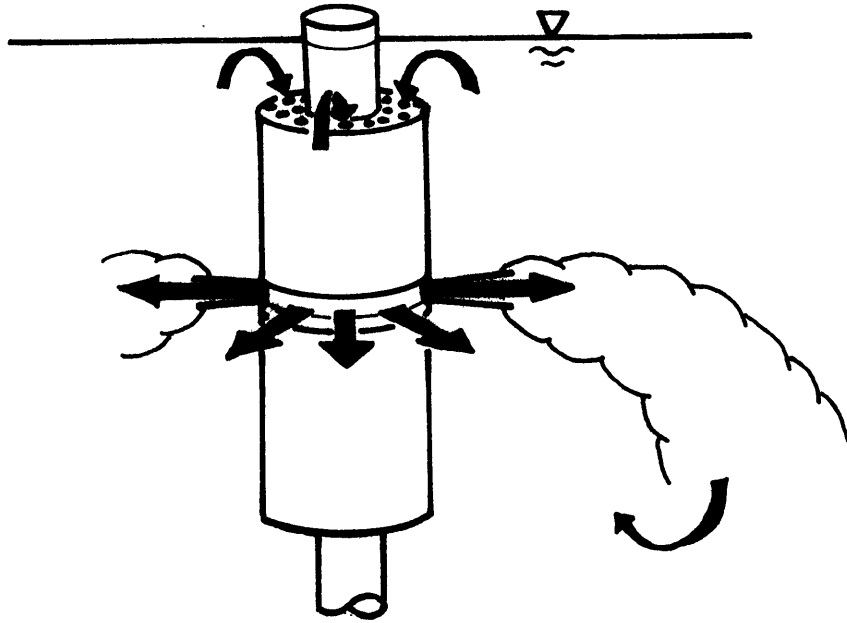
a. Detached Jet

b. Attached Jet
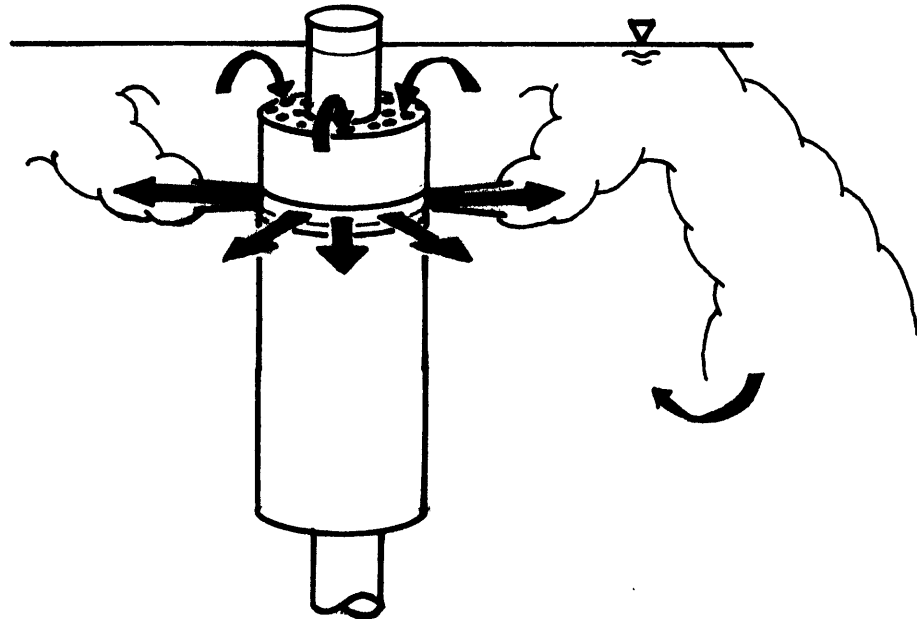
Figure 1-7 Experimental Configuration

20

the jet. In this case neither the top nor the bottom ambient region
has the temperature of the original ambient water and recirculation
into the near surface intake is probable.

Seventeen experiments yielded temperature and trajectory data on
the radial jet in both of the flow regimes. Velocity data also were
collected in the upper ambient region for the detached jet. Finally
discharge conditions that caused transition from one flow regime to the
other were determined. A hysteresis effect was noted as the conditions
for "attaching" a detached jet were different from those needed to
"detach" an attached jet.

Dimensional analysis yielded a single dimensionless number that
was fairly successful at predicting the transition points between regimes.
However, three dimensionless numbers were apparently needed to completely
characterize the experimental behavior. The dimensional analysis was
also helpful in formulating the analytical jet model.

An integral jet model (based on a spreading assumption) was
successfully adapted to include effects of velocity and pressure
fields in ambient regions. The model predicts jet trajectories,
velocities and temperatures, and transitions of experiments between
flow regimes. The model can be applied to plane jets as well and
buoyant and non-buoyant confined plane jet data from other studies were
also compared with model predictions.

II. Results of Related Investigations

Before previous studies are described, the basics of turbulent

jets and two approaches to their analysis are reviewed. The basic

non-buoyant unconfined turbulent jet is described in Section 2.1.

Section 2.2 sets the framework by which physical experiments (guided

by dimensional analysis considerations) can define turbulent jet behavior.

Section 2.3 describes the basic equations and assumptions for a mathematical

approach to turbulent jet problems: integral jet models. Finally

Sections 2.4 and 2.5 present previous investigations relating to this

study. Their description emphasizes information important to the

experimental and mathematical approaches described.

2.1 The Turbulent Jet

Turbulent jets have been studied by many investigators over the

past 50 years. Usually one of three port geometries have been examined:

circular, plane, or radial jets (Figure 2-1). Ambient fluid regions

were usually considered unbounded.

Jets of each of the geometries have certain characteristics in
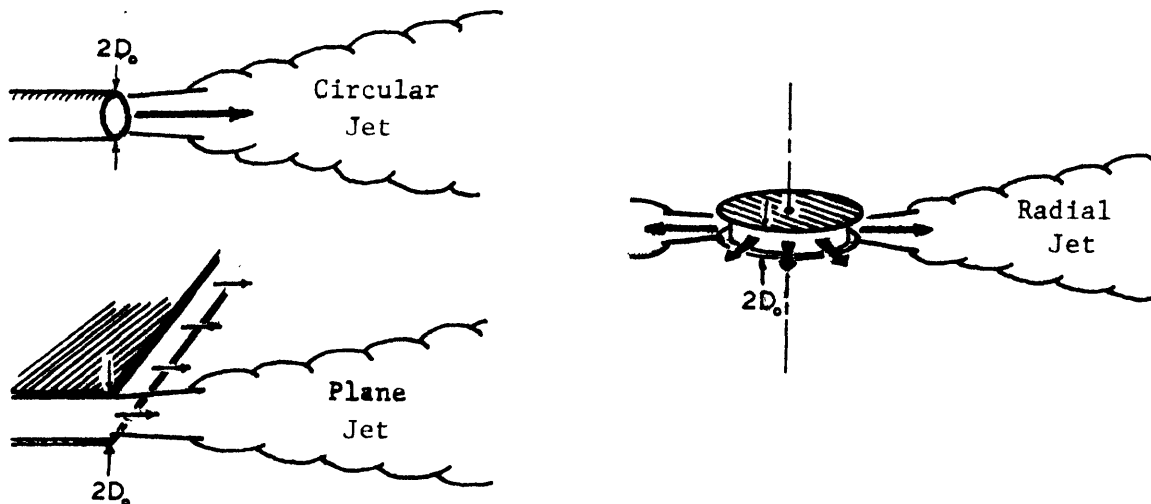
Figure 2-1   Common Jet Discharge Geometries

22

common. Stolzenbach and Harleman (1971) summarize these characteristics

(refer to Figure 2-2).

1. A core region of unsheared flow extending from the jet port.

    This region is gradually engulfed by the spreading turbulent

    zone.

2. A turbulent region that increases in width linearly with

    distance from the port. There is a fluctuating, yet distinct,

    boundary between the turbulent zone and the irrotational flow

    of the ambient fluid. The mean width to this boundary is

    often represented by the sumbol "b". A second width measure,

    $b_{\frac{1}{2}}$, is the width to the point where the time averaged axial

    velocity is one-half of the centerline value. This is the

    width usually measured in experiments.
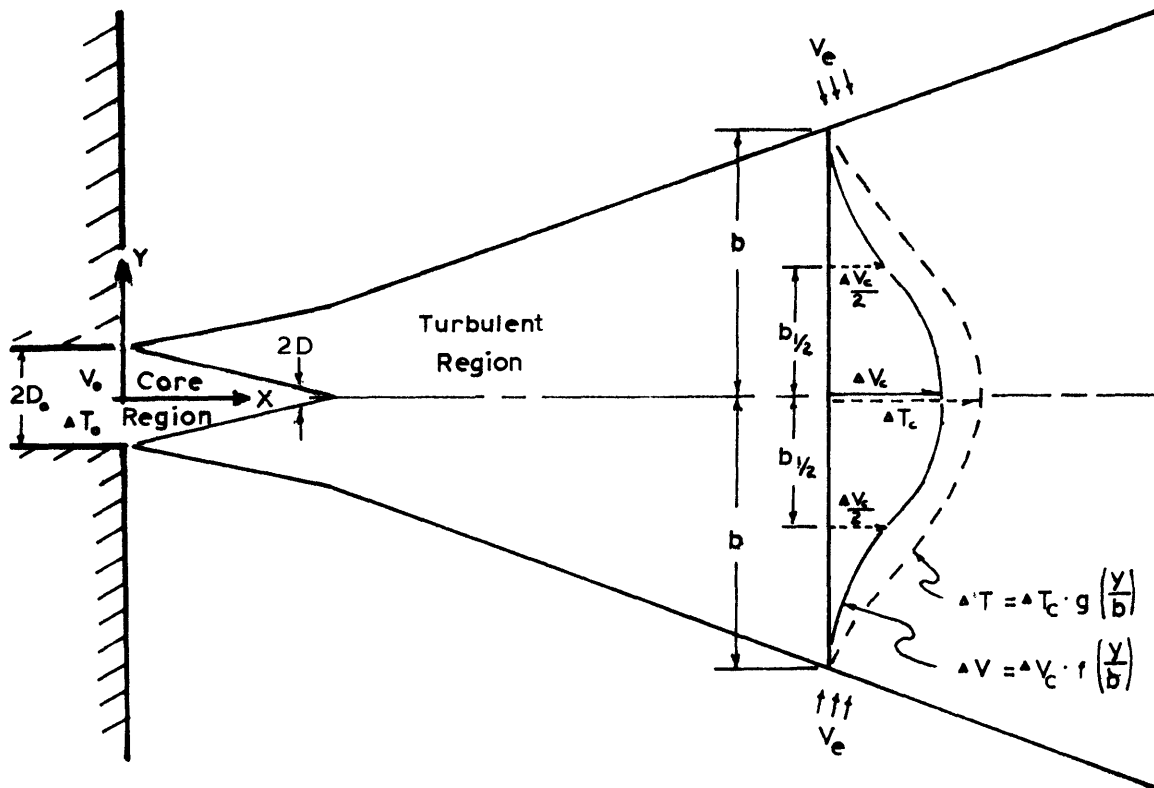
Figure 2-2 Turbulent Jet Characteristics

23

3. Lateral profiles of time-averaged axial velocity in the
   turbulent zone have a similar shape:

   $$\Delta V = \Delta V_c(x) \cdot f\left(\frac{y}{b_{\frac{1}{2}}}\right) \tag{2.1}$$

   where ΔV_c is the centerline velocity and f is the similarity
   function.

4. Scalar quantities such as mean temperature or tracer concentration
   spread at the same rate which is faster than that of the mean
   axial velocity. Lateral profiles of mean temperature excess
   or tracer concentration may be expressed as:

   $$\Delta T = \Delta T_c(x) \cdot g\left(\frac{y}{b_{\frac{1}{2}}}\right) \tag{2.2}$$

   where ΔT_c is the centerline temperature excess (above the
   ambient temperature) and g is the similarity function.

5. Fluctuating components of velocity in the turbulent jet region
   are all of the same order of magnitude. At any lateral section,
   this magnitude is small compared to ΔV_c. Fluctuating
   velocity components (as well as other turbulent quantities)
   are usually observed to develop similarity profiles, too,
   although their development often takes place over a greater
   distance than is required to achieve similarity of time-
   averaged quantities. Similarity of turbulent and time-average
   quantities <u>implies</u> linear jet spreading ($\frac{db_{\frac{1}{2}}}{dx}$ = const.)

6. Entrainment flow from the ambient fluid region is induced by
   turbulent eddies near the jet boundary. The entrainment
   velocity perpendicular to the jet axis is denoted by V_e.

7. Above a minimum Reynold's number ($\mathbb{R}_e$) the jet is fully

   turbulent and its characteristics are independent of $\mathbb{R}_e$.

   The critical value is approximately 1,500 for circular jets.

$$\mathbb{R}_e = \frac{V_o \cdot 2 \cdot D_o}{\nu}$$ (2.3)

where V_o is the discharge velocity, D_o is the port radius,

and ν is the kinematic viscosity.

2.2 Experimental Determination of Jet Behavior

The success of physically modeling and measuring jet behavior

depends on whether a completely similar experiment can be devised and on

how many experiments (taking the desired measurements) are needed to

define the jet over all of its behavior ranges. Jirka et al. (1975)

justify the use of reduced scale physical models for turbulent jet flow

problems similar to OTEC. Dimensional analysis helps determine the

number of experiments needed.

Particular fluid flow fields can be characterized by a set of

independent governing parameters. All flow fields with the same values

of these parameters look exactly alike. Thus a phenomena could conceivably

be analyzed by performing experiments for all possible combinations of

governing parameter values. Referring to Figure 2-3 a convenient list of

independent governing parameters for this study is:

M_o = kinematic discharge momentum flux

B_o = kinematic discharge buoyancy flux

Q_o = discharge flow rate

H_r or H_i = offset distance to remote or coherently impacted

   boundary

25

r_o = radius of discharge port

U_o = ambient region velocity at discharge section (due to

  sources and sinks other than jet entrainment

ϕ_o = vertical angle of discharge port with the dominant boundary

  or a horizontal plane

Intake length scales, dimensions of secondary boundaries, and basic fluid properties such as molecular viscosity and thermal diffusivity are neglected as insignificant. Further simplification of the parameter list is made in the analysis done in Section 3.1. Table 2-1 notes the definitions of M_o, B_o, Q_o for the different jet geometries.
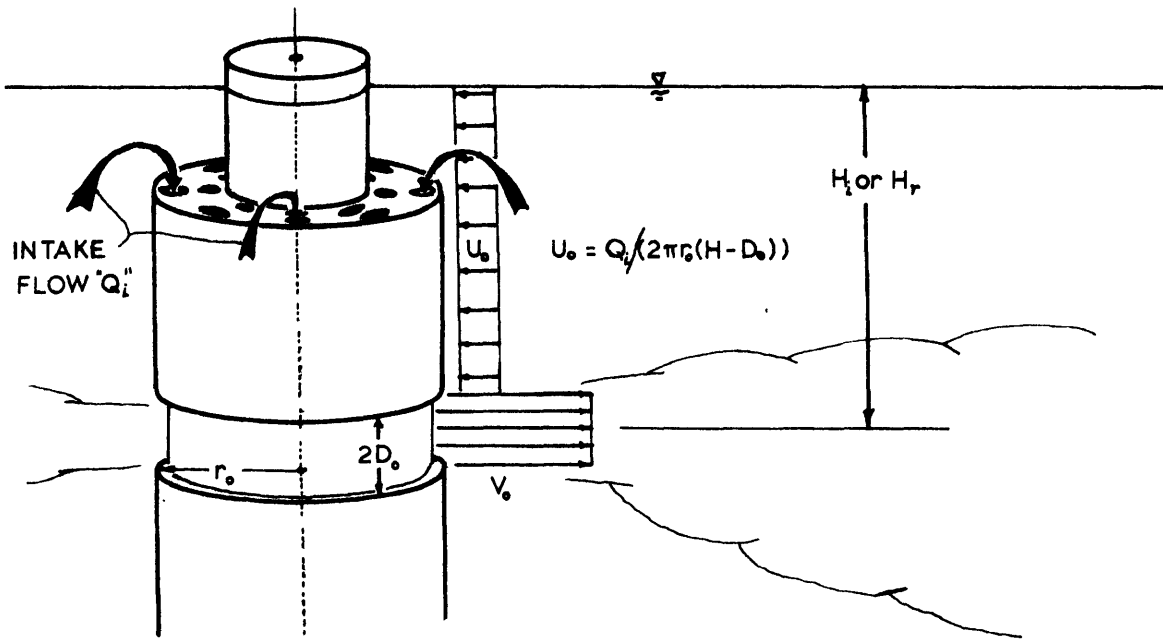
Figure 2-3 Parameter Definition Diagram

	Circular Jet	Plane Jet	Radial Jet
M_o:	$\pi D_o^2 V_o^2$	$2D_o V_o^2$	$4\pi D_o r_o V_o^2$
B_o:	$\pi D_o^2 V_o \dfrac{\Delta\rho}{\rho_a} g$	$2D_o V_o \dfrac{\Delta\rho}{\rho_a} g$	$4\pi D_o r_o V_o \dfrac{\Delta\rho}{\rho_a} g$
Q_o:	$\pi D_o^2 V_o$	$2D_o V_o$	$4\pi D_o r_o V_o$

Table 2-1 Definitions of M_o, B_o and Q_o in Different Geometries

Dimensional (or similarity) analysis calls two flow fields "completely" similar" when a set of independent dimensionless parameters have the same values in each case. Any experimental measurement can be easily scaled to apply to any other "completely similar" flow field. The set of dimensionless parameters involved is derived from the flow field's independent dimensional governing parameters. The Buckingham ∏ theorem states that a phenomena with n independent governing parameters in m dimensions will have a set of n-m independent dimensionless parameters. It is apparent that experiments need only cover the possible combinations of dimensionless parameter values (n-m in number) instead of those for the dimensional governing parameters (n in number).

The parameter list for this study and for the investigations discussed in this chapter are in two dimensions: length and time. Therefore the number of independent dimensionless parameters will be n-2 in each case. Jet phenomena with two or fewer dimensional parameters ($n \leq 2$) are termed self-similar. One experiment can be scaled to describe any example of the phenomena. On the other hand if $n \geq 5$, there are three or more dimensionless parameters whose value ranges must be examined. The number of experiments could easily be unmanageably large.

2.3 Integral Jet Models

Schlichting (1968) simplifies the time-averaged turbulent equations of motion and continuity for the turbulent zone of a plane jet. He uses three assumptions which are consistent with unconfined, turbulent, boundary-layer flows:

1. neglect of molecular transport,

2. neglect of longitudinal gradients of velocity and temperature in contrast to corresponding lateral gradients,

3. constant pressure through the jet.

A similar reduction of the equations is done in Chapter 3 for the experimental jets of this study.

The resulting equations contain turbulent (eddy) flux terms. Eddy viscosity and Prandtl mixing length arguments may be used to rewrite the turbulent terms as functions of mean velocity and temperature qualities (Tollmien, 1926; Goertler, 1942). In contrast, the integral jet model approach assumes a form for the lateral similarity functions of velocity and temperature distribution (Eq. 2.1 and 2.2). The time averaged equations are then integrated between the jet boundaries. The turbulent terms drop out because of the absense of turbulence at the limits of integration (the jet boundary). Neglecting buoyant forces arising from temperature differences, the resulting plane jet equations expressing the conservation of mass, momentum, and heat energy as:

$$\frac{d(\Delta V_c b_{\frac{1}{2}})}{dx} \int_{-\infty}^{\infty} f(\eta)\,d\eta = V_e \Big|_{y=-b}^{y=b} \tag{2.4}$$

$$\frac{d(\Delta V_c^2 b_{\frac{1}{2}})}{dx} \underline{\int_{-\infty}^{\infty} f^2(\eta) \, d\eta} = 0 \qquad (2.5)$$

$$\frac{d(\Delta T_c \Delta V_c b_{\frac{1}{2}})}{dx} \underline{\int_{-\infty}^{\infty} f(\eta)g(\eta)d\eta} = 0 \qquad (2.6)$$

where

$$\eta = y/b_{\frac{1}{2}}$$

2.3.1 Closure Problem

The underlined terms of Eq. 2.4 - 2.6 are all constants derivable from the chosen similarity functions. The four unknowns $b_{\frac{1}{2}}$, ΔV_c, ΔT_c, V_e are functions only of x. So the situation is one of three coupled differential equations in four unknowns. Obtaining another equation is often termed the "closure problem" of integral jet models. The radial and circular jet geometries arrive at an analogous problem.

Closure can be accomplished either by specifying the (linear) rate of jet spreading based on experimental observation:

$$\frac{db_{\frac{1}{2}}}{dx} = \varepsilon_{NB} \qquad (2.7)$$

or by specifying the entrainment velocity at any section as proportional to the centerline velocity:

$$V_e = \alpha \Delta V_c \qquad (2.8)$$

where α is an empirically determined entrainment coefficient. For a complete jet solution integral equations must also be applied to the initial jet region where the unsheared core is present.

29

2.3.2 Buoyancy

The addition of jet buoyancy to integral models is easily accomplished. A new equation (conservation of momentum in the transverse, τ, direction) and a new variable (ϕ, the angle of the jet to the horizontal) are added. Conservation of momentum in the σ direction replaces the x momentum equation (Figure 2-4). Solution in x and y coordinates is also possible but less convenient. Temperature differences ($\Delta T_c \cdot g(\eta)$) allow calculation of the buoyancy forces needed in the new momentum equations.

A choice of correct similarity profiles and a closure assumption is not as easily accomodated to the addition of buoyancy. Some experiments show that buoyant jets do not have constant spreading or entrainment coefficients.

2.3.3 Boundaries

Nearby boundaries in ambient fluid regions may introduce additional considerations into the integral jet formulation. If ambient pressure fields exist (due to confinement), a constant pressure can no longer be assumed for the jet. Ambient fluid velocities will affect jet momentum through entrainment. Similarity profiles for velocity may not go to zero at the jet edge. Jet spreading or entrainment can reasonably be expected to change from their unconfined relationships.

Jet confinements can be divided into two basic boundary types: remote and impacted boundaries (Figure 2-4). Remote boundaries cause pressure and velocity fields in an ambient region without ever contacting the turbulent jet. These fields occur in response to jet entrainment requirements. The ambient region adjacent to a remote boundary contains

30

Remote Boundary

Coherent Impacted Boundary

Diffuse Impacted Boundary

31
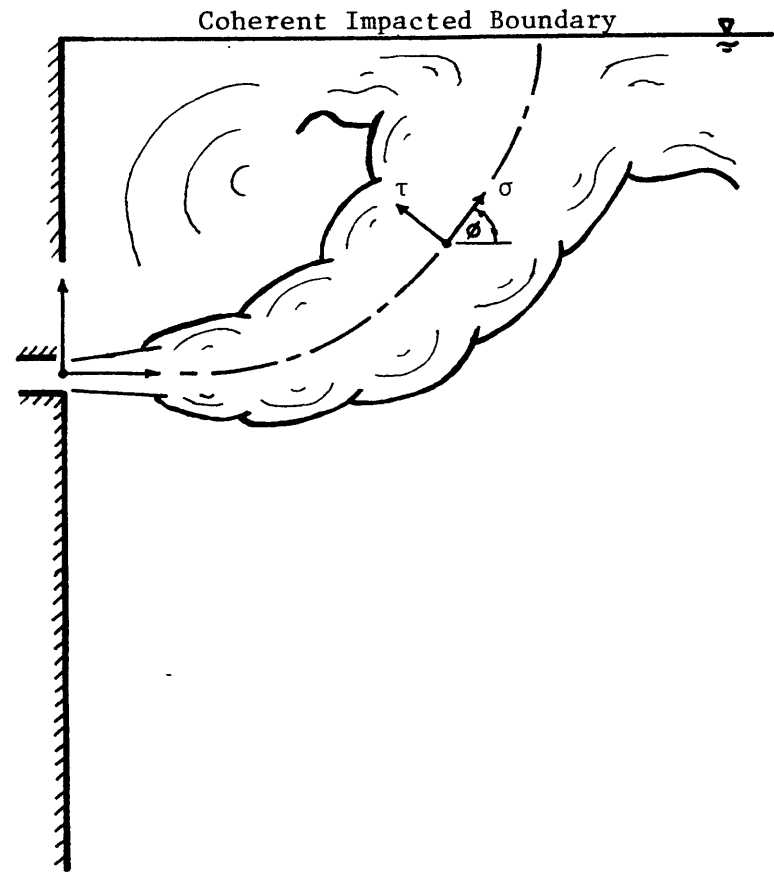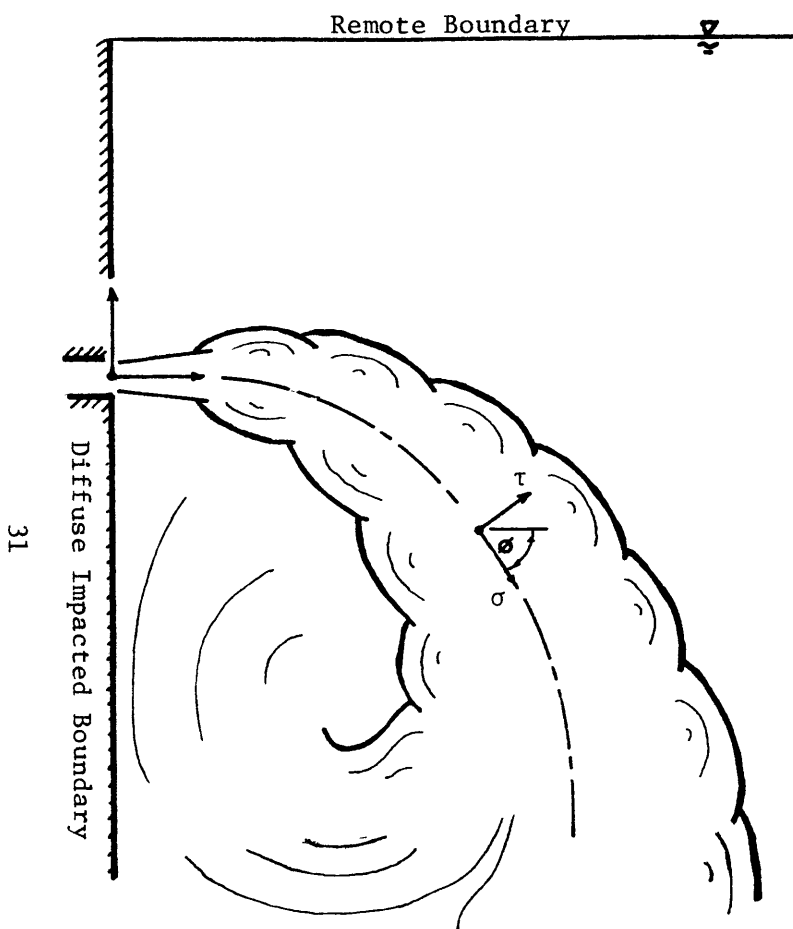
Figure 2-4 Types of Ambient Region Boundaries

no recirculating jet fluid and is therefore irrotational.

Impacted boundaries are those which contact the jet. The flow field in adjacent ambient regions contains jet fluid and is rotational. Impacted boundaries can be loosely sub-divided into those in which the jet retains a coherent structure until impact and those in which the jet loses that structure and becomes diffuse before impact. A coherent jet structure is one in which velocity and temperature similarity functions ($f(\eta)$ and $g(\eta)$) still apply reasonably well. Actually "coherent" and "diffuse" impacted boundaries are the limiting cases of a range of jet behavior depending on the amount of jet bending.

2.4 Review of Basic Jet Investigations

The studies in this section describe experiments with few independent governing parameters. The parameters can be combined to form at most two dimensionless parameters. One or more experimental investigations of jet behavior have usually been performed in each case.

Two problems stand out for integral jet models of the type described in the present study. The first is determining the appropriate shape of lateral temperature and velocity profiles of buoyant jets influenced by ambient pressure, temperature, and velocity fields. The second problem is the formulation of an accurate closure relation in light of the same considerations. Limiting the number of governing parameters allows the effects of several of the parameters of this study to be isolated and examined spearately.

Previous jet investigations have greatly favored the plane and

circular discharge geometries. Some results in those geometries will eventually have to be applied to radial jets without verification due to the lack of data on radial jets.

2.4.1 Unconfined Non-Buoyant Jets

2.4.1.1 Parameterization

The plane and circular jet geometries have only the initial volume and momentum flux (Q_o and M_o) as independent parameters. In radial geometry the port radius (r_o) enters as a third parameter which yields the following dimensionless parameter:

$$A = r_o \sqrt{M_o}/Q_o = \sqrt{\frac{r_o}{2D_o}} \qquad (2.9)$$

As A becomes large, jet behavior should approach that of a plane jet.

2.4.1.2 Profile Data

Many investigators have measured lateral velocity profiles for each of the jet discharge geometries. An important result is that the velocity profile shape ($f(\eta)$) is reasonably independent of the jet geometry considered (see Figure 2-5). The temperature profile shape ($g(\eta)$) appears narrower in the circular jet than in the plane jet, though there is some discrepancy among researchers. Radial jet temperature profiles have apparently not been studied.

The profiles appear in integral jet equations as integral shape constants (Equations 2.4-2.6). The necessary constants for each geometry are defined in Table 2-2.
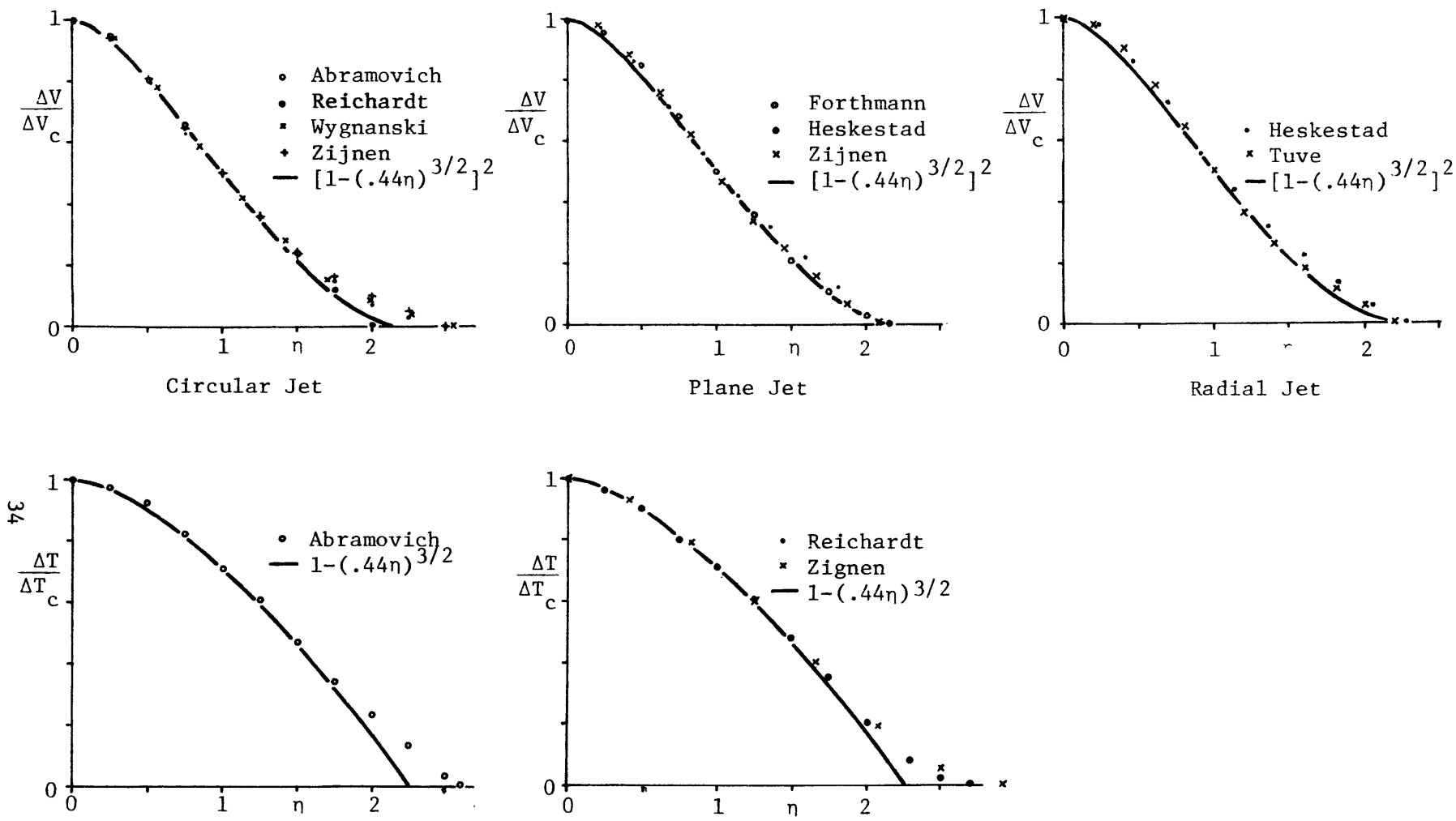
Figure 2-5 Non-Buoyant Jet Mean Profile Data Compared to Polynomial Profiles

34

Radial or Plane Jet	Circular Jet
$I_1 = \int_0^\infty f(\eta)d\eta$	$I_1{}^* = \int_0^\infty \eta f(\eta)d\eta$
$I_2 = \int_0^\infty f(\eta)^2 d\eta$	$I_2{}^* = \int_0^\infty \eta f(\eta)^2 d\eta$
$J_1 = \int_0^\infty g(\eta)d\eta$	$J_1{}^* = \int_0^\infty \eta g(\eta)d\eta$
$J_2 = \int_0^\infty g(\eta)^2 d\eta$	$J_2{}^* = \int_0^\infty \eta g(\eta)^2 d\eta$
$K_1 = \int_0^\infty g(\eta)f(\eta)d\eta$	$K_1{}^* = \int_0^\infty \eta g(\eta)f(\eta)d\eta$

<center>Table 2-2 Integral Shape Constants</center>

Table 2-3 lists constant values determined experimentally and by using two assumed profile forms:

Polynomial Profiles

$$\frac{\Delta V}{\Delta V_c} = f(\eta) = [1 - (.441|\eta|)^{3/2}]^2 \qquad \text{for} - 2.27 < \eta < 2.27$$
$$= 0 \qquad \text{for} \quad |\eta| > 2.27 \qquad (2.10)$$

$$\frac{\Delta T}{\Delta T_c} = g(\eta) = 1 - (.441|\eta|)^{3/2} \qquad \text{for} - 2.27 < \eta < 2.27$$
$$= 0 \qquad \text{for} \quad |\eta| > 2.27 \qquad (2.11)$$

Exponential Profiles

$$\frac{\Delta V}{\Delta V_c} = \exp(- .693 \, \eta^2) \qquad \text{for} - \infty < \eta < \infty \qquad (2.12)$$

$$\frac{\Delta T}{\Delta T_c} = \exp(- .693 \, \eta^2/\gamma^2) \qquad \text{for} - \infty < \eta < \infty \qquad (2.13)$$

where γ is the ratio of the width $b_{\frac{1}{2}T}$ (where temperature difference reaches half of its centerline value) to $b_{\frac{1}{2}}$.

<center>35</center>

2.4.1.3 Closure Relation Data

For the plane and circular jet geometries, the choice between a spreading or an entrainment closure equation is immaterial. A constant spreading rate, ε_{NB}, necessitates a constant entrainment coefficient, α. With spreading, flow, and conservation of momentum equations, Jirka et al. (1975) derive

$$\frac{db_{\frac{1}{2}}}{dx} = \varepsilon_{NB} = \frac{2\alpha}{I_1} \qquad \text{plane jets} \qquad (2.14)$$

$$\varepsilon_{NB} = \frac{\alpha}{I_1^*} \qquad \text{circular jets} \qquad (2.15)$$

For the radial jet discharge geometry, a constant spreading rate and a constant entrainment coefficient give different results. The expression analogous to Eq. 2.14 or 2.15 is

$$\varepsilon_{NB} = \frac{2\alpha}{I_1} - \frac{b_{\frac{1}{2}}}{r} \qquad (2.16)$$

A constant ε_{NB} implies $b_{\frac{1}{2}}$ is proportional to x (or $r-r_0$). Thus $b_{\frac{1}{2}}/r$, and consequently α must change along the jet path (Figure 2-6).

Experimental studies have determined the spreading rate ε_{NB} by measuring lateral velocity profiles. ε_{NB} is found to have a nearly constant value along the jet path for each of the three geometries[1]. Considering the scatter of experimental values in Table 2-3, ε_{NB} is also essentially constant among the three geometries. Temperature profile spreading and jet boundary spreading ($b_{\frac{1}{2}T}$ and b) are also noted in Table 2-3.

---

[1] Heskestad (1965) indicates a 10% increase in the value of ε_{NB} for a plane jet for $\frac{\Delta V_c}{V_0} < .43$.

$$b_{1/2} = \varepsilon_{NB} \, x$$

$$= \varepsilon_{NB}(r-r_o)$$
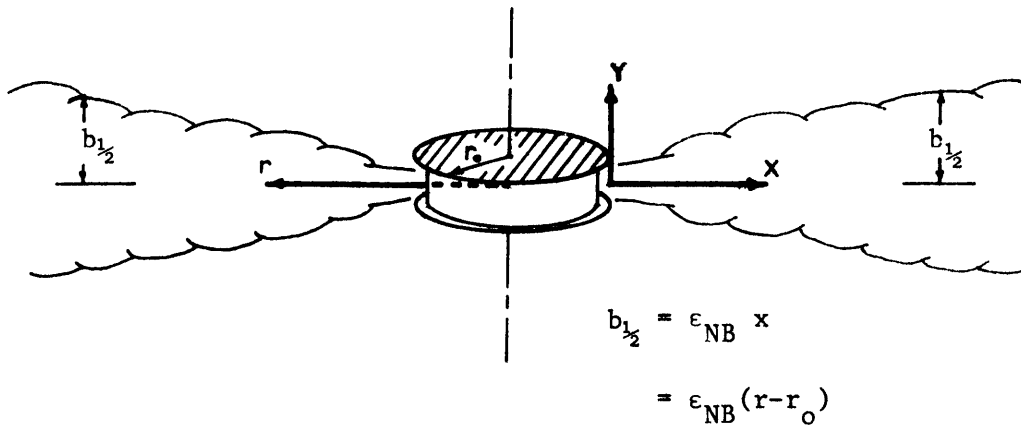
Figure 2-6 Radial Jet Spreading
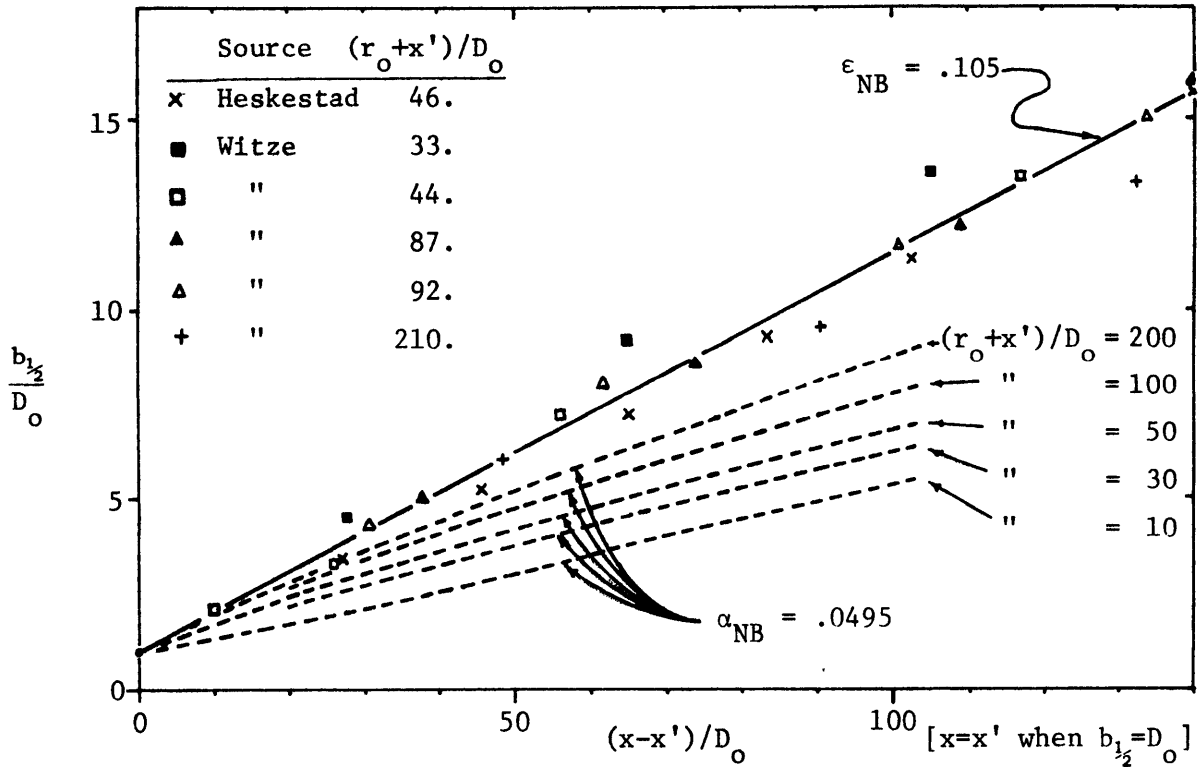
Figure 2-7 Radial Jet Spreading Data and Closure Assumptions

Geometry	Sources	$\varepsilon_{NB} = \dfrac{db_{1/2}}{dx}$	$\dfrac{b}{b_{1/2}}$	$\dfrac{b_{1/2T}}{b_{1/2}}$	I_1	I_2	J_1	J_2	K_1
	Witze (1976)	.106							
	Heskestad (1966)	.110			1.10	0.78			
Radial	Tuve (1953)		1.81[a]		1.06	0.77			
Jet	Polynomial Profiles			1.43	1.02	0.72	1.36	1.02	0.84
	Exponential Profiles				1.06	0.75			
	Kotsovinos (1975)	.108		1.40	1.06[b]	0.75[b]	1.49[b]	1.05[b]	0.88[b]
	Heskestad (1965)	.110	1.77		1.07	0.76			
Plane	v.d. Hegge Zijnen (1957)	.098		1.45	1.05	0.76	1.44	1.06	0.87
Jet	Reichardt (1951)			1.45			1.40	1.03	0.84[c]
	Forthmann (1934)	.099			1.05	0.76			
	Polynomial Profiles			1.43	1.02	0.72	1.36	1.02	0.84
	Exponential Profiles				1.06	0.75	1.54[d]	1.08[d]	0.87[d]
					I_1^*	I_2^*	J_1^*	J_2^*	K_1^*
	Wygnanski (1969)	.088	1.85		0.75	0.37			
	Abramovich (1963)[e]	.097		1.43	0.68	0.36	1.24	0.71	0.47
	Reichardt (1951)				0.73	0.35			
Circular	Albertson (1950)	.097							
Jet	Hinze (1948)	.094		1.17	0.77	0.37	0.84[b]	0.49[b]	0.42[b]
	Corrsin (1946)	.084		1.20					
	Polynomial Profiles			1.43	0.66	0.34	1.10	0.66	0.46
	Exponential Profiles				0.72	0.36	0.85[f]	0.50[f]	0.42[f]

Notes:

a. Actually db/dx was measured, values reflect Heskestad's value for $db_{1/2}/dx$
b. Uses author's fitted exponential profiles
c. Reichardt temperature data with polynomial velocity profile
d. Uses mean experimental value of $b_{1/2T}/b_{1/2}$
e. Based on review of many Russian and German studies
f. Uses value of $b_{1/2T}/b_{1/2} = 1.18$

Table 2-3 Experimental Data for Unconfined, Nonbuoyant Jets

2.4.1.4 Radial Jet Behavior

Radial jet data from Witze (1976), Heskestad (1966), and Tuve (1953) strongly support a closure assumption of a constant spreading rate, independent of A (Figure 2-7). The measured spreading rate is also essentially equal to the plane jet value. A constant entrainment coefficient would be inconsistent with observed non-buoyant radial jet behavior.

Because experimental values for plane and radial jets are indistinguishable in Table 2-3, plane jet data will be used to supplement radial jet data. This practice will be even more imperative in succeeding sections.

Heskestad (1965) suggests the existence of two slightly different plant jet spreading rates, with a transition at $\frac{\Delta V_c}{V_o} \approx .43$. Forthmann (1934) and v.d. Hegge Zijnen (1957) measured jet properties in the region where $\frac{\Delta V_c}{V_o} > .43$. Heskestad (1965) and Kotsovinos (1975) primarily measured spreading at greater distances for which $\frac{\Delta V_c}{V_o} < .43$. A spreading relation exhibiting this transition is:

$$\varepsilon_{NB} = .105 + .005 \tanh[(.43 - \frac{\Delta V_c}{V_o})/.028]$$ (2.17)

2.4.2 Zone of Flow Establishment

An unsheared core of fluid distinguishes spreading in this zone from fully developed jet spreading (Figure 2-2). Lateral velocity and temperature profiles and a closure relation are still required for an integral jet model. An appropriate closure relation is the decay of the unsheared half-width, dD/dx.

Albertson et al. (1950) is one of the few studies with detailed

measurements in this relatively short zone. However experimental work

on turbulent shear layers (Figure 2-8) can be applied. Jet establishment

or shear layer experimental results can be used until the core disappears

(D=0) and before switching to the fully developed jet relations of

Section 2.4.1. However some transition must occur between the two regions

and their different spreading rates.

2.4.2.1 Paramerization

This region is governed by the same non-buoyant jet parameters

discussed in Section 2.4.1.1. The initial flow rate, Q_o, is much more

important to the observed behavior in this zone than for the fully

developed jet.

2.4.2.2 Profile Data

Flow establishment zones and shear layers in the radial geometry

have not been studied. However there is sufficient data for the plane

jet geometry. The mean velocity profiles in the sheared region have the

same shape and integration constants as found for the fully developed

jet (Figure 2-8 and Table 2-4). The mean velocity in the core region

is simply the discharged value, V_o.

Sheared temperature difference profiles spread more quickly

(than velocity profiles) into both the quiescent and the moving fluid.

Jet centerline temperature differences are reduced to below the discharge

value well before the velocity core disappears (v.d. Hegge Zignen 1957).

The turbulence measurements of Wygnanski find $b/b_{1/2}$ significantly

different from fully developed jet profiles.
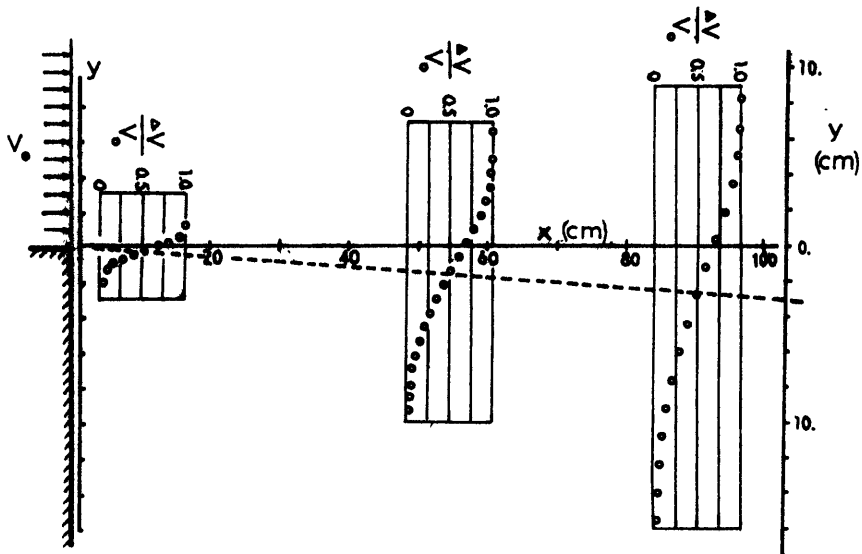
Liepmann and Laufer (1947) Data
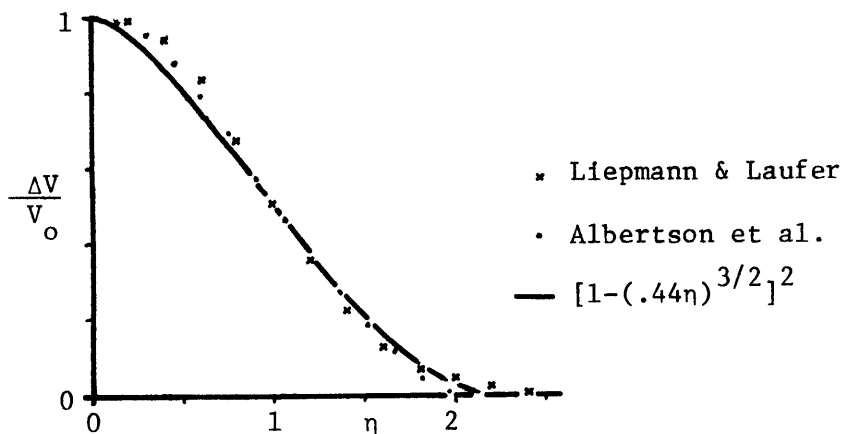
Figure 2-8   Plane Shear Layer Mean Profile Data

41

2.4.2.3 Spreading Relation

Albertson et al. (1950) and Liepmann (1947) observed almost equal

spreading rates (Table 2-3, Figure 2.8) with jets and shear layers respectively.

If dD/dx is assumed constant, then momentum conservation (between the

discharge point and the end of the flow establishment region) may be

written as

$$D_o = b_{\frac{1}{2}} I_2 = (D_o + .031 \ L) \cdot I_2 \qquad (2.18)$$

$$\frac{dD}{dx} = .031/(1 - \frac{1}{I_2}) \approx - .095 \qquad (2.19)$$

where L is the length of the velocity core. This is close to Albertson's

published value of -.097.

The present study found that the following relationships are more

accurate[1] as part of an overall integral jet model:

$$\frac{d(D + b_{\frac{1}{2}})}{dx} = .025 \qquad (2.20)$$

$$\frac{dD}{dx} = - .07 \qquad (2.21)$$

An overall integral jet model applies the fully developed jet relations

as soon as the core disappears without considering any transition

between zones. The revised equations (2.20 and 2.21) enable the overall

integral jet model to better model jet behavior in the transition between

zones and beyond (x $\geq$ L).

2.4.2.4 Radial Jet Behavior

Plane jet velocity profile coefficients from Table 2-4 are applied

---

[1] the data of plane and radial jet data of Heskestad were primarily used for
comparison.

42

Geometry	Source	$\dfrac{d(D+b_{\frac{1}{2}})}{dx}$	$\dfrac{b}{b_{\frac{1}{2}}}$	$\dfrac{b_{\frac{1}{2}T}}{b_{\frac{1}{2}}}$	I_1	I_2	J_1	J_2	K_1
Plane Shear Layer	Wygnanski (1970)	.048[a]	1.36						
	Albertson (1950)	.032			1.03	.76			
	Liepmann (1947)	.029			1.05	0.79			
	Polynomial Profiles			1.43	1.02	0.72	1.36	1.02	0.84
	Exponential Profiles				1.06	0.75	1.36[b]	1.08[b]	0.84[b]

Notes:

a. Because of experimental conditions, probably not applicable to flow establishment of jets
b. Used experimental value of $b_{\frac{1}{2}T}/b_{\frac{1}{2}}$

Table 2-4 Experimental Data for Plane Shear Layer

to the sheared regions in the zone of flow establishment of a radial jet. These are essentially the same as those found in the fully developed radial jet. Velocity in the core is uniform at the discharged value V_o.

The easiest assumption (and perhaps best because of a lack of data) about temperature profiles is that temperature differences also have a core width D. However, the core temperature difference, while uniform, is not fixed at any value. The sheared profile shapes on either side of the core must rely on fully developed plane jet data.

Unlike the profile conclusions, a plane jet spreading relation is probably not directly applicable to radial jets. The core width (D) of the radial jet would be expected to decrease with x even without turbulent shear effects (because of the increasing radial coordinate). With no radial jet data available, a plausible assumption is that the lateral area of the core region decreases at the same rate as in a plane jet. Thus

$$\frac{d(2\pi r \cdot D)}{dr} = - 0.07 \cdot 2\pi r$$

$$\frac{dD}{dr} = - 0.07 - \frac{D}{r} \tag{2.22}$$
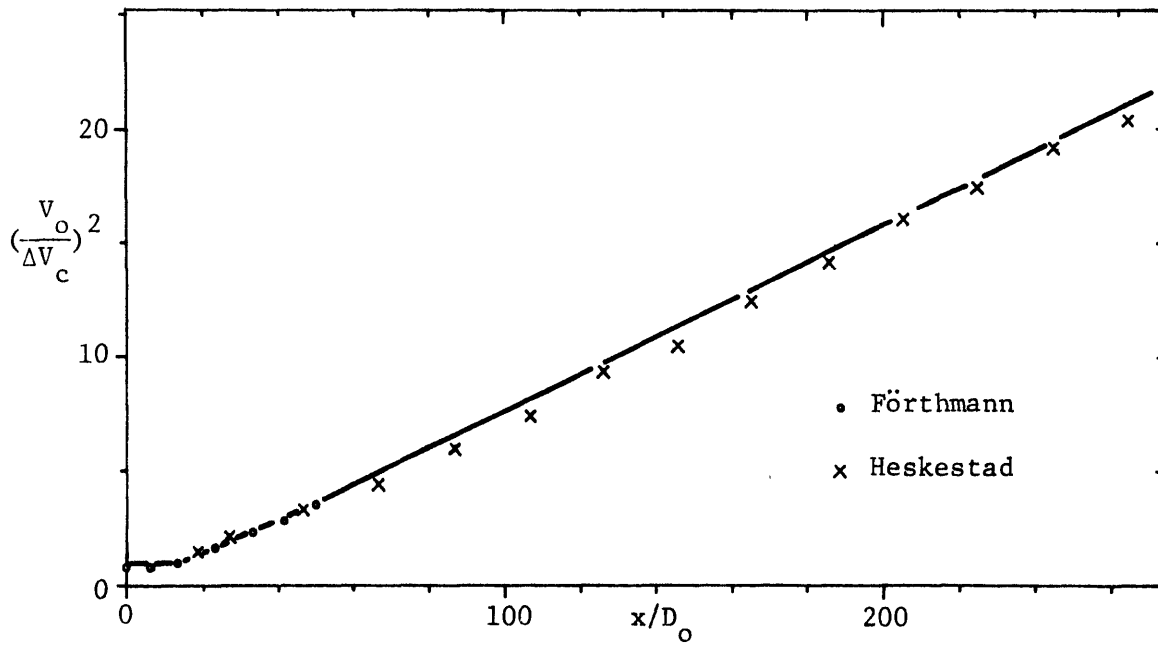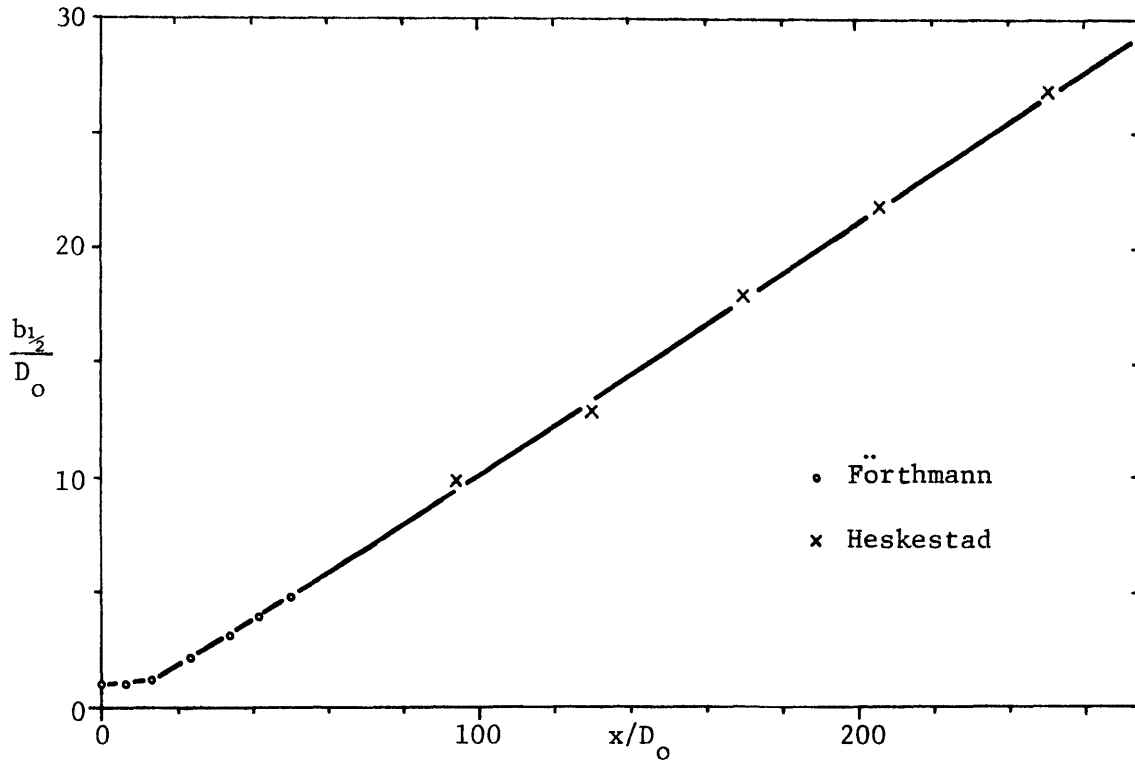
Figure 2-9   Non-Buoyant Plane Jet Integral Model Results
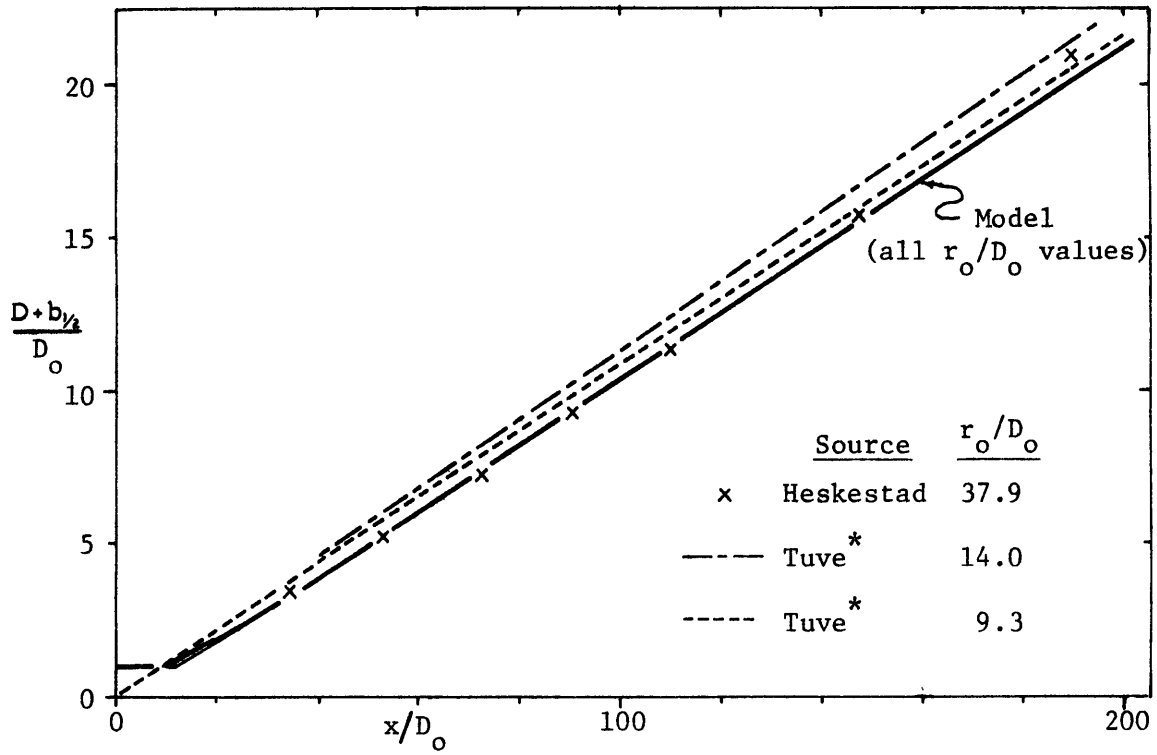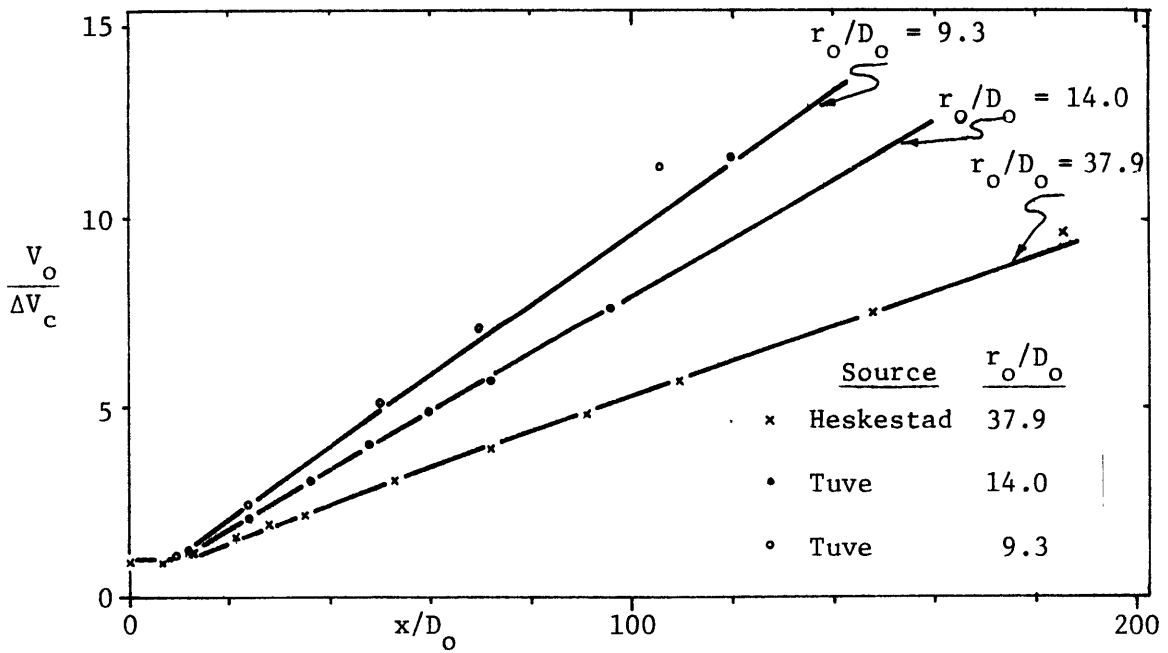
Figure 2-10 Non-Buoyant Radial Jet Integral Model Results

D and hence $b_{\frac{1}{2}}$ no longer vary linearly.

Closure and profile assumptions have now been made for both zones of plane and radial non-buoyant jets. Therefore the integral models are complete. The integral model results are compared with experimental data of jet spreading and centerline velocity decay in Figure 2-9 (plane jets) and Figure 2-10 (radial jets).

2.4.3 Co-flowing Ambient Fluids

This section will deal with non-buoyant jets discharged into uniform co-flowing velocity streams. Since radial jets in an ambient current have not been studied, plane jet data will again be used to infer radial jet behavior.

2.4.3.1 Parameterization

In the circular and plane jet geometries there are three governing dimensional parameters: M_o, Q_o, and U_o. The new parameter, U_o, is the uniform ambient fluid velocity relative to the jet port. (In the context of the present study U_o is the radial inward flow caused by the plant intake. When U is spatially variable, U_o denotes a reference value.) One dimensionless parameter governs behavior.

$$IV = M_o/Q_o \cdot U_o \qquad (2.23)$$

2.4.3.2 Profile Data

The profile shape of excess velocity (velocity above ambient velocity) is identical to the velocity profile of Section 2.4.1. Data from Weinstein (1957) are presented in Figure 2-11. Temperature difference profiles also have shapes similar to jets in nonflowing ambient fluids. This makes all the profile integrals of Table 2-5 the same as well.

46
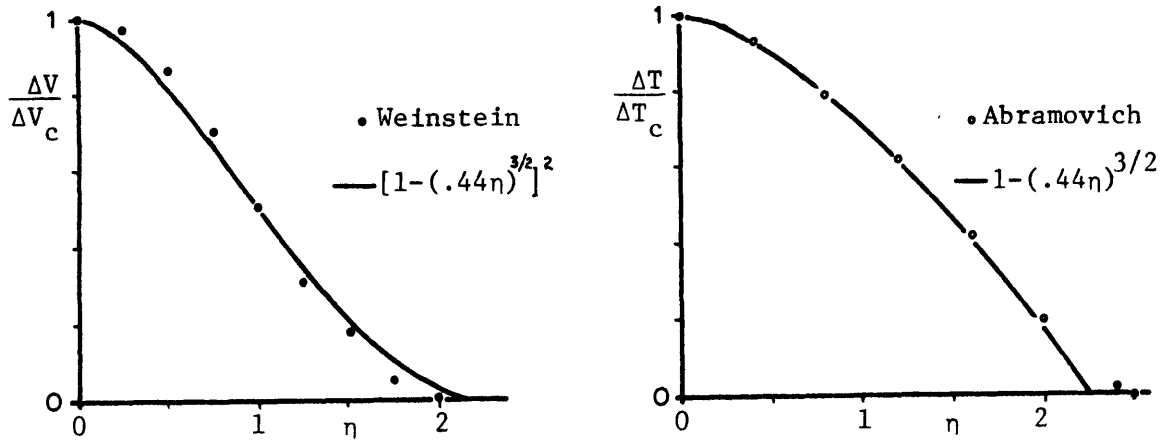
Figure 2-11   Co-flowing Jet Mean Profile Data
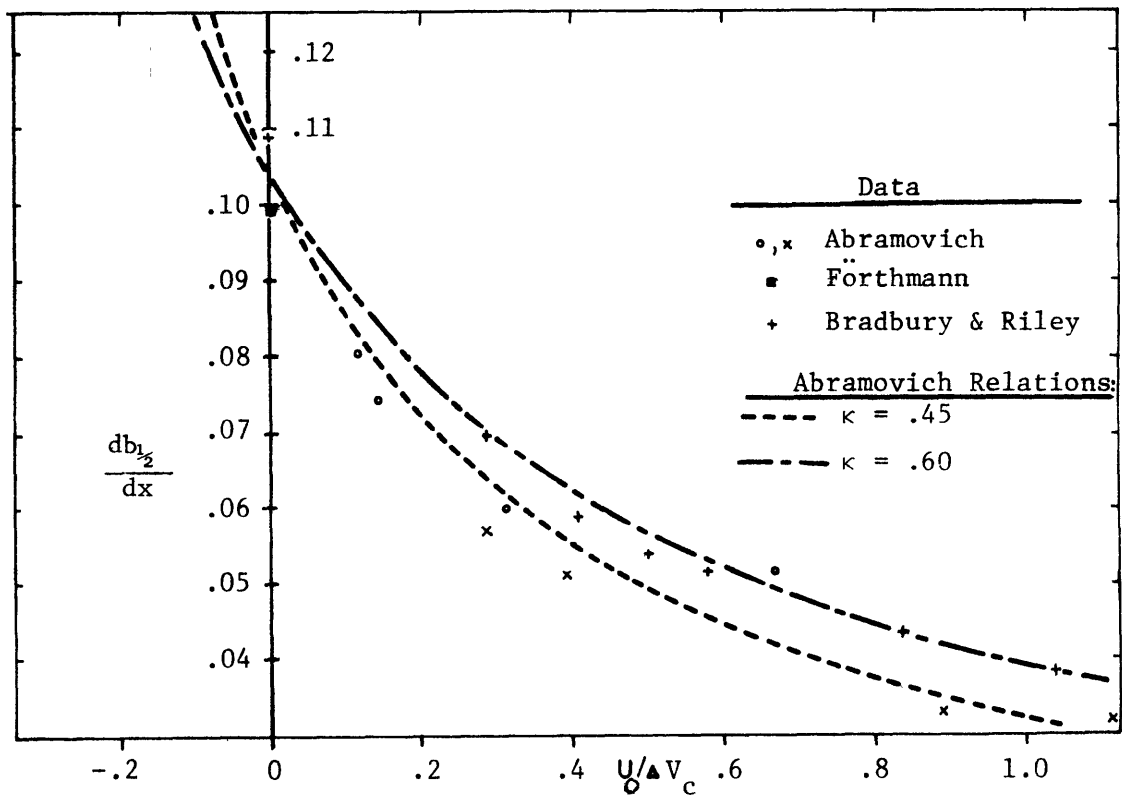
Figure 2-12   Spreading Rate with Ambient Velocities

Geometry	Source	$\dfrac{db_{\frac{1}{2}}}{dx}$	$\dfrac{b}{b_{\frac{1}{2}}}$	$\dfrac{b_{\frac{1}{2}T}}{b_{\frac{1}{2}}}$	I_1	I_2	J_1	J_2	K_1
Plane Co-Flowing Jets	Bradbury (1967)	$f(\frac{U}{V_c})$			1.01	0.73			
	Abramovich (1963)[a]	"		1.46			1.39	1.03	0.85[b]
	Weinstein (1957)	"			1.02	0.76			
	Polynomial Profiles				1.02	0.72	1.36	1.02	0.84
	Exponential Profiles				1.06	0.75	1.55[c]	1.10[c]	0.88[c]

Notes:
a. Actually profile data of CO_2 concentration of a CO_2 jet into air
b. Used polynomial velocity profile
c. Used experimental value of $b_{\frac{1}{2}T}/b_{\frac{1}{2}}$

Table 2-5 Experimental Data for Plane Co-flowing Jets

2.4.3.3 Spreading Relation

Rajaratnam (1976) includes a whole chapter on plane jets in co-flowing streams. His similarity analysis shows that jet spreading is proportional to x for $V \gg 1$ (termed strong jets) and proportional to $\sqrt{x}$ for $V \ll 1$ (termed weak jets). Any discharged "strong" jet goes through a transition between these proportionalities as it becomes a weak jet. Many studies with experimental data and empirical formulas (for spreading and centerline velocity decay) are cited by Rajaratnam.

Abramovich (1963) makes a jet spreading assumption much simpler than many mentioned by Rajaratnam. This assumption fits data well - expecially for "stronger" jets. It is also extendable to counter-flowing ambient fluids (section 2.4.4) which are considerably more important in this radial jet study.

Abramovich's argument (simply stated) is that the jet boundary moves laterally at a speed proportional to the centerline excess velocity, ΔV_c. At the same time, jet fluid moves ahead at an average velocity of

$$\bar{V} = [2b^*U_e + \int_{-\infty}^{\infty} \Delta V dy]/2b^*$$

$$= U_\bullet + \Delta V_c \; \frac{I_1 b_{\frac{1}{2}}}{b^*} \qquad\qquad (2.24)$$

where b^* is the jet half-width over which the velocity is averaged. Jet spreading, according to Abramovich, is simply a ratio of these velocities

$$\epsilon_c = \epsilon_{NB} \; (I_1 \frac{b_{\frac{1}{2}}}{b^*}) \; \frac{\Delta V_c}{U_\bullet + \Delta V_c I_1 \frac{b_{\frac{1}{2}}}{b^*}}$$

$$= \epsilon_{NB} \; \times \; \frac{\kappa}{U_\bullet / \Delta V_c + \kappa} \qquad\qquad (2.25)$$

where ϵ_{NB} is the nonbuoyant jet spreading rate in a stagnant ambient and $\kappa = I_1 b_{\frac{1}{2}}/b^*$. The value of b^* (hence κ) is a fitting coefficient. However it should be closer to b (a measure of the turbulent zone width) than $b_{\frac{1}{2}}$ in value.

Experimental spreading rates are plotted (Figure 2-12) with ϵ_c for two values of b*

$$b_1^* = 2.2 \; b_{\frac{1}{2}} = 1.22 \; b \qquad (\kappa_1 = .45)$$

$$b_2^* = 1.7 \; b_{\frac{1}{2}} = 0.94 \; b \qquad (\kappa_2 = .60) \qquad\qquad (2.26)$$

The first value, b_1^*, is suggested by Abramovich and it fits the data he cites (Figure 2-12, open symbols) well. The second value, b_2^*, is a better fit to the mean curve drawn through results of Bradbury and Riley (1967). Figure 2-13 shows the spread of co-flowing jets of various V values. The use of b_2^* in the spreading relation allows an integral jet model to fit this data better.
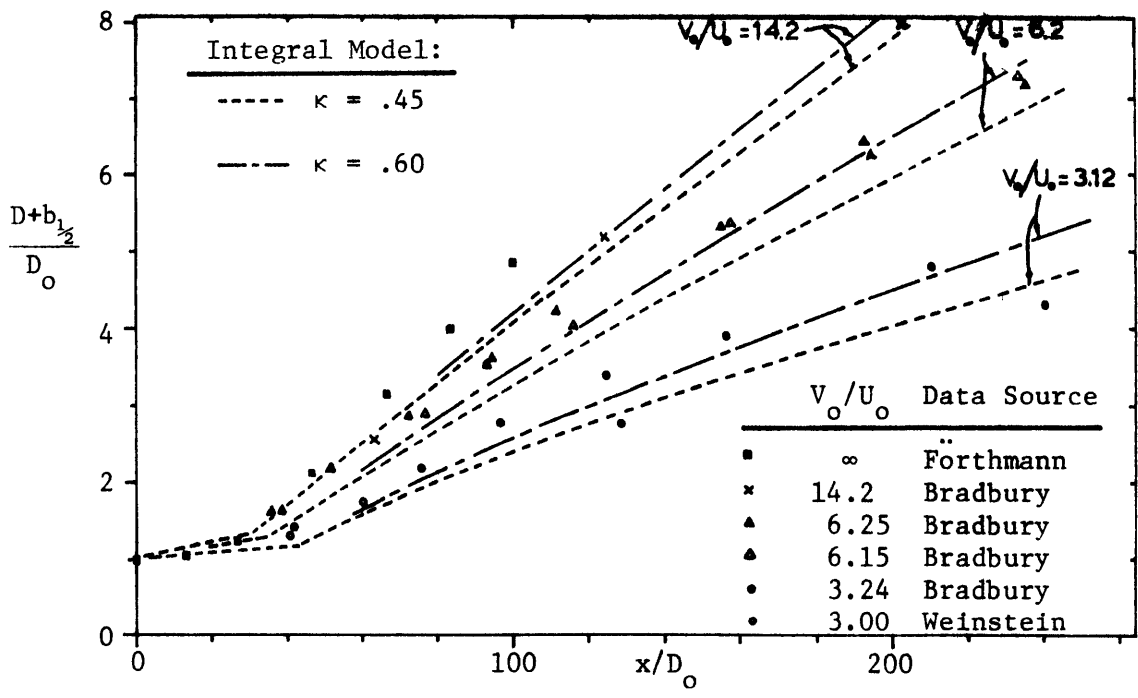
Figure 2-13 Jet Spreading in a Co-Flowing Ambient

2.4.3.4 Radial Jet Behavior

The original profile constants of section 2.4.1 appear applicable in co-flowing stream situations as well.

Radial jet spreading was found to be constant and equal to plane jet spreading in stagnant ambients. Therefore the plane jet spreading relation just derived will be applied directly to radial jets. The choice of fitting constant, κ, will be determined in the next section where the same relation is applied to counter-flowing ambients.

2.4.4 Counter-Flowing Ambient Fluids

A non-buoyant jet discharging into an unbounded uniform counterflow must eventually be "blown" back upon itself. For this reason jet boundaries and other behavior are not easily discerned (Figure 2-14). The relatively scarce data for this situation are for the circular jet geometry only.

2.4.4.1 Parameterization

The parameters and dimensionless number are exactly the same as for the co-flowing case. Only the sign of U_o has changed.

2.4.4.2 Profile Data

Both Rajaratnam (1976) and Abramovich (1963) refer to circular jet studies. Only Abramovich displays excess velocity (above ambient velocity) profile data from the work of Vulis (1955). The unconfined, non-buoyant jet profile shape is again apparent in Figure 2-14.

2.4.4.3 Spreading Relation

The main concern in the experiments cited was for the jet penetra-
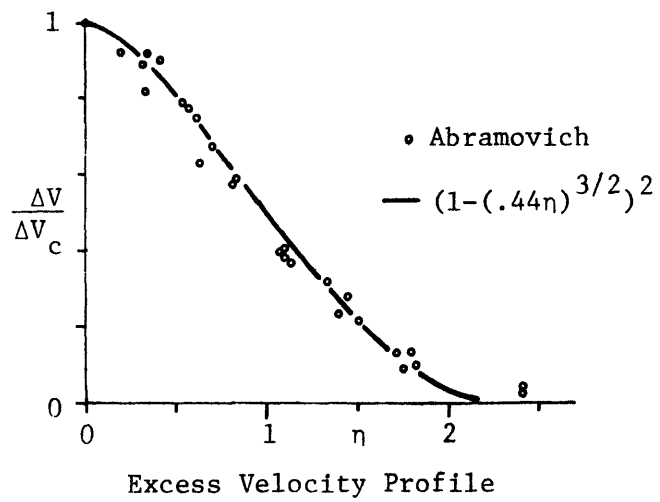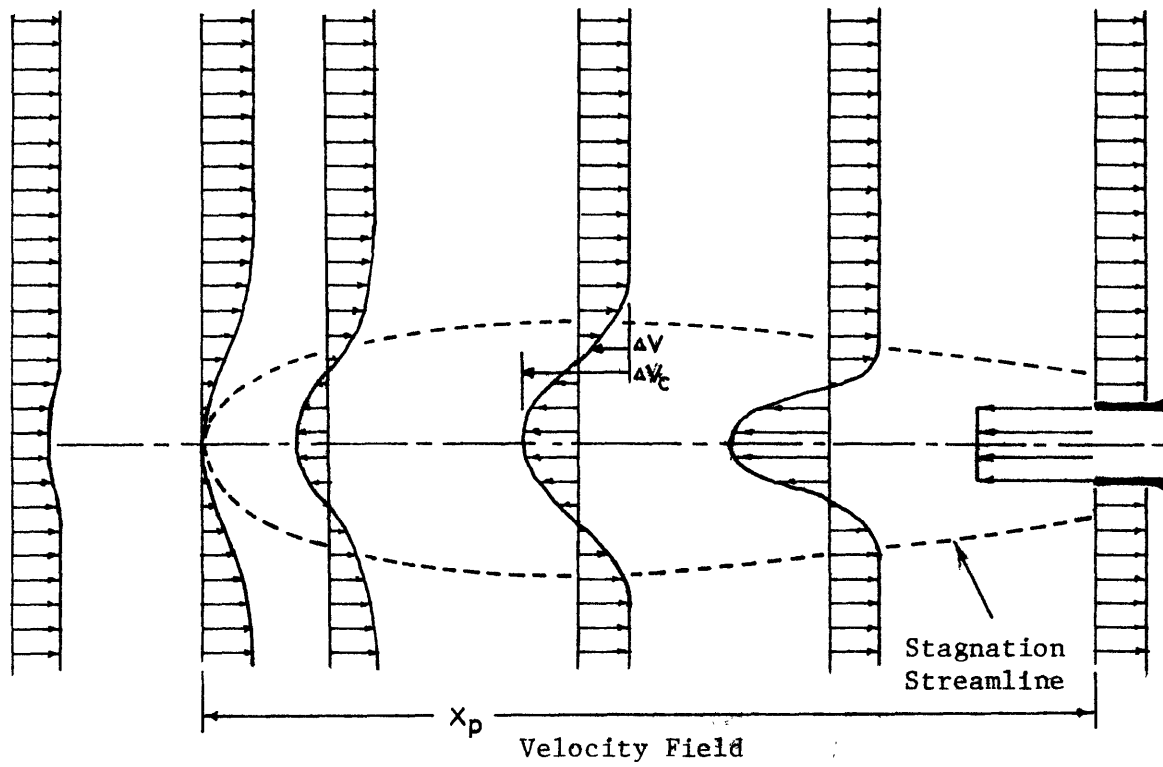
Figure 2-14   Circular Jet in a Counter-Flowing Ambient

tion distance, X_p. Spreading measurements were not made or were not reported completely.

A circular, ducted jet study by Becker, Hottel, and Williams (1962) provides the best data for jet spreading in counter-flowing ambient fluids. Because this is a confined jet situation, the ambient velocity is decreasing or becoming more negative as the jet moves away from its discharge point (Figure 1-3). The governing parameters now include H_i, the radius of the duct wall. This means a second dimensionless governing parameter is needed:

$$M = M_o/H_i^2 U_o^2 \qquad (2.27)$$

However Becker et al. measured the centerline velocity, ΔV_c, the ambient velocity, U, and the jet width $b_{\frac{1}{2}}$ at various sections. Therefore equation 2.25 can be applied for average values of ΔV_c and U between sections to predict the increase in $b_{\frac{1}{2}}$. In this way the more complicated experiment is analyzed as a series of uniform counter-flowing ambient fluid situations.

The spreading results of six experiments by Becker et al. (1962) appear in Figure 2-15. Velocity and jet width data appear in the accompanying Table 2-6. It is apparent that spreading is greatest for the highest values of M - those experiments in which ambient counter velocities occur earliest and with the largest magnitudes. Various values of κ were tried in Eq. 2.25 (with $\varepsilon_{NB} = .097$) to fit the data. The best fit was for $\kappa = .44$ which is almost equal to the Abramovich suggestion of .45 (Figure 2-16). Table 2-7 lists the variance of jet width predictions for various values of κ.

53
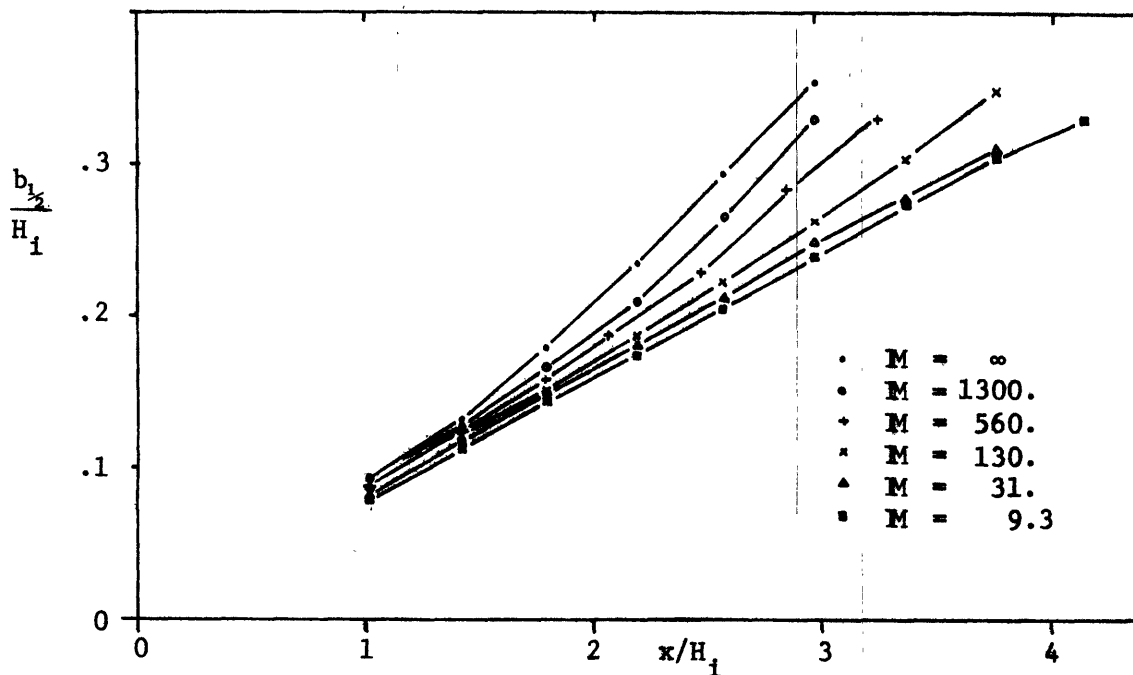
Figure 2-15 Circular Ducted Jet Spreading

Exp. No.	x/Hi	1.01	1.42	1.79	2.19	2.57	2.96	3.36	3.76
#1 "■"	$b_{1/2}$/Hi	.081	.114	.146	.174	.206	.241	.276	.305
M = 9.3	U	+1.13	+1.09	+1.07	+0.93	+0.86	+0.79	+0.79	+0.71
	ΔV	13.62	9.54	7.34	6.06	5.24	4.46	4.03	3.60
#2 "▲"	$b_{1/2}$/Hi	.083	.120	.150	.182	.213	.250	.278	.310
M = 31.	U	+0.64	+0.55	+0.52	+0.49	+0.46	+0.43	+0.37	+0.16
	ΔV	13.62	9.54	7.34	6.06	5.24	4.46	3.94	3.56
#3 "x"	$b_{1/2}$/Hi	.086	.122	.151	.188	.223	.263	.305	.349
M = 130.	U	+0.29	+0.28	+0.26	+0.21	+0.11		-0.18	-0.31
	ΔV	13.62	9.54	7.34	6.06	5.24	4.72	4.26	3.98
#4 "+"	$b_{1/2}$/Hi	.088	.124	.159	.188	.229	.284	.331	
M = 560.	U	+0.02	-0.01	-0.15	-0.20	-0.31	-0.47	-0.52	
	ΔV	13.1	9.1	7.11	6.52	5.42	4.74	4.16	
#5 "○"	$b_{1/2}$/Hi	.089	.127	.167	.211	.267	.330		
M = 1300.	U	-0.04	-0.13	-0.22	-0.32	-0.45	-0.55		
	ΔV	13.0	9.0	7.11	5.74	4.76	4.14		
#6 "●"	$b_{1/2}$/Hi	.094	.132	.180	.236	.294	.353		
M = ∞	U	-0.26	-0.35	-0.43	-0.52	-0.61	-0.70	-0.82	
	ΔV	12.67	8.93	6.79	5.29	4.50	3.82	3.33	

Table 2-6 Circular Ducted Jet Data (Becker et al., 1962)
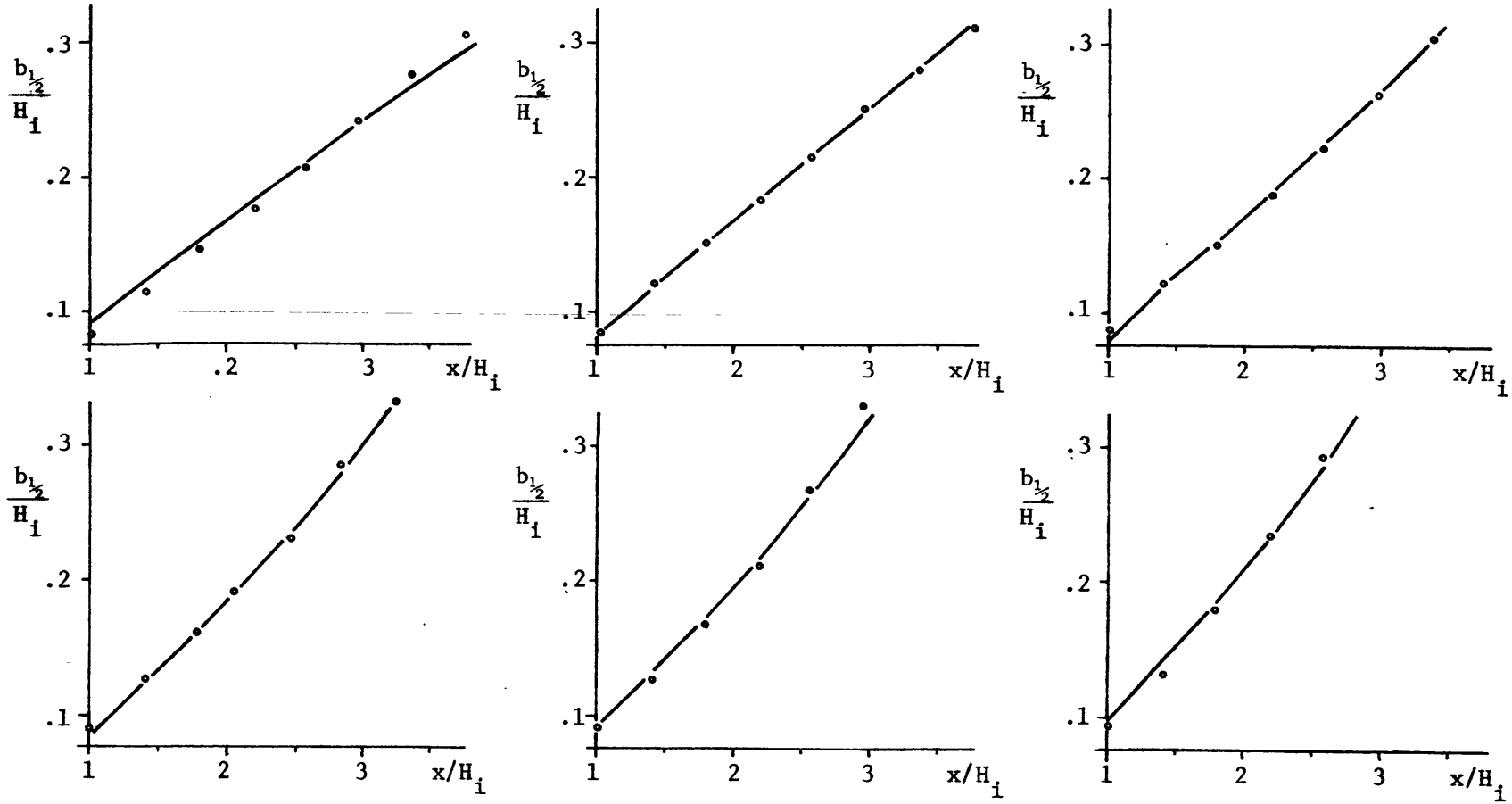
Figure 2-16 Becker et al. Data Fit ($\kappa = .44$, $\varepsilon_c = .097$)

κ	.35	.40	.42	.44	.46	.48	.50	.55	.60	.65
$\sigma^2 \times 10^6$	5.9	4.5	4.4	4.4	4.4	4.6	4.8	5.4	6.1	6.9

Table 2-7 Variance of Spreading Predictions for Various κ Values

2.4.4.4 Radial Jet Behavior

As in the previous section, jet profile results in Section 2.4.1 are applicable. The appropriate spreading relation appears to be equation 2.25 with $\kappa = 0.44$. The non-buoyant spreading rate, ε_{NB}, should be the relation found applicable to plane and radial jets in Section 2.4.1.

$$\varepsilon_c = \{.105 + .005 \tanh[(.43 - \frac{\Delta V_c}{V_o})/.028]\} \frac{.44}{U/\Delta V + .44} \qquad (2.28)$$

It should be remembered that the experiments by Becker et al. (1962) had turbulent counterflowing ambient fluid. This may cause spreading somewhat different from that observed in the detached jet of this study (where the ambient flow is irrotational).

2.4.5 Buoyant Unconfined Jets

As in other sections, the radial geometry for this situation has apparently not been studied. Geometrical similarities and the equivalence of spreading rates for plane and radial jets was noted in Section 2.4.1. Therefore buoyant plane jet data will be emphasized and then assumed to apply to the radial case.

An important property of these jets is that (in an unstratified ambient fluid) their behavior eventually becomes that of a pure plume as buoyancy overcomes initial momentum effects.

2.4.5.1 Parameterization

Buoyancy adds a new governing parameter, B_o, to those of the unconfined non-buoyant jet. Also the directional nature of the buoyancy

force makes ϕ_o or the jet discharge angle important (horizontal discharge: $\phi_o = 0°$; vertical discharge: $\phi_o = 90°$). Thus the following dimensionless numbers result:

1. ϕ_o initial jet angle to the horizontal   (2.29)

2. $\mathbb{F}' = [M_o^3/B_o Q_o^2]^{1/2}$ plane jet densimetric Froude number

    or

    $\mathbb{F} = [M_o^{5/2}/B_o Q_o]^{1/2}$ radial or circular jet densimetric
    Froude number   (2.30)

3. $\mathbb{A} = r_o \sqrt{M_o}/Q_o$ radial jets only

Pure plume spreading ($M_o = 0$ and $\phi_o = 90°$) has two governing parameters (B_o and Q_o) and no dimensionless numbers. Therefore the property of jet spreading (or the entrainment coefficient) should be the same for all plumes (just as is the case for a non-buoyant jet with governing parameters of M_o and Q_o).

Only three major studies were found of a plane plume. Rouse et al. (1952) studied the pure plane "plume" ($M_o = 0$) created from a heat source. The jets of Kotsovinos (1975) had initial momentum but were all discharged vertically ($\phi_o = 90°$) and did not bend. Cederwall (1971) considered a horizontal discharge. However experimental boundaries made his jets somewhat confined. Cederwall's results will be discussed later in Section 2.5.2.
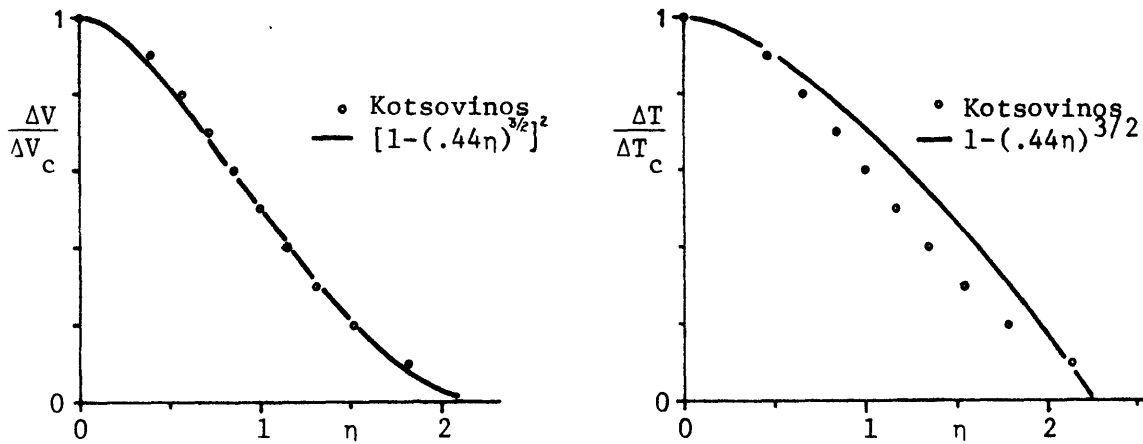
Figure 2-17 Plane Plume Mean Profile Data

Geometry	Sources	$\dfrac{b_{\frac{1}{2}}}{dx}$	$\dfrac{b}{b_{\frac{1}{2}}}$	$\dfrac{b_{\frac{1}{2}T}}{b_{\frac{1}{2}}}$	$\dfrac{db_{\frac{1}{2}T}}{dx}$	I_1	I_2	J_1	J_2	K_1
Plane Buoyant Jets	Kotsovinos[a] (1975)	.097	1.88	1.35	.131					
	Rouse et al. (1952)	.147		.89	.130					
	Polynomial Profiles					1.02	0.72	1.36	1.02	0.84
	Exponential Profiles					1.06	0.75	1.44[b]	1.02[b]	0.85[b]

Notes:
  a. Experimental flows had some initial momentum
  b. Uses Kotsovinos experimental value of $b_{\frac{1}{2}T}/b_{\frac{1}{2}}$

Table 2-8 Experimental Data for Plane Buoyant Jets

2.4.5.2 Profile Data

Both Rouse et al. (1952) and Kotsovinos (1975) fitted exponential profiles to their measurements of the lateral distribution s of velocity and temperature. Figure 2-17 shows the mean results of Kotsovinos' measurements. The integral profile coefficients appear in Table 2-8.

2.4.5.3 Spreading Relation

The closure problem for integral models of buoyant plane jets has received considerable attention in the literature. A transition takes place from the spreading rate (or entrainment coefficient) of non-buoyant

jets to the spreading rate (or entrainment coefficient) of pure plumes (toward which buoyant jets will evolve).

Most of the discussion in the literature is based on plume behavior reported by Rouse et al. (1952). They found a spreading rate (or entrainment coefficient) for the plane plume larger than ε_{NB}(or α_{NB}).

$$\varepsilon_B = \frac{db_{\frac{1}{2}}}{dx} = .147 \qquad (2.31)$$

$$\alpha_B = \frac{V_e}{\Delta V_c} = .157 \qquad (2.32)$$

Abraham (1965) suggests a transition depending on only the local jet angle to the horizontal. Fox (1970), using an integral energy equation, derives a transition based on local jet angle and densimetric Froude number

$$\mathbb{F}_\ell = \Delta V_c / [\frac{\Delta\rho_c}{\rho} gb_{\frac{1}{2}}]^{1/2} \qquad (2.33)$$

List and Imberger (1973), in dimensional arguments, confirm that the transition should depend on the local densimetric Froude number and jet angle. They also note that the spreading and entrainment values of Rouse et al. appear ill-fitted to the data and unconfirmed.

Kotsovinos (1975) reported careful velocity measurements for vertical buoyant jets. He found a spreading rate (given some experimental scatter) that was independent of local Froude number (i.e. always approximately ε_{NB}). The corresponding entrainment coefficient however ranges from $\alpha_{NB} = .055$ to $\alpha_B = .110$.

A spreading-based closure relation has been chosen for this study. Therefore the form of the jet to plume transition can be ignored because

spreading values at the endpoints (non-buoyant jet and pure plume)

are similar. Buoyant jets in the circular geometry exhibit the same

behavior. List and Imberger (1973) cite plume spreading values only

8% higher than for non-buoyant jets (almost insignificant considering

the scatter of values reported from different experiments).

2.4.5.4 Radial Jet Behavior

This section presents no reason to change the plane jet profile

constants or the spreading closure relation from their non-buoyant

values. A radial buoyant jet approaching a vertical trajectory and plume

conditions closely resembles a plane plume as the radial coordinate

no longer increases. So non-buoyant profile constants and the spreading

relation of Section 2.4.1 apply.

2.4.6 Symmetry in Deflected Plane Jets

Many have studied plane jet behavior under the deflecting influence

of buoyancy or boundaries. Most assume symmetry: 1. symmetrical lateral

velocity profiles and 2. equal entrainment through both jet boundaries

(e.g. Morton, Taylor, & Turner (1956), Fan (1967), Abraham (1963),

Bourque and Neuman (1960), Stoy, Stenhouse, & Hsia (1973)). Sawyer (1960)

explains that while lateral profile symmetry has been confirmed by measure-

ment, the second symmetry does not follow necessarily and in fact, should

not be expected. He cites as evidence the experimentally determined

spreading rates of wall jets on curved walls. Jets on the outside of

a sharply curved wall spread much faster than jets on the inside of a

sharply curved wall (Figure 2-18).

Sawyer (1963) also tries to quantify this effect for bending jets.
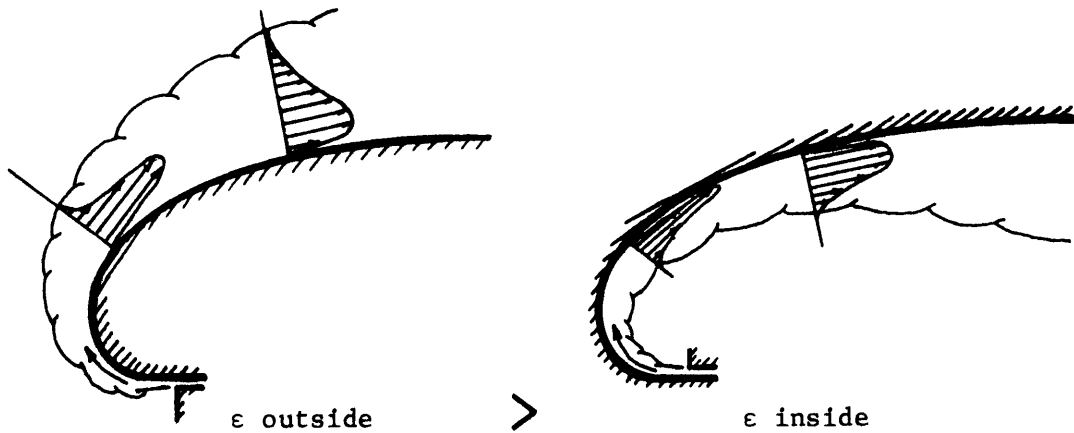
Figure 2-18 Turbulent Wall Jets on Curved Surfaces

Mean Velocity Distribution

$$\Delta V = \Delta V_c f(\eta)$$

Mean Centripetal Acceleration
    Distribution:

$$|F| = |F_c| h(\eta) = \frac{|\Delta V_c|^2}{r_2} f(\eta)^2$$

1. outside fluid parcel
   moving out

2. inside fluid parcel
   moving in
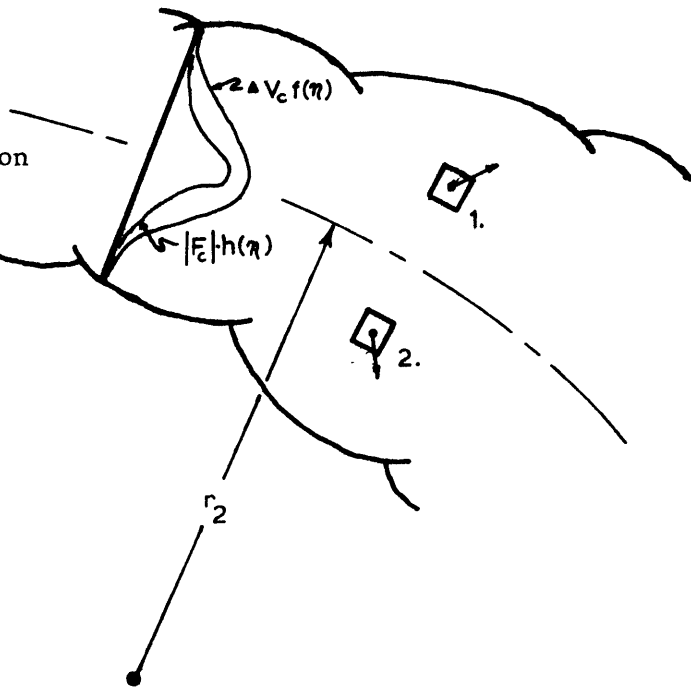
Figure 2-19 Asymmetrical Entrainment Definition Diagram

61

He uses a mixing length argument originally put forward by Prandtl.
The basis for entrainment difference is the change in centripetal force
experienced by a fluid parcel (with definite angular momentum) moving
laterally. Parcels outside the jet axis moving laterally outward, are
forced out even further by their constant angular momentum. Inside
parcels moving laterally inward are forced back by their angular
momentum (Figure 2-19). Sawyer obtains the following forms for the
resulting entrainment rates:

$$\frac{\alpha \ (\text{outside})}{\alpha \ (\text{no bending})} = 1 + c_1 \ \frac{b_{\frac{1}{2}}}{r_2}$$

$$\frac{\alpha \ (\text{inside})}{\alpha \ (\text{no bending})} = 1 - c_1 \ \frac{b_{\frac{1}{2}}}{r_2} \qquad (2.34)$$

where r_2 is the radius of curvature of the jet axis and c_1 is a constant
in this first order analysis. Note that for no curvature ($r_2 \to \infty$), the
two entrainment coefficients are the same and equal to the non-buoyant,
unconfined jet value. Also, curvature does not change the total
entrainment - only the relative amounts passing through each jet
boundary. In fitting his analytical model to Coanda effect data, Sawyer
suggests two different values for c_1:

$$c_1 = 2.95 \qquad (\text{offset plate problem})$$

$$c_1 = 4.92 \qquad (\text{angled plate problem}) \qquad (2.35)$$

2.4.6.1 Radial Jet Behavior

In integral plane jet formulations the entrainment flow through
one boundary over an interval ds can be written:

$$Q_{ent} = V_e \, ds \qquad (2.36)$$

For deflecting jets, V_e does not represent the ambient fluid's real velocity because ds is not the jet boundary length. Instead,

$$V_{e_{real}} = \frac{Q_{ent}}{ds(1 + \frac{b}{r_2})} \qquad \text{(outside)}$$

$$V_{e_{real}} = \frac{Q_{ent}}{ds(1 - \frac{b}{r_2})} \qquad \text{(inside)} \qquad (2.37)$$

If a bending jet ($b = 1.8 \, b_{\frac{1}{2}}$) had equal $V_{e_{real}}$ values at each jet boundary than Eq. 2.34 would be

$$\frac{\alpha(\text{outside})}{\alpha(\text{no bending})} = 1 + 1.8 \, \frac{b_{\frac{1}{2}}}{r_2}$$

$$\frac{\alpha(\text{inside})}{\alpha(\text{no bending})} = 1 - 1.8 \, \frac{b_{\frac{1}{2}}}{r_2} \qquad (2.38)$$

Sawyer's values of c_1 indicate that bending indeed does more than simply change the jet boundary area.

For radial bending jets, vertical bending effects are assumed equal to those in plane jets. However, the difference in radius between the two jet boundaries (when the jet is not horizontal) causes a boundary area effect like that just described. Therefore the following relationship between radial jet entrainment flows through the "outside" and "inside" boundary are assumed

$$\frac{Q_{ent}(\text{outside})}{Q_{ent}(\text{inside})} = [\frac{1 + c_1 b_{1/2}/r_2}{1 - c_1 b_{1/2}/r_2}] \times [\frac{1 + 1.8\ \sin(\phi)b_{1/2}/r}{1 - 1.8\ \sin(\phi)b_{1/2}/r}] \qquad (2.39)$$

<center>(bending   (radial
effect)   effect)</center>

2.5 Other Confined Jet Studies

This section will describe, briefly, previous experimental and analytical studies that have dealt with confined jets. They were not used in developing the jet spreading relation. The more basic experiments cited in the previous section were deemed more appropriate. However plane jet results from the studies described below will be used later in Chapter 6 as a check of the analytical model of the present study (by setting $r_o = \infty$).

2.5.1 Ducted Jets

Some experiments in this category (Figure 2-20) have been used in Section 2.4.4 to examine jet spreading in a counterflow. Much more data exists for the circular geometry than for the plane jet geometry. A radial geometry has apparently never been studied. The dimensional nature of this problem is discussed in Section 2.4.4.3.

Rajaratnam (1976) summarizes the existing data and analyses in this area. Analyses of ducted jets all have integral formulations with profile assumptions like those found for jets in co-flowing and counter-flowing ambient fluids. Buoyancy is usually not considered, and thus (for symmetrical orientations) there is no jet curvature. Momentum and mass flux conservation equations are integrated from duct wall to duct wall (not between jet boundaries). A closure problem again exists

<center>64</center>
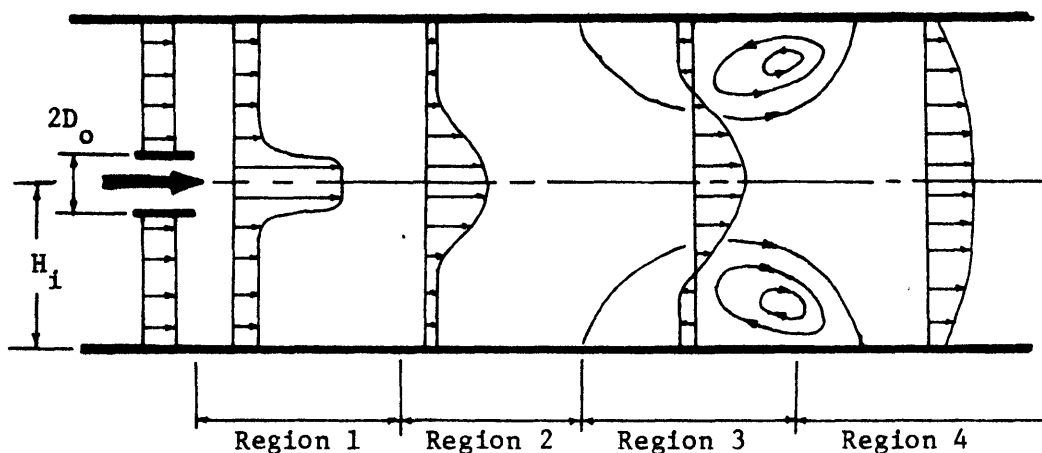
Figure 2-20 Definition of Ducted Jet Regions

because there are three unknowns: U, b, ΔV_c. Other analysis difficulties

include: 1. wall shear effects (sometimes neglected), 2. the evaluation

of pressure in Region 3 with a counter-flowing ambient, 3. some additional

profile assumption for Region 4 (not discussed below).

Hill (1965) used an integral moment of momentum equation (multiply

the momentum equation by the transverse coordinate and then integrate

between the duct walls) for closure. He assumed a Bernoulli relation

for pressure when the ambient was co-flowing $(\frac{dP}{dx} = - \rho U \frac{dU}{dx})$ and a

constant pressure for a counter-flowing ambient. Integral profile

constants (including one involving the shear stress) were obtained

from free jet data. Duct boundary effects were included only as a

force in the momentum equation. Region 1 was neglected.

Brighton et al. (1969) used an assumed eddy viscosity to evaluate

the shear at a radius of $b_{\frac{1}{2}}$.   This basically allowed him to close his

set of equations. Specifically the equations involved integrating

the momentum equation from the axis to three different radii (method

introduced by Squire and Trouncer (1944)). A polynomial lateral velocity

65

distribution was assumed for the jet region. The shear and velocity profile effects of the duct wall boundary layer were considered. The analysis covered only Regions 1, 2, and 4.

Mikhail (1960) also used the integration method of Squire and Trouncer. However a mixing length formulation evaluated the shear at $r = b_{\frac{1}{2}}$. He also assumed a constant ambient fluid velocity in all of Region 2 and a cosine function distribution of velocity for the jet. Duct wall shear was neglected. No attempt was made to analyse Region 3.

Curtet (1958) alone, analyzed and experimented with the plane jet geometry. He generated a shear parameter by multiplying an integral momentum equation by an arbitrary function and then laterally integrating (see Rajaratnam 1976). The shear parameter did not have a constant value as determined by fitting experimental results. Duct wall shear was neglected. His experiments and analysis did not include Region 3.

2.5.2 Offset Plane Boundaries

This is one of the plane jet Coanda effects (Figure 2-21) mentioned in Section 1.1. Three parameters characterize the behavior of a non-buoyant jet in this situation. This means one dimensionless parameter governs the flow:

$$\mathbb{L}' = H_i \, Q_o^2/M_o$$

The plate boundary appears experimentally to be a coherent impacted boundary. An additional parameter, B_o, brings in an additional dimensionless number, $\mathbb{F}'$ to govern jet behavior. As $\mathbb{F}' \to \infty$ non-buoyant jet behavior is approached.

66
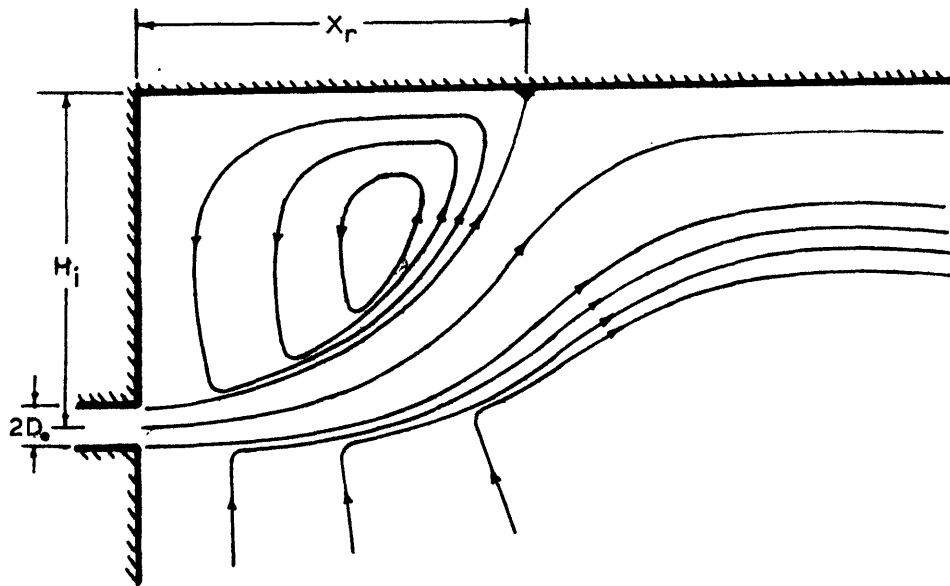
Figure 2-21 Mean Flow Streamlines for Offset Plane Boundary
(from Bourque, 1960)
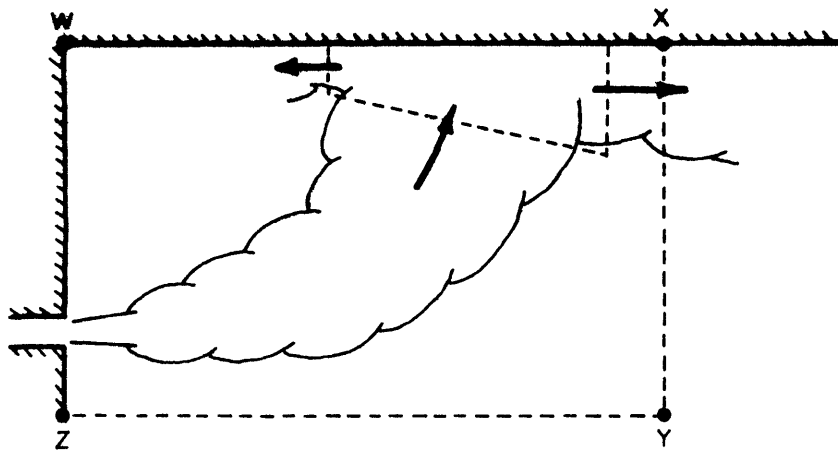
Figure 2-22 Alternate Control Volume for Analyses

An early analytical and experimental study of this situation
was performed by Bourque and Newman (1960). Experimental data consisted
of measuring pressure in the recirculating bubble and locating the
position x_r where the jet's dividing streamline intersects the plate.

The analysis was based on the Goertler jet solution. This solution
has a constant spreading rate from a virtual source and lateral profiles
determined by an assumption of laterally constant eddy viscosities.
The analysis assumes that the jet has a constant radius of curvature
under the influence of a uniform bubble pressure. The pressure (and jet
curvature) must be such that momentum fluxes balance at the point of jet
impact (Figure 2-22). An alternative momentum balance applied to control
volume WXYZ is also tried. The authors' assumption of equal entrainment
from each side of the jet is important in this analysis. For the
momentum balances, they make several simplifying assumptions: 1. The
jet solution is carried up to the point of intersection with the plate.
2. The momentum magnitude of flows (on either side of the dividing
streamline) are the same before and after impact. 3. Some pressure terms
are omitted. The analysis is also simplified by assuming the virtual
and real origins are at the same location. A satisfactory data fit
is obtained only for the local momentum balance and only with an
unrealistic spreading rate reduced by 40% from its free jet value.

Sawyer (1960)introduced a refinement in the local momentum
balance at the point of jet impact. He stopped the jet solution when
the inner boundary (where $\Delta V/\Delta V_c = .1$) strikes the plate. Also, Sawyer
obtained velocity profile measurements and confirmed their symmetry and
similarity to free jet profiles. However, not enough data was

collected to establish the spreading rate quantitatively. He raised

the question of unequal entrainment (at the two jet boundaries) but

could not include it.

Sawyer (1963) refined his analysis of the offset plate problem.

He included a zone of flow establishment for the jet (based on Liepman

and Laufer (1947)). He also determined a first order unequal entrainment

relation (Section 2.4.6). This as well as local pressure forces is

included in his momentum balance at the jet impact point. By adjusting

a constant in his unequal entrainment equation, Sawyer obtained a

marked improvement in fitting the data (for free jet spreading).

Stoy, Stenhouse, and Hsia (1973) include buoyancy in this problem.

Unlike the present study, buoyancy bends the jet in the same direction

as the boundary induced pressures (resulting from the free surface).

They photographically recorded the jet path (its dividing streamline)

by a bubble streak technique. Their analysis used an integral jet model

with an entrainment closure assumption. The recirculating bubble

pressure, P_i, was determined locally by an empirical equation based on

dimensional considerations:

$$P_i = k \ \frac{b_{\frac{1}{2}} \Delta V_c^2}{H} \qquad (2.40)$$

There is no consideration of unequal jet entrainment on the jet boundaries

(such a consideration would be meaningless because there is no momentum

balance at the impact point) and the bubble is incorrectly assumed to

have the same temperature as the outside ambient.

Cederwall (1971) performed a similar experiment, except that

buoyancy was in the opposite direction. All his jets were detached

and the offset plate served as a remote boundary. Cederwall measured

salt concentrations (source of negative buoyancy in his water jet) to

obtain jet path and dilution information. There was no second confining

boundary as in the detached regime of this study.

2.5.3 <u>Angled Plane Boundaries</u>

Bourque and Newman (1959) and Sawyer (1960,1963) studied this

situation in conjunction with the offset plate problem (Figure 2-23).

The same analyses were applied - only the geometry of the jet boundary

impact location changed. A search for independent parameters yields three:

M_o, Q_o, ϕ_o. Dimensionless behavior depends, then, on one parameter: ϕ_o.

There are two distinct flow regimes, depending on ϕ_o, that closely

resemble the attached and detached flows of this study. There are values

of ϕ_o where only one flow regime can exist (small ϕ_o - attached jet;

large ϕ_o - detached jet). There is also an intermediate range of ϕ_o

where either flow can exist. Like a fluidic device, the flow in this

range of ϕ_o exhibits memory (or hysteresis) remaining attached/detached

until an outside force (or a change in ϕ_o) causes detachment/attachment.

(Figure 2-24).

Bourque and Newman (1959) compiled the only available data on

this situation. They determined the point where the dividing stream-

line intersected the plate, x_p. They also measured pressures along

the plate. In some experiments they looked at the effect of a plate

of finite length, ℓ, which adds another dimensionless number for

consideration: $\ell/[Q_o^2/M_o]$.

Bourque and Newman's theories fit their data poorly even with
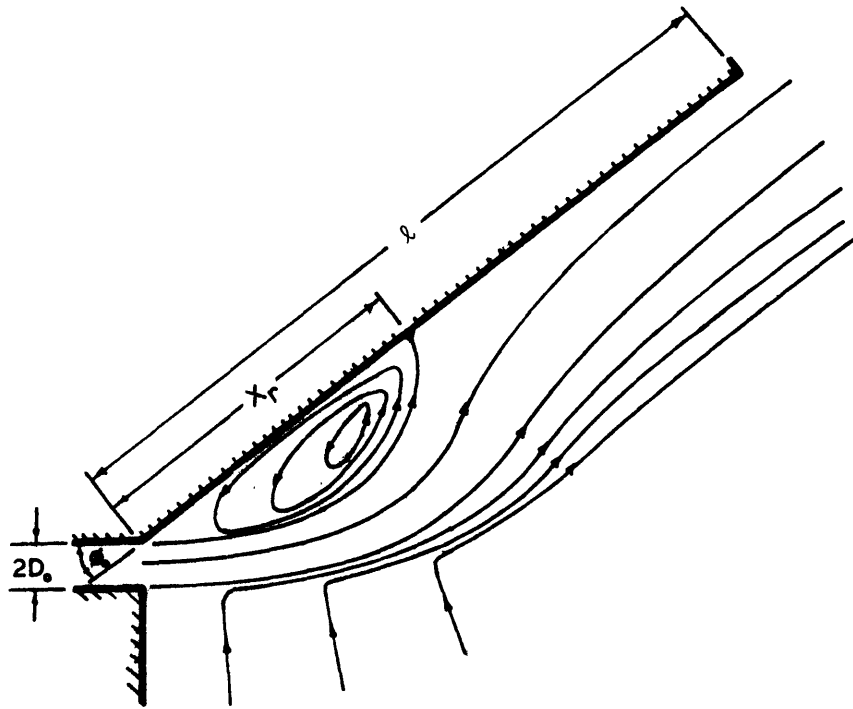
Figure 2-23   Mean Flow Streamlines for Angled Plane Boundary;
Attached Flow Regime (from Bourque, 1960)
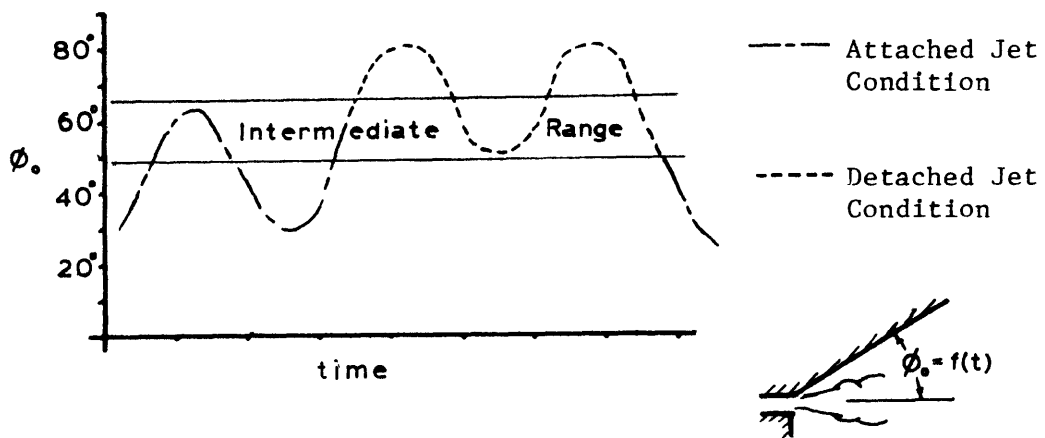
Figure 2-24   Plane Jet Behavior with Time Varying Boundary Angle

reduced (from free jet values) spreading rates. Sawyer (1963) obtained

much better agreement but needed, in his unequal entrainment formula,

a constant (c_1 in equation 2.34) that differed by 70% from its value

for an offset plate.

2.6 Summary

Table 2-9 lists the governing dimensional and dimensionless

parameters of all the studies reviewed. The parameters of this study

are included for comparison. A purely experimental approach to this

study seems hopeless (5 dimensionless parameters) unless the list of

governing dimensional variables can be reduced.

Table 2-10 lists the best estimates of profile, spreading, and

entrainment relationships for a radial jet. As pointed out in Section

2.4.4 data based on plane and circular jet geometries often were

assumed to apply due to a lack of data covering the radial geometry.

	M_o	B_o	H_i	H_r	r_o	Q_o	U_o	ϕ_o	Dimensionless Numbers	Investigators
Unconfined, Non-Buoyant, Circular Jet	X				X				None	Hinze & Zijnen(1949) Albertson(1950) Abramovich(1963)
Unconfined, Non-Buoyant, Plane Jet	X				X				None	Förthmann(1934) Heskestad(1965)
Unconfined, Non-Buoyant, Radial Jet	X				X	X			$A = r_o M_o / Q_o$	Tuve(1963), Witze(1976) Heskestad(1966)
Co-Flowing, Non-Buoyant, Plane Jet	X					X	X		$V = M_o / Q_o U_o$	Weinstein(1955) Abramovich(1963) Bradbury(1965), Bradbury and Riley(1967)
Counter-flowing, Non-Buoyant, Circular Jet	X					X	X		$V = M_o / Q_o U_o$	Abramovich(1963) Rajaratnam(1976)
Unconfined Buoyant Plane Jet	X	X				X			$F' = [M_o^3 / B_o Q_o^3]^{1/2}$	Kotsovinos(1975) Rouse, Yin, & Humphries(1952)
Ducted, Non-Buoyant, Circular Jet	X			X		X	X		$V = M_o / Q_o U_o$ $M = M_o / H_r^2 U_o^2$	Becker et al.(1962) Curtet & Ricou(1964) Hill(1965)
Ducted, Non-Buoyant, Plane Jet	X			X		X	X		$V = M_o / Q_o U_o$ $M' = M_o / H_r U_o^2$	Curtet(1958)
Offset Plane Boundary Non-Buoyant, Plane Jet	X		X			X			$L' = H_i M_o / Q_o^2$	Bourque & Newman(1960) Sawyer(1960,1963)
Offset Plane Boundary Buoyant, Plane Jet	X		X or X			X			$L' = H_i M_o / Q_o^2$ $F' = [M_o^3 / B_o Q_o^3]^{1/2}$	Stoy, Stenhouse, and Hsia(1973) Cederwall(1971)
Angled Plane Boundary Non-Buoyant Plane Jet	X					X		X	ϕ_o	Bourque & Newman(1960) Sawyer(1960,1963)
Present Study:										
Attached Jet	X	X	X		X	X	X	X	$Q = U_o H / Q_o$	Present Study
Detached Jet	X	X	X		X	X	X	X	$R = M_o^{3/4} / r_o B_o^{1/2}$ $L = H B_o^{1/2} / M_o^{3/4}$ $F = [M_o^{5/2} / B_o Q_o^2]^{1/2}$ ϕ_o	

Table 2-9 Summary of Previous Investigations

Profile Constants

$$I_1 = \int_0^\infty f(\eta)d\eta = 1.06 \qquad\qquad J_1 = \int_0^\infty g(\eta)d\eta = 1.42$$

$$I_2 = \int_0^\infty f^2(\eta)d\eta = 0.75 \qquad\qquad J_2 = \int_0^\infty g^2(\eta)d\eta = 1.04$$

$$K_1 = \int_0^\infty f(\eta)g(\eta)d\eta = 0.86 \qquad\qquad b/b_{\frac{1}{2}} = 1.8$$

Spreading Relations

$$\frac{dD}{dx} = (-.07 - \frac{D}{r}) \cdot (\frac{1}{U/V_o + 1}) \qquad \text{Flow Establishment Zone}$$

$$\frac{db_{\frac{1}{2}}}{dx} = \{.105 + .005 \tanh [(.43 - \frac{\Delta V_c}{V_o})/.028]\}(\frac{.44}{U/\Delta V_c + .44})$$

<div align="right">Fully Developed Zone</div>

Entrainment Relation

$$\frac{Q_{ent}(\text{outside})}{Q_{ent}(\text{inside})} = \frac{1 + c_1 b_{\frac{1}{2}}/R_2}{1 - c_1 b_{\frac{1}{2}}/R_2} \times \frac{1 + 1.8 \sin(\phi)b_{\frac{1}{2}}/r}{1 - 1.8 \sin(\phi)b_{\frac{1}{2}}/r}$$

Table 2-10   Profile, Spreading and Entrainment Relationships
Used in this Study

III. Theoretical Considerations

The two possible flow regimes for this confined jet study are described in Section 1.4. The parameter listings of Table 2-9 shows the complexity of the flow. Clearly this problem has not been directly attacked by the studies reviewed in Chapter 2.

In this chapter, two chosen analysis approaches are developed in detail. As previously described, the first approach uses dimensional analysis to determine a set of governing dimensionless parameters. Experiments then are performed to document behavior over all possible ranges and combinations of parameter values. This approach is taken in Section 3.1. It is left uncompleted, however, because of the large number of experiments that are indicated as necessary.

The second approach is an analytical model that requires only a limited number of experiments for verification. The analytical approach chosen used integral jet model techniques. Sections 3.2 and 3.3 develop the equations used in the integral jet model of this study. It should be added that another type of mathematical models has been applied to similar situations (a finite element model; Roberts, 1976). However such models are computationally more complex and need careful adjustment of equation constants and boundary conditions to fit experimental and field data.

3.1 Experimental Determination of Flow Field

Table 2-9 lists the seven independent parameters governing fluid flow behavior for the submerged, negatively buoyant, confined, radial jet. The straightforward application of dimensional analysis yields five

independent governing dimensionless parameters. An impractical number of

experiments would be needed to even grossly define jet behavior over every

possible combination of five values. Fortunately there are some

simplifications that can be made.

Two of the governing dimensional parameters can be eliminated because

they will be assumed to take on only certain values. The jet angle ϕ_o will be

eliminated as only horizontal discharges will be considered. Experiments held

this parmeter to within 5° of horizontal. Secondly, for OTEC applications U_o

has limits. (Remember, U_o is the intake-induced, not the external ambient

velocity.) At the discharge point, U_o is determined by the intake flow

rate, jet port geometry, and submergence,

$$U_o = \frac{Q_i}{2\pi r_o (H-D_o)} \tag{3.1}$$

But in OTEC applications Q_i must be one of three possible multiples of

Q_o (Figure 3-1). Hence if one breaks the problem into three parts

$(Q_i = 0, \ Q_i = \frac{1}{2}Q_o,$ and $Q_i = Q_o)$, U_o is eliminated as an independent

dimensional parameter, and instead can be computed as

$$U_o = kQ_o / [2\pi r_o (H-D_o)]$$

$$= kQ_o / [2\pi r_o H - Q_o^2 / 2M_o] \tag{3.2}$$

where $k = 0, \frac{1}{2},$ or 1.

Confined jet behavior has been reduced to three problems, each

with five independent dimensional parameters and three dimensionless

ones ($\mathbb{L}$, $\mathbb{F}$, and $\mathbb{R}$). It would still be a formidable task to define jet

behavior through experimentation.

76

Further simplification of the dimensional problem requires assumptions

that will only be true in certain parameter ranges. One way to approach this

is by examining "length scales" associated with the independent dimensional

parameters. The initial jet momentum flux (M_o), because it is a nearly conserved

quantity, is taken as a base parameter. Each of the other four dimensional

parameters can be combined with M_o to form a parameter with the dimensions of

length:

$$\ell_Q = Q_o M_o^{-1/2} \tag{3.3}$$

$$\ell_B = B_o^{-1/2} M_o^{3/4} \tag{3.4}$$

$$\ell_H = H^1 M_o^o \tag{3.5}$$

$$\ell_r = r_o^1 M_o^o \tag{316}$$

Similar length scales ℓ_Q', ℓ_B', ℓ_M' and ℓ_r' can be derived for plane jets using

flow quantities per unit width, q_o, m_o, b_o.
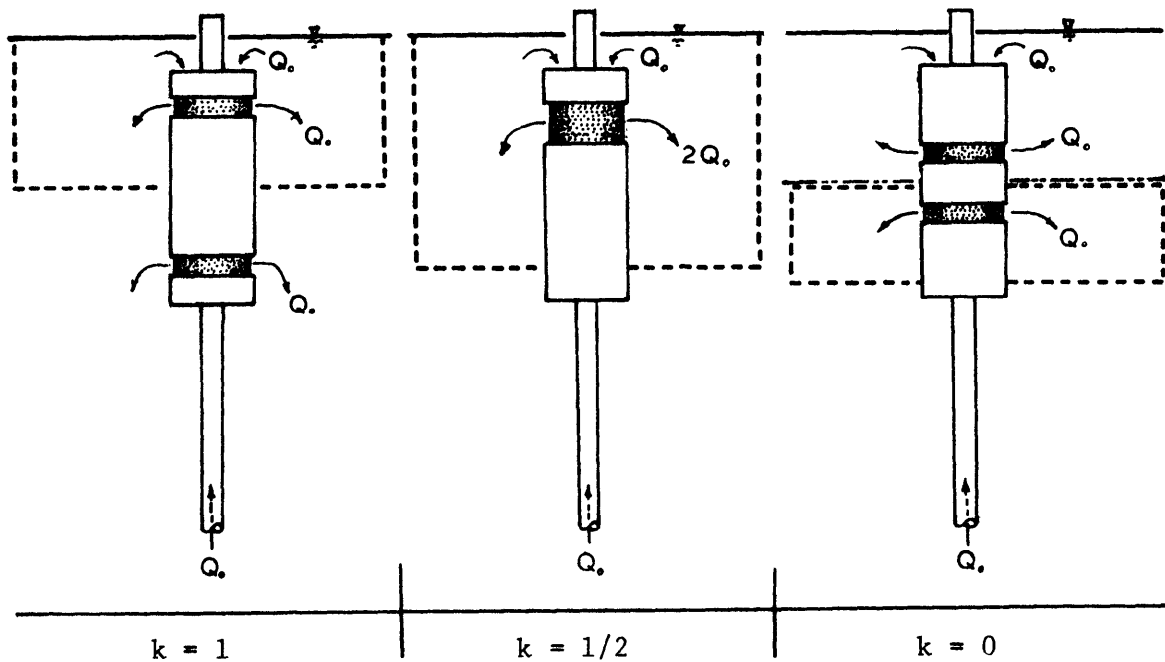
Figure 3-1 Intake Strength for Possible OTEC Flow Fields

3.1.1 Flow Rate Length Scale ℓ_Q

This length scale establishes the distance that the influence of Q_o extends out from the jet discharge orifice. This can be illustrated by data from the jet studies of Chapter 2.

If Q_o is assumed unimportant, the non-buoyant radial jet (Section 2.4.1) has no dimensionless governing parameters. Jet characteristics, suitably normalized by the parameters M_o and r_o, should not vary between experiments. Figure 2-10 is replotted in such non-dimensional variables (Figure 3-2):

$$b^\circ = (b_{\frac{1}{2}} + D)/r_o$$

$$x^\circ = x/r_o$$

$$\Delta V^\circ = M_o^{\frac{1}{2}}/\Delta V_c r_o = \frac{V_o}{\Delta V_c}[\frac{D_o}{r_o}]^{\frac{1}{2}} \qquad (3.7)$$

Invariant behavior is apparent for $x^o > \ell_Q/r_o$.

If Q_o is neglected in the non-buoyant plane jet with an offset boundary (Section 2.52), there are again no dimensionless governing parameters. Two of the measurements taken in this situation are the distance to jet reattachment (x_r) and the minimum pressure on the offset plate ($\frac{\Delta P}{\rho}$). These can be normalized by the remaining parameters M_o and H_i:

$$P^\circ = \frac{\Delta P H_i}{\rho M_o}$$

$$x^\circ = x_r/H_i \qquad (3.8)$$

These are plotted in Figure 3-3 for various values of ℓ_H'/ℓ_Q'.

The path length of the curving jet must be of order ℓ_H. Measure-
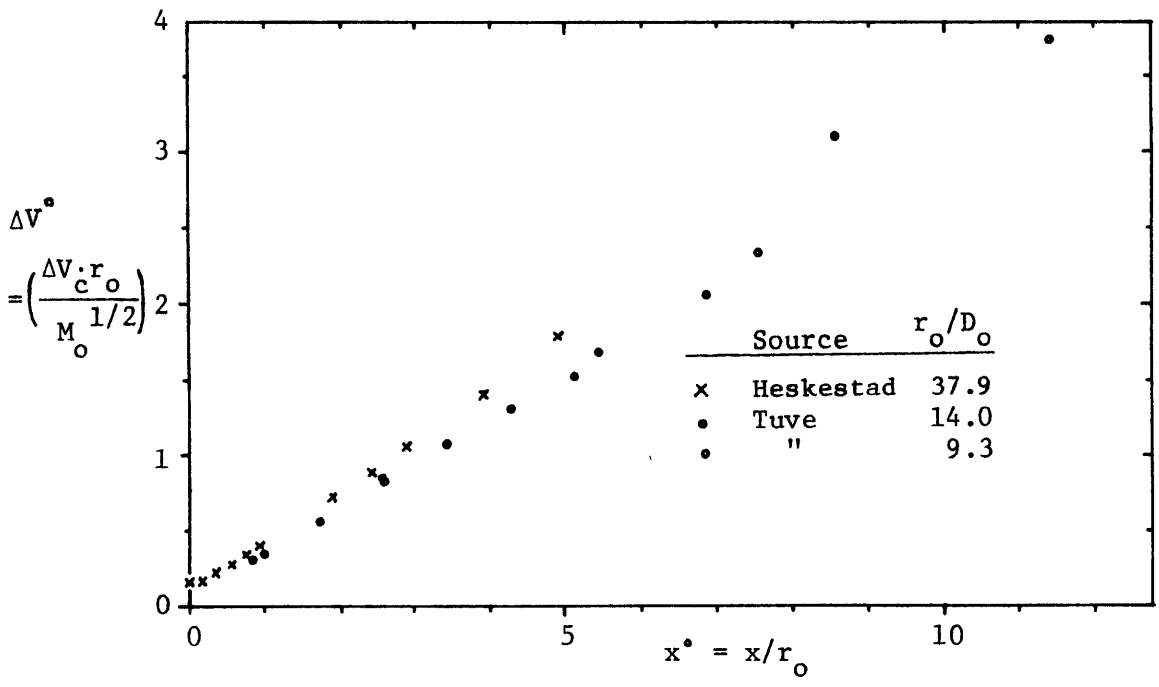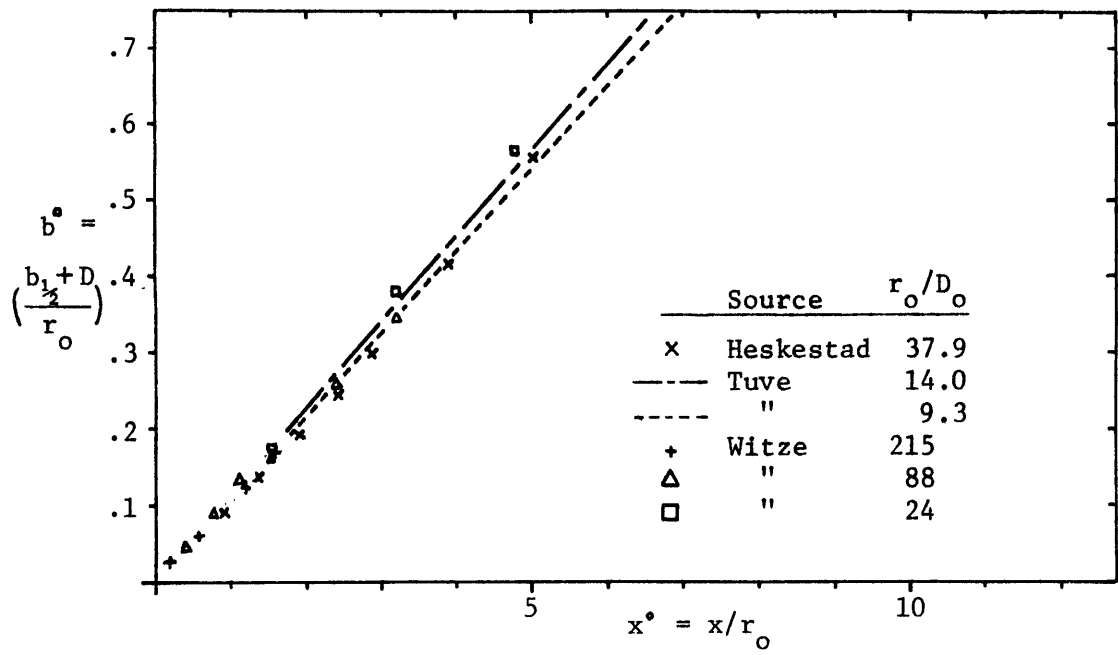
Figure 3-2   Normalized Radial Jet Behavior
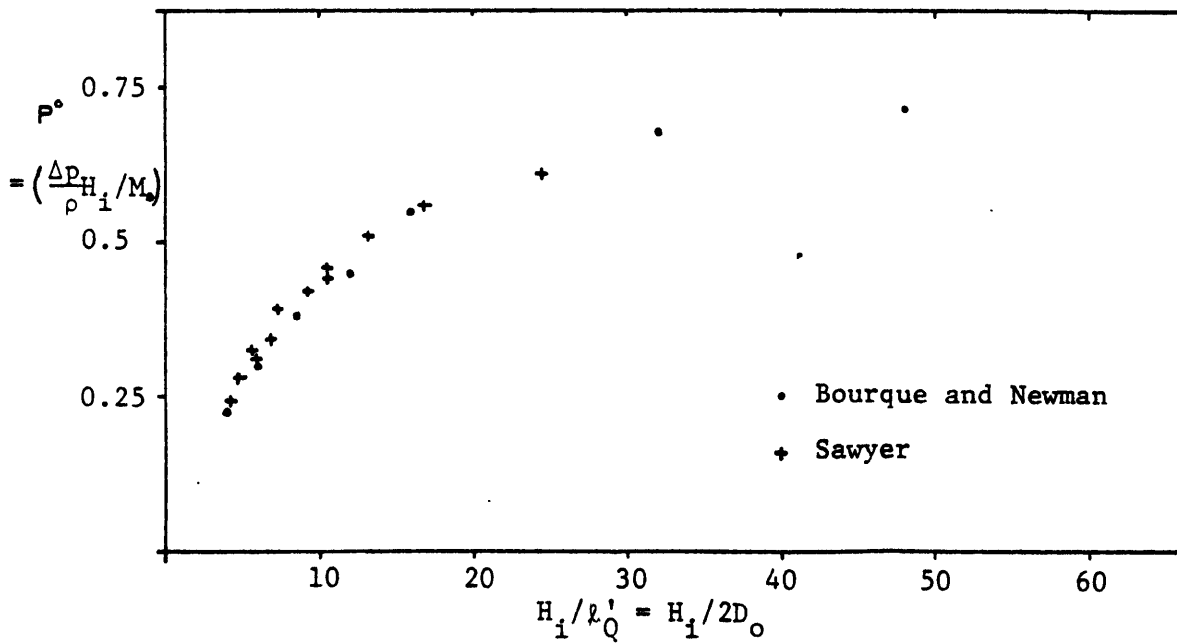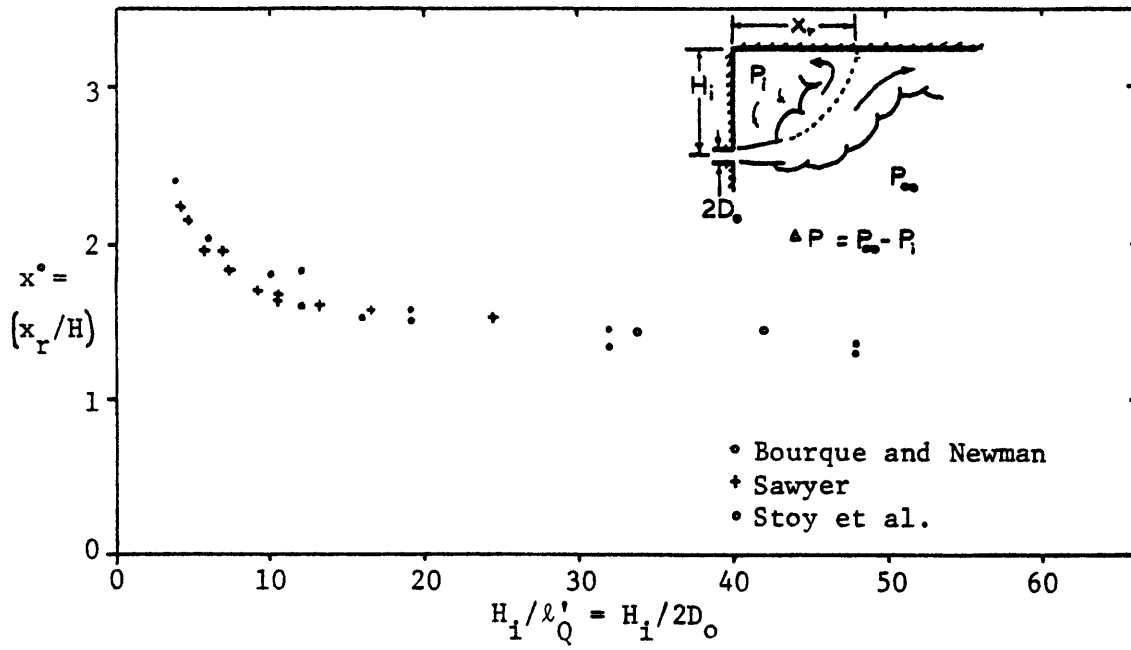
Figure 3-3   Normalized Behavior of Offset Plate Coanda Effect

ments such as ΔP and x_r reflect overall flow conditions and are therefore uninfluenced by Q_o when ℓ_H'/ℓ_Q' is greater than 20. (i.e., when the jet path length is much greater than the extent of Q_o's influence).

3.1.2 Buoyancy Flux Length Scale – ℓ_B

Buoyancy flux causes horizontal jets to bend towards the vertical direction. The length scale ℓ_B is indicative of the longitudinal distance, σ, at which significant bending takes place. Increasing the buoyancy flux B_o, decreases ℓ_B. Thus for $\sigma \ll \ell_B$, buoyancy effects are negligible. The data of Cederwall (1971) for a horizontal plane buoyant jet indicate significant bending only for $\sigma' > \ell_B'$ (Figure 3-4).

$\phi' = \arctan(2Y_i/X_i)$

$\sigma' = 0.5(X_i + Y_i + \sqrt{X_i^2 + Y_i^2})$

$\ell_B' = M_o/B_o^{2/3}$
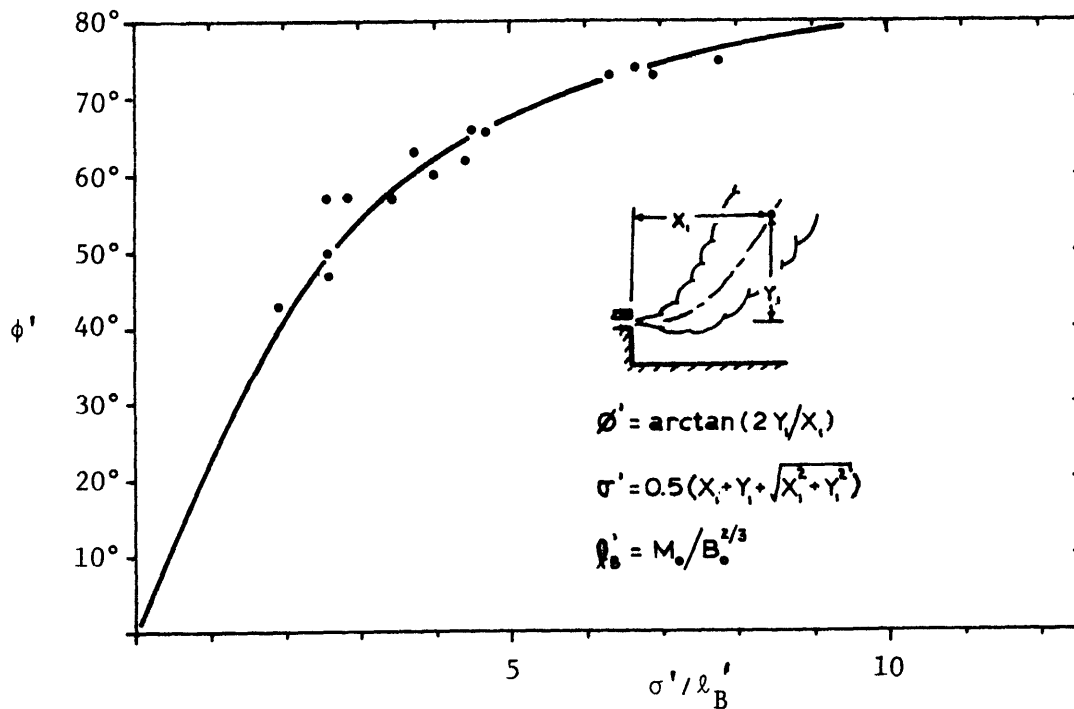
Figure 3-4 Cederwall Data for Buoyant Plane Jet Bending

3.1.3 Confinement Length Scale - ℓ_H

For a coherently impacted boundary, this length scale helps establish jet path length before boundary impact. However, for remote boundaries, if H is much larger than ℓ_Q or ℓ_B then it can be assumed that unconfined jet behavior is approached. In this case U_o and H can both be neglected.

3.1.4 Radial Length Scale - ℓ_r

It is apparent that this length scale $(\ell_r = r_o)$ can be neglected when it is much larger than the jet path length σ over which there is interest in jet behavior. Under these circumstances, plane jet behavior is approached.

Similarly, ℓ_r can be neglected for distances σ considerably greater than ℓ_r, since the behavior of a radial point source $(\ell_r = 0)$ is approached. If both Q_o and r_o (or ℓ_Q and ℓ_r) are assumed unimportant, the non-buoyant radial jet (Section 2.4.1) has only one governing parameter M_o. Jet characteristics normalized by M_o and the coordinate x should not vary between experiments or within the same experiment. Figure 2-10 is replotted showing such normalized variables as a function of x/ℓ_r (Figure 3-5).

$$b^{\circ\circ} = (b_{\frac{1}{2}}+D)/x$$

$$\Delta V^{\circ\circ} = M_o^{\frac{1}{2}}/(\Delta V_c \cdot x) \qquad\qquad (3.9)$$

As was the case for ℓ_Q, behavior becomes independent of ℓ_r at distances greater than 2 ℓ_r from the discharge port.

3.1.5 Conclusions

Because the interplay of confinement and buoyancy effects are
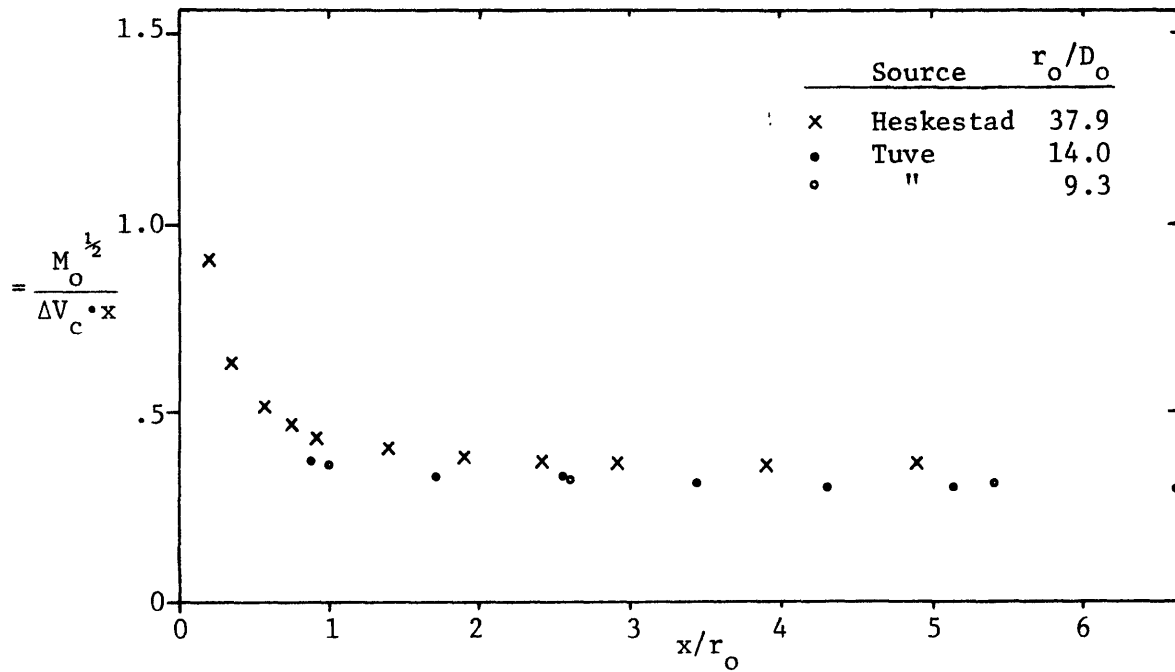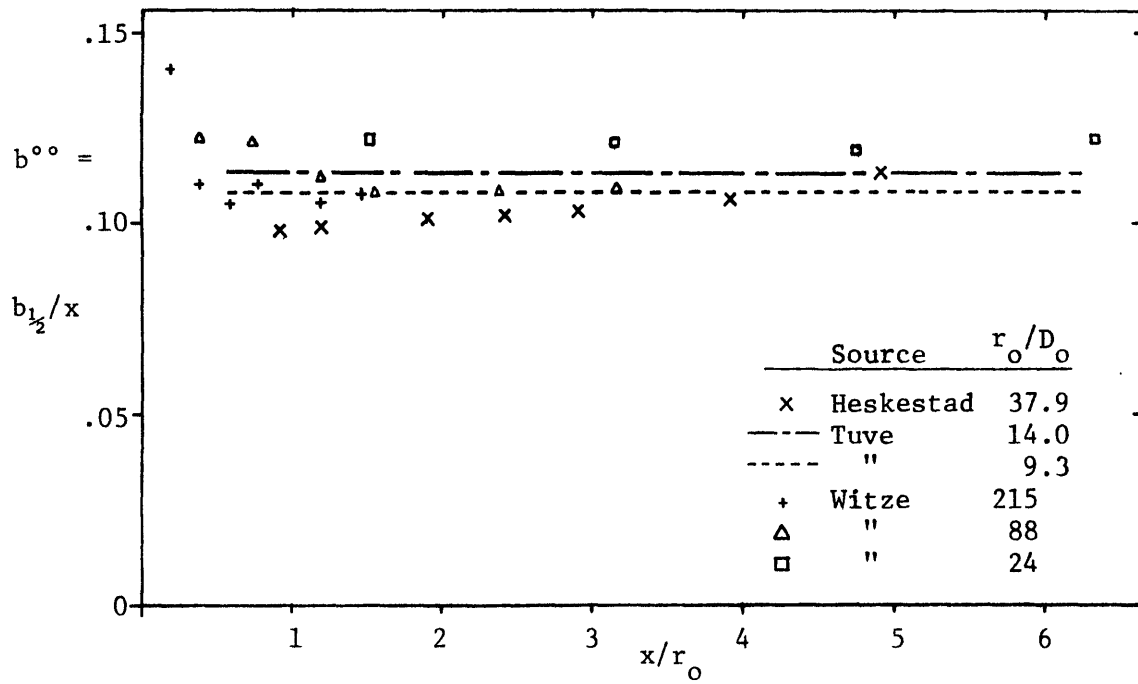
Figure 3-5 1_r Independence of Non-Buoyant Radial Jets

known to dictate jet behavior (e.g. in determining attachment vs. non-attachment), both H and B_o must be considered primary governing parameters. The initial momentum flux (M_o), which initiates the horizontal jet flow and is nearly conserved must also be important. Length scale and conservation arguments have just shown that r_o and Q_o may be considered as secondary dimensional parameters (at distances large compared with ℓ_Q and ℓ_r. This leaves one primary dimensionless governing parameter for each of the three intake flow situations (k = 0, ½, 1):

$$\mathbb{L} = H \; B_o^{\frac{1}{2}} \; M_o^{-3/4} = \ell_H/\ell_B \qquad (3.10)$$

The effect of ℓ_Q and ℓ_r on jet behavior has been found noticeable in some experiments (Figure 3-3) and at some locations (Figure 3-2 and 3-5). In general they cannot be neglected unless ℓ_B, ℓ_H, and r (the radial position where jet behavior is of interest) are all much larger ℓ_Q and ℓ_r. Thus the final simplification above will not always be adequate. A major objective of the experimental program and the integral jet analytical model is to identify this dependence on Q_o and r_o.

3.2   Integral Jet Model – Jet Equations

This section develops the integral jet equations for a radial buoyant jet discharged between an upper remote boundary and a lower impacted boundary. This confinement configuration can be adapted to both flow regimes of this study as well as many of the studies reviewed in Chapter 2. Confined behavior in the ambient fluid regions will be

discussed in Section 3.3. However the following assumptions pertaining to the ambient fluid - jet boundary are needed now:

Ambient regions with remote boundaries are characterized by:

- A spatially varying dynamic pressure P_r

- Fluid velocities adjacent to the jet boundary which have a spatially varying axial component U_σ

- Uniform, ambient fluid temperature, T_a

Ambient regions with impacted boundaries are characterized by:

- A single uniform dynamic pressure, P_i

- Fluid velocities adjacent to the jet boundary which are directed primarily perpendicular to the jet axis

- Uniform fluid temperature reflecting recirculating jet flow, $T = T_a + \Delta T_i$

3.2.1 Coordinate System

A local coordinate system in σ, τ, and θ is defined in Figure 3-6. The σ axis runs along the jet centerline. θ is the same angle coordinate used in cylindrical coordinates. For given values of σ and τ, mean flow field characteristics of a radial jet are independent of θ. The τ axis is everywhere perpendicular to the other two. Thus this is an orthogonal coordinate system. Standard cylindrical coordinates are also noted in the diagram. Note that they, along with ϕ and r_2 are functions of the local coordinates σ, τ, and θ.

local coordinate system: relations:

$$\sigma, \tau, \theta$$

$$\phi = f(\sigma)$$
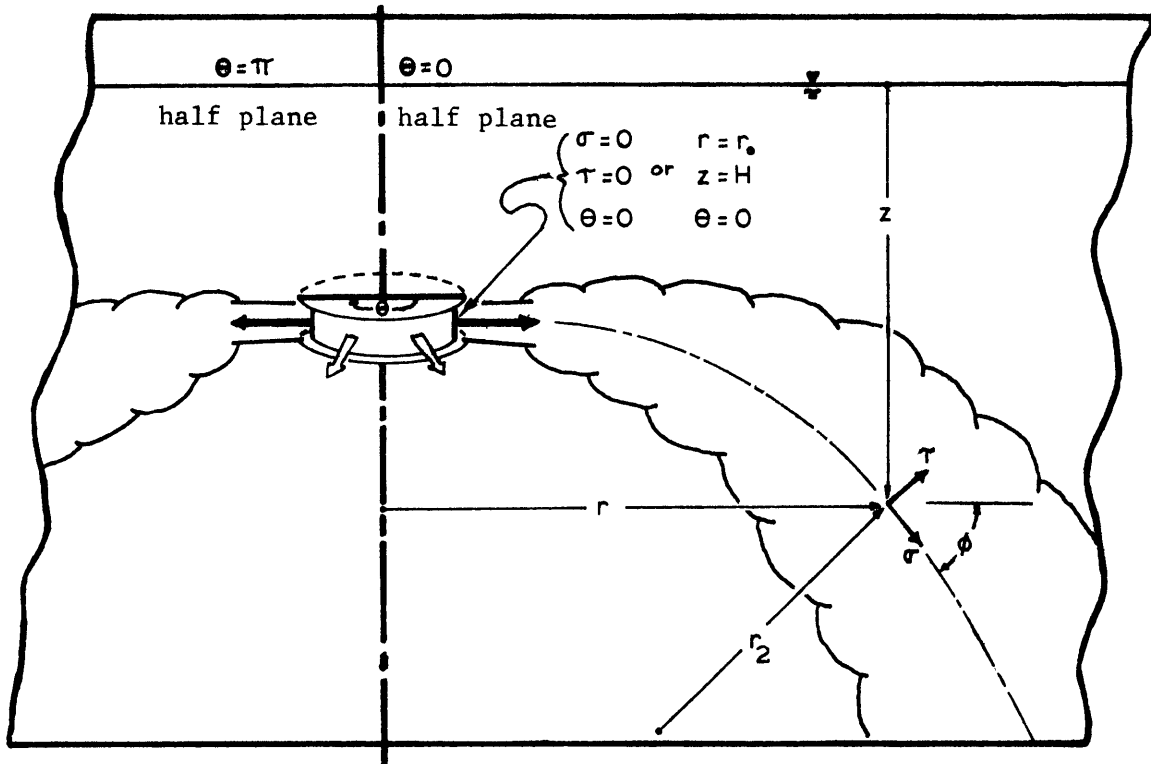
global coordinate system

$$r, z, \theta$$

$$r_2 = [\frac{d\phi}{d\sigma}]^{-1}$$

$$\frac{dr}{d\sigma} = \cos \phi \qquad \frac{dz}{d\sigma} = \sin \phi$$

Figure 3-6   Jet Coordinate Systems

3.2.2 Basic Equations

A fluid flow is characterized by its spatial and temporal variation of velocity, temperature, pressure and density. The basic fluid equations relate these variables using principles of momentum, mass, and thermal energy conservation. In vector notation and including the Boussinesq approximation these are

Conservation of Mass

$$\nabla \cdot \rho \vec{v} = 0 \tag{3.11}$$

Conservation of Momentum

$$\rho(\vec{v} \cdot \nabla \vec{v}) = -\nabla(P_h + P_d) = \rho g + \rho \nu \nabla \vec{v} \tag{3.12}$$

Conservation of Thermal Energy

$$\vec{v} \cdot \nabla T = K[\nabla^2 T] + \Phi/\rho c_p \tag{3.13}$$

where

$\vec{v}$ = velocity vector

T = temperature

P_h = hydrostatic pressure

P_d = dynamic pressure

ρ = density

ν = kinematic viscosity

K = thermal conductivity

Φ = heat generated by viscosity

c_p = thermal capacitance

These can be rewritten in component form for the local coordinate system of Section 3.2.1.

Conservation of Mass

$$\frac{1}{r\beta}\left[\frac{\partial}{\partial\sigma}(\rho r v) + \frac{\partial}{\partial\tau}(\rho r\beta u) + \frac{\partial}{\partial\sigma}(\rho\beta w)\right] \tag{3.14}$$

Conservation of Momentum

$$\underline{\sigma}: \quad \rho\left\{\left[v\frac{\partial v}{\partial\sigma} + \frac{vu}{r_2}\right]/\beta + u\frac{\partial v}{\partial\tau} + \frac{w}{r}\left[\frac{\partial v}{\partial\theta} - w\cos\phi/\beta\right]\right\} = \frac{-\partial(P_h+P_d)}{\partial\sigma}/\beta$$

$$+ \rho g\sin\phi + \rho\nu[i_\sigma\cdot\nabla^2\vec{v}]^1 \tag{3.15}$$

$$\underline{\tau}: \quad \rho\left\{\left[v\frac{\partial u}{\partial\sigma} - \frac{v^2}{r_2}\right]/\beta + u\frac{\partial u}{\partial\tau} + \frac{w}{r}\left[\frac{\partial u}{\partial\theta} - w\sin\phi\right]\right\} = \frac{-\partial(P_h+P_d)}{\partial\tau} - \rho g\cos\phi$$

$$+ \rho\nu[i_\tau\cdot\nabla^2\vec{v}]^1 \tag{3.16}$$

$$\underline{\theta}: \quad \rho\left\{\left[v\frac{\partial w}{\partial\sigma}\right]/\beta + u\frac{\partial w}{\partial\tau} + \frac{w}{r}\left[\frac{\partial w}{\partial\theta} + v\cos\phi/\beta + u\sin\phi\right]\right\} = \frac{-1}{r}\frac{\partial(P_h+P_d)}{\partial\theta}$$

$$+ \rho\nu[i_\theta\cdot\nabla^2\vec{v}]^1 \tag{3.17}$$

Conservation of Thermal Energy

$$\frac{v}{\beta}\frac{\partial T}{\partial\sigma} + u\frac{\partial T}{\partial\tau} + \frac{w}{r}\frac{\partial T}{\partial\theta} = K\frac{1}{r\beta}\left[\frac{\partial}{\partial\sigma}\left(\frac{r}{\beta}\frac{\partial T}{\partial\sigma}\right) + \frac{\partial}{\partial\tau}\left(r\beta\frac{\partial T}{\partial\sigma}\right) + \frac{\partial}{\partial\tau}\left(\frac{\beta}{r}\frac{\partial T}{\partial\theta}\right)\right]$$

$$+ \Phi/c_p \tag{3.18}$$

where v, u, w are the velocity components in the σ, τ, θ coordinate directions, $\beta = 1 + \frac{\tau}{r_2}$, and r, r_2, ϕ are defined in Figure 3-6.

Additionally an equation of state generally links local temperature, pressure, and density. For the water flows of OTEC this can be simplified to

$$\frac{\partial\rho}{\partial T} = m(T-T_b) \tag{3.19}$$

---

[1]the viscosity terms are kept in vector form because they will be later considered negligible.

88
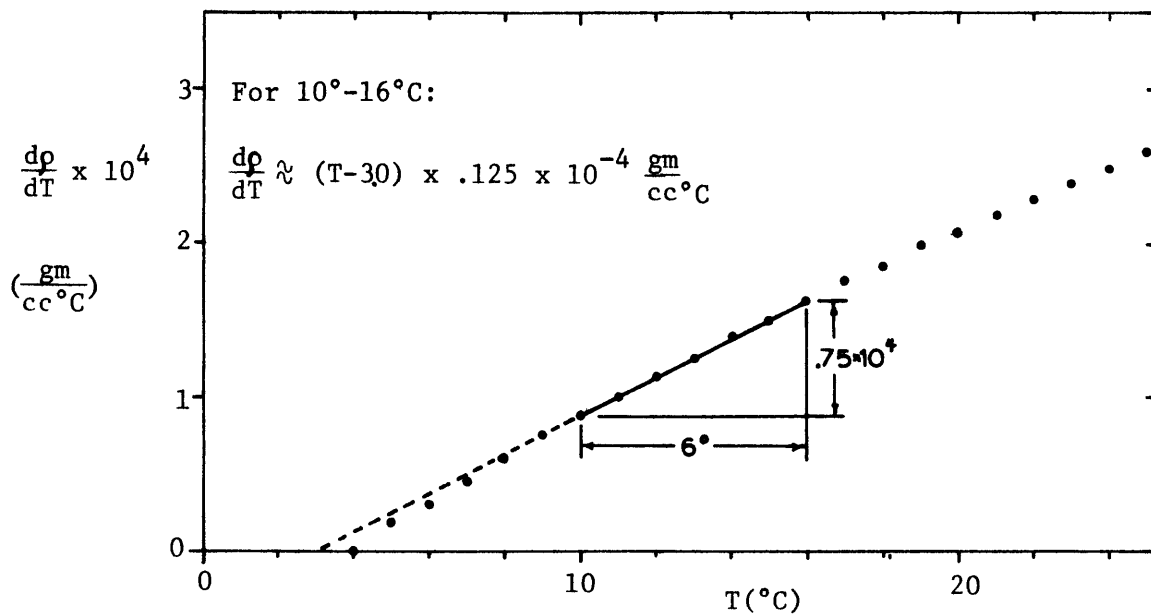
Figure 3-7   Temperature-Density Relationship for Distilled
            Water (Handbook of Chemistry and Physics, 1958)

where m and T_b are constants depending on the temperature range and uniform salinity concentration being considered (Figure 3-7).

Equations (3.15-3.19) together with initial and boundary conditions, govern the flow field. However, there is no closed form solution of them without further approximations and simplifications.

3.2.3 Steady, Turbulent Flow Equations

This section applies the standard procedure for time-averaging turbulent terms in the basic conservation equations above. This requires separating velocity, temperature, pressure, and density variables into mean and fluctuating components.

$$v = \bar{v} + v'$$
$$u = \bar{u} + u'$$
$$w = \bar{w} + w'$$
$$T = \bar{T} + T'$$
$$P = \bar{P} + P' = \bar{P}_h + \bar{P}_d + P'$$
$$\rho = \bar{\rho} + \rho'$$

$$\frac{\text{Total}}{\text{Variable}} = \frac{\text{Mean}}{\text{Component}} + \frac{\text{Fluctuating}}{\text{Component}} \qquad (3.20)$$

The mean component can vary over time periods longer than those of turbulent fluctuations. However, this study considers a case where they are steady.

The θ symmetry of the flow field of a radial jet implies

$$\bar{w} = 0 \qquad (3.21)$$

$$\frac{\partial}{\partial \theta}(\bar{x}) = 0 \qquad \text{for } \bar{x} = f(\bar{u},\ \bar{v},\ \bar{w},\ \bar{P},\ \bar{\rho},\ \bar{T}) \qquad (3.22)$$

90

Rewriting equations 3.15 - 3.19, using equations 3.20 - 3.22 and time averaging, results in the time-averaged turbulent equations (although in an unfamiliar coordinate system). The θ momentum equation drops out because the substitutions and averaging make each term equal zero. These equations are:

Conservation of Mass

$$\frac{1}{\beta}\frac{\partial r\bar{v}}{\partial \sigma} + \frac{\partial r\bar{u}}{\partial \tau} + \frac{r\bar{u}}{r_2\beta} = 0 \tag{3.23}$$

Conservation of Momentum

$$\underline{\sigma}: \quad \frac{1}{r\beta}\frac{\partial r\bar{v}^2}{\partial \sigma} + \frac{2\bar{v}\bar{u}}{\beta} + \frac{1}{r}\frac{\partial r\bar{v}\bar{u}}{\partial \tau} = \frac{-\partial(P_h+P_d)}{\partial \sigma}/\rho\beta + g\sin\phi$$

$$+ \nu[i_\sigma \cdot \nabla^2\tilde{\bar{v}}] - [\frac{1}{r\beta}\frac{\partial \overline{rv'^2}}{\partial \sigma} + \frac{2\overline{v'u'}}{r_2\beta} + \frac{1}{r}\frac{\partial \overline{rv'u'}}{\partial \tau} - \frac{\overline{w'^2}\cos\phi}{r\beta}] \tag{3.24}$$

$$\underline{\tau}: \quad \frac{1}{r\beta}\frac{\partial r\bar{v}\bar{u}}{\partial \sigma} + \frac{1}{r^2\beta}[\bar{u}^2-\bar{v}^2] + \frac{1}{r}\frac{\partial r\bar{u}^2}{\partial \tau} = \frac{\partial(\bar{P}_h-\bar{P}_d)}{\partial \tau}/\rho - g\cos\phi$$

$$+ \nu(i_\tau \cdot \nabla^2\tilde{\bar{v}}) - [\frac{1}{r\beta}\frac{\partial \overline{rv'u'}}{\partial \sigma} + (\overline{u'^2} - \overline{v'^2})/r_2\beta + \frac{1}{r}\frac{\partial \overline{ru'^2}}{\partial \tau} - \frac{\overline{w'^2}\sin\phi}{r}] \tag{3.25}$$

Conservation of Thermal Energy

$$\frac{1}{r\beta}\frac{\partial r\bar{v}\bar{T}}{\partial \sigma} + \frac{\partial r\bar{u}\bar{T}}{\partial \tau} + \frac{\bar{u}\bar{T}}{r_2\beta} = \frac{\Phi}{\bar{\rho}C_p} - [\frac{1}{r\beta}\frac{\partial \overline{rv'T'}}{\partial \sigma} + \frac{1}{r}\frac{\partial \overline{ru'T'}}{\partial \tau} + \frac{\overline{u'T'}}{r_2\beta}]$$

$$+ \frac{k}{r\beta}[\frac{\partial}{\partial \sigma}(\frac{r}{\beta}\frac{\partial \bar{T}}{\partial \sigma}) + \frac{\partial}{\partial \tau}(r\beta\frac{\partial \bar{T}}{\partial \tau})] \tag{3.26}$$

Henceforth the mean components of each variable will be written without the overbar.

3.2.4 Scale Variables

In order to eliminate the insignificant terms in each equation, the magnitude of each variable and its spatial changes must be estimated. Therefore the following "scale" variables are defined:

$$\sigma^*, \tau^*, \phi^*, r^* = \text{scale of changes in } \sigma, \tau, \phi, r \text{ directions}$$

$$v^*, u^* = \text{scale of mean velocity components}$$

$$T^* = \text{scale of mean temperature changes}$$

$$(\Delta\rho/\rho)^* = \text{scale of mean density changes}$$

$$v'^*, u'^*, w'^* = \text{scale of velocity fluctuations in } \sigma, \tau, \theta \text{ directions}$$

$$T'^* = \text{scale of temperature flucturations}$$

$$\nu^* = \text{scale of molecular kinematic viscosity}$$

$$K^* = \text{scale of molecular thermal conductivity}$$

$$\Phi^* = \text{scale of viscous heat generation}$$

$$(\frac{P_d}{\rho})^* = \text{scale of dynamic pressure} \qquad (3.27)$$

Certain scale assumptions can be made for turbulent jets. These are summarized in Table 3-1. Most of the relations follow directly from the turbulent jet description of Section 2.1.

Further simplification of the momentum equations can now be made concerning the hydrostatic pressure.

$$\frac{\partial P_h}{\partial \sigma} = \rho_a \cdot g \cdot \sin \phi$$

$$\frac{\partial P_h}{\partial \tau} = \rho_a \cdot g \cdot \cos \phi$$

$$\rho = \rho_a + \Delta\rho \qquad (3.29)$$

where ρ_a is the ambient undisturbed density and $\Delta\rho$ is the change in mean density due to jet temperature effects. With the Boussinesq approximation

92

Jet Characteristic	Scale Relation

1) **Boundary Layer Flow** $\qquad\qquad \delta_1 = \dfrac{\tau^*}{\sigma^*} \ll 1$

2) **Jet Bending Geometry** $\qquad \sin(\phi^*),\ \cos(\phi^*) \approx 1$

$$\frac{r_2^*}{\sigma^*} \approx 1;\quad \frac{r_2^*}{r^*} \approx 1$$

so: $\quad \delta_2 = \dfrac{\tau^*}{r_2^*} \approx \delta_1 \ll 1$

3) **High Reynold's Number** $\qquad \mathbb{R}_e = \dfrac{v^* \tau^*}{\nu^*} \gg 1$

$$\delta_3^2 = (\frac{v'^*}{v^*})^2 \approx (\frac{u'^*}{u^*})^2 \approx (\frac{w'^*}{w^*})^2 \approx (\frac{T'^*}{T^*})^2 \ll 1$$

4) **Reynolds-Prandtl Number** $\qquad \mathbb{R}_e \mathbb{P}_r = \dfrac{v^* \tau^*}{K^*} \gg 1$

5) **Viscosity Generated Heat Flux** $\qquad (\dfrac{\Phi}{\rho})^* = \dfrac{u^* v^{*2}}{\sigma^{*2}}$

$$\frac{v^{*2}}{c_p T^*} \ll 1$$

6) **Boussinesq Approximation Condition** $\qquad (\dfrac{\Delta\rho}{\rho})^* \ll 1 \qquad\qquad (3.28)$

<div align="center">

Table 3-1 Basic Jet Scale Relations

</div>

and the assumption of mild jet curvature,

$$g \cdot \sin \phi - \frac{\partial P_h}{\partial \sigma} / \rho \beta = \frac{\Delta \rho}{\rho_{amb}} \cdot g \cdot \sin \phi + \frac{\tau}{r_2} \cdot g \cdot \sin \phi$$

$$g \cdot \cos \phi - \frac{\partial P_h}{\partial \tau} / \rho = \frac{-\Delta \rho}{\rho_{amb}} g \cos \phi \qquad (3.30)$$

Tables 3-2 through 3-5 illustrate the application of the scale

variables and the scale relations to the time averaged equations 3.23-

3.26. Scaling of the conservation of τ-momentum equation reveals the

scale of $(P_d/\rho)^*$ if it is an important term (Table 3-3). When this scale

is applied to the σ momentum equation (Table 3-4), it is apparent that

dynamic pressure gradients can be neglected in the σ direction. A term

of questionable significance (order δ_1^2/δ_2) is retained in the simplified

τ momentum equation. This is the only term of this order in all the

equations. It is retained because there is no way to be certain of the

relative sizes of δ_1 and δ_2 and, in any case, the integral jet model

can incorporate this particular term.

3.2.5 Jet Structure

The lateral mean axial velocity and temperature difference profiles

must account for the jet boundary conditions mentioned at the beginning

of Section 3-2. One jet boundary has a non-zero axial velocity while

the other has a temperature different from ambient (Figure 3-8).

Temperature and velocity profile shapes are assumed to take the almost

universal forms found in Chapter 2. However, in order to match different

boundary conditions, the profiles are not symmetrical.

94

Conservation of Mass

$$\frac{1}{\beta}\frac{\partial rv}{\partial \sigma} + \frac{\partial ru}{\partial \tau} + \frac{ru}{r_2\beta} = 0 \tag{3.23}$$

1. Scale Individual Terms

$$\underbrace{\frac{r^*v^*}{(1+\delta_2)\sigma^*}} \qquad \underbrace{\frac{r^*u^*}{\tau^*}} \qquad \underbrace{\frac{\delta_2 r^*u^*}{(1+\delta_2)\tau^*}}$$

2. $\div\ r^*v^*/\sigma^*$ and reduce using 3.28

$$1 - \delta_2 \qquad \frac{u^*\sigma^*}{\tau^*v^*} \qquad \frac{\delta_2 u^*\sigma^*}{\tau^*v^*} - \frac{\delta_2 u^*\sigma^*}{\tau^*v^*}$$

3. Find Significant Terms

   $\checkmark$ $\qquad\qquad$ $\checkmark$

4. Reduced Equation:

$$\frac{\partial rv}{\partial \sigma} + \frac{\partial ru}{\partial \tau} = 0 \tag{3.31}$$

5. Additional Scale Relations;

$$\frac{u^*}{\tau^*} = \frac{v^*}{\sigma^*} \quad \text{or} \quad \frac{u^*}{v^*} = \frac{\tau^*}{\sigma^*} = \delta_1 \tag{3.32}$$

Table 3-2

Conservation of Momentum - τ Direction

$$\frac{1}{r\beta}\frac{\partial rvu}{\partial\sigma} + \frac{1}{r_2\beta}[u^2-v^2] + \frac{1}{r}\frac{\partial ru^2}{\partial\tau} = \frac{-\partial P_d}{\partial\tau}\cdot\frac{1}{\rho} - \frac{\Delta\bar{\rho}}{\rho_{amb}} g \cos\phi + \nu(i_\tau\cdot\nabla^2\vec{v}) - \frac{1}{r\beta}\frac{\partial\overline{rv'u'}}{\partial\sigma} + \frac{\overline{u'^2}-\overline{v'^2}}{r_2\beta} + \frac{1}{r}\frac{\partial\overline{ru'^2}}{\partial\tau} - \frac{\overline{w'^2}}{r}\sin\phi \qquad (3.25)$$

1. Scale Individual Terms

$$\frac{v^*u^*}{(1+\delta_2)\sigma^*} \quad \frac{\delta_2(u^{*2}-v^{*2})}{(1+\delta_2)\tau^*} \quad \frac{u^{*2}}{\tau^*} \quad \frac{(P_d/\rho)^*}{\tau^*} \quad (\frac{\Delta\epsilon}{\epsilon})^* g \quad \nu(\frac{v^*}{\sigma^{*2}}) \quad \frac{v'^*u'^*}{(1+\delta_2)\sigma^*} \quad \frac{\delta_2[(u'^*)^2-(v'^*)^2]}{(1+\delta_2)\tau^*} \quad \frac{(u'^*)^2}{\tau^*} \quad \frac{(w'^*)^2}{r^*}$$

2. $\pm v^{*2}/r_2^*$ and reduce using 3.28 and 3.30

$$\delta_1-\delta_1\delta_2 \quad \delta_1^2-\delta_1\delta_2-1+\delta_2^2 \quad \delta_1^2/\delta_2 \quad \frac{(P_d/\rho)^*}{\delta_2 v^{*2}} \quad \frac{(\Delta\rho/\rho)^* g\, r_2^*}{v^{*2}} \quad \frac{\delta_1}{R} \quad \delta_3^2-\delta_2\delta_3^2 \quad \delta_3^2-\delta_2\delta_3^2 \quad \delta_3^2/\delta_2 \quad \delta_3^2$$

3. Find Significant Terms

$$\checkmark \qquad ? \qquad \checkmark \qquad \checkmark \qquad\qquad\qquad\qquad\qquad\qquad\qquad\qquad\qquad \checkmark$$

4. Reduced Equation

$$-\frac{v^2}{r_2} + \frac{1}{r}\frac{\partial ru^2}{\partial\tau} = \frac{-\partial P_d}{\partial\tau}\frac{1}{\rho} - \frac{\Delta\bar{\rho}}{\rho} g \cos\phi + \frac{1}{r}\frac{\partial\overline{ru'^2}}{\partial\tau} \qquad (3.33)$$

5. Additional Scale Relations

if important: $(P_d/\rho)^* = \delta_2 v^{*2}$ $\qquad (\frac{\Delta\rho}{\rho})^* g = v^{*2}/r_2^*$ $\qquad (3.34)$

Table 3-3

Conservation of Momentum - σ Direction

$$\frac{1}{r\beta}\frac{\partial rv^2}{\partial\sigma} + \frac{2vu}{r_2\beta} + \frac{1}{r}\frac{\partial rvu}{\partial\tau} = \frac{-\partial P_d}{\partial\sigma}\frac{1}{\rho\beta} + \frac{\overline{\Delta\rho}}{\rho_{amb}}g\sin\phi + \frac{\tau}{r_2}g\sin\phi - \nu[i_\sigma\cdot\nabla^2\vec{v}] - \frac{1}{r\beta}\frac{\partial \overline{rv'^2}}{\partial\sigma} - \frac{2\overline{v'u'}}{r_2\beta} - \frac{1}{r}\frac{\partial \overline{rv'u'}}{\partial\tau} + \frac{\overline{w'^2}}{r\beta}\cos\phi \qquad (3.24)$$

1. Scale Individual Terms

$$\frac{v*^2}{(1+\delta_2)\sigma*} \qquad \frac{\delta_2 v*u*}{(1+\delta_2)\tau*} \qquad \frac{v*u*}{\tau*} \qquad \frac{(P_d/\rho)*}{(1+\delta_2)\sigma*} \qquad (\Delta\rho/\rho)*g \qquad \delta_2 g \qquad \nu\left(\frac{v*}{\sigma*^2}\right) \qquad \frac{(v'*)^2}{(1+\delta_2)\sigma*} \qquad \frac{\delta_2 v'*u'*}{(1+\delta_2)\tau*} \qquad \frac{v'*u'*}{\tau*} \qquad \frac{(w'*)^2}{(1+\delta_2)r*}$$

2. ÷ v*²/σ* and reduce using 3.28, 3.30, and 3.32

$$1-\delta_2 \qquad \delta_2 - \delta_2^2 \qquad 1 \qquad \delta_2 - \delta_2^2 \qquad 1 \qquad \delta_2\frac{g\sigma*}{v*} \qquad \frac{\delta_1}{R_e} \qquad \delta_3^2 - \delta_2\delta_3^2 \qquad \frac{\delta_2\delta_3^2}{\delta_1} - \frac{\delta_2\delta_3^2}{\delta_1} \qquad \frac{\delta_3^2}{\delta_1} \qquad \delta_3^2 - \delta_2\delta_3^2$$

3. Find Significant Terms

✓   ✓   ✓   ✓

4. Reduced Equation:

$$\frac{1}{r}\frac{\partial rv^2}{\partial\sigma} + \frac{1}{r}\frac{\partial rvu}{\partial\tau} = \frac{\Delta\rho}{\rho}g\sin\phi - \frac{1}{r}\frac{\partial \overline{rv'u'}}{\partial\tau} \qquad (3.35)$$

Table 3-4

Conservation of Heat Energy

$$\frac{1}{r^2}\frac{\partial rvT}{\partial \tau} + \frac{1}{r}\frac{\partial ruT}{\partial \tau} + \frac{uT}{r_2\beta} = \frac{\phi}{\rho c_p} - \frac{1}{r\beta}\frac{\overline{rv'T'}}{\partial \sigma} + \frac{1}{r}\frac{\partial \overline{ru'T'}}{\partial \tau} + \frac{\overline{u'T'}}{r_2\beta} + \frac{K}{r\beta}[\frac{\partial}{\partial \sigma}(\frac{r}{\beta}\frac{\partial T}{\partial \sigma}) + \frac{\partial}{\partial \tau}(\frac{r}{\beta}\frac{\partial T}{\partial \tau})] \quad (3.26)$$

1. Scale Individual Terms

$$\frac{v^*T^*}{(1+\delta_2)\sigma^*} \qquad \frac{u^*T^*}{\tau^*} \qquad \frac{\delta_2 u^*T^*}{(1+\delta_2)\tau^*} \qquad \frac{(\phi/\rho)^*}{c_p} \qquad \frac{v'^*T'^*}{(1+\delta_2)\sigma^*} \qquad \frac{u'^*T'^*}{\tau^*} \qquad \frac{\delta_2 u'^*T'^*}{(1+\delta_2)\tau^*} \qquad \frac{kT^*}{(1+\delta_2)^2\sigma^{*2}} \qquad \frac{kT^*}{(1+\delta_2)^2\tau^{*2}}$$

2. $\div V^*T^*/\tau^*$ and reduce using 3.28, 3.30, 3.32

$$1 - \delta_2 \qquad 1 \qquad \delta_2 - \delta_2^2 \qquad \frac{\delta_1}{\mathbf{R}_e}\frac{v^{*2}}{c_p T^*} \qquad \delta_3^2 - \delta_2\delta_3^2 \qquad \frac{\delta_3^2}{\delta_1} \qquad \frac{\delta_2\delta_3^2}{\delta_1} - \frac{\delta_2^2\delta_3^2}{\delta_1} \qquad \frac{k}{\nu}\frac{\delta_1}{\mathbf{R}_e} - \frac{k}{\nu}\frac{\delta_2\delta_1}{\mathbf{R}_e} \qquad \frac{k}{\nu}\frac{1}{\delta_1\mathbf{R}_e} - \frac{k}{\nu}\frac{\delta_2}{\delta_1\mathbf{R}_e}$$

3. Find Significant Terms

    ✓   ✓   ✓

4. Reduced Equation

$$\frac{\partial rvT}{\partial \sigma} + \frac{\partial ruT}{\partial \tau} = \frac{\partial \overline{ru'T'}}{\partial \tau} \quad (3.36)$$

Table 3-5

The approximate jet section integrals of flow, momentum flux, thermal energy flux, and buoyancy (Q,M,B and G) are calculated in Table 3-6. The approximation involved is caused by $f(\eta)$ and $g(\eta)$ not being exactly zero at $\eta = b/b_{\frac{1}{2}} = 1.8$. The profile cutoff at $\pm b$(instead of ∞) is needed to define a distinct ambient region adjacent to the remote boundary (described in Section 3.3.1).

3.2.6 Conservation Equations of the Integral Jet Model

Equations 3.31, 3.33, 3.35, 3.36 are now ready to be integrated laterally from jet boundary to jet boundary. In many cases the integral involves r which is a function of the lateral coordinate τ.

$$r(\tau) = r_c + \tau \sin \phi \qquad (3.41)$$

where r_c is the jet centerline radius. In these integrals r is considered a constant (= r_c) which results in an error of order $(\frac{\tau}{r_c} \sin \phi)^2 \leq \delta_2{}^2$. This is clearly in line with the previous scaling done in Tables 3-2 through 3-5.

The resulting equations are listed in Table 3-7.

Condensed Equations:		
$\dfrac{dQ}{d\sigma} - \dfrac{dQ_r}{d\sigma} - \dfrac{dQ_i}{d\sigma} = 0$	Mass Conservation	(3.42)
$\dfrac{M}{r_2} + \dfrac{dQ_r}{d\sigma} U_\tau = \dfrac{P_r - P_i}{\rho_a} r_i - \cos(\phi) \cdot G$	τ Momentum Conservation	(3.43)
$\dfrac{dM}{d\sigma} - \dfrac{dQ_r}{dr} U_\sigma = \sin(\phi) \cdot G$	σ Momentum Conservation	(3.44)
$\dfrac{dB}{d\sigma} - \dfrac{dQ_i}{d\sigma} \Delta T_i = 0$	Heat Flux Conservation	(3.45)

Table 3-7 Integral Jet Model

$$Q = r_c \int_{-b}^{b} v \, d\tau = r_c \left[\int_{0}^{b} (\Delta V_c f(\eta) + U_\sigma) d\tau + \int_{-b}^{0} (\Delta V_c + U_\sigma) f(\eta) d\tau + 2D(\Delta V_c + U_\sigma) \right]$$

$$\approx r_c \{ b_{\frac{1}{2}} [I_1 (2\Delta V_c + U_\sigma) + U_\sigma \frac{b}{b_{\frac{1}{2}}}] + 2D(\Delta V_c + U_\sigma) \}$$

(3.37)

$$M = r_c \int_{-b}^{b} v^2 \, d\tau = r_c \left[\int_{0}^{b} (\Delta V_c f(\eta) + U_\sigma)^2 d\tau + \int_{-b}^{0} \left[(\Delta V_c + U_\sigma) f(\eta) \right]^2 d\tau + 2D(\Delta V_c + U_\sigma)^2 \right]$$

$$\approx r_c \{ b_{\frac{1}{2}} [2\Delta V_c^2 I_2 + 2\Delta V_c U_\sigma (I_1 + I_2) + U_\sigma^2 (\frac{b}{b_{\frac{1}{2}}} + I_2)] + 2D(\Delta V_c + U_\sigma)^2 \}$$

(3.38)

$$B = r_c \int_{-b}^{b} v \Delta T \, d\tau = r_c \left[\int_{0}^{b} (\Delta V_c f(\eta) + U_\sigma) \Delta T_c g(\eta) d\tau + \int_{-b}^{0} (\Delta V_c + U_\sigma) f(\eta) [\Delta T_i + (\Delta T_c - \Delta T_i) g(\eta)] d\tau + 2D(\Delta V_c + U_\sigma) \Delta T_c \right]$$

$$\approx r_c \{ b_{\frac{1}{2}} [(\Delta V_c + U_\sigma)(2\Delta T_c K_1 + \Delta T_i (I_1 - K_1)) + \Delta T_c U_\sigma (J_1 - K_1)] + 2D(\Delta V_c + U_\sigma) \Delta T_c \}$$

(3.39)

$$G = r_c \int_{-b}^{b} \frac{\Delta \sigma}{\sigma} g \, d\tau = \frac{r_c g}{\sigma} \left\{ \int_{0}^{b} m[(\Delta T_c g(\eta))^2 + \Delta T_c g(\eta)(T_a - T_b)] d\tau + \int_{-b}^{0} m\{[(\Delta T_c - \Delta T_i)g(\eta) + \Delta T_i]^2 + [(\Delta T_c - \Delta T_i)g(\eta) + \Delta T_i](T_a - T_b)\} d\tau \right.$$

$$\left. + 2D\Delta T_c (\Delta T_c + T_a - T_b) \right\}$$

$$\approx \frac{r_c g m}{\sigma} \left\{ b_{\frac{1}{2}} 2\Delta T_c^2 H_2 + 2\Delta T_c [(T_a - T_b) J_1 + 2\Delta T_i (J_1 - J_2)] + [\Delta T_i^2 (J_2 - 2J_1 + \frac{b}{b_{\frac{1}{2}}}) + \Delta T_i (T_a - T_b)(\frac{b}{b_{\frac{1}{2}}} - J_1)] \right\}$$

$$\left. + 2D\Delta T_c (\Delta T_c + T_a - T_b) \right\}$$

(3.40)

Table 3-6 Profile Integrals

All the turbulent fluctuation terms have dropped because their values at the jet boundaries are zero. Entrainment flows through the two jet boundaries are distinguished. Q_r is entrainment flow ($\div 2\pi$) from the ambient region with the remote boundary, while Q_i is for the ambient region with the impacted boundary ($\div 2\pi$). It was argued in Section 2.4.6 that Q_r and Q_i are not equal. Finally the new symbol U_τ appears in equation 2.42. A straightforward development of the equation reveals U_τ to be the τ-component of velocity at the jet boundary closest to the remote boundary. An argument is made in Section 3.3 that this should <u>not</u> simply be the entrainment velocity, V_e. If it were, the unintegrated term could have been considered small when the equation was scaled (Table 3-3).

It is perhaps significant to note that almost all of the terms in the scaled equations of order δ_1 or δ_2 (that were previously dropped) would have become even smaller (of order $\delta_1{}^2$ or $\delta_2{}^2$) when integrated laterally. This results because the profiles are nearly even functions and τ is an odd function about the jet centerline.

3.2.7 Additional Jet Equations

The following radial jet profile constants and entrainment ratio equations of Table 2.10 can be directly applied to this study:

$$I_1 = 1.06 \qquad\qquad J_1 = 1.42$$

$$I_2 = .75 \qquad\qquad J_2 = 1.04$$

$$K_1 = .86 \qquad\qquad \frac{b}{b_{\frac{1}{2}}} = 1.8 \qquad\qquad (3.46)$$

$$\frac{dQ_r/d\sigma}{dQ_i/d\sigma} = \left[\frac{1+4.93b_{\frac{1}{2}}/r_2}{1-4.93b_{\frac{1}{2}}/r_2}\right]\left[\frac{1+1.8b_{\frac{1}{2}} \cdot \sin \phi/r}{1-1.8b_{\frac{1}{2}} \cdot \sin \phi/r}\right]\frac{\Delta V_c}{\Delta V_c + U_\sigma} \qquad (3.47)$$

The spreading relations are not directly applicable because there is a counterflowing ambient at only one jet boundary. The spreading rate is assumed to be an arithmetic average of the rates expected for each jet boundary if each acted independently. The same type of relation is applied to the core decay in the zone of flow establishment. Thus in the establishment zone,

$$\frac{dD}{dx} = (-.07 - \frac{D}{r_c}) \frac{1 + .5 U_\sigma / \Delta V_c}{1 + U_\sigma / \Delta V_c} \tag{3.48}$$

while in the full jet zone,

$$\frac{db_{\frac{1}{2}}}{dx} = \left[.105 + .005 \tanh[(.43 - \frac{\Delta V_c}{V_o})/.028] \right] \left[\frac{1 + U_\sigma / .88 \Delta V_c}{1 + U_\sigma / .44 \Delta V_c} \right] \tag{3.49}$$

An additional equation is needed for the zone of flow establishment. It is provided by the fact that the core velocity should remain unchanged from its discharge value (except for acceleration by buoyancy effects). A relation expressing this is

$$\Delta V_c = - U_\sigma + [V_o^2 - \frac{2 \Delta \rho_o}{\rho} g (H_i - z)]^{\frac{1}{2}}$$

$$\frac{d \Delta V_c}{d\sigma} + \frac{dU_\sigma}{d\sigma} = \frac{(\Delta \rho_p / \rho) g \sin (\phi)}{[V_o^2 - 2(\Delta \rho_o / \rho) g (H_i - z)]^{\frac{1}{2}}} \tag{3.50}$$

Finally, three additional equations are needed to relate the various coordinates (see Figure 3-6).

$$\frac{d\phi}{d\sigma} = \frac{1}{r_2} \qquad \frac{dr_c}{d\sigma} = \cos\phi \qquad \frac{dz_c}{d\sigma} = \sin\phi \qquad\qquad (3.51)$$

3.3 Integral Jet Model - Ambient Region Equations

3.3.1 Ambient Region with Remote Boundary

The fluid in this region is irrotational and of uniform temperature, T_a. The fluid moves to satisfy the distributed sink along the jet boundary and the intake flow (if any) at the discharge port axis. The horizontal velocity, U, at each jet section is assumed to be vertically uniform (Figure 3-9). The pressure in this ambient region should obey a Bernoulli relation and can be estimated as:

$$P_r = -\rho_a \frac{U^2}{2} \qquad\qquad (3.52)$$

In order to satisfy continuity:

$$U \cdot [z_c - (b+D)\cos\phi] \cdot [r_c + (b+D)\sin\phi] = -k[V_o \cdot r_o \cdot 2D_o] - Q_r$$

$$U \cdot z_{up} r_{up} = -k[V_o 2D_o r_o] - Q_r \qquad\qquad (3.53)$$

where k is the intake flow factor (0, ½, 1) defined in Chapter 2. In differential form this is:

$$\frac{dU}{d\sigma}[r_{up} z_{up}] + \frac{db_{\frac{1}{2}}}{d\sigma} [(z_{up}\sin\phi - r_{up}\cos\phi)U \frac{b}{b_{\frac{1}{2}}}] + \frac{dD}{d\sigma}[z_{up}\sin\phi - r_{up}\cos\phi] U_h$$

$$+ [(1+(b+D)\frac{d\phi}{d\sigma}][z_{up}\cos + r_{up}\sin\phi]U = \frac{-dQ_r}{d\sigma} \qquad\qquad (3.54)$$

Finally U must be related to U_σ and U_τ which are velocity components in the jet axial and lateral directions at the ambient region - jet interface. A kinematic boundary condition will not be satisfied because
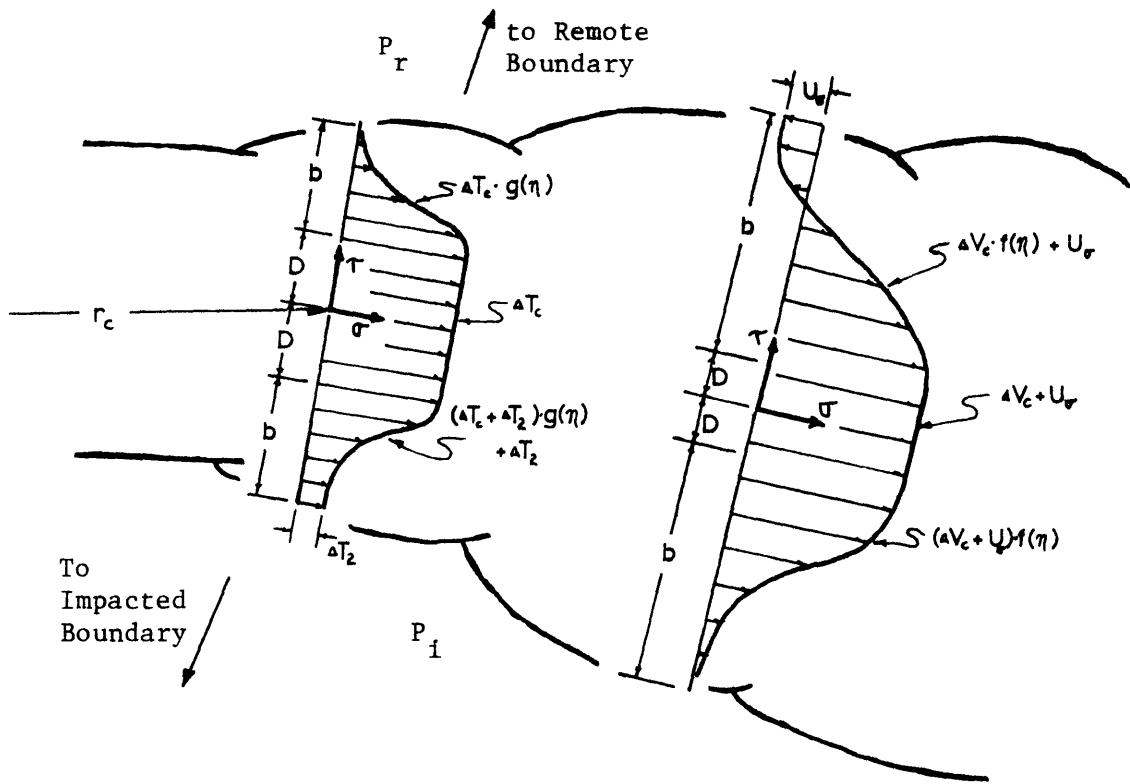
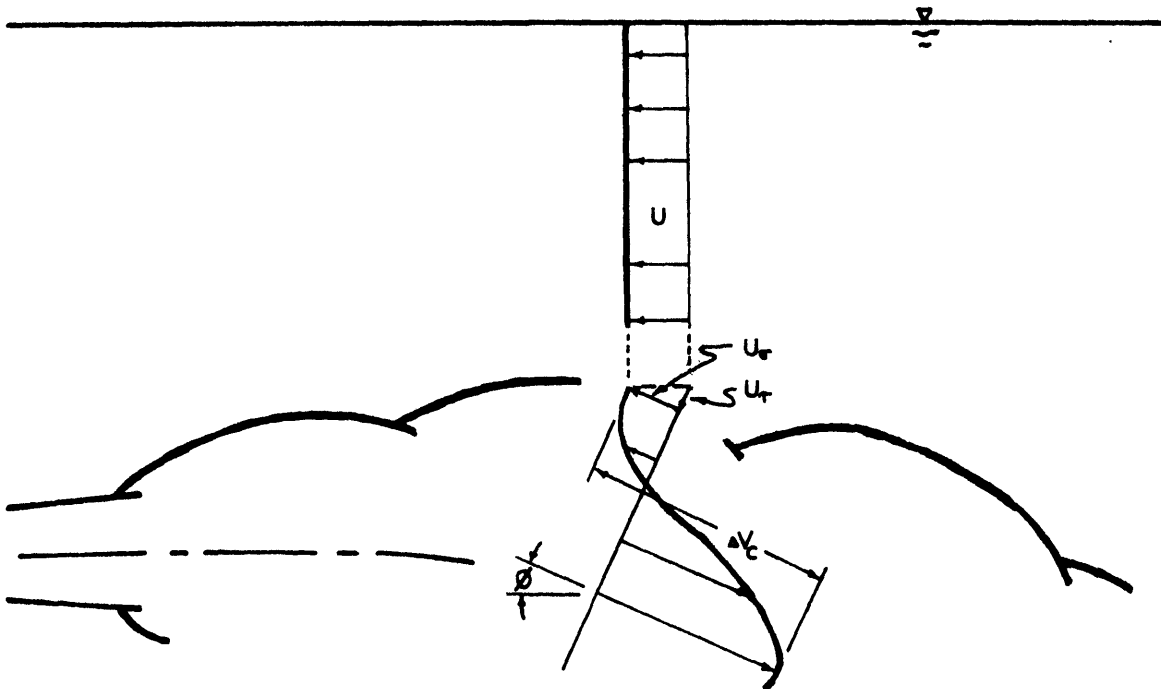Figure 3-8   Assumed Mean Temperature and Velocity Profiles

Figure 3-9   Remote Boundary Ambient Region Velocity Assumptions

of the very simple distribution chosen for U. Instead the following

simple geometric relations are chosen:

$$U_\sigma = U \cos \phi \qquad\qquad (3.55)$$

$$U_\tau = U \sin \phi \qquad\qquad (3.56)$$

The value for U_τ can be much greater than the entrainment velocity

(prescribed by a kinematic boundary condition). In real flow cases,

lateral ambient velocity components approaching the jet should be of order

$U \sin \phi$ in magnitude. However, the jet boundary must decelerate the

entrainment flow to the average velocity across the jet boundary, V_e.

This deceleration requires a positive pressure gradient not accounted

for by equation 3.52. The magnitude of the pressure increase is

$$\frac{\Delta P_d}{\rho} \; \alpha \; V_e \cdot (U \sin \phi - V_e) \qquad\qquad (3.57)$$

For $U \sin \phi \gg V_e$ the calculation of U_τ by equation 3.56 essentially

adjusts the dynamic pressure to include this increase.

Thus equations 3.52, 3.54, 3.55, and 3.56 constitute the relations

added by the ambient fluid region adjacent to the remote boundary.

3.3.2 Ambient Region with Impacted Boundary

As stated in Section 3.2, this region is assumed to be characterized

by its temperature, $T_i (=T_a + \Delta T_i)$ and a pressure, P_i. Both are assumed

to be uniform over the entire region. The determination of these values

for the integral jet model is entirely different for the two types of

impacted boundaries: coherent and diffuse.

3.3.2.1 Coherent Impacted Boundary

This boundary occurs in the attached flow regime of this study.

The temperature difference ΔT_i is caused by recirculating jet flows. P_i

is primarily a dynamic pressure caused by the strong vortexlike motion

in this region (Figure 3-10). Both ΔT_i and P_i are determined by iteration.

Reasonable values for P_i/ρ (proportional to M_o/H_i^2) and ΔT_i (propor-

tional $\Delta T_o \frac{Hi}{D_o}$) are chosen initially and the jet calculations are carried

out to determine conditions at a final point just before the jet impacts

the boundary ($z_c = c_2 b$; see Figure 3-10). At that point a local,

horizontal momentum balance is performed. The balance is similar to

those suggested by Bourque and Newman (1960) and Sawyer (1960, 1963)

in Section 2.5.2, but includes excess entrainment associated with jet

impact of the boundary and head loss associated with the flow turning

corners. Referring to Figure 3-10, the excess entrainment increases the

final jet flow at the impact point ($z_c = c_2 b$) by a factor of $1 + c_3$. The

constants c_2 and c_3 are determined by fitting experimental data. Their

values should be within certain logical ranges.

$$0 < c_2 < 1 \quad \text{and} \quad 0 < c_3 < .5 \tag{3.58}$$

The energy losses are expressed as

$$f(\phi_f) \cdot [\int_{\tau'}^{b} v^2 d\tau] \Big|_{z_c = c_2 b} = U_{out}^2 H_{out} \tag{3.59}$$

$$f(\pi - \phi_f) [\int_{-b}^{\tau'} v^2 d\tau] \Big|_{z_c = c_2 b} = U_{in}^2 H_{in} \tag{3.60}$$

where τ' locates the dividing streamline in the jet and ϕ_f, U_{out}, U_{in},

Figure 3-10   Coherent Impacted Boundary
Definitions and Equations

Flow Eq.

$$H_{out} \cdot U_{out} = (1+c_3) \cdot \int_{\tau'}^{bf} v \, d\tau$$

$$H_{in} \cdot U_{in} = (1+c_3) \int_{-b}^{\tau'} v \, d\tau$$

Momentum Eq.

$$H_{out} \cdot U_{out}^2 - H_{in} \cdot U_{in}^2 = \cos(\phi_f) \cdot \int_{-b_f}^{b_f} v^2 \, d\tau$$

H_{out}, and H_{in} are defined in Figure 3-10. The energy loss function, $f(\phi)$, is derived from pipe flow data of energy loss coefficients in elbows of various angles (Ito, 1960) as

$$f(\phi) = .113\phi - .0439\phi^2 + .00658\phi^3 \qquad (3.61)$$

For $0 < \phi < \pi$, the exact momentum balance appears in Figure 3-10.

If horizontal momentum is not balanced, or if the average jet temperature at impact is not ΔT_i, the estimated values of P_i/ρ and ΔT_i are adjusted. The entire jet solution and momentum balance check are repeated until convergence to successful values of P_i/ρ and ΔT_i is obtained.

3.3.2.2 Diffuse Impacted Boundary

In this study a diffuse impacted boundary is associated with detached flow. In this case jet equations cannot be applied all the way to the impacted boundary. In fact, observations of jet structure do not justify applying them beyond the point at which the jet of trajectory becomes approximately vertical. Therefore experimentally deduced values of P_i and ΔT_i must be used in the analysis. However it is possible, through dimensional analysis and physical reasoning, to predict the functional form for P_i and ΔT_i. Thus when calibrated with the experimental observations of Chapter 5, these relationships can be used more generally.

The ambient region being considered (Figure 3-11) brings diluted jet water back to supply the initial jet entrainment. The magnitude of ΔT_i is inversely proportional to the jet flow rate, Q_f, at the point

of recirculation, or

$$\frac{\Delta T_i}{\Delta T_o} \sim \frac{Q_o}{Q_f} \qquad (3.62)$$

The pressure magnitude P_i has two contributing components (Figure 3-11). Hydrostatic pressures develop because the recirculating jet water has a different density than the ambient water on the outside of the jet. In addition dynamic pressures must exist (as in Section 3.3.2.1) because of the vortex-like motion in the ambient region.

Referring to the arguments of Section 3.1, the initial momentum flux, M_o, and buoyancy flux, B_o are the primary dimensional governing parameters of the detached flow regime. However the secondary influence of the initial flow rate Q_o and the initial radius r_o are not always found to be insignificant. These influences suggest dimensionless equations where ΔT_i (or Q_f) and P_i/ρ are normalized by the primary dimensional governing parameters M_o and B_o:

$$\frac{Q_f}{M_o^{5/4}B_o^{-1/2}} = \frac{Q_o \Delta T_o}{\Delta T_i M_o^{5/4}B_o^{-1/2}} = f_1\left(\frac{r_o}{M_o^{3/4}B_o^{-1/2}}, \frac{Q_o}{M_o^{5/4}B_o^{-1/2}}\right) = f_1\left(\frac{\ell_r}{\ell_B}, \frac{\ell_Q}{\ell_B}\right)$$

$$\qquad (3.63)$$

$$\frac{P_i/\rho}{M_o^{-1/2}B_o} = f_2\left(\frac{r_o}{M_o^{3/4}B_o^{-1/2}}, \frac{Q_o}{M_o^{5/4}B_o^{-1/2}}\right) = f_2\left(\frac{\ell_r}{\ell_B}, \frac{\ell_Q}{\ell_B}\right) \qquad (3.64)$$

These relationships may be simplified somewhat through the following arguments.

Radial jets in the literature and in this study all have port radius, r_o significantly greater than port width, D_o. (There would be severe

$$\frac{\Delta P_h}{\rho} \sim \ell_B \cdot \left[\frac{\rho(T_a + \Delta T_i) - \rho(T_a)}{\rho(T_a)}\right] \cdot g$$

$$\mathbb{F}_i^2 = \frac{\left(V_e\big|_{max.}\right)^2}{\Delta P_h / \rho}$$

$$\left[P_r , T_a\right]$$

$$V_e\big|_{max.}$$

$$\left[P_i , T_a + \Delta T_i\right]$$

$$\left[P_r , T_a + \Delta T_i\right]$$

hydrostatic
component
of pressure
in ambient
region

$\sim \ell_B$
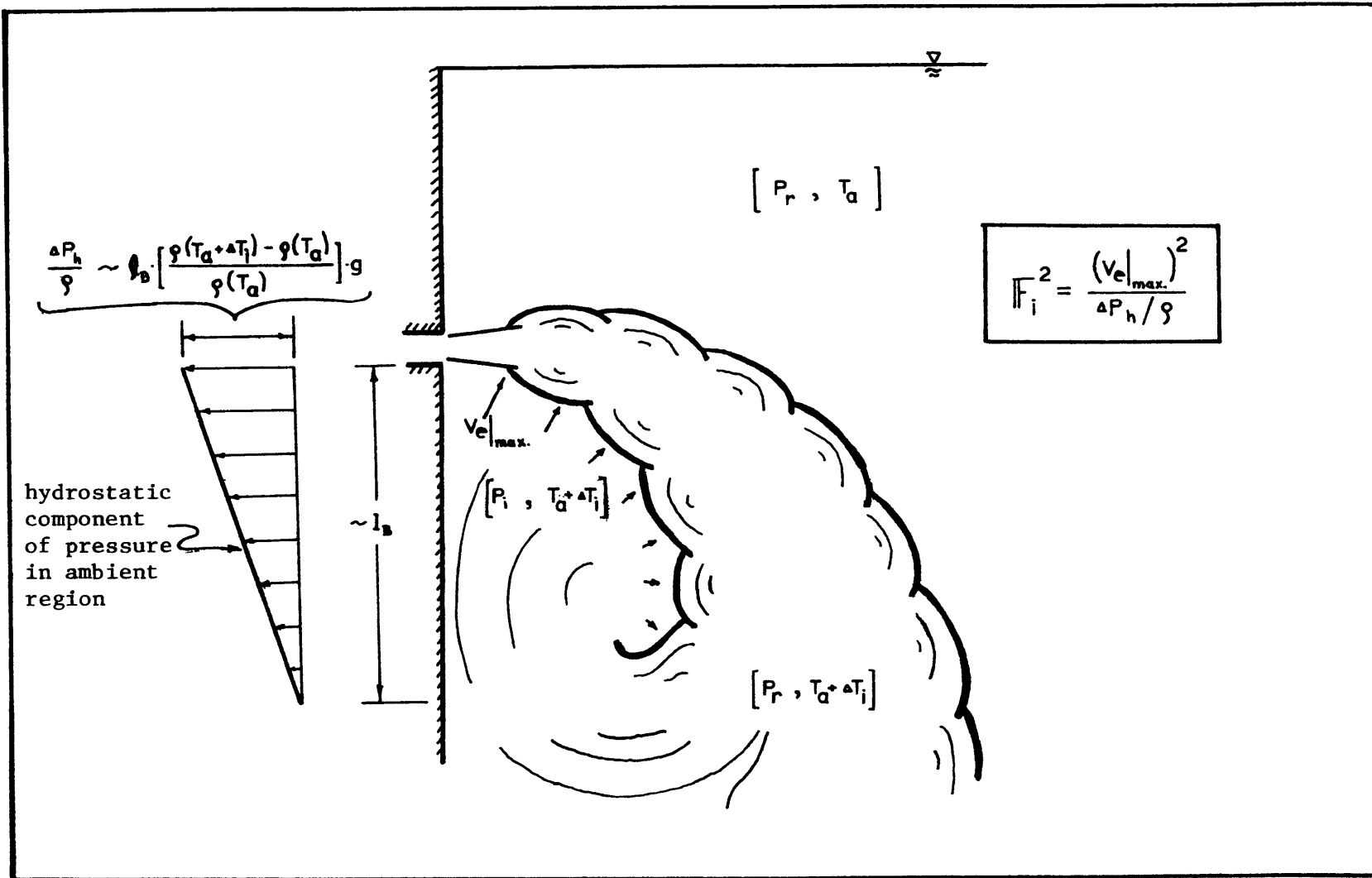
Figure 3-11   Parameters for Ambient Region with a Diffuse Impacted Boundary

flow distribution problems in any real jet where the port width exceeded the port radius.) Therefore ℓ_r, which depends solely on r_o, is greater in magnitude than ℓ_Q, which depends equally on r_o and D_o. The influence of both length scales should become insignificant at large distances, but the influence of ℓ_r should be felt the longest. Therefore the final jet flow rate Q_f should depend more heavily on ℓ_r than ℓ_Q, suggesting

$$\frac{Q_o \Delta T_o}{\Delta T_i M_o^{5/4} B_o^{-1/2}} \simeq f_1(\frac{\ell_r}{\ell_B}) = f_1(\mathbb{R}) \tag{3.65}$$

The same argument _cannot_ be made to reduce the parameter dependency of P_i; the dynamic component of this pressure is controlled by entrainment velocity magnitudes that are largest very close to the jet port where both Q_o and r_o are important. Instead it is postulated that equation 3.64 may be simplified to the form

$$\frac{P_i/\rho}{M_o^{-1/2} B_o} \simeq f_2(\mathbb{F}_i) \tag{3.66}$$

where $\mathbb{F}_i$ is a densimetric Froude number defined by

$$\mathbb{F}_i = \frac{V_e|_{max}}{[\frac{\rho(T_a + \Delta T_i) - \rho(T_a)}{\rho(T_a)} g \, l_B]^{1/2}} \tag{3.67}$$

and $V_e|_{max}$ is the maximum entrainment velocity occuring in the ambient region. $\mathbb{F}_i$ is suggested as a governing parameter because it expresses the relative importance of the two components of the pressure P_i/ρ. Large values of $\mathbb{F}_i$ indicate the dominance of the dynamic or vortex

111

component of pressure while small values indicate the dominance of the hydrostatic component. $\mathbb{F}_i$ is found by calculating $V_e|_{max}$ based on the integral jet model and ΔT_i based on equations 3.62 and 3.65.

Equations 3.65 and 3.66 have thus reduced the normalized dependency of the two unknowns ΔT_i and P_i to one parameter each; $\mathbb{R}$ and $\mathbb{F}_i$ respectively.

3.4 Integral Jet Model - Solution Method

3.4.1 General

The solution of either flow regime of this study requires the same set of equations. The only difference is in the strategy used for obtaining the temperature ΔT_i and pressure P_i. If they are assumed known (by whatever method applies) and the variables P_r/ρ_a, U_σ, and U_τ are calculated according to equations 3.52, 3.55, and 3.56 respectively, then the integral jet model contains eleven basic variables:

$$\Delta V_c, \; U \; , \; \Delta T_c, \; D, \; b_{\frac{1}{2}}, \; Q_i, \; Q_r, \; r_2, \; r_c, \; z_c, \; \phi$$

that are functions of the independent variable σ only. Eleven[1] differential equations developed in Section 3.2 and 3.3 specify the way the variables change with σ. These appear in Table 3-8. The equations are linear and constitute an initial value problem since all the variables are known at the discharge point ($\sigma=0$).

The eleven governing equations were solved using a fourth order Runge-Kutta integration technique. The computer program that performed the integration.

---

[1] One of the equations 3.48 and one of the variables, D apply only to the zone of flow establishment. $D = 0$ in the fully developed jet.

Expanded Conservation Equations

1. $\dfrac{dQ}{d\sigma} - \dfrac{dQ_r}{d\sigma} - \dfrac{dQ_i}{d\sigma} = 0$ (3.42)

2. $\dfrac{d\phi}{d\sigma} M + \dfrac{dQ_r}{d\sigma} U_\perp = \dfrac{P_r - P_i}{\rho_a} r_c - G \cos (\phi)$ (3.43)

3. $\dfrac{dM}{d\sigma} - \dfrac{dQ_r}{d\sigma} U_\sigma = G \sin \phi$ (3.44)

4. $\dfrac{dB}{d\sigma} - \dfrac{dQ_i}{d\sigma} \Delta T_i = 0$ (3.45)

Entrainment Asymmetry

5. $\dfrac{dQr/d\sigma}{dQi/d\sigma} = [\dfrac{1+4.93b_\frac{1}{2}/r_2}{1-4.93b_\frac{1}{2}/r_2}][\dfrac{1+1.8b_\frac{1}{2} \cdot \sin \phi/r}{1-1.8b_\frac{1}{2} \cdot \sin \phi/r}] \dfrac{\Delta V_c}{\Delta V_c + U_\sigma}$ (3.47)

Jet Spreading

6. $dD/dx = [.07 - \dfrac{D}{r_c}] \dfrac{1+.5 \, U_\sigma/V_o}{1+U_\sigma/V_o}$ (3.48)

or

$db_\frac{1}{2}/dx = \{.105+.005 \tanh[(.43 - \dfrac{\Delta V_c}{V_o})/.028]\} \dfrac{1+U_\sigma/(.88 \, \Delta V_c)}{1+U_\sigma/(.44 \, \Delta V_c)}$ (3.49)

Geometry

7. $\dfrac{dr_c}{d\sigma} = \cos \phi$ 8. $\dfrac{dz_c}{d\sigma} = \sin \phi$ 9. $\dfrac{d\phi}{d\sigma} = r_2$ (3.51)

Flow Fields Connection

10. $\dfrac{dU}{d\sigma} [r_{up} Z_{up}] + \dfrac{db_\frac{1}{2}}{d\sigma} [(+Z_{up}\sin\phi - r_{up}\cos\phi) \cdot U \dfrac{b}{b_\frac{1}{2}}] + \dfrac{dD}{d\sigma} [(Z_{up}\sin\phi - r_{up}\cos\phi)U \,] + [1+(b+D) \dfrac{d\phi}{d\sigma}][Z_{up}\cos\phi + r_{up}\sin\phi] \, U = \dfrac{-dQ_r}{d\sigma}$ (3.54)

Core Velocity (Zone of Flow Establishment Zone Only)

$\dfrac{d\Delta V_c}{d\sigma} + \dfrac{dU_\sigma}{d\sigma} = \dfrac{(\Delta\rho_o/\rho)g \sin(\phi)}{[V_o^2 - 2(\Delta\rho_o/\rho)g(H_i - z)]^\frac{1}{2}}$ (3.50)

Table 3.8 Complete Integral Jet Equations

113

was written in PL1 on MIT's Multics computer system. The integration
step size was a user input. Intermediate results were periodically
checked against calculations at a reduced step size. The step size
was automatically halved if a specified accuracy was not obtained.

3.4.2 Flow Regime Limits with the Integral Jet Model

The integral jet model just described naturally signals the
limiting conditions for which a certain flow regime can exist. With
everything else constant, experiments show that decreasing the dimension-
less number $\mathbb{L}$ causes a detached jet to finally reach a transition point
and become attached. Likewise, integral model results show that, for
a jet which is assumed to be detached, decreasing $\mathbb{L}$ moves the jet trajec-
tory closer to the remote boundary until finally they intersect. This
naturally signals a limit to the detached jet flow regime.

The attached jet flow regime has a similar natural limit. This
time the $\mathbb{L}$ value of an attached jet is increased to cause detachment.
The integral model solution for attached jets requires that a pressure
P_i be found such that horizontal momentum fluxes into and out of the
impact region balance. Beyond a certain value of $\mathbb{L}$, no value of pressure
will satisfy this requirement. For even higher values of $\mathbb{L}$, it is not
even possible to effect attachment, let alone satisfy the momentum
balance. Pressures that are sufficiently high (in absolute value) to
overcome buoyancy and make the jet bend toward the impact boundary, in
fact, cause the jet to bend back on itself. Thus boundary impact never
occurs. This clearly signals a limit to the attached flow regime.

A comparison of experimental and integral model results shows

that the two natural limits just discussed are conservative. The actual
flow regime limits are more restrictive; i.e. initially detached jets
are observed to attach at somewhat larger values of L and initially
attached jets are observed to detach at somewhat smaller values of L
than indicated by this analysis. This motivated the following,
more refined analysis of these transitions.

3.4.2.1 Detached Jet Limits

Experimentally, it was observed that as soon as any jet fluid
reached the (upper) remote boundary, shutting off the remote ambient
region, the jet quickly became attached (changing the remote boundary to
a coherently impacted boundary). Once attached, the jet flow was
stable because of a hysterisis effect very similar to the one described
for plane jets with an angled boundary (Section 2.5.3). It was apparent
that the extreme rather than the mean jet behavior created the transition
to the attached flow regime.

The integral model is formulated in terms of the mean jet width
$b(= 1.8 \, b_{1/2})$. However, plane jet data from Heskestad (1965) shows that
jet eddies extend to a distance of $2.7 \, b_{1/2}$ with an intermittency of 10%.
Because it is these larger eddies which experiments show to be associated
with attachment, the integral model computed the wider boundary, as well,
for purposes of predicting attachment.

The attachment indicator chosen involved calculating the ambient
fluid velocity U' that would occur for a jet boundary of $2.7 \, b_{1/2}$. When
$U'/\Delta V_c$ equalled .44 (the value when the spreading rate, equation 3.49,
becomes infinite) spontaneous attachment of the jet was assumed to

occur. The jet governing parameters were assumed to be outside the limits of the detached flow regime.

3.4.2.2 Attached Jet Limits

Experimentally, attached jets approaching the detachment transition were observed to lose a significant amount of their initial momentum in overcoming buoyancy forces on the way to the impacted boundary. When whole eddies began to sink vertically without reaching the boundary, a spontaneous transition (detachment) to the detached flow regime was imminent. Once detached, the jet flow was stable because of the hysterisis effect.

An attached jet, as analyzed by the integral model, has a nearly constant spreading rate and a decreasing momentum flux as it climbs to the coherently impacted boundary. If the decrease in momentum flux is fast enough, the integral model calculates a decreasing jet flow rate or negative entrainment. Negative entrainment was taken as the indicator that spontaneous detachment of the jet would occur. The jet governing parameters were assumed to be outside the limits of the attached flow regime.

IV. Physical Experiments

4.1 Experimental Layouts

4.1.1 Model Basin

The physical experiments were conducted in a 12.2 m x 18.3 m x 0.60 m (40' x 60' x 24") basin located on the first floor of the Ralph M. Parsons Laboratory for Water Resources and Hydrodynamics at M.I.T. There was a 4.57 m (15 ft) long plexiglass window in one wall of the basin which allows for visual observation and photography of the velocity field close to the wall. Figure 4-1 presents a general layout of the basin. A 60° radial jet sector was defined by a false wall inside the basin. Experimental observations were confined to that region.

4.1.2 Experimental Model

Figure 4-2 shows a cutaway three-dimensional view of the plexiglass model constructed for OTEC experiments at MIT and described by Adams et al.,1979 and Coxe, et al, 1981. Half of the model was mounted on the plexiglass window. Intake and discharge flows could be controlled in 30° sectors. Only two sectors (totalling 60°) were active in these experiments.

The model was designed to allow variation of a number of parameters including intake port height relative to the water surface and the depth to the discharge port. The discharge ports were easily removed and modified to allow different radial slot widths to be tested.

4.1.3 Flow Circuits

Figure 4-1 illustrates schematically the water flow circuits. A constant temperature discharge flow was maintained by mixing cold tap

117

18.3 m

H: Head Tank

F: Flow Meter

M: Manifold

P: Pump

X: Control Valve

12.2 m

False Wall ········
(length = 3.7 m)

OTEC ········
Model

Window
(length = 4.6 m)

P

F

to Drain

M

F

P

H

Cold Hot
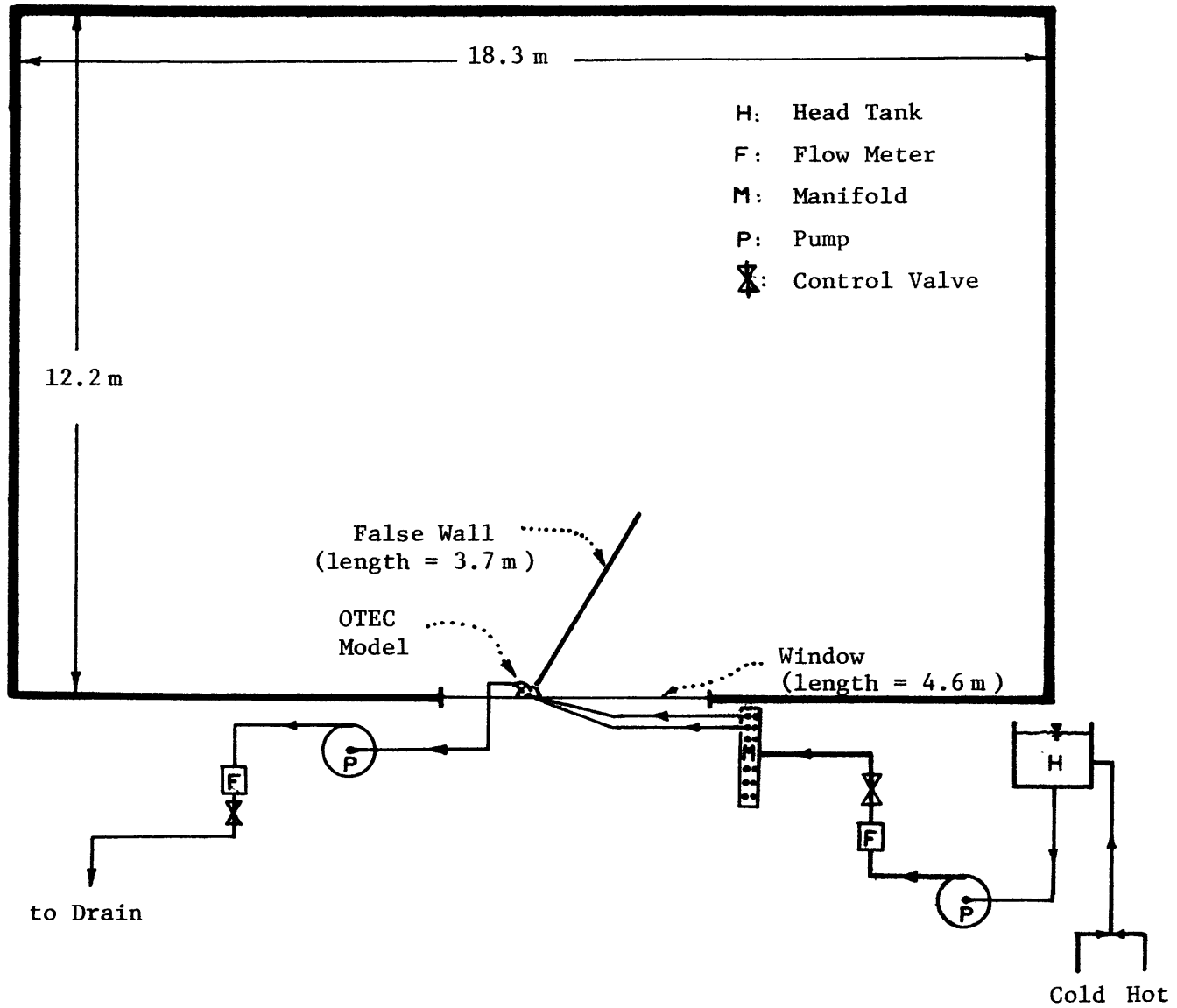
Figure 4-1   Model Basin Layout
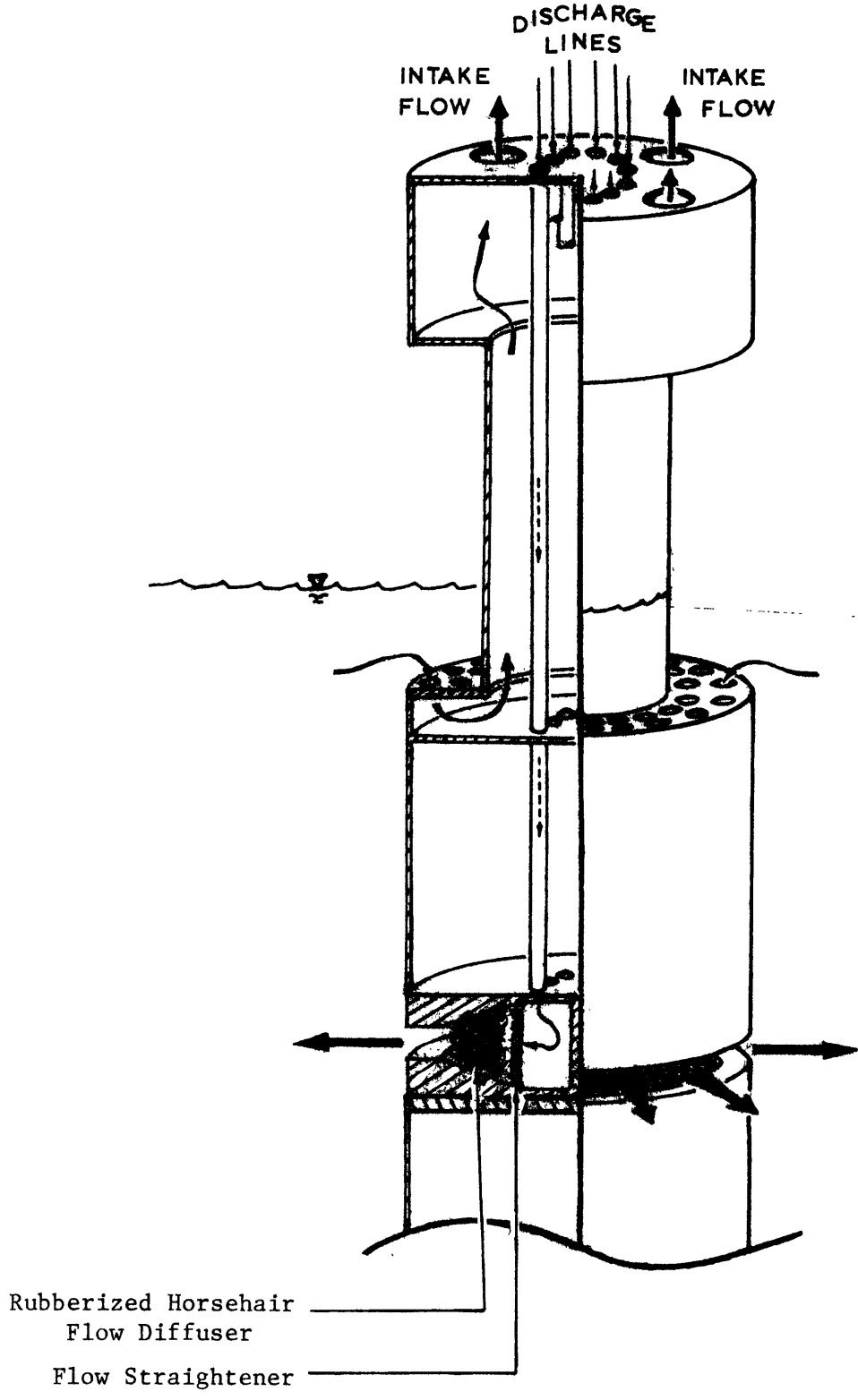
Figure 4-2   Cutaway View of M.I.T. OTEC Model

water with hot water that had passed through a steam heat exchanger. A mixing valve adjusts the relative flow of hot and cold water to achieve any desired temperature.

From the mixing valve, the water flows to a constant head tank which provides a constant pressure in the delivery to the model, and helps to damp out short term temperature fluctuations in the hot water system.

The discharge water is pumped from the constant head tank through a flow meter and control valve to a manifold. The manifold has twelve valves with hoses connected to individual orifice meters for the purpose of adjusting and monitoring the flow rate to each of the model's 30° sectors. For these experiments, in a 60° sector, only two were used. Hoses from the flow meters are connected to brass tubes in the upper portion of the model which direct the flow to the discharge ports in the center of the model. The discharge temperature was monitored at the model and in the flow lines.

The intake circuit draws water from the basin through the radial hole configuration near the top of the model. All holes outside the 60° sector of interest were blocked. The water was withdrawn by a pump, measured by a flow meter, and controlled by a valve where it flowed to a drain. The intake temperature was monitored at the model and in the flow lines.

4.2 Measurement Systems
4.2.1 Temperature Measurement Systems
4.2.1.1 Equipment

Temperature was measured by 26 Yellow Springs, Inc. thermistors (time constant = 1 sec.) located as shown in Figure 4-3. Three probes
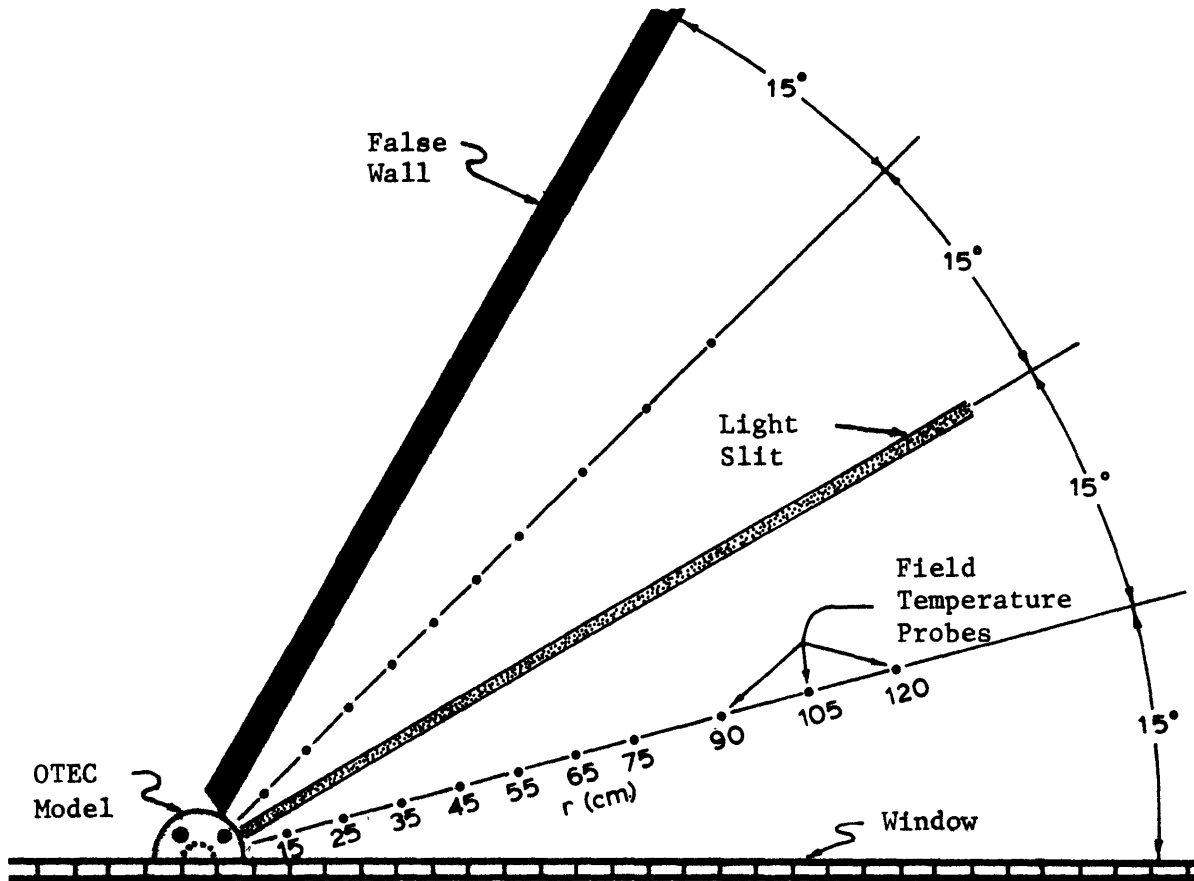
Figure 4-3   Experimental Measurement Systems

were used to monitor the intake temperature and three were used for the discharge temperature. The remaining probes, designated field probes, were fixed to a vertically traversing frame (electric motor driven) to monitor temperatures found in the basin. The field probes were all at the same elevation and arranged in two rays extending out from the model. They were far enough from the walls to avoid measuring boundary effects.

A digital electronic volt meter recorded temperatures on a paper printout and on punched paper tape. All the probes could be scanned in 10 seconds. During a typical experiment between 1200 and 1600 temperature readings were recorded.

4.2.1.2 Calibrations

The small differences in temperature ($\sim.1°C$) that needed to be discerned required careful calibration of the thermistor probes. Before the series of tests all the probes were calibrated at three different temperatures (10°C, 20°C, 30°C) using a constant temperature bath (accurate to .05°C). In addition there were calibration checks conducted throughout the experimental series. After each experiment, intake and discharge probes were calibrated against a thermometer (accuracy to .05°C) placed in the actual intake or discharge port. This procedure also allowed accounting for the change in water temperature from the hoses, leading to the model (in which some probes were located), to the actual discharge or intake point. This temperature change could be as much as .5°C.

The "field probes" were checked for calibration every experiment using the horizontal temperature uniformity that existed in the basin prior to the start of an experiment. Neighboring calibrated temperature measurements were checked to find probes in error (with changed calibrations).

The temperature calibrations (at 3 temperatures) measured in the constant temperature bath prior to the experimental series were the basis for calibrating the data. For each experiment, the calibrations were _uniformly_ adjusted up or down according to what the single temperature checks (described above) indicated. A typical experiment had 10% of its probe calibrations adjusted more than 0.1°C. The adjustment of all three temperature calibrations on the basis of a single temperature check is based on the demonstrated linearity of the thermistor probes.

The single temperature checks also isolated probes that had gone bad
and needed replacement.

4.2.1.3 Data Reduction

The 1200-1600 temperature readings for each experiment were
entered into MIT's Multics computer system (Honeywell 6180 computer).
Computer programs calibrated the data and produced two data sets for
each experiment: (1) temperatures in °C; (2) percent of the discharge
temperature difference ($\Delta T/\Delta T_o$).

A plotting program (PL1 language) was used to examine each of the
data sets. Temperature maps of any plane in the basin could be created.
Of primary interest in these experiments were vertical planes extending
radially out from the model. The program could average the data spa-
tially or in time. For example, three temperature readings (separated by
approximately 15 seconds) were taken by the field probes at most posi-
tions in the basin. The program could average the three readings and plot
the average rather than any single reading. This was useful in averaging
out turbulent temperature fluctuations. Also, for the radially symmetric
discharge, it was useful to average together the two radial sections and
plot them as one (Figure 4-4).

The temperature data were used to determine discharge, intake, and
ambient region temperatures. Also the minimum temperature recorded at
each radius served as an estimate of the jet centerline temperature at
that radius.
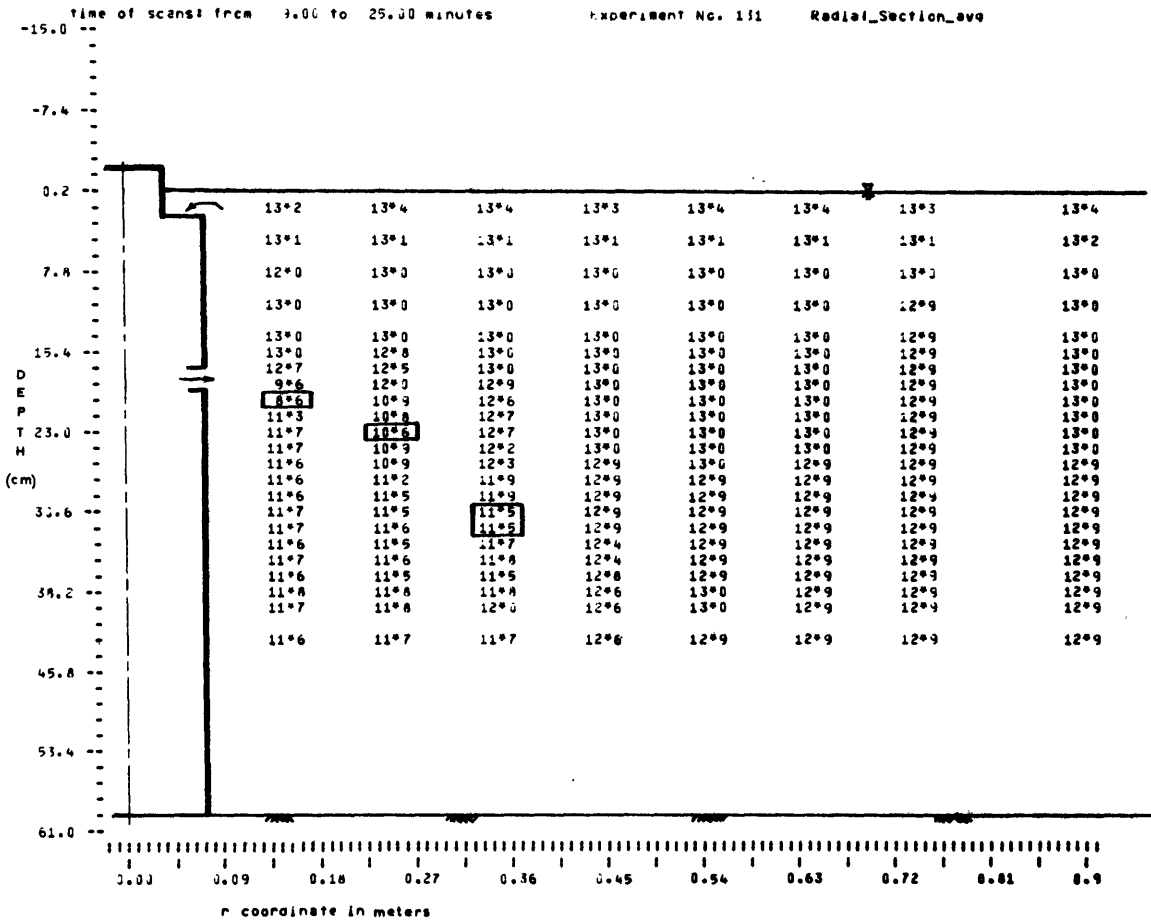
T_a = 12.99°C   (ambient temperature

T_d = 5.33°C   (discharge temperature)

T_i = 11.64°C   (temperature below jet)

Experiment XIII-1

$\Delta T_o = T_a - T_d = 7.66°C$

$\Delta T_i = T_a - T_i = 1.35°C$
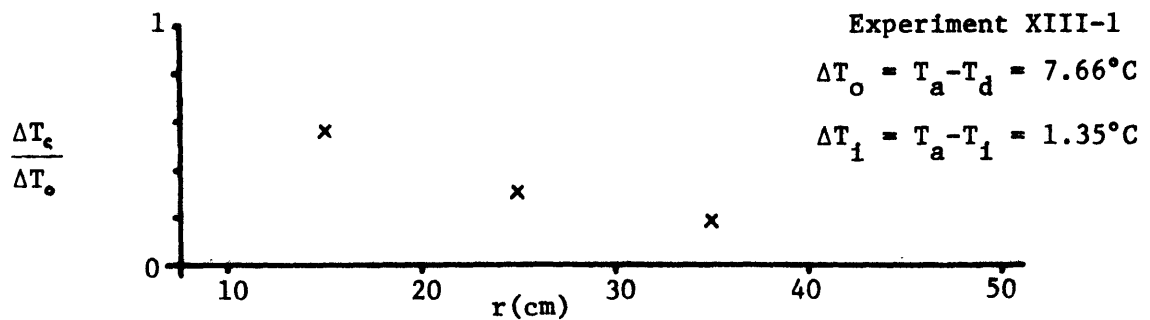
Figure 4-4   Data Reduction of Temperature Measurements

4.2.2 Trajectory Photographs

4.2.2.1 Equipment

Injection of a fluorescent dye (Rhodamine B) into the discharged flow served to tag the jet for photographis purposes. A pair of photographic slide projectors supported above the water was used to emit a narrow slit of light which illuminated a cross-section (radial-vertical) of the flow field (Figure 4-3). This illumination was most effective in an otherwise dark laboratory. The slit extended out from the model on a ray 30° from the plexiglass window. Photographs through the window recorded the jet trajectory on this cross-section only. Wall boundary effects were again avoided.

4.2.2.2 Calibration

A (vertical-radial) grid was placed temporarily in the basin along the same 30° ray where experimental photographs were taken. Photographs of this grid were taken from the same camera position and for the same lens focal lengths used in the experiments. The photographed grid included the same camera angle and light refraction distortions as the experimental photographs.

4.2.2.3 Data Reduction

At least five black and white photographs of the dyed jet were taken. A photo-enlarger was used to transfer the jet outlines to the same distorted grid (created by the photographs described in the calibration section). The jet boundary adjacent to the recirculating ambient region (that became dyed as well) was hardest to discern (Figure 4-5). The average position of the jet boundary outlines were taken as

126

Surface

Single Photograph
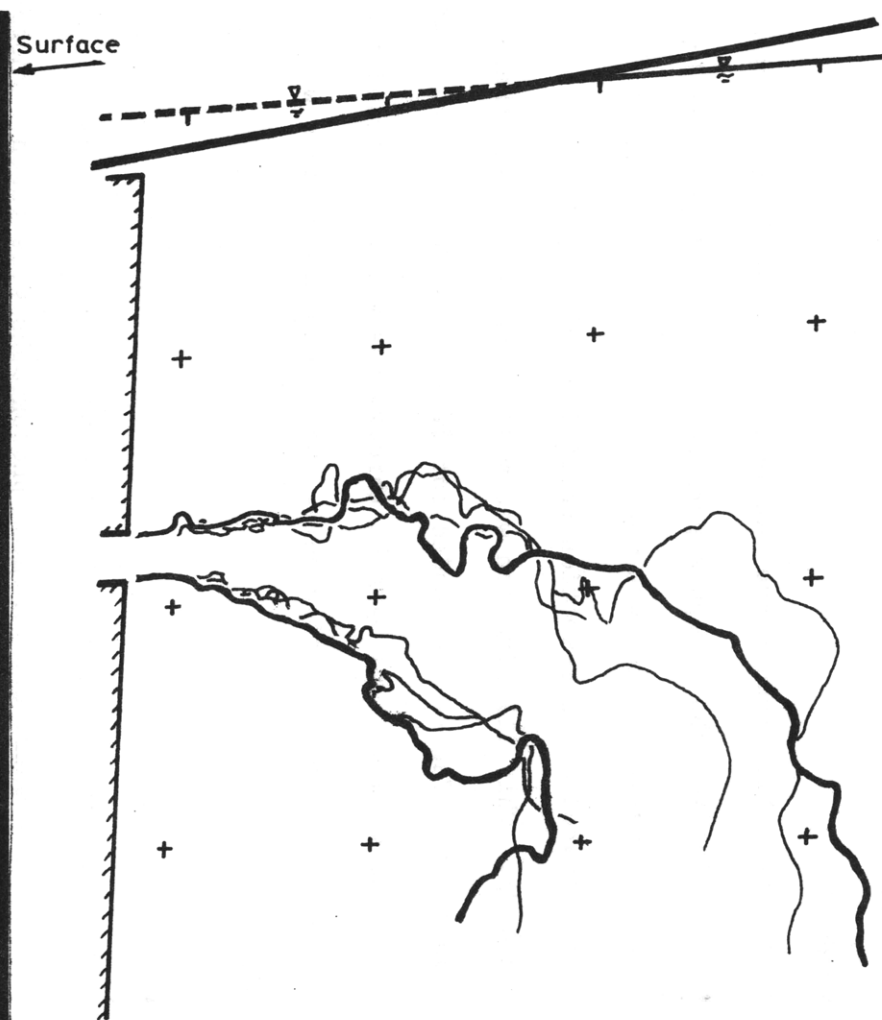
Photographic Tracings

Figure 4-5 Photographic Trajectory Measurement (exp. XIII-1)

indicators of the jet width b (see Section 2.1) from the jet centerline.

4.2.3 Hydrogen Bubble Velocity Photographs

4.2.3.1 Equipment

This technique produces small hydrogen bubbles by the electrolysis of water. Hydrogen bubbles created at the cathode are advected away by the surrounding fluid motion. Velocity measurements are made by creating bubbles only at certain time intervals. The distance between sets of bubbles (obtained from a photograph) and the time interval used, can be combined to calculate fluid velocities. The bubbles need to be small enough so that buoyant forces do not significantly affect their motion.

Copper stock and fine stainless steel wire were used to construct the cathode used in these experiments. An insulating varnish was applied everywhere except for the central two centimeters of the fine wire where the hydrogen bubbles were created.
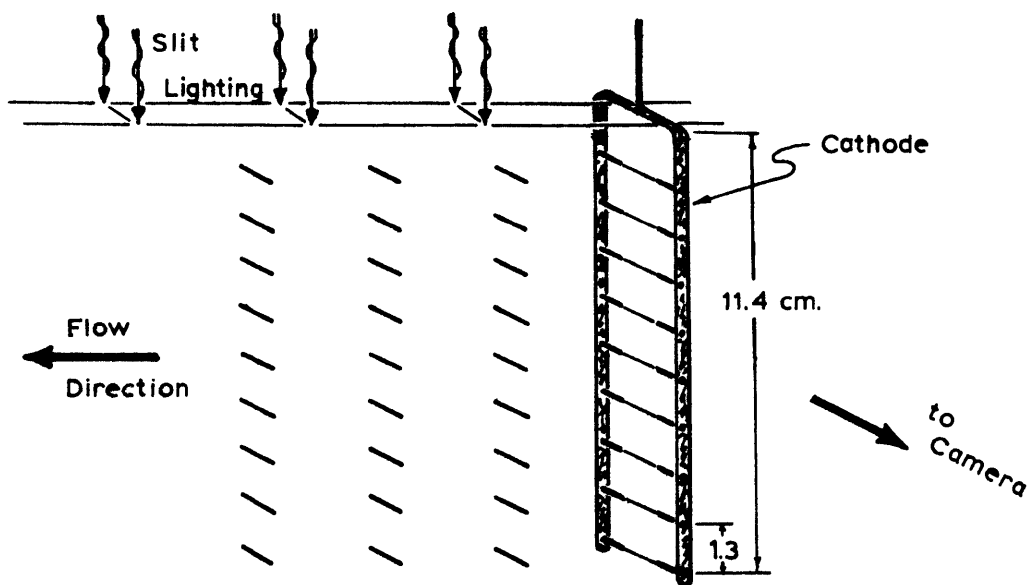
Figure 4-6   Hydrogen Bubble Apparatus

It was only practical to measure velocites in the irrotational ambient region above a detached jet. The cathode was placed in the plane illuminated by the light slit used for trajectory photographs (Figure 4-6). The camera orientation allowed photographing a line of hydrogen bubbles as one dot and thus increasing their visibility. The anode (simply a copper wire) was immersed in the water outside of the illuminated viewing plane.

A D.C. power supply was applied through a switch operated by a signal generator. The signal generator controlled the timing and duration of electrical, and hence hydrogen bubble, pulses. A time interval was chosen to keep successive bubble pulses less than two centimeters apart. Velocities down to 0.5 cm/sec could be measured.

4.2.3.2 Calibrations

The distorted grid used for jet trajectory photographs was also used for bubble photographs. The time intervals produced by the signal generator were calibrated by an oscilloscope (error ± .02 sec.).

Buoyant forces in this study were ignored because only the horizontal component of velocity was of interest. The photograph in Figure 4-7 shows that the forces were negligible anyway.

4.2.3.3 Data Reduction

Black and white photographic negatives of the produced bubble pattern were transferred to distorted grid drawings (Section 4.2.2.2). The apparent bubble size is due to dispersion of the line of bubbles, not individual bubble diameters (Figure 4-7).

An average horizontal velocity (as a function of radius from the
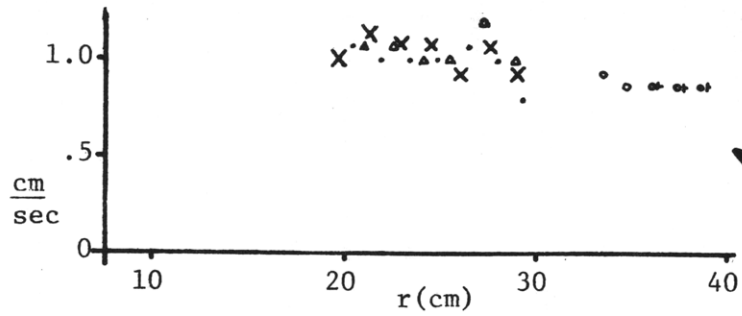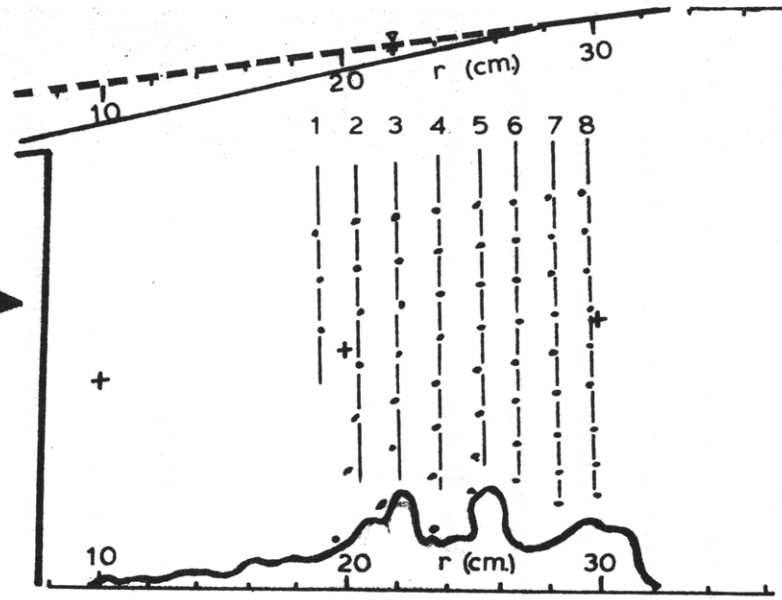
Symbol: **X**

$\Delta t = 1.5$ sec.

No.	1	2	3	4	5	6	7	8
r (cm.)	18.9	20.4	22.1	23.7	25.3	26.7	28.3	29.7

Figure 4-7 Data Reduction of Hydrogen Bubble Velocity Measurements

model) was sought. To this end, "average" vertical lines were drawn
through each set of bubbles (all released at the same time). The dis-
tance of each line from that of the last bubble set created was estimated
from the distorted grid. The distance between successive lines was
then calculated. An average horizontal velocity estimate (at a parti-
cular radius) was found by dividing that distance by the bubble genera-
tion time interval (Figure 4-7).

4.3 Experiments

4.3.1 Experimental Parameters

The seventeen experiments were conducted in sets of two or three.
Each set was conducted at one time under the same basin conditions. The
experiments of a set had successively increasing discharge flows and in-
take flows (if applicable). For a particular intake depth, discharge
depth, and ratio of intake to discharge flow rate (k value), the experi-
ments of a set covered the range of behavior from the detached to the
attached jet flow regime. The last experiment was always an attached
jet (Table 4-1).

All three types of measurements were made for each experiment
(except velocity measurements for the attached jet which had no irrota-
tional ambient region). The experimental parameters appear in Table 4-1.
The dimensional parameters Q_o, M_o and B_o are based on values for an
equivalent full radial jet (360° rather than the actual 60° sector).
The initial jet angle (ϕ_o) was determined by enlargement of photographs
of the initial 4 cm of jet trajectory.

4.3.2 Experimental Procedure

A standard procedure for performing the experiments was established

130

Exp. Set	No.	k	ϕ_o[1]	H	r_o	D_o	V_o	$g\frac{\Delta\rho}{\rho_a}$	$M_o(*10^{-3})$	$B_o(*10^{-3})$	$Q_o(*10^{-3})$	$R_e(*10^{-3})$	F_i
			radians	cm	cm	cm	cm/sec	cm/sec^2	cm^4/sec^2	cm^4/sec^3	cm^3/sec	$(2D_oV_o/\nu)$	
I	1	1	-.03	11.9	7.6	.64	11.35	.764	8.5	0.55	0.72	1.2	.343
	2	1	+.05	11.8	7.6	.64	27.64	.882	46.5	1.48	1.68	2.7	.637
II	1	1	-.05	11.9	7.6	.64	15.79	.808	15.2	0.78	0.96	1.5	.423
	2	1	-.02	11.9	7.6	.64	19.74	.819	23.7	0.98	1.20	1.9	.497
	3	1	-.03	11.8	7.6	.64	23.69	.898	34.1	1.29	1.44	2.3	.563
III	1	0	-.03	11.3	7.6	.64	15.79	.650	15.2	0.62	0.96	1.5	.446
	2	0	-.03	11.5	7.6	.64	23.69	.672	34.1	0.97	1.44	2.3	.575
	3	0	-.04	11.8	7.6	.64	27.64	.683	46.4	1.15	1.68	3.1	.623
IV	1	1	-.11	12.3	7.6	.32	15.78	.642	7.6	0.31	0.48	0.8	.536
	2	1	-.08	12.3	7.6	.32	23.67	.682	17.2	0.49	0.73	1.2	.702
	3	1	+.01	12.3	7.6	.32	31.56	.677	30.5	0.65	0.97	1.6	.836
V	1	0	-.12	11.6	7.6	.32	23.67	.760	17.2	0.55	0.73	1.2	.667
	2	0	-.03	11.7	7.6	.32	31.56	.773	30.5	0.75	0.97	1.6	.793
	3	0	-.07	11.8	7.6	.32	37.48	.796	43.0	0.91	1.15	1.8	.860
XIII	1	1	-.01	18.0	7.6	1.02	12.35	.570	14.8	0.68	1.20	1.9	.326
	2	1	+.00	18.0	7.6	1.02	17.28	.565	29.0	0.95	1.68	2.7	.426
	3	1	-.03	18.0	7.6	1.02	24.69	.583	59.2	1.40	2.40	3.8	.514

Table 4-1 Dimensional Experimental Parameters

1 ϕ_o is negative when pointing toward the free surface (Figure 3-6)

and used for every set of experiments.

The basin was filled approximately five hours before the experiment was to start. A combination of cold tap water and hot water flows was used. The basin was vertically mixed by hand at least three times. A plunger moved vertically accomplished the mixing without creating significant horizontal flows. The basin was left undisturbed for at least one hour to insure stagnant conditions.

Before the start of an experiment, the water for the discharge line was turned on and run through a bypass to a drain. This allowed for adjustment and stabilization of the discharge temperature. During this time, the temperature probes were scanned to establish the ambient temperature and to obtain a probe calibration. Basin temperatures were found to be uniform to within .2°C. When the discharge flow had stabilized to the desired temperature, the intake pump was turned on and the first experiment's intake flow rate (if any) was established. The experiment began when the dyed discharge flow was routed through the model and injected into the basin.

The flow field for the initial experiment was allowed to establish itself for about ten minutes. Temperature measurements were commenced with the field probes just below the water surface. When scans were completed at one level, the frame supporting the probes was lowered (usually 1.5 or 3.0 cm) to a new depth. Ten to fifteen seconds were allotted for the probes to reach equilibrium at the new depth and then the scans were repeated. Approximately fifteen minutes were required to scan the entire basin depth (∿20 scan depths).

The dye was turned off and the jet flow field became almost transparent. The dye was then reapplied to the discharge flow. A series

132

of trajectory photographs was taken as this freshly dyed discharge water emerged from the model. The photographic contrast between the jet flow and recirculating ambient regions was thereby maximized. The process was repeated a second and sometimes a third time to obtain more photographs.

Finally the hydrogen bubble generator was positioned at the desired depth and radius. Photographs were taken as the bubbles were being generated. Because of bubble dispersion several bubble generator radial positions were needed to record the entire velocity field above detached jets.

The measurements for the first experiment were then complete and new, larger flow rates were established for the second experiment of the set. Measurement procedures for subsequent experiments were similar to those for the first except that no velocity measurements were made in the last experiment (in the attached jet flow regime).

Because the flow rates were adjusted slowly between experiments, the discharge conditions for the transition from detached to attached jet flow (attachment transition) could be recorded. The discharge conditions for the detachment transition (from attached to detached jet) were also found by gradually lowering the discharge and intake flow rates until the attached jet of the final experiment became detached.

The set of two or three experiments took about ninety minutes to fully complete. By this time a layer of dyed water (diluted jet water) almost covered the entire basin floor. Buildup of this layer would have affected experiments lasting much longer.

V. Analytical Predictions of Experimental Results

5.1 Preliminaries

5.1.1 Pressure and Temperature Below a Detached Jet

Pressure and temperature functions for ambient regions with a diffuse impacted boundary were left undetermined in Section 3.3.2.2. Functional forms were suggested by dimensional arguments (equations 3.65 and 3.66), but the exact relation was left to be determined by experimental data.

Figure 5-1 plots the experimentally determined values of ΔT_i in the form suggested by equation 3.65. A line is fitted to the data trend.

$$\frac{\Delta T_o}{\Delta T_i} \frac{\ell_Q}{\ell_B} = 1.44 - .061 \ \mathbb{R} \tag{5.1}$$

This equation can clearly not be used for very large values of $\mathbb{R}$ as the temperature difference ratio $\Delta T_o / \Delta T_i$ cannot be negative. Some plane jet condition ($\mathbb{R} \to \infty$) must be approached asymptotically. The equation, however, applies well to the experiments of this study considering possible temperature measurement errors ($\pm 0.1°C$) and ΔT_o values ($\sim 7°C$).

No measurements of P_i were possible since its magnitude was too small. Instead, P_i was "experimentally determined" for each detached jet experiment by selecting that value of P_i which provided the best agreement between model predictions and experimental observations of jet trajectory. Figure 5-2 displays the experimentally determined values of P_i normalized in the form suggested by equation 3.66. The following relationship provides a reasonable fit to the values:

$$\frac{P_i/\rho}{B_o M_o^{-1/2}} = .55 + .15 \ \tanh \ [(\mathbb{F}_i - .60)/.08] \tag{5.2}$$

134
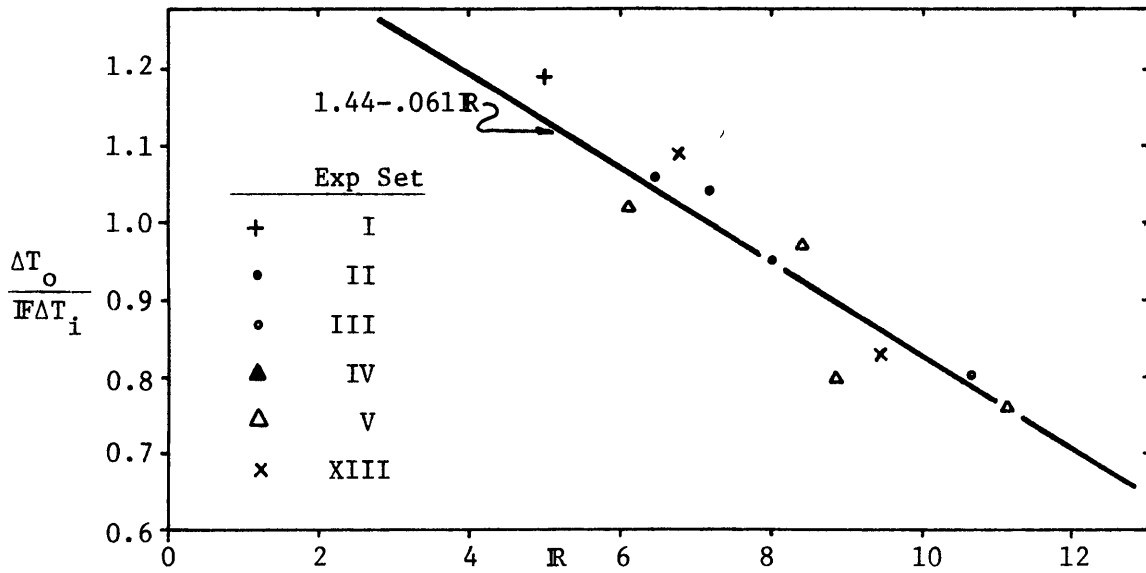
Figure 5-1   Proposed Relation for ΔT_i
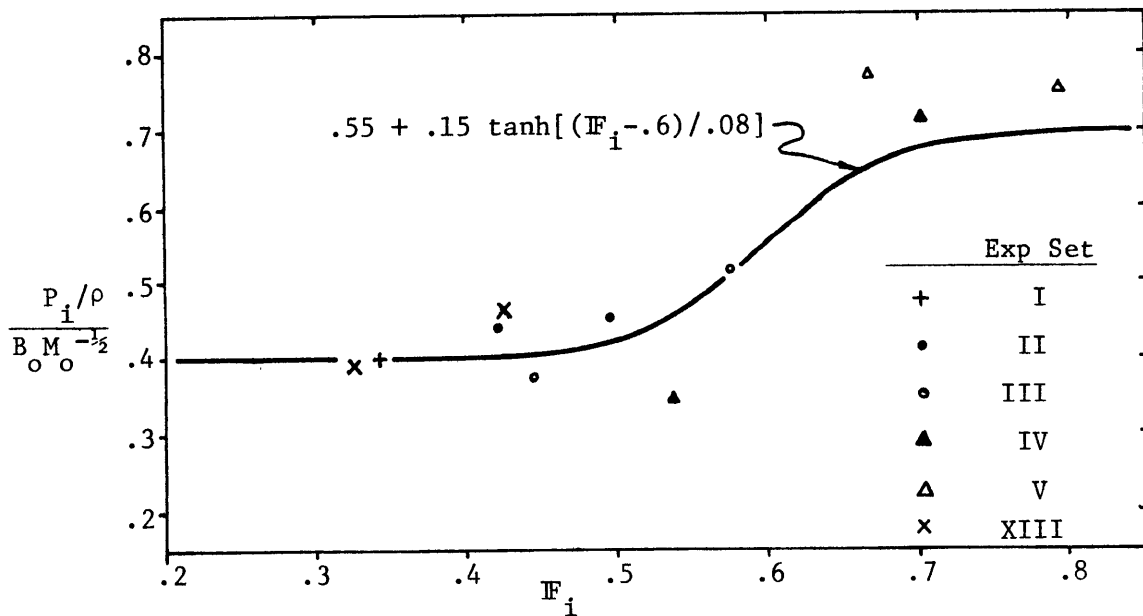
Figure 5-2   Proposed Relation for P_i/ρ

135

The integral jet model sensitivity to the exact value of P_i is examined later in Section 5.4.

5.1.2 Temperature Below an Attached Jet

The ambient region below an attached jet was complicated by diluted jet water falling to the basin floor after impacting the surface. The jet buoyancy is still calculated relative to the undisturbed basin conditions. However, the water being entrained from below the attaching jet clearly did not have the undisturbed basin temperature. The temperature instead was related to some final (after impact) jet dilution just as ΔT_i was for the detached jet.

The integral jet model considers this region to have a remote boundary and a uniform ambient temperature, T_a. The difference between this temperature and the initial basin temperature (ΔT_a) was measured in the experiments. The same arguments that applied to ΔT_i in the previous section suggest a relationship

$$\frac{\Delta T_o}{\Delta T_a} \cdot \frac{\ell_Q}{\ell_H} = f(\mathbb{R})$$ (5.3)

where ΔT_o is the difference between the jet discharge temperature and the initial basin temperature. Figure 5-3 plots the six available data points according to this relation. The limited number of data points does not make a relation clear. Therefore, in simulating the experiments of this study, measured ΔT_a values will be used, while in other cases the following relation will be applied.

$$\frac{\Delta T_o}{\Delta T_a} \cdot \frac{\ell_Q}{\ell_H} = 5.3$$ (5.4)
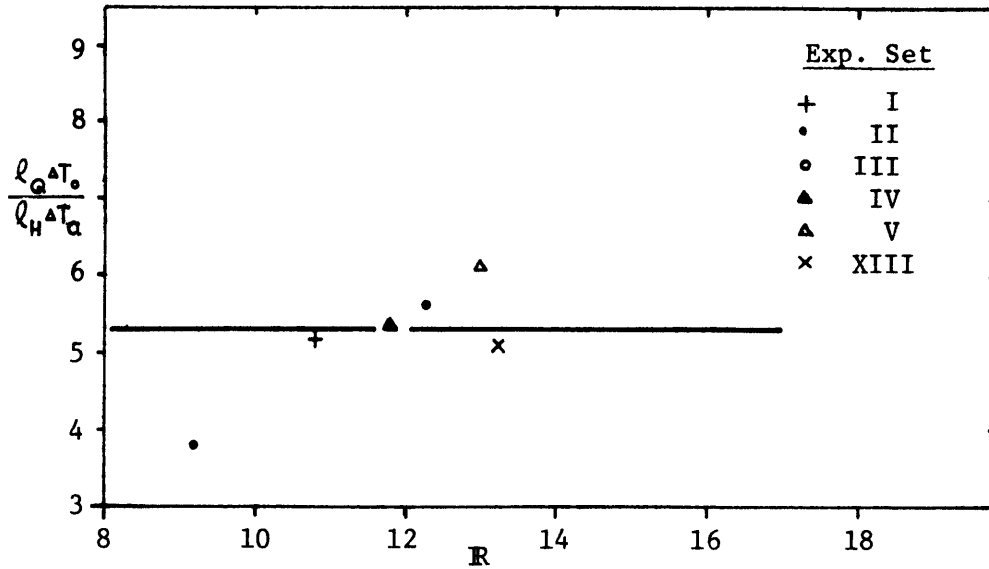
Figure 5-3   Relation for Temperature Below an Attached
Jet

5.1.3   Impact Momentum Balance for an Attached Jet

The coefficients c_2 and c_3 (equation 3.58) were only specified in Section 3.3.2.1 in terms of ranges that made physical sense. Values within those ranges were chosen by comparing integral model results to experimental data.

$$c_2 = 0.45$$

$$c_3 = 0.25 \tag{5.5}$$

5.1.4   Comparisons with Dimensionless Numbers

Chapter IV has described how experimental measurements were reduced

to some of the dependent variables of the integral jet model. A comparison is done directly in Appendix I. However, many comparisons in this chapter will be made in light of the dimensional analysis of Section 3.1. Presentation of normalized measurements as functions of the governing dimensionless parameters has two advantages. Both the integral model results and the asymptotic dimensional analysis result (that normalized dependent variables depend primarily on the parameter $\mathbb{L}$) can be compared simultaneously to the data. Also the range of behavior covered <u>and</u> not covered by experiments is readily apparent.

Table 5-1 lists the dimensionless parameter values for the experiments of this study. Experimental values of H_r have been adjusted (in calculation of $\mathbb{L}$) for an observed surface boundary layer caused by a surface tension induced zero velocity at the water surface (detached jet only). Hydrogen bubble velocity measurements revealed that the reduction in H_r by .45 cm allowed the velocity field to be considered vertically uniform. This adjustment was small relative to H_r values which were greater or equal to 12 cm.

From the results of Section 3.1 any normalized jet behavior for one of the three possible flow cases ($\phi_o \stackrel{\sim}{} 0°$ and the intake flow ratio $k = 0, \frac{1}{2}$ or 1) is a function of the three dimensionless numbers $\mathbb{L}$, $\mathbb{R}$ and $\mathbb{F}$. That is, each point in the three-dimensional space defined by $\mathbb{L}$, $\mathbb{R}$ and $\mathbb{F}$ values has a normalized jet parameter associated with it. The analysis of Section 3.1 suggests that for "large" values of $\mathbb{R}$ (or $\mathbb{F}$) jet parameters (normalized by M_o, B_o and H) should be independent of $\mathbb{R}$ (or $\mathbb{F}$) values. For large values of both $\mathbb{R}$ and $\mathbb{F}$, normalized parameters should depend only on $\mathbb{L}$.

Exp. Set	No.	ℓ_B cm	ℓ_H cm	ℓ_r cm	ℓ_Q cm	k	ϕ_o^{1} radians	F ℓ_B/ℓ_Q	R ℓ_B/ℓ_r	$\mathbb{L}^2$ ℓ_H/ℓ_B $(\frac{\ell_H-\S}{\ell_b})$
I	1	37.9	11.9	7.6	7.8	1	-.03	4.9	5.0	.314 (.302)
	2	82.2	11.8	7.6	7.8	1	+.05	10.5	10.8	.144
II	1	49.1	11.9	7.6	7.8	1	-.05	6.3	6.4	.243 (.234)
	2	60.9	11.9	7.6	7.8	1	-.02	7.8	8.0	.195 (.188)
	3	69.8	11.8	7.6	7.8	1	+.03	9.0	9.2	.169
III	1	54.7	11.3	7.6	7.8	0	-.03	7.0	7.2	.206 (.198)
	2	80.7	11.5	7.6	7.8	0	-.03	10.4	10.6	.143 (.137)
	3	93.4	11.8	7.6	7.8	0	-.04	12.0	12.3	.126
IV	1	46.3	12.3	7.6	5.5	1	-.11	8.4	6.1	.266 (.256)
	2	67.4	12.3	7.6	5.5	1	-.08	12.2	8.9	.183 (.176)
	3	90.2	12.3	7.6	5.5	1	+.01	16.3	11.8	.136
V	1	63.9	11.6	7.6	5.5	0	-.12	11.5	8.4	.181 (.174)
	2	84.5	11.7	7.6	5.5	0	-.03	15.3	11.1	.139 (.134)
	3	98.8	11.8	7.6	5.5	0	-.07	17.8	13.0	.119
XIII	1	51.4	18.0	7.6	9.9	1	-.01	5.2	6.8	.351 (.342)
	2	72.2	18.0	7.6	9.9	1	+.00	7.3	9.5	.250 (.244)
	3	100.5	18.0	7.6	9.9	1	-.03	10.3	13.2	.177

Table 5-1 Dimensionless Governing Parameters

1 ϕ_o is negative when pointing toward the free surface (Figure 3-4)

2 $\S$ is a surface boundary layer (due to surface tension). It existed only for the detached flow regime, and was estimated from the photographs of the hydrogen bubbles.

139

5.2 Flow Regime Limits

The observation of the existing flow regime was one experimental result that needed no normalization and which also had only two discrete values (attached or detached). Flow regime limits were determined in the experiments by starting with one of the two flow regimes and slowly (though incrementally) changing the experimental conditions (L, R and F values). Eventually the initial flow regime could no longer sustain itself and a transition was made to the other flow regime (jet attachment or jet detachment). The experimental conditions when this occured are the best indication of the initial flow regime's limits. However, the determination of the exact transition point was limited by the incremental way in which L, R and F values were changed.

Table 5-2 presents the experimentally determined flow regime limits. They were all determined by incremental adjustments in the jet and intake flow rates. The only exception was the second attachment limit in experiment set V. This was determined by slowly (0.2 cm per minute) dropping the water surface level while keeping the same jet discharge conditions (there was no intake). This changing jet submergence only affected L and not the dimensionless parameters F and R.

Six transitions appropriate to this study can be identified in terms of L, R and F. They are the attachment and detachment transitions for each of the intake flow ratio values ($k = 0$, $\frac{1}{2}$, or 1) considered. Because no experiments were performed for the intermediate value of $k = \frac{1}{2}$, only four transitions are available for data comparisons.

The two discrete values that the flow regime can take on (attached or detached) allow a unique method of comparing integral model and experi-

Exp. Set	Flow Regime Limit	k	ϕ_o	$\mathbb{F}$	$\mathbb{R}$	$\mathbb{L}$
I	Detachment	1	+.05	4.9	5.0	.312
II	Attachment	1	−.02	9.0	9.2	.163
III	Attachment	0	−.03	12.0	12.3	.121
	Detachment	0	−.04	7.2	7.4	.213
IV	Attachment	1	−.08	16.3	11.8	.131
	Detachment	1	+.01	8.9	6.5	.249
V	Attachment	0	−.03	17.8	13.0	.114
	Attachment	0	−.12	11.5	8.4	.114
	Detachment	0	−.07	12.6	9.2	.169
XIII	Attachment	1	+.00	10.6	13.5	.169
	Detachment	0	−.03	6.1	7.9	.301

Table 5-2   Flow Regime Limits Data

.

141

mentally determined transitions. Figures 5-4 through 5-7 graph a contour map of a transition predicted by the integral jet model.[1] The experimental determination of the same transition is also indicated. Experiments are located at their appropriate $\mathbb{R}$ and $\mathbb{F}$ values and their $\mathbb{L}$[2] value is noted in parenthesis next to the point. An experimental observation of a detached jet is noted by a solid symbol, while open symbols indicate the attached flow regime.

The ability of the integral jet model to predict flow regime transitions can be judged by comparing $\mathbb{L}$ values of the transition contour map and the experiments. If the experimental value is greater than the local contour value of $\mathbb{L}$, the integral jet model would judge that experiment to be "above" the transition-plane and hence a detached jet flow. The opposite is true for experimental $\mathbb{L}$ values less than the local contour value.

The experimental data, though limited in scope, fits the integral jet model predictions very well. The integral jet model transition plane also becomes noticeably independent of $\mathbb{R}$ and $\mathbb{F}$ at large values of these parameters ($\mathbb{F}$, $\mathbb{R} > 12$). This is indicated by the contours becoming parallel to the $\mathbb{R}$ axis (or $\mathbb{F}$ axis) for large values of $\mathbb{R}$ (or $\mathbb{F}$). At large values of both $\mathbb{R}$ and $\mathbb{F}$ the contours are widely spaced indicating a nearly unique value of $\mathbb{L}$ that signals the transition. This value should be the same for all values of the intake flow ratio, k, if $\mathbb{F}$ is large enough (i.e., if initial intake and discharge flow rates are

---

[1]The initial jet angle ϕ_o was set ($\phi_o = -.03$ for detached jets; $\phi_o = +.03$ for attached jets) based on comparison of measured and predicted trajectories near the origin.

[2]$\mathbb{L} = (\ell_H - \delta)/\ell_B$ as described in Table 5-1.
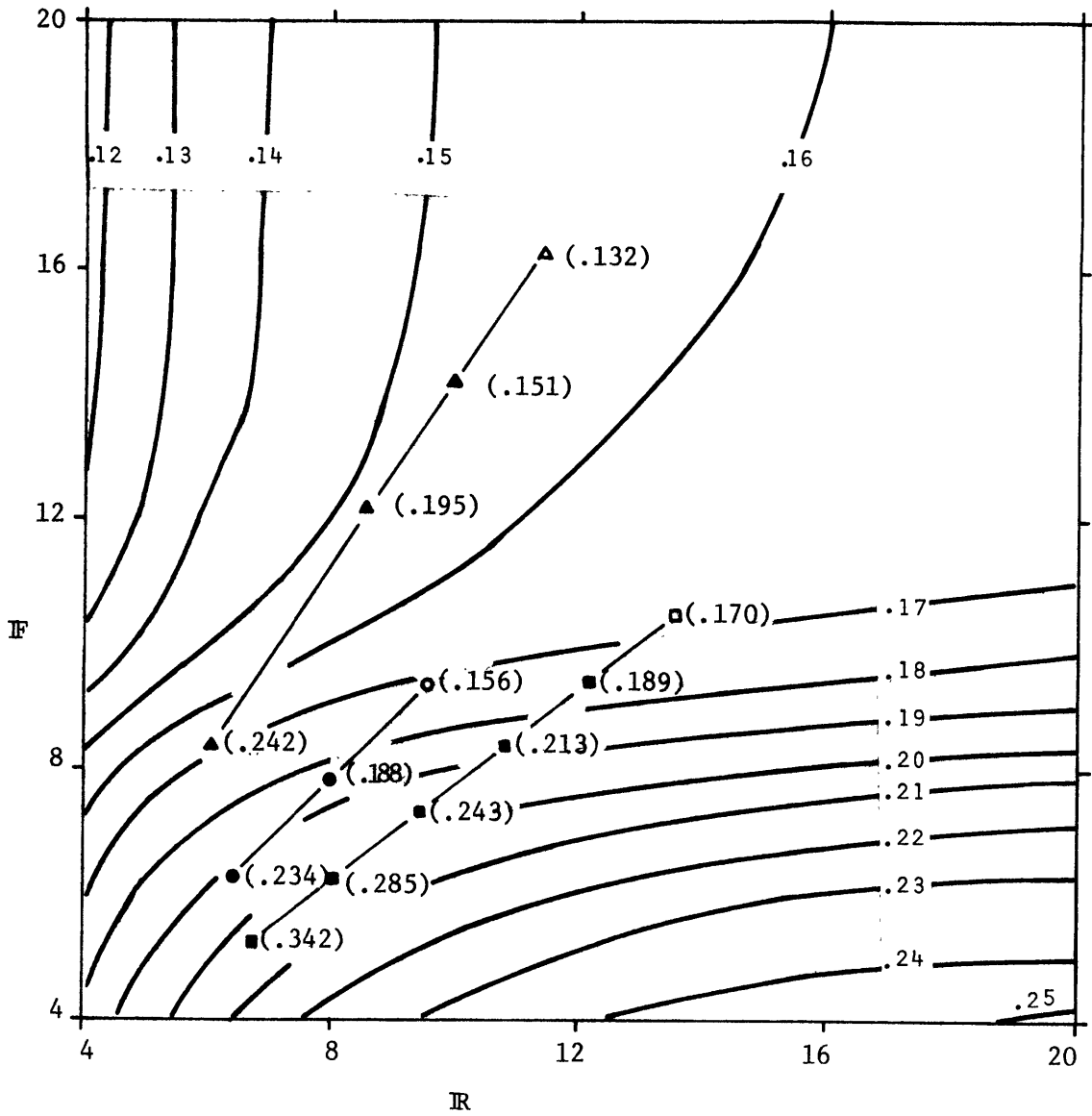
Figure 5-4   Integral Model Predictions and Experimental Data of
L Values at Attachment (with Intake, k = 1)

k = 0
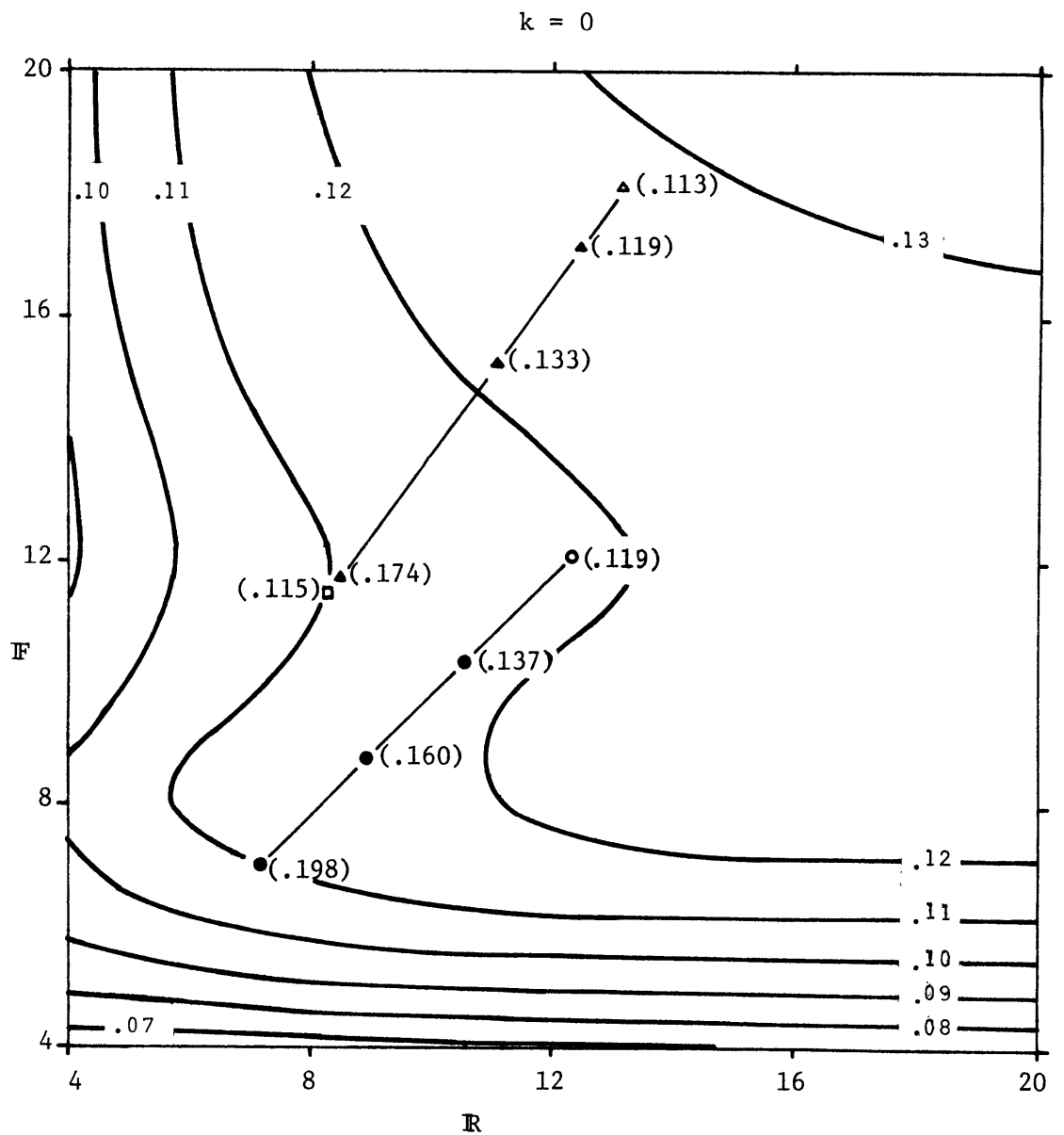
Figure 5-5   Integral Model Predictions and Experimental Data
of L Values at Attachment (No Intake, k = 0)

144
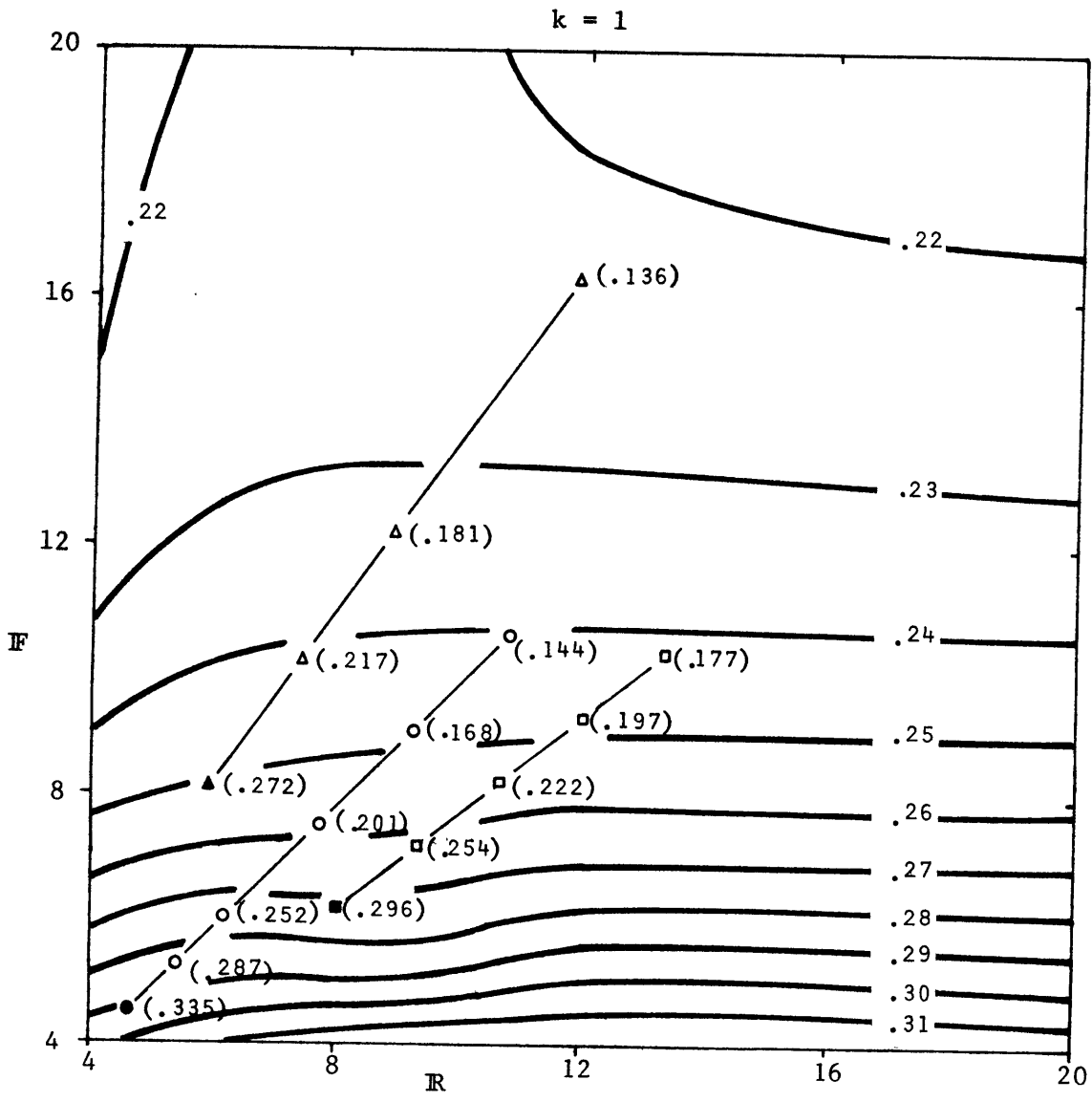
Figure 5-6 Integral Model Predictions and Experimental Data of
L Values at Detachment (with Intake, k = 1)
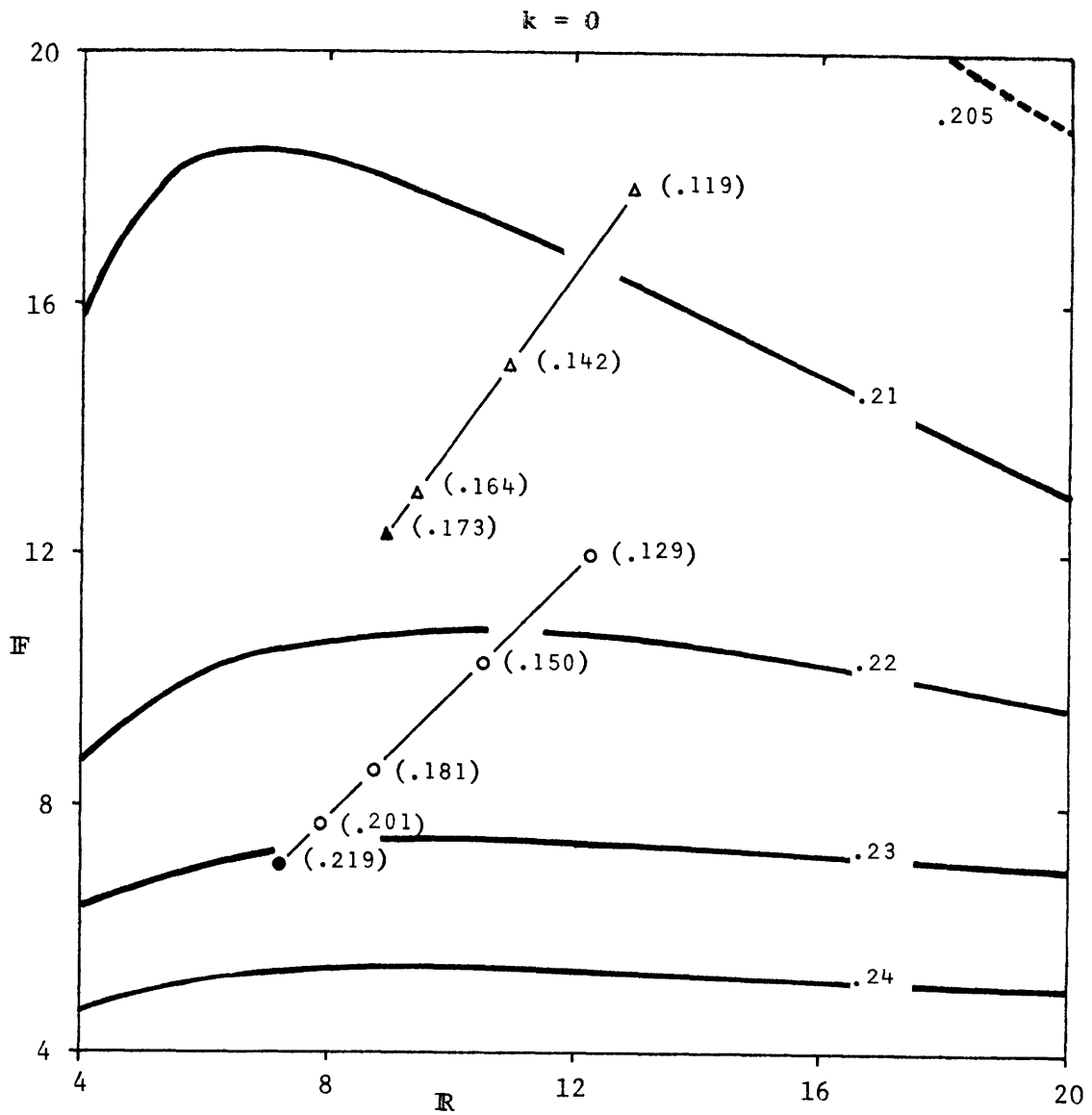
Figure 5-7   Integral Model Predictions and Experimental Data of
L Values at Detachment (without Intake, k = 0)

insignificant). This is apparent in the detachment transitions, while the attachment transitions are still evolving at $\mathbb{F}$ = 20.

The integral jet model does have some difficulty predicting attachment transitions at large values of $\mathbb{R}$ and small values of $\mathbb{F}$. In these cases the jet port width, $2D_o$, becomes greater than the port radius, r_o. Near the attachment transition, D_o also approaches H_r in value , as the top lip of the port gets very close to the water surface. The zone of flow establishment becomes very critical in these cases and possible inaccuracies in core decay rate (equation 3.48) are very important. The integral jet model should be used cautiously in this range.

Appendix III shows three dimensional views of the transition surfaces.

5.3 Jet Behavior

The most extensive comparison of the integral jet model behavior with experimental data is possible only in dimensional terms. Measured jet trajectories, remote ambient region velocities and jet centerline temperatures for each experiment appear in Appendix I. The integral model was used to generate jet boundaries, U, and centerline jet temperature differences. These predictions appear with the data for comparison.

The three lines in the jet centerline temperature graphs of Appendix I are an attempt by the integral model to account for the discrete depths at which experimental temperature measurements were taken. Temperature measurement locations were separated vertically by 1.52 cm (.05 ft) and hence the exact jet centerline may have been "missed" by as much as .76 cm. The solid line indicates the expected value of the peak jet temperature given a polynomial temperature profile and a random "miss" distance between 0 and .76 cm. The broken lines indicate the upper and lower

bounds of predicted temperature corresponding to the measurement resolution. The upper broken line, therefore gives the actual jet centerline prediction of the integral jet model, while the lower broken line indicates predicted temperature at a vertical distance of .76 cm from the jet centerline. The broken and solid lines converge as the jet width becomes much greater than the measurement resolution. The integral model prediction of jet boundaries (open circles) show jet widths of 1.8 $b_{1/2}$. This width was found in Chapter II to correspond to a jet intermittency level of 50%. Thus the model predictions should correspond to the median position of the experimentally observed jet boundaries.

The integral model prediction of U is based on the assumption of vertically uniform velocity profile in the remote ambient region (after the surface boundary layer is accounted for). Therefore the prediction should correspond to the velocities found by drawing average vertical lines in the hydrogen bubble photographs (Section 4.2.3). Vertical velocity profiles were found nearly uniform (see Figure 4-7) in all the detached jet experiments.

Two dimensionless comparisons of the integral model and jet data were also performed for experiments in each flow regime. This essentially requires a four-dimensional plot ($\mathbb{L}$, $\mathbb{R}$, $\mathbb{F}$ and the normalized-dependent parameter). However, five of the six experimental sets had about the same value of water surface-jet port separation (H = 12 cm) and the same port radius, r_o (7.6 cm). Therefore, for these experiments

$$\mathbb{L} \cdot \mathbb{R} = \frac{\ell_H}{\ell_B} \cdot \frac{\ell_B}{\ell_r} = \frac{\ell_H}{\ell_r} \simeq const. \tag{5.6}$$

This reduces the plots to three dimensions: (1) normalized-dependent

parameter; (2) $\mathbb{F}$; (3) $\mathbb{R}$ or const./$\mathbb{L}$; and contour plots as used in the previous section are possible. This time the contour represents the normalized parameter value as indicated on the particular figure.

Figures 5-8 through 5-11 plot detached jet data and integral model predictions for k equal to 0 and 1. The two normalized measurements are of

$$(1) \quad \frac{r_c\big|_{max} - r_o}{1_B}$$

$$(2) \quad \frac{U(\sigma = 1_B/3)}{M^{1/2}/H_r}$$

where $r_c\big|_{max}$ is the jet centerline radius when it reaches a vertical trajectory and the U value is taken at $\sigma = \ell_B/3$. These contour plots are bounded by the attachment transition found in Figures 5-4 and 5-5. They exhibit behavior independent of $\mathbb{F}$ for values of $\mathbb{F}$ greater than approximately 12. $\mathbb{R}$ does not vary independently of the primary parameter $\mathbb{L}$. The data agreement is good although the whole range of behavior exhibited in the contours is certainly not verified.

Figures 5-12 through 5-15 plot attached jet data and integral model predictions for k equal to 0 and 1. The two normalized measurements are of

$$(1) \quad \frac{\Delta T_i}{\Delta T_o} \frac{1_H}{1_Q}$$

$$(2) \quad \frac{r_{c_i} - r_o}{1_H}$$

where r_{c_i} is the jet centerline radius upon impact with the surface. The contour plots are bounded by the detachment transition obtained in Figures

149

Figure 5-8 Detached Jet Experimental Data Comparison ($\mathbb{R} \cdot \mathbb{L} = 1.51$) with no Intake (k = 0)

Figure 5-9   Detached Jet Experimental Data Comparison ($\mathbb{R}\cdot\mathbb{L}$ = 1.51)
with no Intake (k = 0)
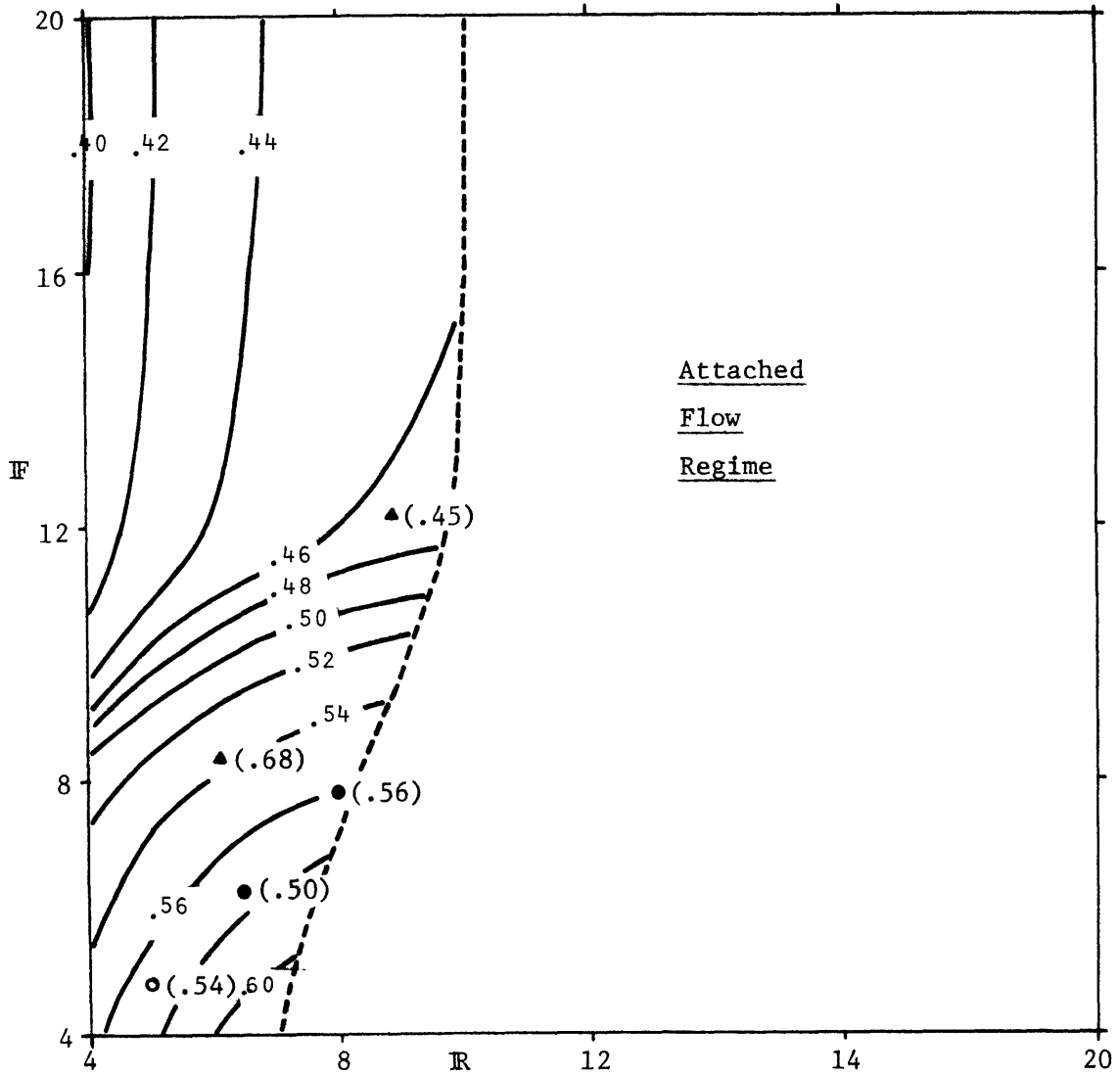
Figure 5-10   Detached Jet Experimental Data Comparison
(IR·IL = 1.58) with an Intake (k = 1)
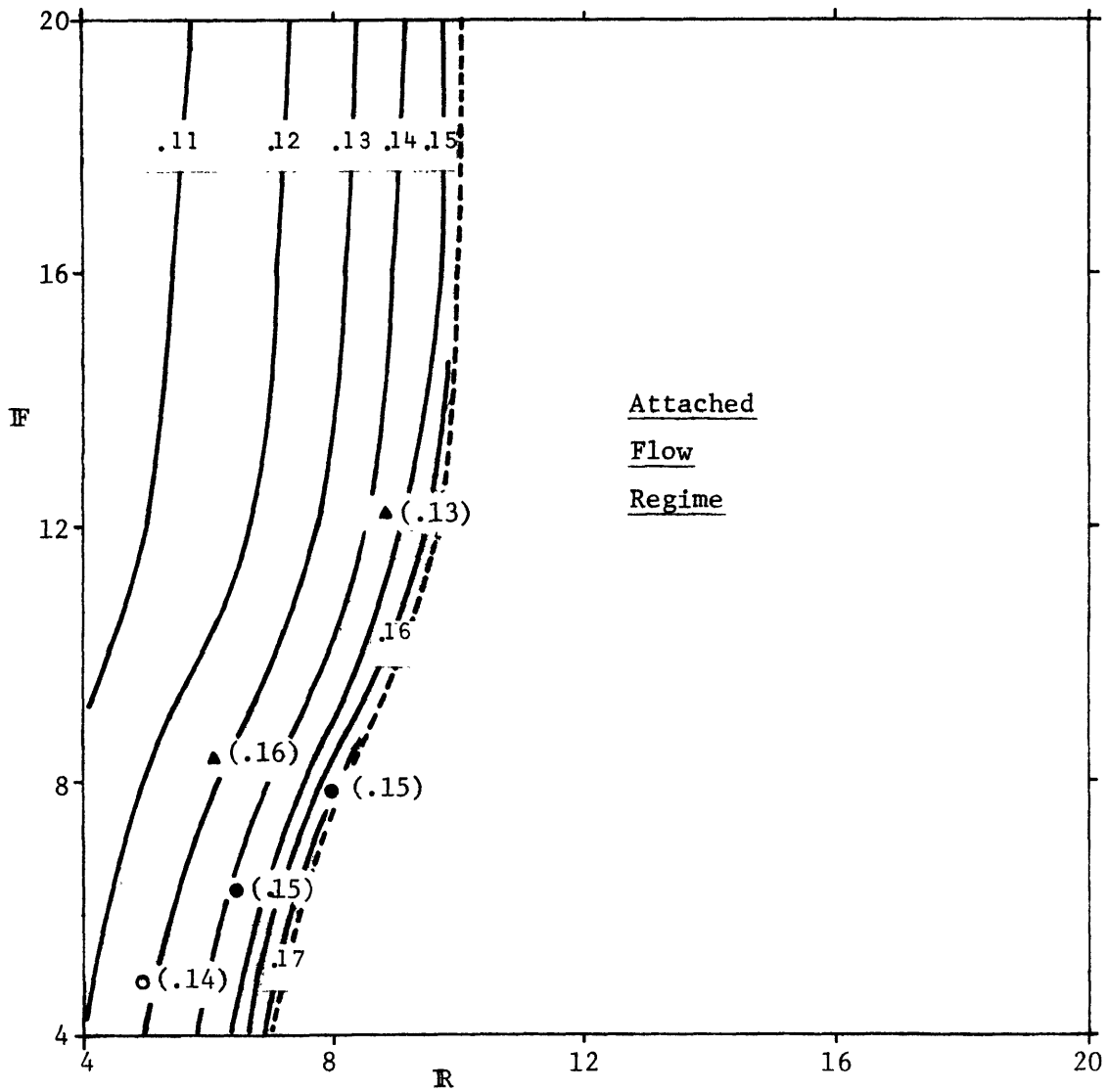
Figure 5-11   Detached Jet Experimental Data Comparison
($\mathbb{R} \cdot \mathbb{L}$ = 1.58) with an Intake (k = 1)
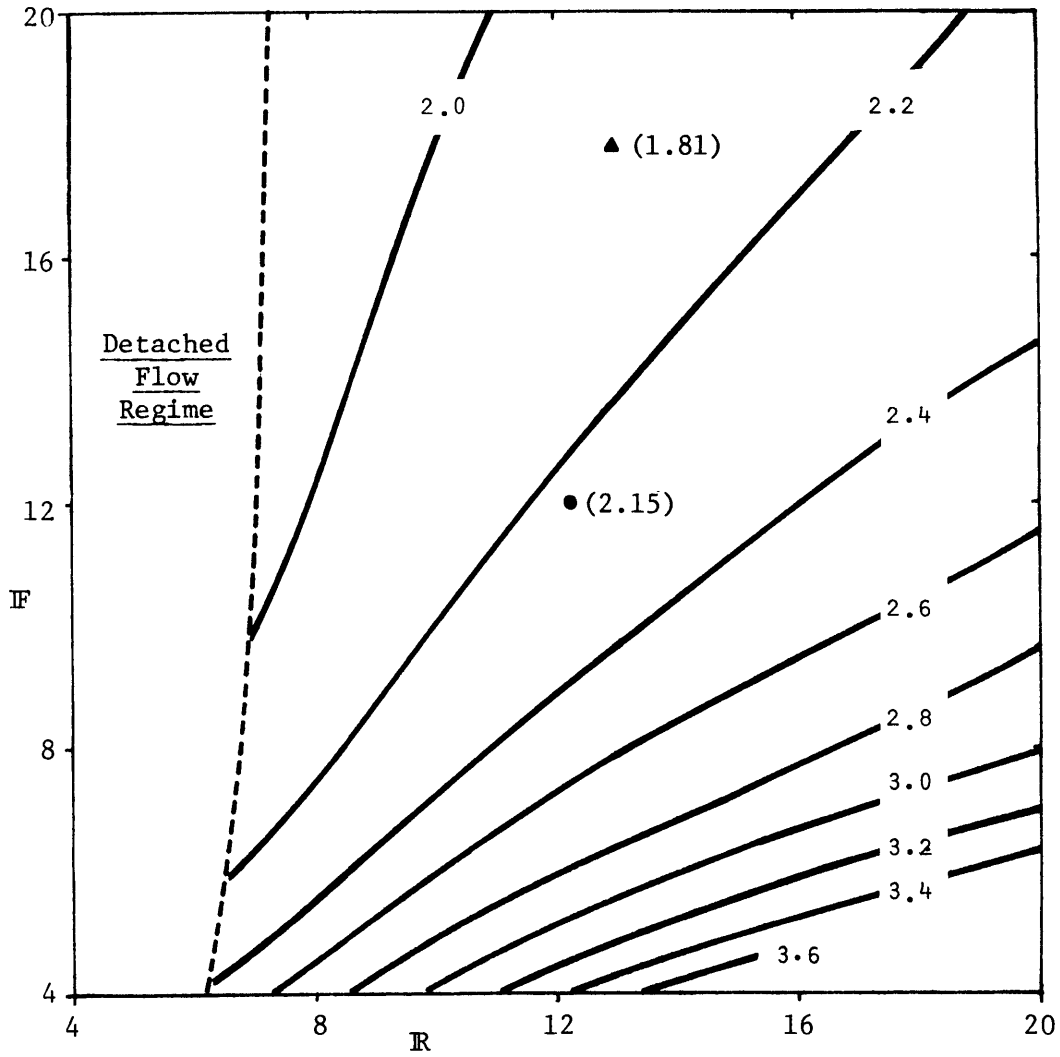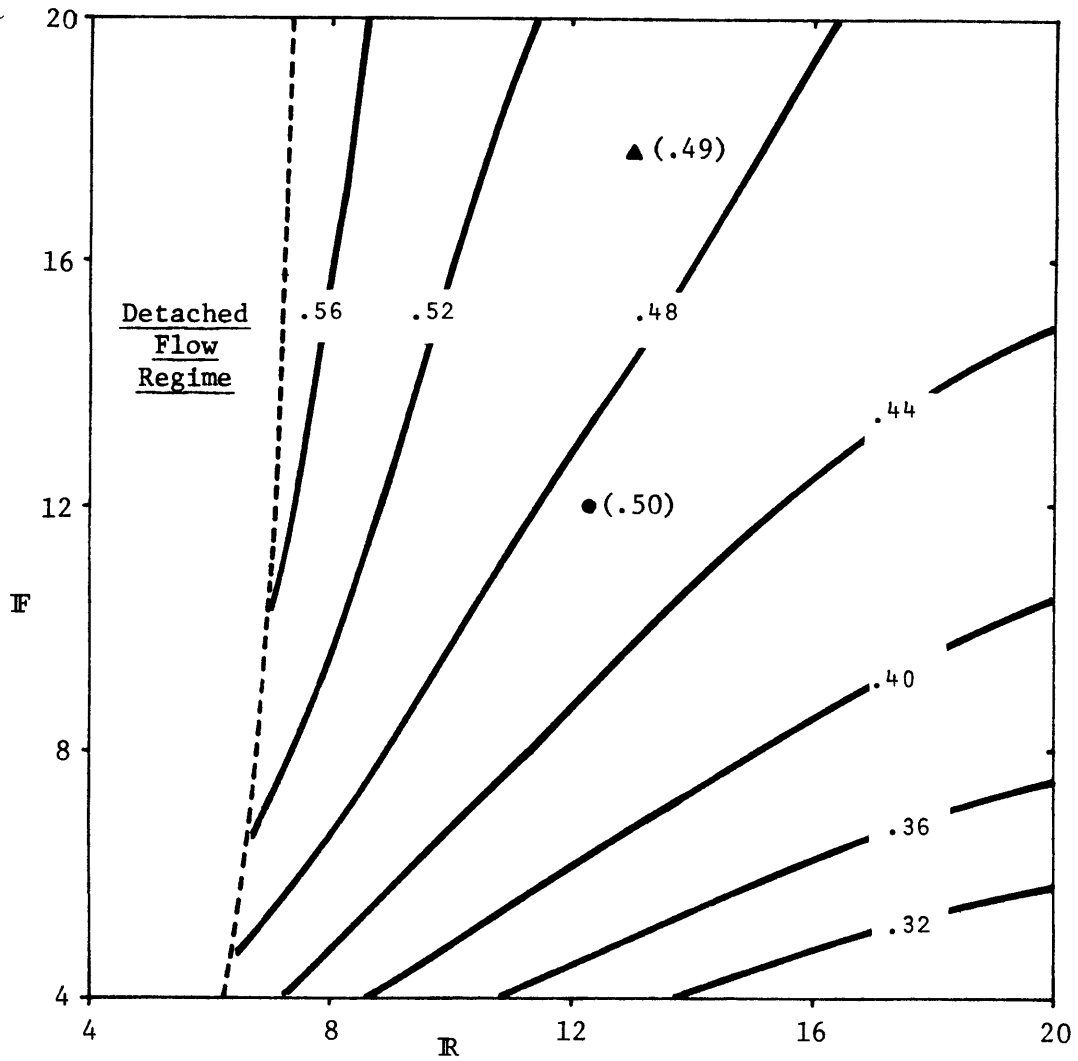
Plotted Values:

$$\frac{r_{c_i} - r_o}{\ell_H}$$

Symbol	Exp. Set
●	III
▲	V

Figure 5-12 Attached Jet Experimental Data Comparison ($\mathbb{R} \cdot \mathbb{L}$ = 1.54) with no Intake (k = 0)

Figure 5-13 Attached Jet Experimental Data Comparison ($\mathbb{R} \cdot \mathbb{L}$ = 1.54) with no Intake (k = 0)
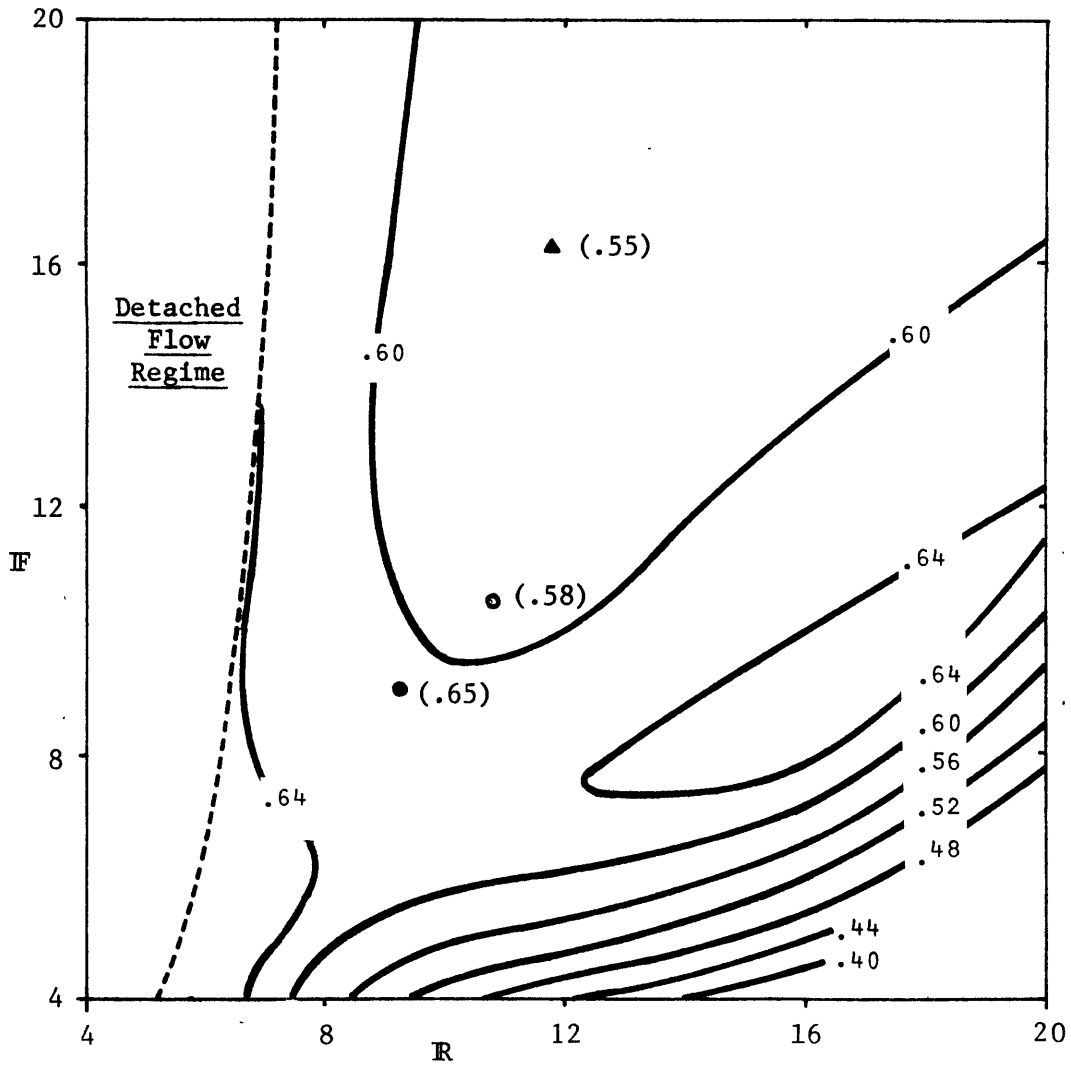
Figure 5-15   Attached Jet Experimental Data Comparison
($\mathbb{R} \cdot \mathbb{L}$ = 1.58) with an Intake (k = 1)

5-6 and 5-7. The data, although very sparse, show good agreement with the integral model.

5.4 Integral Jet Model Sensitivities

As developed in Chapter II, several approximations and extrapolations based on previous studies had to be made for the integral jet model of this study. Also some initial conditions have an inherent measurement limitation This section explores the sensitivity of the model results to these approximations and accuracies. The method is to take the model predictions for a single experiment in each flow regime (experiments XIII-2 and XIII-3) and compare them to the model results when the model inputs are varied.

5.4.1 Detached Jet Sensitivities

For a detached jet the following sensitivity ranges were checked:

(1) P_i - pressure below the jet as determined in equation 5.2
       ($\pm$ 10%)

(2) ϕ_o - jet discharge angle ($\pm$ .02 radians)

(3) c_1 - asymmetric entrainment coefficient in equation 2.34
       (varied from 3.0 $\rightarrow$ 4.0 $\rightarrow$ 4.9)

(4) κ - coefficient of spreading in an ambient current in
       equation 2.25 (.44 $\pm$ 15%).

The results of the sensitivity checks appear in Appendix II. The comparisons appear in the same form as the results plotted in Appendix I.

The jet centerline temperature decay is insensitive to any of the variations except for its cutoff point determined by when the jet reaches a vertical trajectory.

P_i has a modest influence on jet trajectory and the ambient velocity

158

when varied about the value determined by equation 5.2. The pressure relation of equation 5.2 suggests that the "experimentally determined" value of P_i varies at most by only ± 27% as a function of the dimensionless number $I\!F_i$. The exact nature of this somewhat weakly justified relation is apparently not critical to the model results since the integral model is insensitive to most of the variation that the relation accounts for.

The influence of ϕ_o is modest over the range tested. However, the importance of determining the experimental value of ϕ_o to with ±.04 radians is emphasized. The photographic means used for this determination was within this accuracy. However, every experiment needed to be checked for ϕ_o because the short port radius was insufficient to guarantee an absolutely horizontal discharge. Also the port flow rate (and flow conditions within the port itself) had an influence of ϕ_o.

The asymmetric entrainment coefficient was varied between the two values suggested by Sawyer (Section 2.4.6). There were no significant effects on the jet behavior within this range.

The variation of the spreading coefficient κ by ±15% had only a modest effect on the detached jet results. Thus the choice of κ equal to exactly .44 was not critical. This is consistent with the finding of an optimal κ value in Table 2-6. Values of κ ranging from .40 through .50 did not vary much in the ability to predict the data of Becker et al. (1962).

5.4.2 Attached Jet Sensitivities

For an attached jet the following sensitivity ranges were checked:

(1) ϕ_o — jet discharge angle (horizontal ±.02 radians)

(2) c_1 — asymmetric entrainment coefficient in equation 2.34

(varied from 4.9 → 4.0 → 3.0)

(3) c_2 - impact point location coefficient in equation 3.58

(.45 ± 33%)

(4) c_3 - extra entrainment (near the impact point) coefficient

in equation 3.58 (.25 ± 40%)

The sensitivity results also appear in Appendix 2.

As before the jet centerline temperature predictions are independent (except for the "cutoff" point) of all the parameters varies.

The influence of ϕ_o on jet trajectories again shows the importance of determining its value for each experiment. The upper ambient region temperature (or ΔT_i) is not affected as much as by the other parameter activities.

Sawyer's asymmetrical entrainment coefficient shows some influence in this flow regime. This is because of the tighter jet curvatures (smaller values of r_2) and the importance of the division of flow for the impact point momentum balance.

The model results show significant sensitivity to the coefficients c_2 and c_3 indicating that these coefficients could not be chosen arbitrarily within the "reasonable" ranges set by equation 3.58. The actual values used (c_2 = .45; c_3 = .25) were chosen so that the integral model matched experimental results. The extra entrainment coefficient, c_3 apparently exerts an influence on ΔT_i but not on the jet trajectory. The impact point location coefficient, c_2, affects trajectory because the impact momentum balance requires that the jet reach the impact point at a certain angle (for a given intake flow ratio, k). Moving the impact point away from the water surface (increasing c_2) requires a "tighter" jet

curvature to reach the impact point at the correct angle (i.e., the impact point moves radially in).

VI. Comparison of Integral Model with Other Sources of Data

This chapter compares integral model results to several confined,
plane jet experiments in the literature. The experiments have been
previously described in Section 2.5. The radial integral jet model of
this study can be extended to plane jets by simply specifying a very
large initial radius (as compared to other experimental length scales
ℓ_B, ℓ_Q, and ℓ_H). The empirical constants (κ, c_1, c_2, and c_3) retain
the same values used in the radial jet comparisons of Chapter 5.

6.1 Ducted Plane Jets

The flow field associated with ducted jets is described in Section
2.5.1. Only one experimental study (Curtet, 1958) of the plane jet
geometry was found in the literature. The ambient regions were
entirely co-flowing and irrotational in all of the experiments
(i.e. referring to Figure 2-20, no region 3).

The integral model used in this study requires some modification
beyond specifying a large initial radius to get plane jet behavior.
The spreading effects of the ambient fluid flow are symmetrical so
equations 2.28 and 2.41 apply.

$$\varepsilon_c = \{.105 + .005 \tanh [(.43 - \frac{\Delta V_c}{\Delta V_o})/.028]\} \frac{.44}{U/\Delta V_c + .44} \qquad (2.28)$$

$$\frac{dD}{dx} = - .07[\frac{1}{U/\Delta V_c + 1}] \qquad (2.41)$$

The pressure in the ambient fluid is also symmetrical and calculated as
if both duct boundaries are remote (equation 3.52).

162
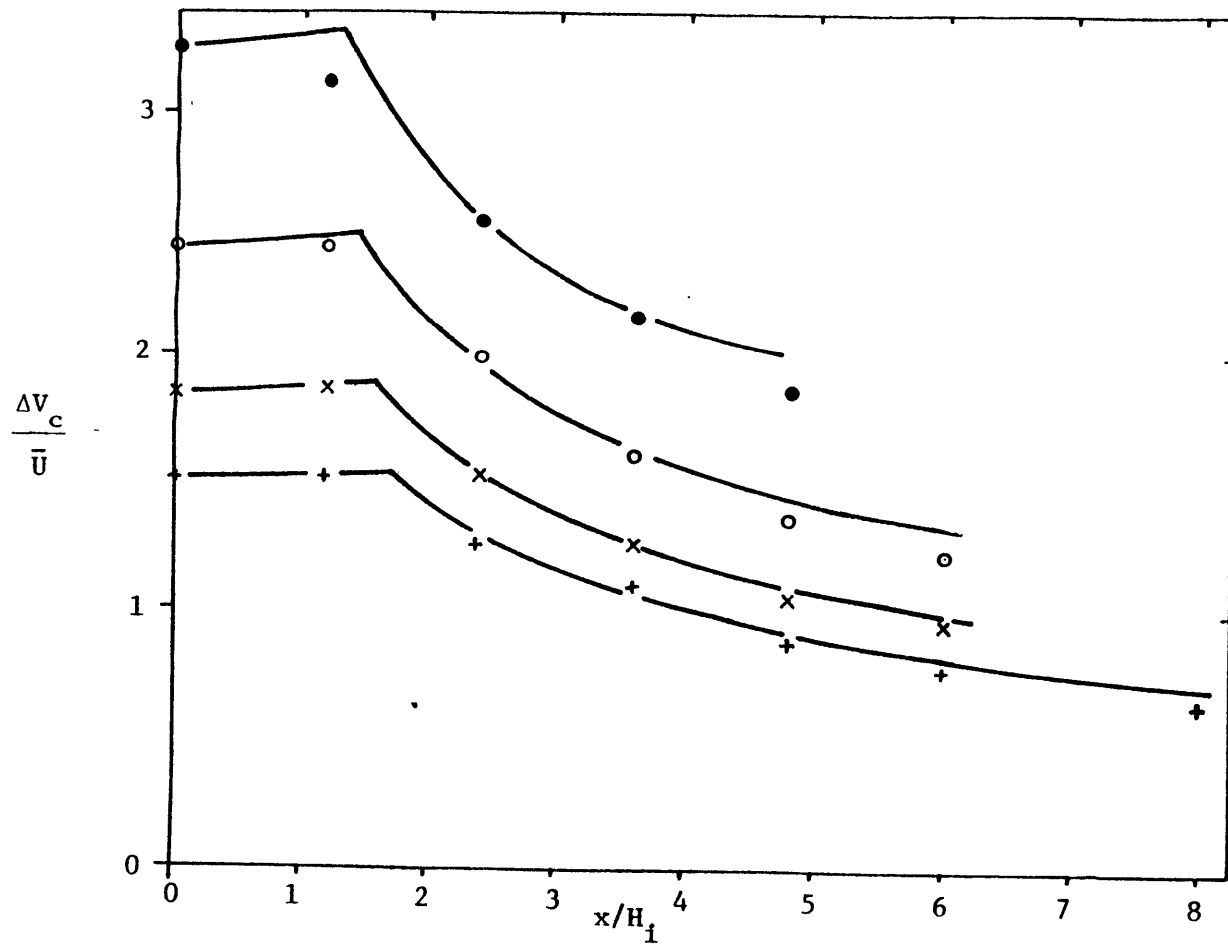
Figure 6-1 Plane Ducted Jet Centerline Velocity Decay(Curtet Data)

This situation does not include some of the complications of the present experimental study. There is no jet buoyancy or jet bending. As a result the entrainment flows from each side of the jet are equal. The ambient fluid is irrotational and co-flowing until it disappears when the jet boundary reaches the duct wall. Therefore none of the empirical pressure determinations for impacted boundaries are needed. The integral model predictions must stop however when the jet boundary reaches the duct wall.

Curtet's primary measurement was that of the jet's centerline velocity. He normalized the velocity difference ΔV_c (between the jet centerline and ambient region) with the average duct velocity $\overline{U}$ (the total flow in the duct divided by the duct cross-sectional area). His data for four experiments appears in Figure 6-1 along with the results of the modified integral jet model. There is good agreement in all cases.

6.2   Plane Jets with an Offset Plane Boundary

Data were taken from three studies for the case of a non-buoyant jet (Bourque and Newman, 1960; Sawyer, 1963; Stoy et al., 1973). Buoyant jets were considered by Stoy et al. (1973) and Cederwall (1971).

6.2.1   Non-Buoyant Jet Cases

The integral jet model of this study was readily adapted to this case. The initial jet radius and buoyancy were simply chosen appropriately $(r_o = \infty;\ \Delta\rho_o/\rho = 0)$.

The primary measurements taken in these studies are: (1) the point along the offset plate which is intersected by the jet's dividing streamline; (2) the minimum fluid pressure along the plate. These

164
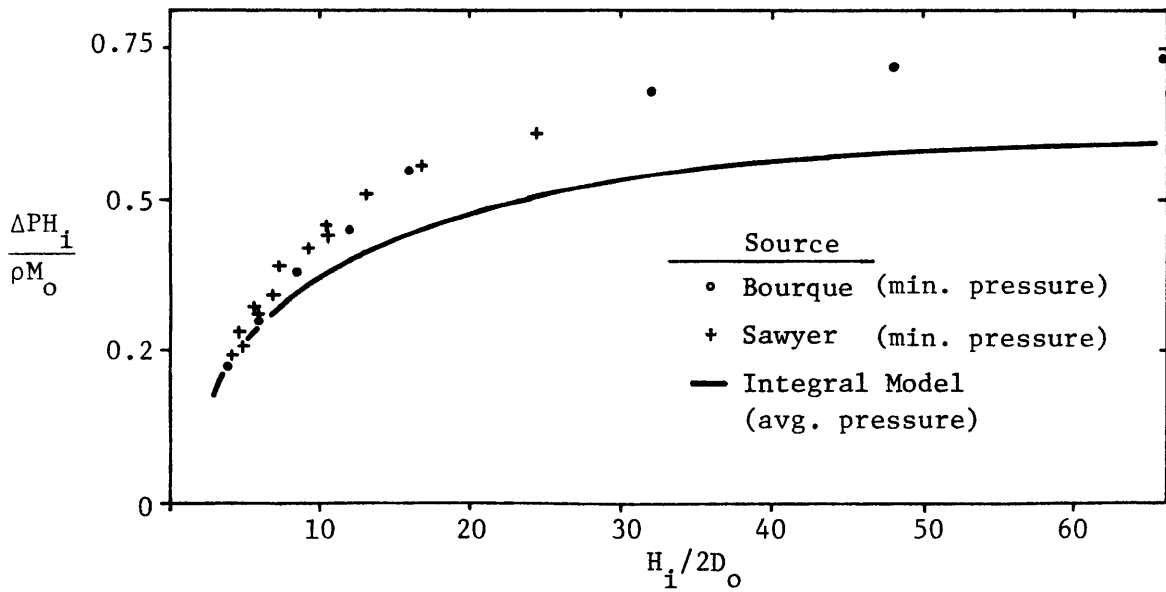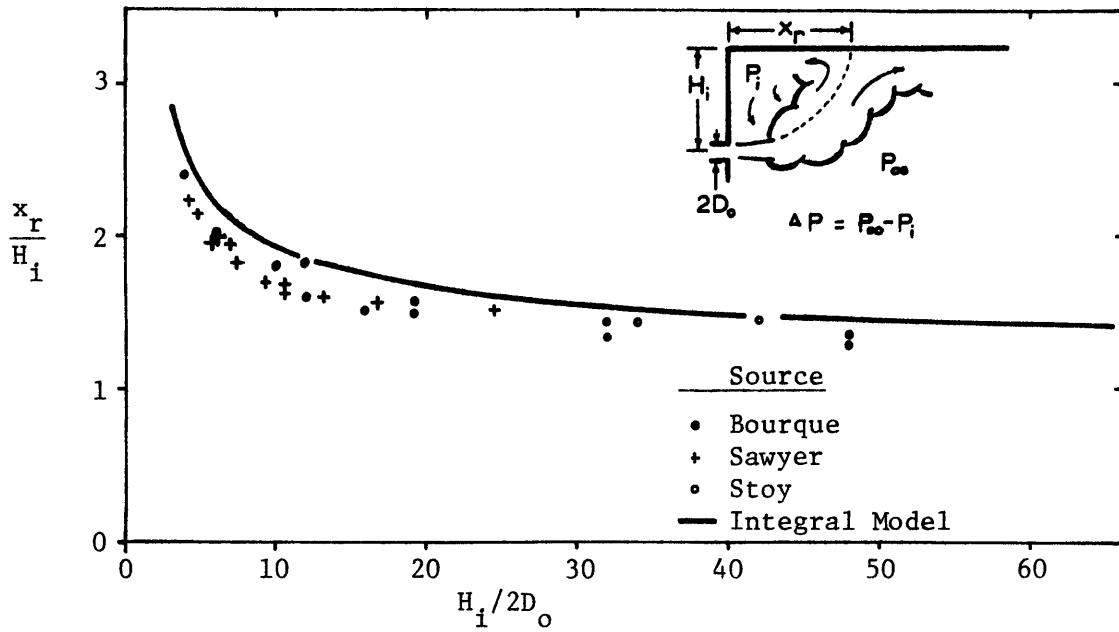
Figure 6-2 Offset Plane Boundary Coanda Effect

165

measurements have already appeared in Section 3.1 (Figure 3-3) during the dimensional analysis discussion. They are replotted in Figure 6-2 along with the predictions of the integral model.

The integral model prediction of x_r comes from the location of the dividing streamline when the jet reaches its "impact point" (see Section 3.3.2.1). The average pressure ΔP calculated by the integral model ($P_\infty = 0$) is plotted in the graph of pressure values.

The model predictions of x_r exhibit the same behavior as the experimental results although the predictions are slightly larger than the data. The pressure calculations likewise show the correct behavior but are smaller in magnitude than the data. This should be expected because the model pressure is an average pressure and the data are the maximum values of ΔP at the plate. If the model predictions are uniformly multiplied by a factor of 1.2, they match the experimental data very well.

6.2.2 Buoyant Jet Cases

6.2.2.1 Complementary Buoyancy and Confinement Effects

Stoy et al. (1973) had an experimental situation exactly like that of the previous section, only jet buoyancy helped to lift the jet and attach it to the offset boundary (in this case a free surface). This is exactly the opposite buoyancy direction as in the attached flow regime of this study. A detached flow regime is not possible since confinement and buoyancy effects deflect the jet in the same direction.

The integral jet model of the present was readily adapted to this case. Plane jet behavior was simulated by using a large initial radius.

The initial jet buoyancy of the two cases reported by Stoy et al. was not entirely clear. They reported an initial jet temperature difference (discharge temperature minus ambient temeprature) but not the ambient temperature. Because of the non-linear temperature density relation illustrated in Figure 3-8, the initial jet buoyancy is dependent on the ambient temperature. A reasonable laboratory value of water temperature (20°C) was assumed for the ambient temperature.

Stoy et al. report jet trajectory data based on visual observations. The intersection of the dividing streamline with the boundary is normalized and plotted in Figure 6-3. The integral model results are plotted on the same figure. Stoy's limited data shows some variation with jet buoyancy. The integral model trajectories show no sensitivity to jet buoyancy. The pressure P_i however responds to jet buoyancy.

Though Stoy's data is far from complete, it does suggest why the model predictions of x_r are greater than the "positively" buoyant and non-buoyant plane jet data presented in this chapter. The values of model constants (c_2 and c_3) were based on experiments with negative buoyancy. The trend of Stoy's data shows that such data would have greater values of x_r (for a given value of $H_i/2D_o$) than for non-buoyant or positively buoyant jets. The insensitivity of the integral model's trajectory prediction's to buoyancy then causes over-prediction of x_r when non-buoyant or positively buoyant jets are modeled.

The insensitivity of the integral jet model trajectories to buoyancy is a result of the model formulation. If pressure effects (P_i) had been included in the momentum balance at jet-boundary impact point (see Figure 3-10), then the proper sensitivity (as reported by Stoy)
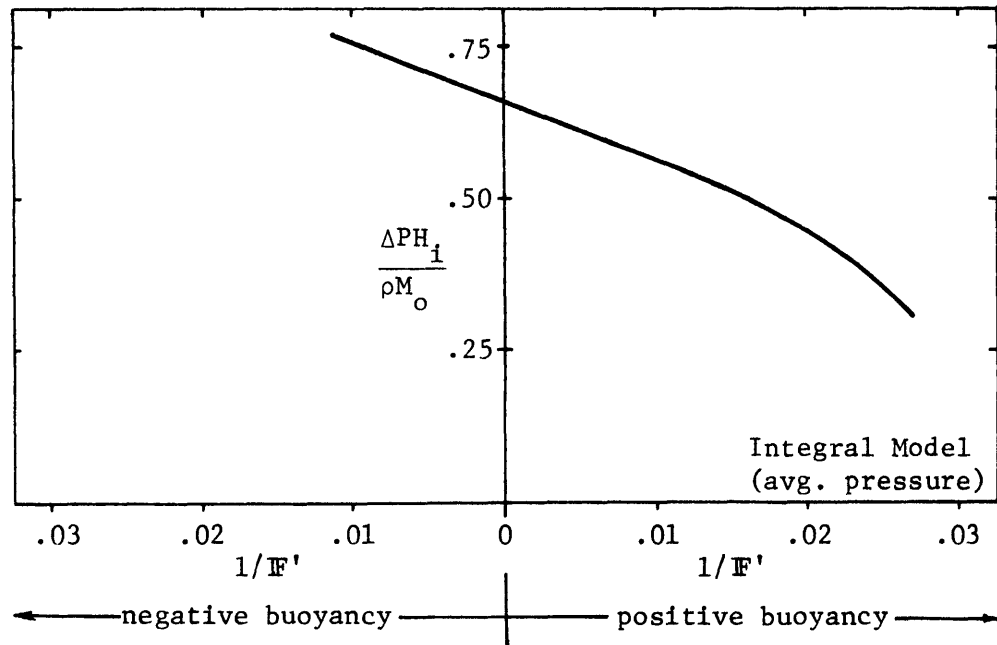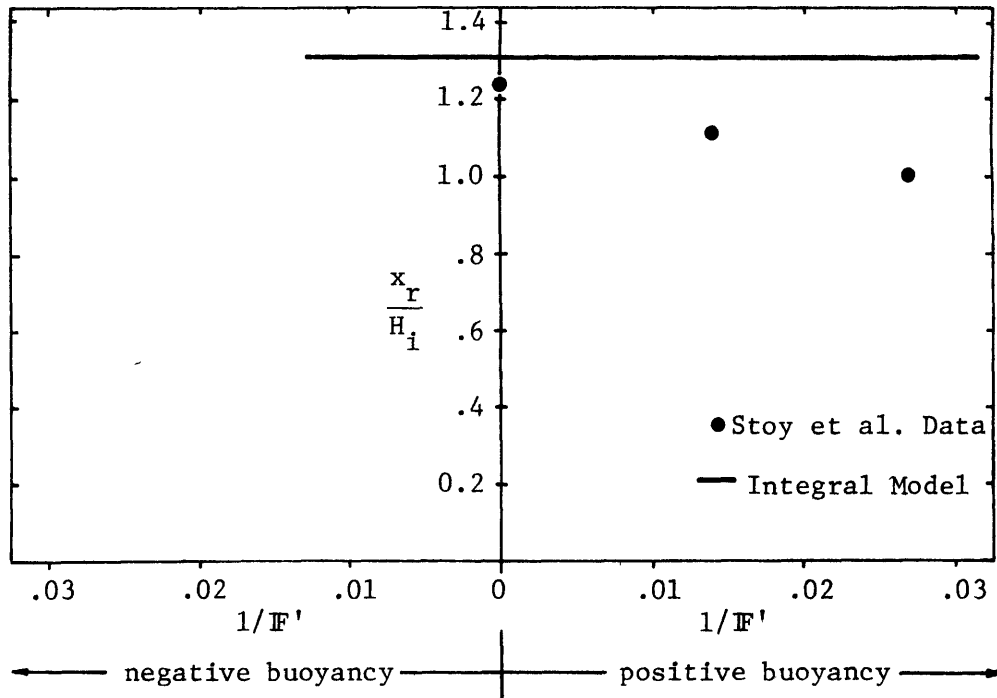
Figure 6-3   Offset Plate Coanda Effect with Buoyancy$(H_i/2D_o=126)$
(Stoy et al. Data)

would have occurred. However given the extremely small number of data points and the interest (of this study) in negatively buoyant jets, the integral model would only be slightly improved.

6.2.2.2 Opposing Buoyancy and Confinement Effects

Cederwall (1973) sought to investigate the dilution and trajectory of a horizontal, unconfined, plane buoyant jet. However the reported geometry of his experiments (Figure 6-4) suggests that jet confinement may have been a factor. He produced a negatively buoyant jet by having a measured concentration of salt in his discharge flow. The jet centerline location was determined (at only one point for each experiment) with either a conductivity probe or by taking water samples. The result was

$\frac{1}{16}$ in. Slot

Saline Solution Feed Line

2 in. Plastic Pipe

50 cm.

2 ft. Wide Flume
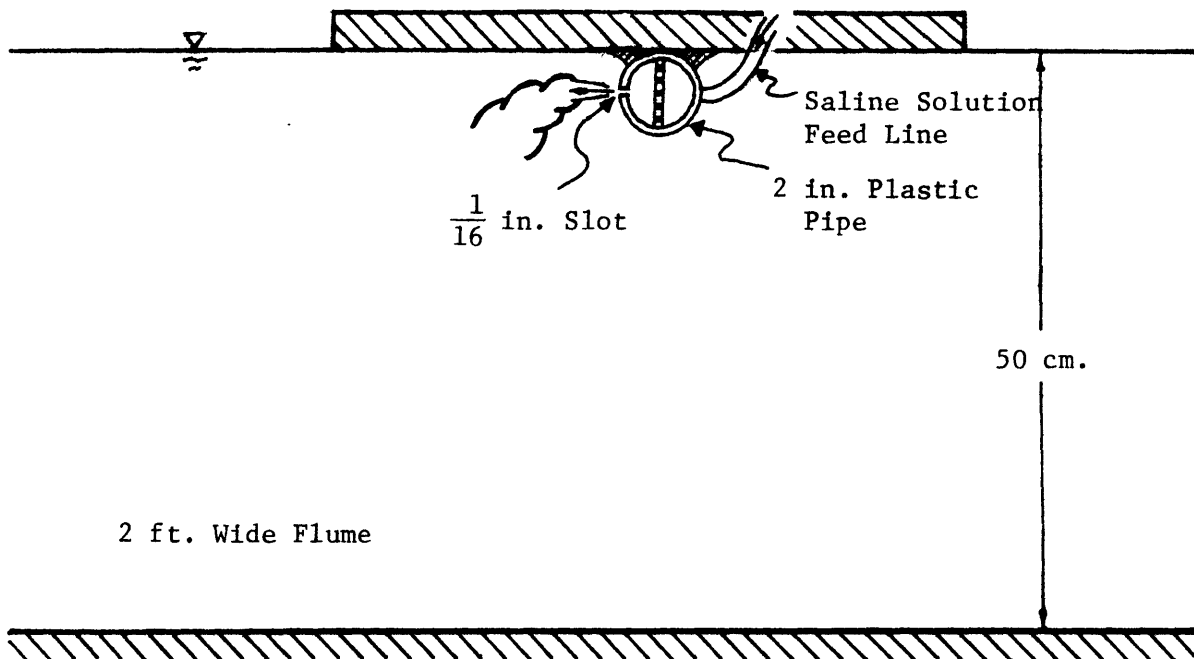
Figure 6.4 Cederwall's Buoyant Slot Jet Experiments

a plane jet case exactly analogous to the detached jet flow regime of

this study. An attached jet flow regime was also possible.

The integral model of this study could be easily adapted to this

set of experiments. Besides specifying a large initial radius, the

temperature - density relation (equation 3.19) had to be replaced by

a linear salinity-density relation. Also because of the geometry of

the experiments, P_i and ΔT_i did not need to be calculated according to

the empirical relations of Section 5.1. There was no recirculating region

below the jet ($\Delta T_i = 0$; $P_i = P_\infty$).

Because Cederwall did not consider confinement, the value of H_r

in his experiments is somewhat uncertain. He reports using a "two inch

pipe" in his discharge device; therefore an offset distance of 1.125 inches

is used (normal plexiglass tube dimensions refer approximately to the

inner diameter and Cederwall reports a .125 inch wall thickness).

However it is uncertain if an additional offset occured in attaching

the pipe to the plate.

Figure 6-5 displays Cederwall's trajectory data normalized by

the initial jet momentum and buoyancy flux. His data is divided into

three groups based on the value of $\mathbb{F}'$

$$\mathbb{F}' = \frac{\ell_Q'}{\ell_B'} = \frac{V_o}{\sqrt{\dfrac{\Delta\rho_o}{\rho}\, g \cdot 2D_o}} \tag{6.1}$$

Integral model trajectories are also plotted on the figure. The integral

model suggests that a detached flow (given the assumed value of H_r)

can only be maintained for $\mathbb{F}' \leq 19$.

The integral model predictions of confined jet behavior are
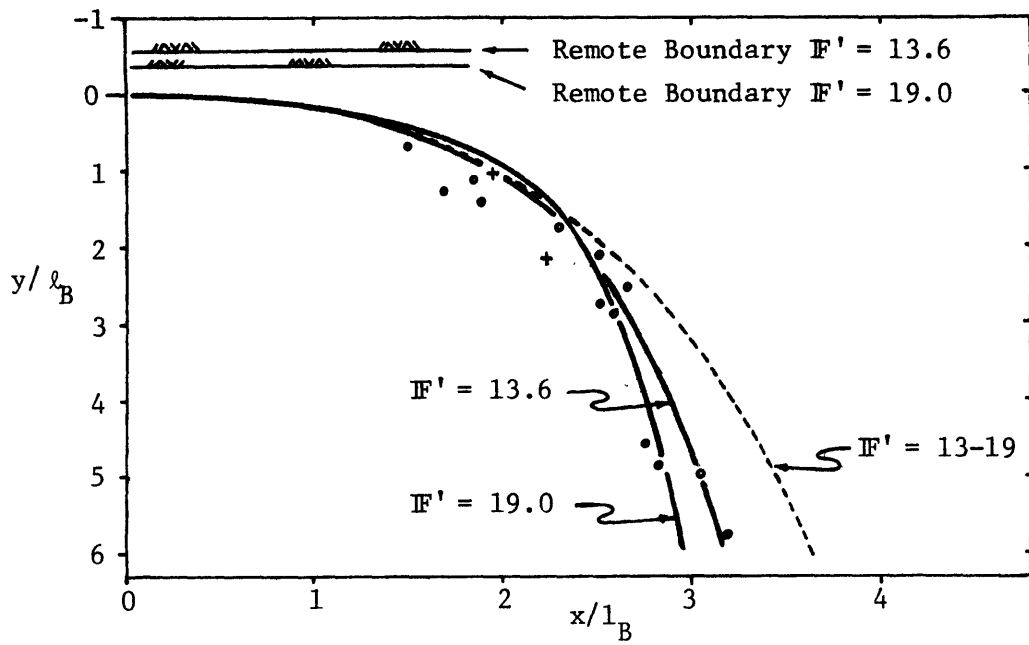
170

Figure 6-5 Offset Plane Boundary Confinement with
Buoyancy (Cederwall Data)

within the data scatter reported by Cederwall although there is a general

under-prediction of jet bending for the data points closest to the discharge

point. Two effects of jet confinement are apparent from the model

predictions. Firstly, a low pressure in the remote ambient region works

against the jet bending caused by buoyancy. For a given confinement,

this effect increases with the jet value of $\mathbb{F}'$. Secondly, the ambient

region counter-flow reduces jet horizontal momentum flux well below the

discharge value. This increases jet bending. At the end of the model

predictions $(y/\ell_B = 6.0)$:

$$M_{horiz} = .59\ M_o' \quad \text{for } \mathbb{F}' = 13.6$$

$$M_{horiz} = .40\ M_o' \quad \text{for } \mathbb{F}' = 19.0$$

The combination of these two effects causes the confined jet path

predictions to cross.

Figure 6-5 also includes a model prediction for unconfined jet

behavior where the horizontal jet momentum is conserved. Without

confinement, the normalized jet trajectory becomes independent of $\mathbb{F}'$

at large distances from the port. This predicted trajectory universally

under-estimates jet bending.

Cederwall does not report the occurance of an attached flow

regime. He has,however,only two data points for jets with $\mathbb{F}' > 19.6$.

The single trajectory point located in each of these experiments is

consistent with either jet flow regime.

6.3 Plane Jets with Angled Plane Boundaries

The fluid flows in this situation are described in Section 2.5.3.

The only experimental study was done by Bourque and Newman (1960) on non-buoyant jets. They varied the angle and length (relative to the jet port width) of the plane boundary. Two flow regimes,analogous to the attached and detached flow regimes of this study,were observed.

The integral jet model of this study was readily adapted to this case. Again a large initial radius was used to get plane jet behavior. The angled boundary was accounted for by giving the jet an initial angle and setting the boundary offset:

$$H = D_o \cdot \cos(\phi_o) \tag{6.2}$$

In modeling the detached flow regime, the remote boundary was given the offset H. The impacted boundary offset was effectively set at ∞ and $P_i - P_\infty$ was assumed to be zero.

In modeling the attached flow regime, the impacted boundary (assumed to be coherently impacted) was given the offset H. The remote boundary offset was effectively set to ∞.

Figure 6-6 plots the normalized value of x_r (distance to attachment of jet dividing streamline)versus ϕ_o for very long plane boundaries ($\ell >> x_r$). The integral model predicts x_r in exactly the same way as for the offset plane boundary. The prediction fits the data well and does not exhibit the slight overprediction of x_r (which occurred in the case of an offset plane boundary).

Figure 6-7 plots the experimentally determined flow regime limits as a function of initial jet angle, ϕ_o, and the relative plane boundary length, $\frac{\ell}{2D_o}$. It is not obvious how to get integral model predictions of the same transitions. The model only considers infinitely long

173
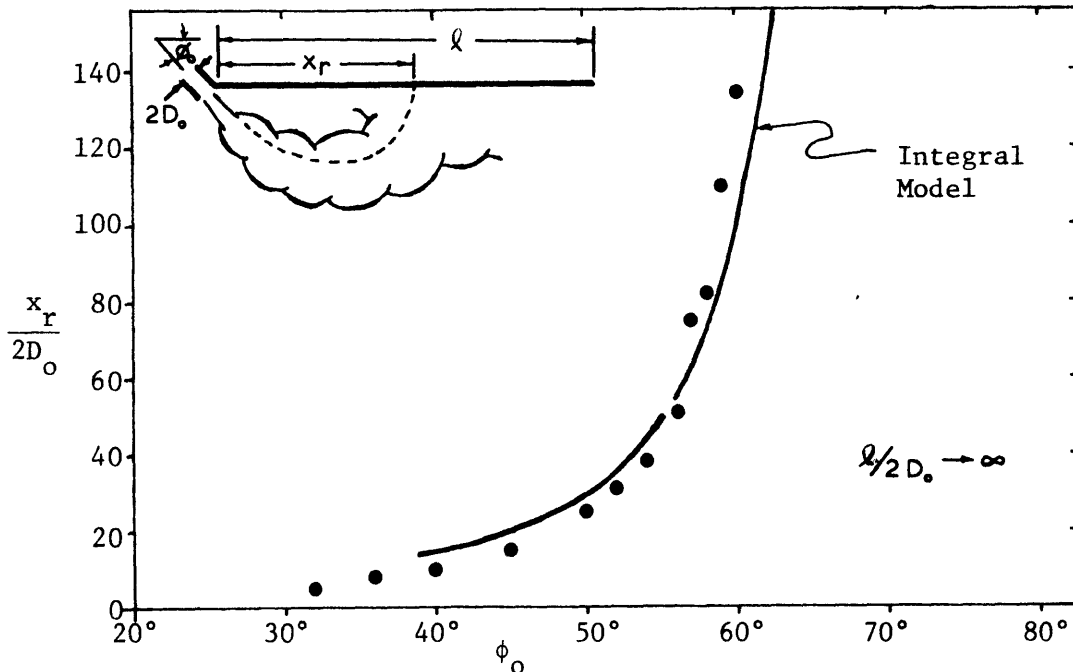
Figure 6-6   Attachment Distance for Angled Plane Boundary
Coanda Effect (Bourque Data)

boundaries.

For a given value of ϕ_o, the attachment transition value of

$\dfrac{\ell}{2D_o}$ was estimated by running the integral model for detached flow

$(H_r = D_o \cos (\phi_o); \; H_i = \infty)$. The model was stopped when attachment

was indicated according to the criteria used for attachment in this study

(Section 3.5.2.1). The x coordinate of this stopping point was reduced

by the distance from the inner jet boundary $(\tau = 1.8 \; b_{\frac{1}{2}})$ to the confining

plate. This value was used as the critical plate length. The described

reduction is pictured in Figure 6-7 and attempts to account for the

confinement that effectively extends beyond the end of the confining

plate.
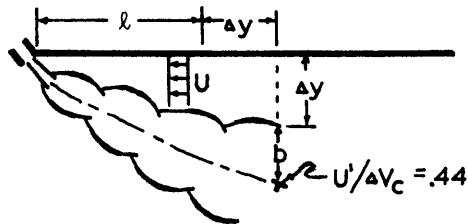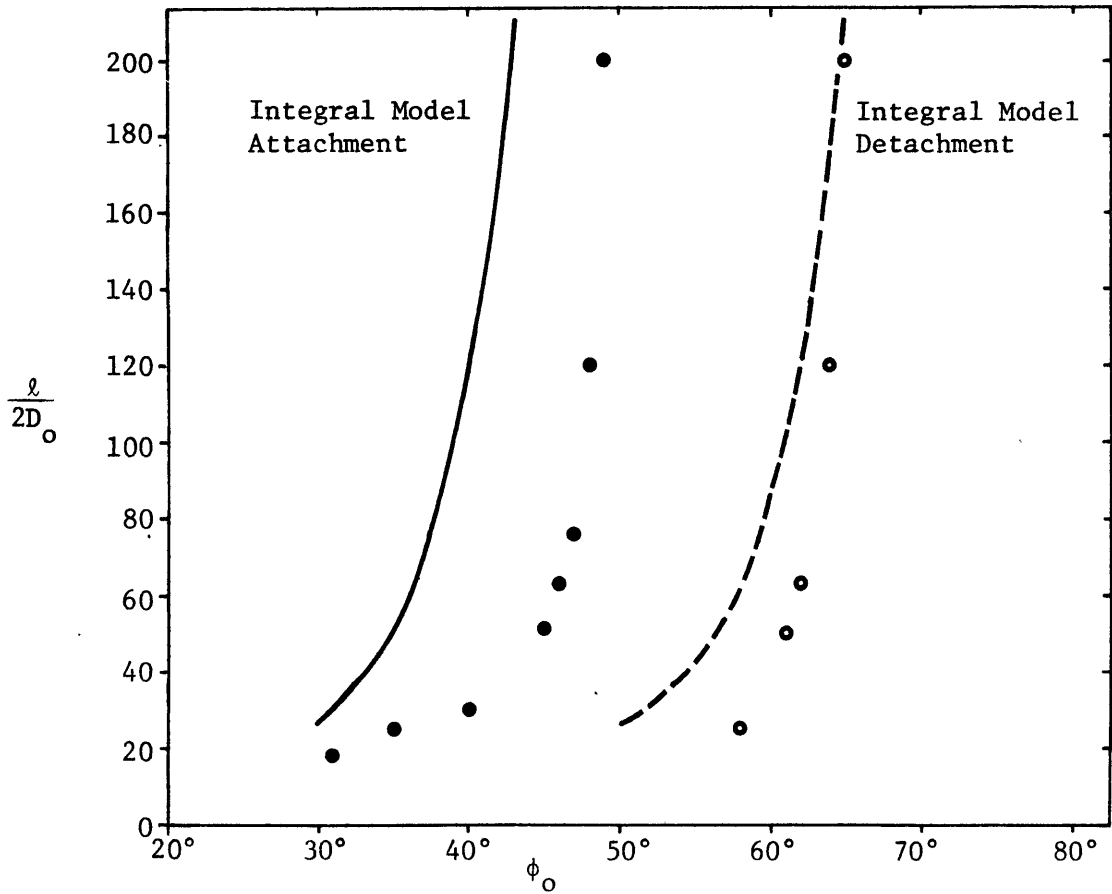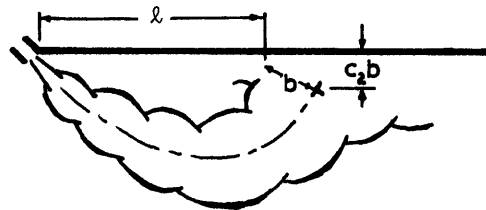
Figure 6-7   Flow Regime Limits for Angled Plane Boundary
Coanda Effect (Bourque Data)

For a given value of ϕ_o, the detachment transition value of $\frac{\ell}{2D_o}$ was found by running the integral model for attached flow ($H_i = D_o \cos \phi_o$; $H_r = \infty$). When the boundary impact point was reached, the critical confining plate length was taken as the x value of the inner jet boundary (see Figure 6-7). A shorter plate length "ℓ" was assumed to be unable to maintain an attached flow.

The integral model and the above criteria are not entirely successful at predicting the flow transitions. The detachment prediction is much better than the attachment prediction. The model is within 1° of the long plate ($\ell = 400\ D_o$) detachment value of $\phi_o = 65°$. The model however is off by 6° from the long plate ($\ell = 400\ D_o$) attachment value of $\phi_o = 49°$. The prediction of attachment is possibly limited by the simple flow that the model assumes for the ambient region between the jet and remote boundary (Section 3.3.1). These flow assumptions are much more appropriate to the offset plane boundary found in this study.

VII. Applications to OTEC Plant Operation

This chapter will initially apply the integral jet model to an

example 100 MW OTEC plant under stagnant ocean conditions. The following

sections will then deal with the problems of generalizing the mathematical

model to more typical OTEC operating conditions that include: 1) stratified

ambient ocean; 2) non-radial discharge ports; 3) non-horizontal discharges;

4) ambient ocean currents.

7.1 Example Applications to a 100 MW OTEC Plant

Using baseline conditions developed by the Department of Energy's

OTEC program (Allender, et al., 1978), a typical 100 MW OTEC plant might

have the characteristics listed in Table 7-1. The evaporator intake and

discharge temperatures are for conditions of no recirculation.

To be consistent with the integral model as developed in Chapter

III, the discharge ports are assumed to be horizontal (ϕ_o = 0°) and

radial in geometry. The assumed discharge flow rates and velocities

fix the port widths at 1.27 m. (or 2.55 m. for a mixed discharge of

evaporator and condenser flows). The integral model also assumes a

uniform stagnant receiving water body and thereby allows direct application

of the model to only certain ocean stratifications (e.g. large ocean

mixed layer depths). The fresh water temperature-density relation

(equation 3.19) will be assumed instead of including salinity effects.

7.1.1 Evaporator Discharge Recirculation

In this section the integral jet model will be applied to the

evaporator discharge jet only. The condenser discharge will be assumed

to be deep enough to have little effect on the evaporator jet. The mixed

177

OTEC Plant:

        Hull Type: Spar
        Radius (r_o): 20m

Evaporator Intake Flow:

        Flow rate: 400 m^3/sec
        Temperature: 27°C
        Depth: 5 m.
        Velocity: .7 m/sec

Evaporator Discharge Flow:

        Flow rate: 400 m^3/sec
        Temperature: 25°C
        Depth: 5-70 m.
        Velocity: 2.5 m/sec

Condenser Intake Flow:

        Flow rate: 400 m^3/sec
        Temperature: 6°C
        Depth: 600 m.
        Velocity[1]: 2.3 m/sec

Condenser Discharge Flow:

        Flow rate: 400 m^3/sec
        Temperature: 8°C
        Depth: 5-70 m.
        Velocity: 2.5 m/sec
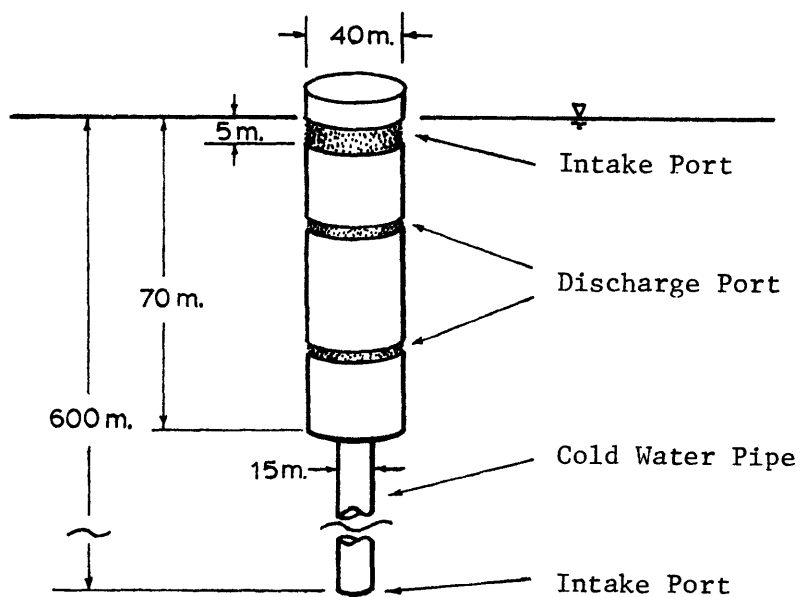
[1] Based on 15 m. diameter cold water pipe

Table 7-1 Typical Design Parameters for a 100 MW OTEC Plant

layer depth is also assumed to be much larger than the evaporator port

depth. Under these conditions the evaporator intake and discharge

conditions can be used directly in the integral model.

Figure 7-1 shows the expected evaporator intake temperature as a

function of the evaporator port depth. The two curve segments represent

conditions for the two possible flow regimes. Over a significant range

of discharge port depths (16 m to 30 m) both flow regimes are possible.

The one that actually occurs depends on the plant startup.(This is similar

to the hysterisis phenomena explained in Section 2.5.3.)

When recirculation exists (attached jet flow regime) the discharge

temperature is assumed to be 2°C below the intake temperature. The

expected power output of the plant (rated at 100 MW for no recirculation)
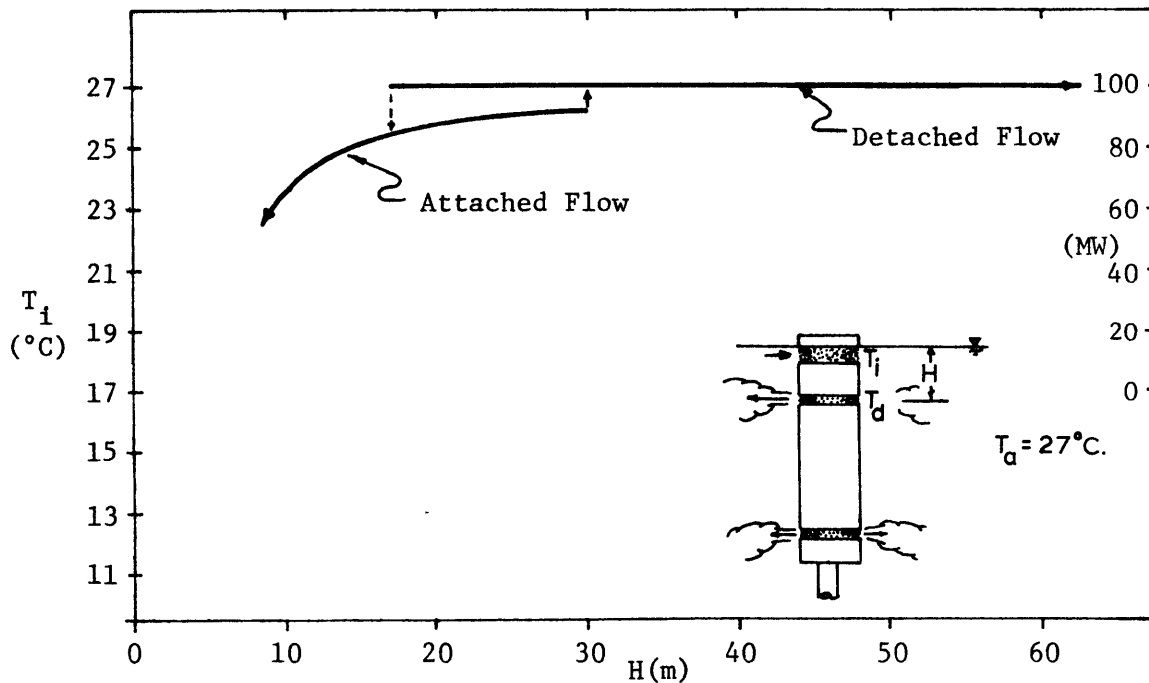
Figure 7-1   OTEC Intake Temperature for Evaporator Discharge
             Example   (IF = 9.7, IR = 6.2, k = 1)
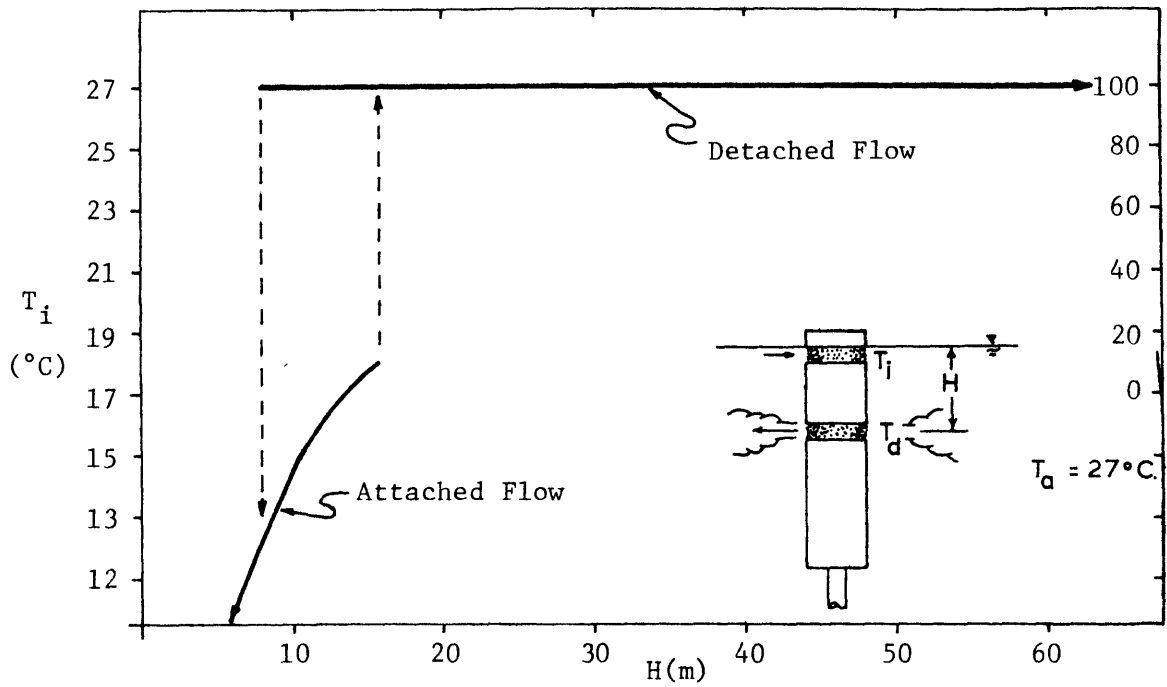
Figure 7-2   OTEC Intake Temperature for Mixed Discharge Example
(𝔽 = 3.9; ℝ = 3.5, k = 1/2)

can be read off the right hand axis of Figure 7-1. A ten percent loss is assumed for every degree Centigrade drop in the intake temperature (Allender et al., 1978).

7.1.2 Mixed Discharge Recirculation

Under this mode of operation the two OTEC flows are discharged as one with the combined temperature of 16.5°C. The discharge velocity is 2.5 m/sec. Again the mixed layer depth is assumed to be much larger than the discharge port depth.

Figure 7-2 shows the expected evaporator intake temperature and the plant's net power output as a function of the mixed discharge port depth. Both the attached and detached flow regimes are again possible.

When recirculation occurs (attached flow regime) the discharge temperature is modified by assuming the evaporator discharge temperature is 2°C lower than the evaporator intake temperature.

$$T_{discharge} = 16.5° - [(27° - T_{intake})/2] \quad (°C) \quad\quad (7.1)$$

Recirculation from an evaporator discharge can occur at greater jet submergences than recirculation from a mixed discharge, but recirculation from a mixed discharge has a greater effect on T_i.

7.1.3 External Plant Mixing of Evaporator and Condenser Discharges

The integral jet model is only applicable to the case where the two jets have equal but opposite (one positive and one negative) buoyancies (see insert, Figure 7-4). The ambient water temperature therefore needs to be uniform at a density halfway between that of the two jets (T_a=18.8°C).

Several sets of experiments were conducted at MIT of this flow
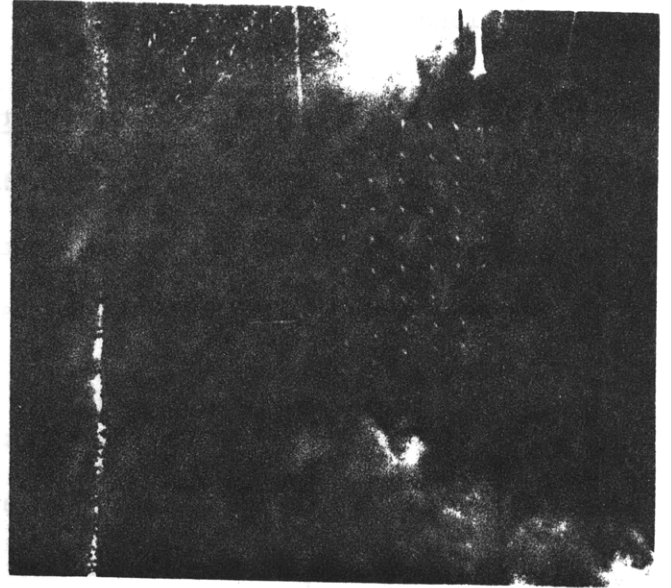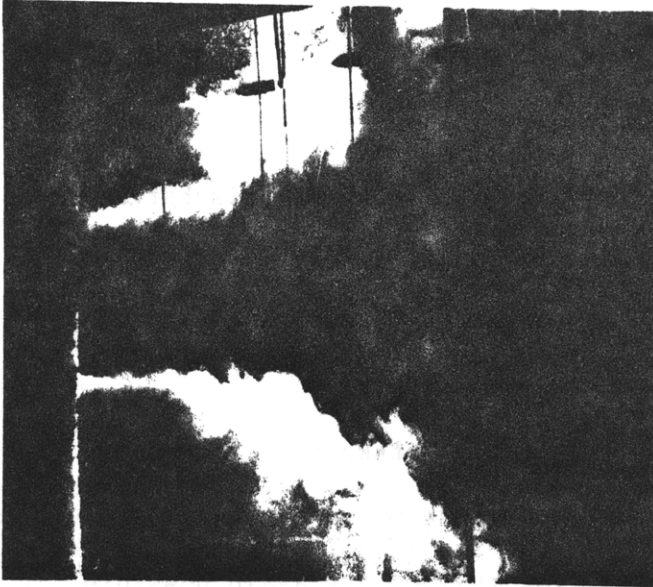
Separate Jet Case
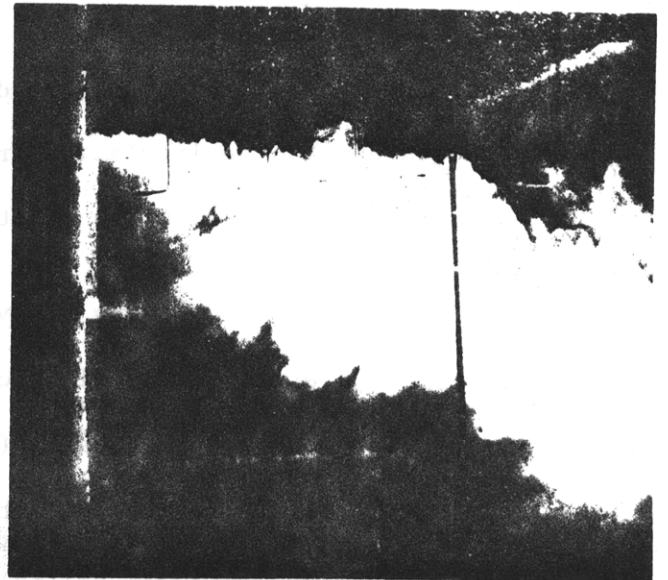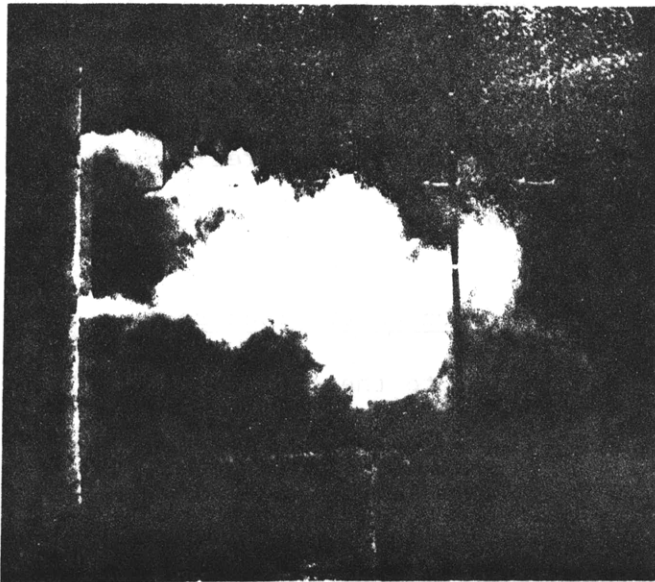
Mixed Jet Case

Figure 7-3 Mixing of Positively Buoyant and Negatively Buoyant Radial Jets

situation. The purpose was to confirm that the flow field, if split on its line of symmetry, was similar to the attached, detached flow regimes for a single jet and offset plane boundary (k = 0). This was found to be the case, as the photographs in Figure 7-3 indicate.

Figure 7-4 plots the two possible flow regimes (attached and detached or in this case mixed jets and separate jets) as a function of port separation.

It would be hard to find an ocean stratification where the assumed ambient conditions would apply. The results in Figure 7-4 are then just a gross indication of the radial port separation needed to effect an externally mixed discharge.

7.2 Integral Model Extensions for Ambient Stratifications

An extensive series of experiments with radial discharges into a stagnant, stratified ambient was carried out at MIT (Adams et al., 1979).
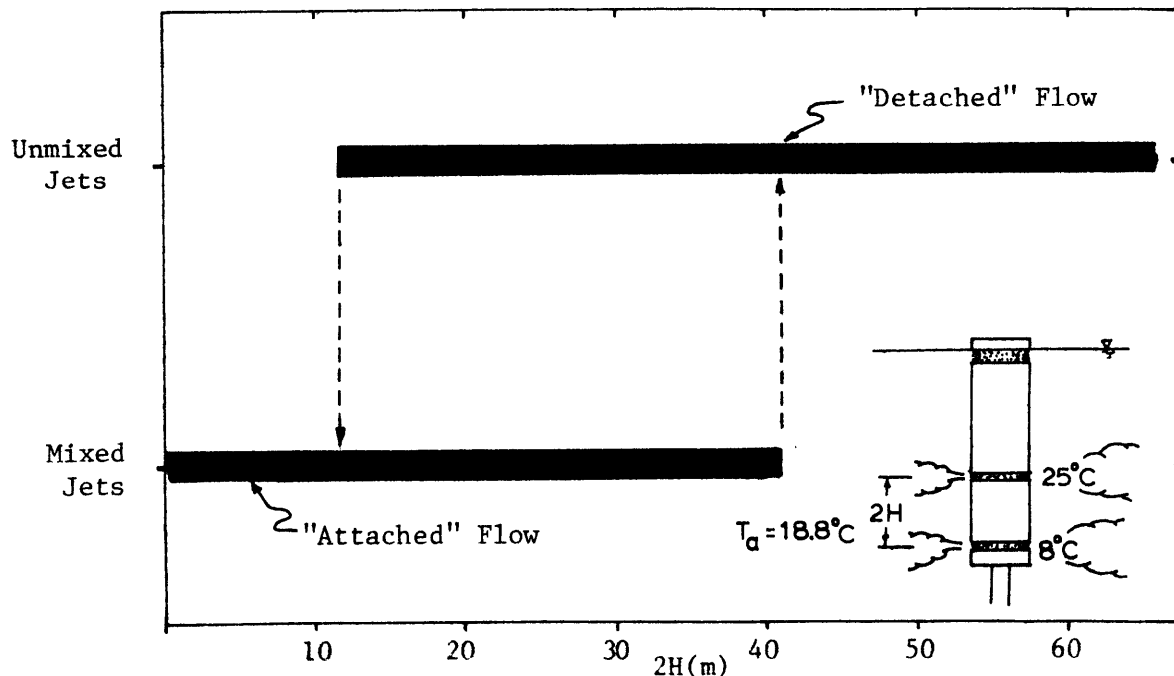
Figure 7-4 OTEC External Mixing of Evaporator and Condenser
Discharges ($F = 6.0$, $R = 3.8$, k=0)

183

Basically the same equipment and procedures described for this study were employed. This time,however, the model basin had an initial stratification resembling real ocean profiles at a scale of 1:300.

The photographs in Figure 7-5 indicate the jet spreading and trajectory for two experiments. Several features are readily apparent that are different from the jet flows in this study:

1) The jet rises (or falls) only until it reaches a neutrally buoyant level.

2) Stratification inhibits and eventually stops jet spreading.

3) Stratification affects the extent and uniformity of the ambient flow fields making up the intake and entrainment flows (not visible).

4) The diffuse impacted boundary of this study (detached flow regime) is not present.

Even with all these differences two flow regimes very much like those of this study were found in the experiments (Figure 7-6).

7.2.1 Neutral Buoyancy Levels

The inclusion of ambient stratification in integral jet models has been done before (Abraham, 1972; Fan, 1967; Hirst 1971), but ambient region flow effects were not considered. The jets were assumed, at each trajectory location, to simply entrain water (with no momentum) at the undisturbed ambient temperature of that level. The challenge remains to include the effects of the ambient flow fields (which are the only effects that might cause OTEC recirculation).
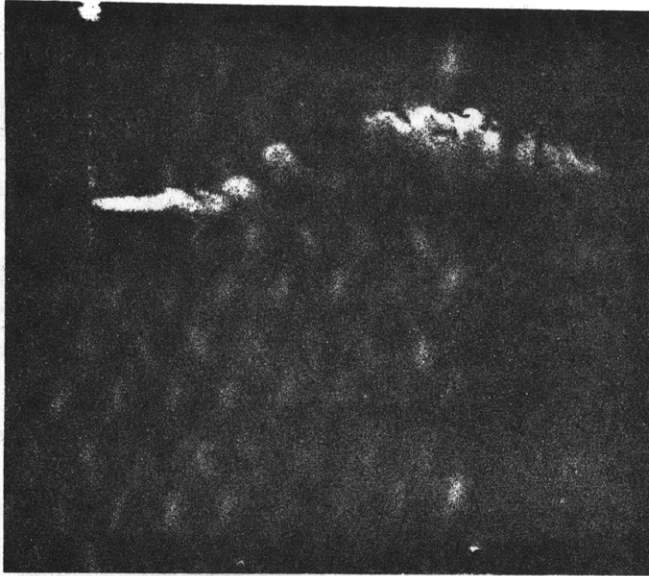
OTEC Evaporator Discharge Jet Simulations
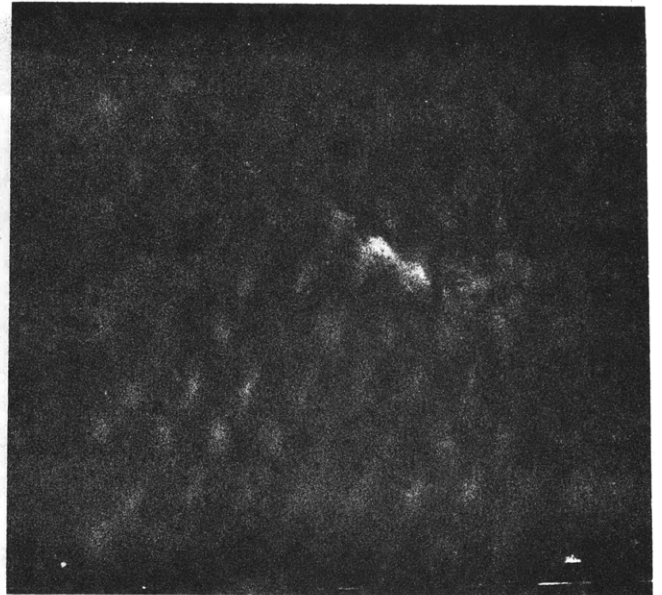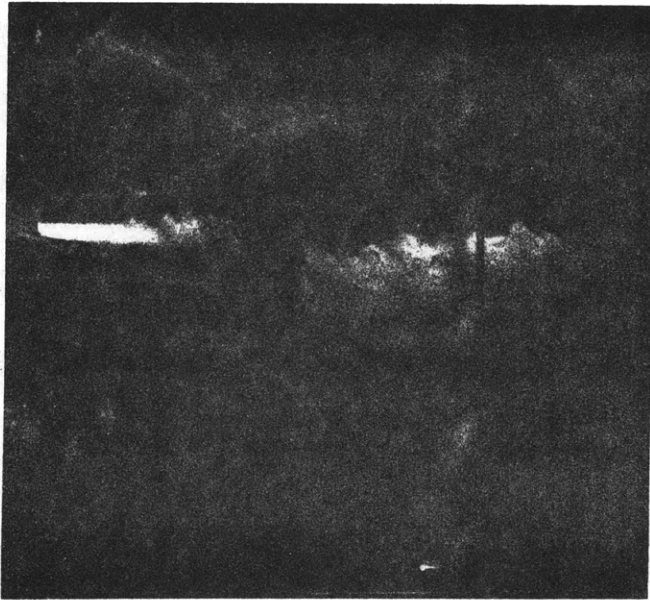
OTEC Mixed Discharge Jet Simulation

Figure 7-5 Radial Buoyant Jets in a Stagnant, Stratified Ambient Fluid
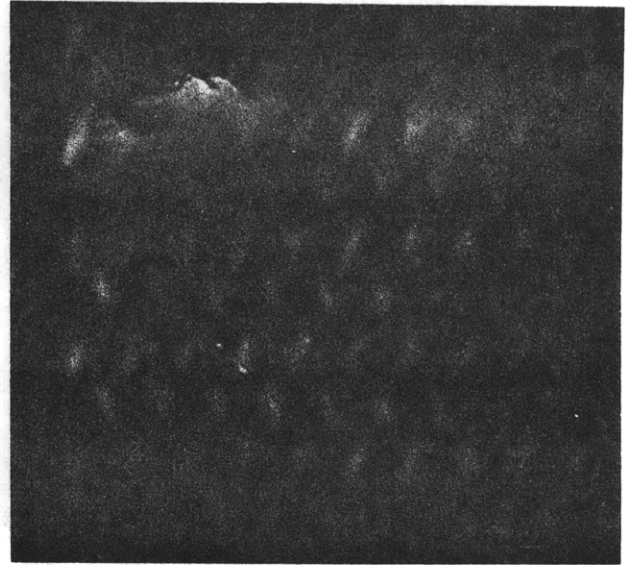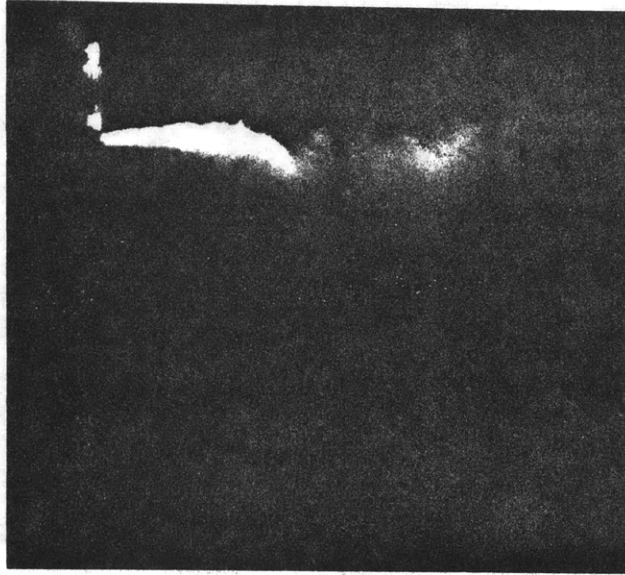
No Discharge Jet Recirculation (L = .160; F = 9.3; R = 9.5)
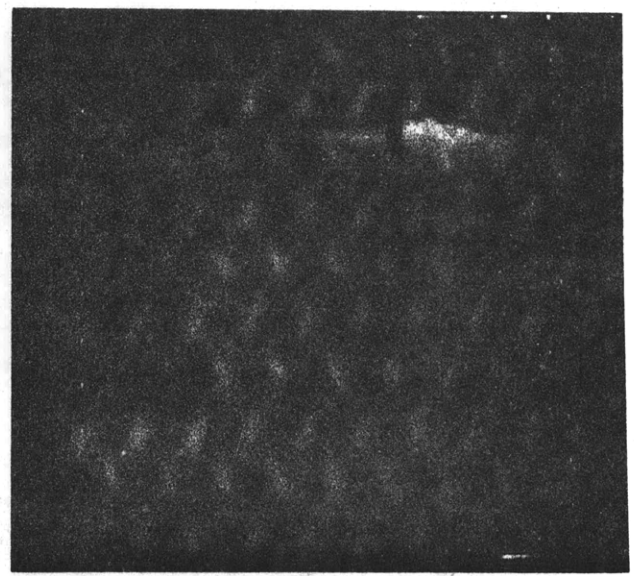
Strong Discharge Jet Recirculation (L = .137; F = 10.2; R = 10.51)

Figure 7-6 Discharge Jet Attachment in a Stagnant Ambient Fluid (k=1)

7.2.2 Stratification and Jet Spreading

The stratification effects on jet spreading occur only near the location where the jet reaches its neutrally buoyant level. Basic studies on heated surface jets have quantified this effect. The results of Ellison and Turner (1959) appear in Figure 7-7. The spreading relation (equation 3.49) could be easily expanded to include this effect.

7.2.3 Extent of Ambient Flow Fields

The problem of the extent and uniformity of ambient flow fields can be discussed by taking an example. The solution of this problem provides information needed for ambient flow field effects on jet trajectories (Section 7.2.1).

Consider the ambient region below the falling jet of Figure 7-8.

$$1/\mathbb{F}_1' = \frac{[(b_{\frac{1}{2}})(\Delta\rho_c/\rho)g]^{\frac{1}{2}}}{\Delta V_c}$$
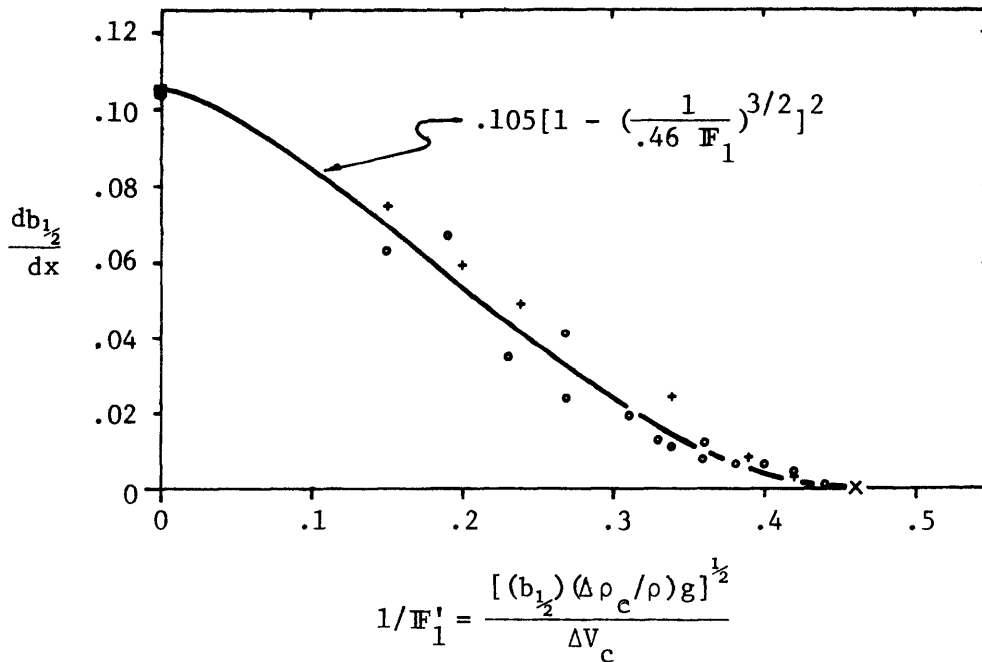
Figure 7-7 Buoyant Surface Jet Spreading (Ellison and Turner, 1958)

187

At the point where jet spreading ceases, the entrainment flow layer will

not be extremely deep because of the low pressures that would be needed

to lift the very dense water up to the jet boundary. On the other hand

the flow layer will not be extremely thin because of the low pressures

that would be needed to achieve the high ambient velocities associated

with that thin layer. If the jet entrainment is simulated by a set of

sinks at appropriate locations, the stratified flow problem could be

attacked under the assumption of a frictionless irrotational flow. An

alternative simpler approach would be to experimentally determine an

ambient densimetric Froude number that should be of order 1 in magnitude

and not vary widely among different jets.

$$\mathbb{F}_a = \frac{U_a}{[\frac{\Delta\rho_a}{\rho} g \, H_a]^{\frac{1}{2}}} \tag{7.2}$$

$$\mathbb{F}_a = \frac{U_a}{[(\Delta\rho_a/\rho)g \, H_a]^{\frac{1}{2}}}$$
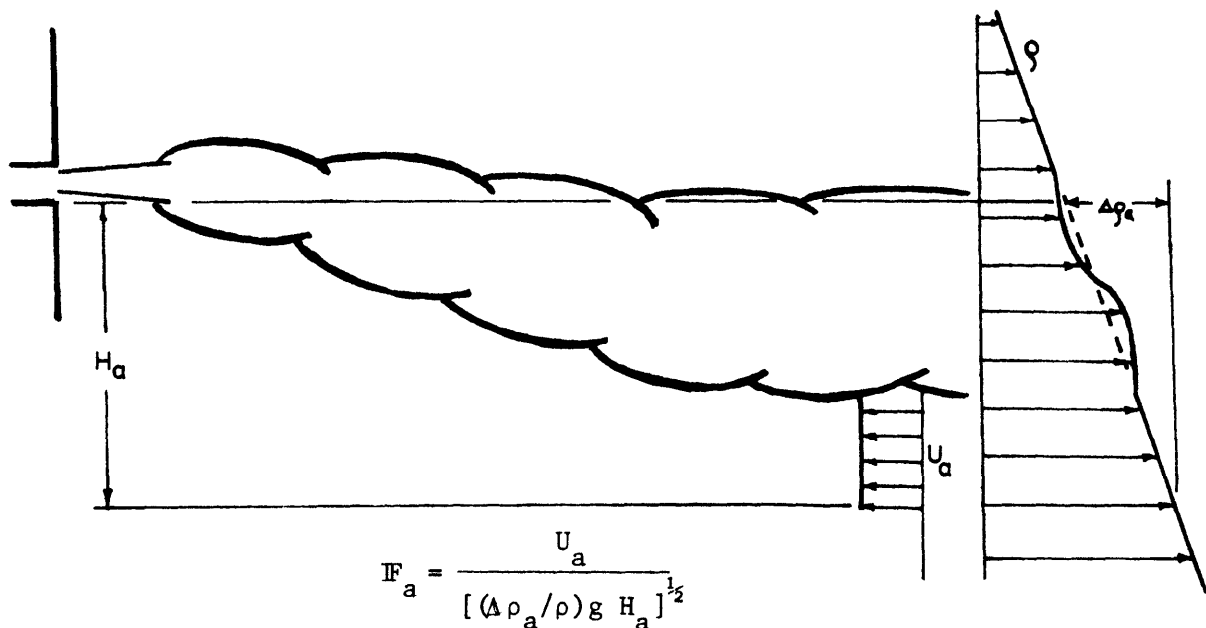
Figure 7-8   Flow under a Buoyant Jet in a Stratified Ambient

An ambient velocity profile shape can be assumed or measured. Pressures

and velocities below the jet are estimable from frictionless flow and

buoyancy considerations (using a Bernoulli relation along streamlines).

In either of the above approaches, the jet flow solution is

needed as a boundary condition. Therefore the total solution must be

an iterative process because of the interdependence of the jet and

ambient flow fields. The solution procedure would be similar to that

commonly employed for boundary layers on solid bodies. An inviscid

external flow is needed to give a pressure distribution over the body.

The boundary layer calculations use that pressure distribution. At the

same time the newly calculated boundary layer serves as the boundary

condition for the external inviscid flow that now needs to be recalculated.

7.2.4 Diffuse Impacted Boundaries

Such boundaries can exist for horizontal jets in a stratified

ambient if the buoyancy length scale l_B is less than the jet fall (or

rise) distance to achieve neutral buoyancy. However the MIT OTEC

simulations for stagnant stratified conditions (Adams et al., 1979)

observed no such occurrence for horizontal radial jets. This means

that the empirical correlations (equations 5.1 and 5.2) for

temperature and pressure in this region are no longer needed, thus

simplifying the model.

7.3 Separate Ports

The radial jet model is not easily extendable to separate ports

unless the port approaches slot jet conditions (simply let $r_o \to \infty$ in the

model).

However separate port recirculation behavior could be simulated by an equivalent radial port. Such an equivalency is illustrated in Figure 7-9. This "equivalent" radial jet can be expected to be a conservative estimator of the onset of recirculation. No account is made of the entrainment flow originating from the sides of the jet. This means lower velocities (U) above the jet and less tendency for attachment. The choice of $\frac{db_{\frac{1}{2}}}{dx}$ (rather than $\frac{db}{dx}$ or any other multiple of $\frac{db_{\frac{1}{2}}}{dx}$) for relating lateral spreading to radial spreading insures that the 12° radial jet sector has the same flow as the separate port jet ($I_1 \approx 1$).

A more theoretically satisfying model of separate port behavior is not possible without considering the three dimensionality of the ambient flow field.

7.4 Non-Horizontal Discharges

The integral model is formulated to accept discharges of any initial vertical angle (ϕ_o). However the correlations for the diffuse impacted boundary (equations 5.1 and 5.2 for the detached flow regime) really only apply for horizontal or near horizontal (± 15°) discharges. Note that this restriction may not apply to a stratified ambient integral model where this type of ambient region may not exist.

7.5 Ambient Currents

MIT OTEC simulations of stratified flowing ambients show that stagnant ambient behavior applies only to very slow ocean currents (Coxe, et al., 1981). A fifth length scale appears because of the new variable, ambient current velocity. Figure 7-10 shows a range of possible OTEC discharge jet
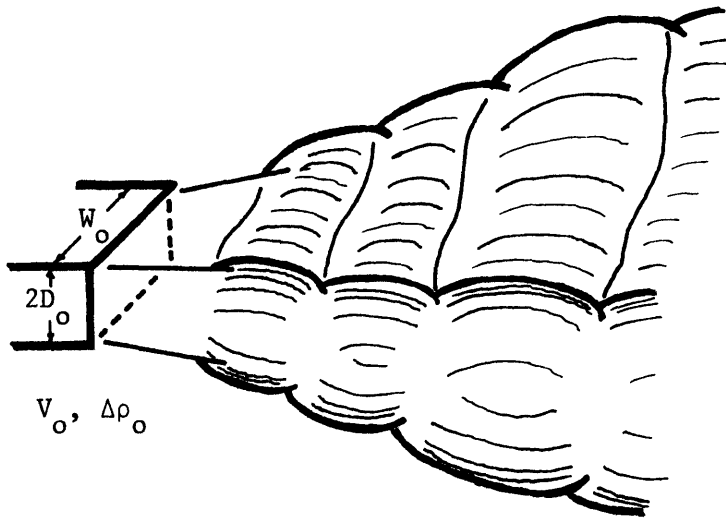
$$Q_o'' = 2D_o W_o V_o$$

$$M_o'' = 2D_o W_o V_o^2$$

$$B_o'' = 2D_o W_o \frac{\Delta\rho_o}{\rho} g$$

$$\frac{db_{\frac{1}{2}}}{dx} = .105$$

$12°$

Equivalent Radial
Jet Discharge
Point
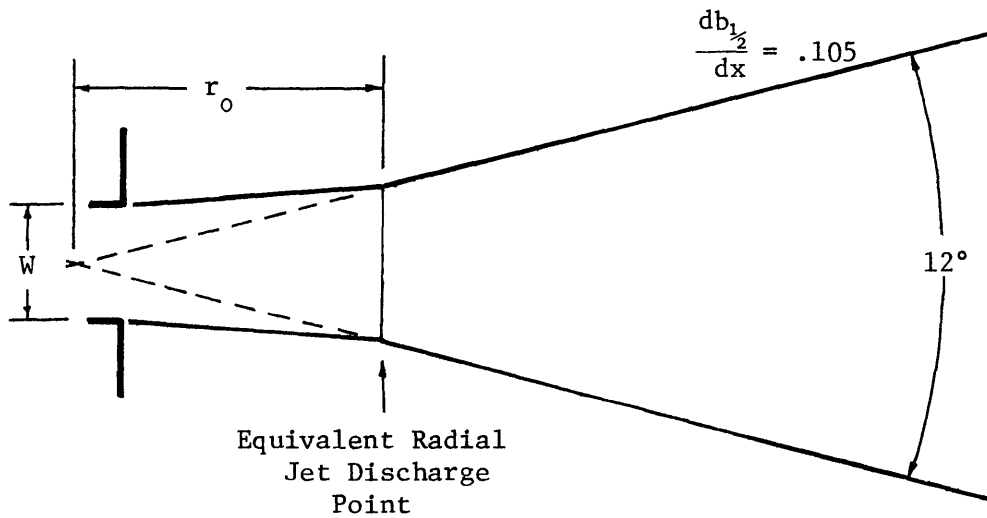
Equivalent Radial Jet

$$b_{\frac{1}{2}_o} \approx 1.4 \, D_o + 6(W_o - 2D_o) \cdot .105$$

$$r_o \approx 6W_o$$

$$Q_o \approx [360/12] \cdot [b_{\frac{1}{2}_o}/D_o] \cdot Q_o''$$

$$M_o = [360/12] \cdot M_o''$$

$$B_o = [360/12] \cdot B_o''$$

Figure 7-9   Radial Equivalent Jet to Rectangular Separate Port

191

behavior. A new recirculation mode is made possible because of a "billowing" of the jet discharged into the ambient current. This recirculation mode is less severe (smaller evaporator intake temperature changes) but more likely to occur. F, R, and L values that do not produce recirculation in stagnant ambients may very well do so under the influence of non-zero ocean currents.

The two-dimensional model of this report is not extendable to the three-dimensional flow field found around OTEC plants in a current. However it may be useful in sorting out the relative importance and mutual interaction of the length scales ℓ_B, ℓ_H, ℓ_Q, and ℓ_r. This may allow problem simplification and greater ease in applying empirically determined effects of an ambient current length scale.
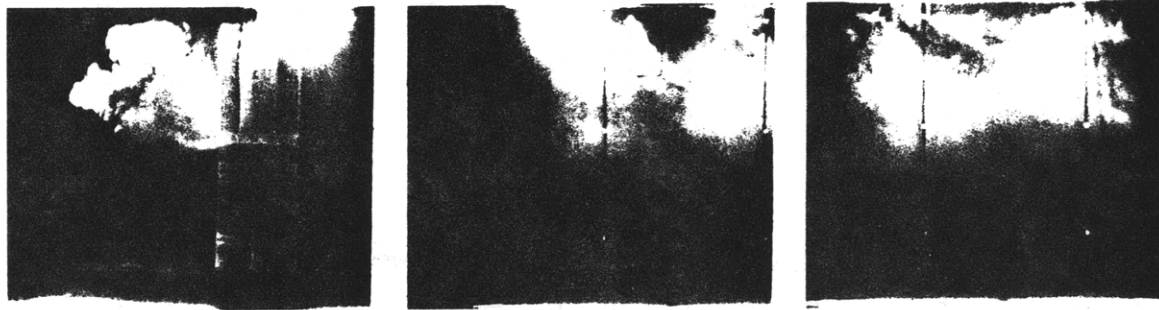
Prototype Current Speed of 0.51 m/sec (L = .317; F = 10.1; R = 10.5)

Prototype Current Speed of 0.15 m/sec (L = .317; F = 10.1; R = 10.5)

Figure 7-10   OTEC Discharge Jet Behavior in a Stratified Flowing Ambient

VIII. <u>Summary and Conclusions</u>

8.1 <u>Motivation</u>

This study has explored the behavior of a horizontal, negatively

buoyant, radial jet discharging beneath a free surface. In such a

situation the action of buoyancy and dynamic pressures (induced by

the confinement of the free surface) are opposed. The jet was observed

to be detached or attached to the free surface depending on whether

negative buoyancy (tending to detach) or dynamic pressure (tending to

attach) forces dominated.

The motivation for this research is the need to predict characteris-

tics of the external fluid flow field of OTEC. Central to the feasibility

of any OTEC concept is the need to withdraw large flows of warm water

from near the ocean surface. The efficiency of any OTEC plant is highly

dependent on the temperature of this intake flow. Even temperature

changes on the order of 0.5°C are significant. Thus the prediction of

warm water intake temperature should be a key characteristic of any

modeling of OTEC's external fluid flow field.

Some previous analyses appropriate to this problem have considered

only an intake in a stratified ocean and neglected the effects of OTEC

discharges on the fluid flow field (Craya, 1949; Lavi et al., 1975;

Fry, 1976). Possible discharge jet recirculation to the warm water

intake could obviously not be modeled.

Other OTEC modeling attempts have applied unconfined integral

jet models to the discharge jets of preliminary OTEC designs (Lockheed

Missile and Space Company, Inc., 1975; Kirchhoff et al., 1975; Fry, 1976).

Discharge jet dilution and trajectories result, but there is no good

way of predicting when or by how much the warm water intake temperature is affected.

It is obvious that a successful OTEC model must consider the combined effects of jet flows and ambient region flows (including OTEC intake and jet entrainment flows) in one model. The experiments and analytical models of Johnson (1977) and this study answer this need for certain OTEC designs and ambient conditions. In addition, the analytical model of this study appears to be extendable to less restrictive ambient ocean and OTEC design characteristics.

8.2 Summary

For a given intake flow strength, a dimensional analysis of this problem yielded three primary dimensionless governing parameters ($\mathbb{L}$, $\mathbb{F}$, and $\mathbb{R}$). An experimental program was devised to measure jet trajectories, ambient region velocities, and temperatures throughout the flow field for a range of $\mathbb{L}$, $\mathbb{F}$, and $\mathbb{R}$ values.

Next an analytical (integral jet) model was developed using a spreading relation for closure. This model synthesized the results of basic jet studies that considered separately the many effects found in this study: 1) jet flow establishment zone; 2) ambient region velocities and pressures; 3) jet buoyancy; 4) jet curvature effects on entrainment; 5) the impingement of jets on boundaries. Two constants (c_2 and c_3) and two relations (equations 5.1 and 5.2) were empirically determined from the experiments of this study. The approximate magnitude of the constants and form of the relations were derivable from dimensional analysis and they matched the empirically chosen values and relations.

The analytical model of this study can be successfully applied to more basic flow situations (e.g. plane jets, non-buoyant jets, and unconfined jets) as well as less basic confined jet studies cited in the literature (ducted plane jets, buoyant and non-buoyant jets with offset plane boundaries, and non-buoyant plane jets with angled boundaries).

8.3 Important Results and Conclusions

1. The dimensionless variable $\mathbb{L} = M_o^{-3/4} B_o^{1/2} H$ (where M_o is the kinematic discharge momentum flux, B_o is the kinematic discharge buoyancy flux, and H is the jet submergence) was found to be the primary independent variable for jet behavior. See Table 2-1 and Figure 2-3. $\mathbb{F} = M_o^{5/4}/B_o^{1/2} Q_o$ and $\mathbb{R} = M_o^{3/4}/r_o B_o^{1/2}$ were found to be variables of secondary importance.

2. For large values of $\mathbb{F}$ and $\mathbb{R}$ (negligible effects of initial jet discharge flow and radius) attached jets could be effected for $\mathbb{L}$ < .20 while detached jets could be effected for $\mathbb{L}$ > .14. The overlap in $\mathbb{L}$ values indicates that under some conditions (.14 < $\mathbb{L}$ < .20) both flow regimes are possible. This corresponds to the experimentally observed hysterisis in jet behavior. An attached jet stays attached even when $\mathbb{L}$ is raised above the value needed to achieve attachment of a detached jet. A detached jet remains detached even when $\mathbb{L}$ is lowered below the value needed to detach an attached jet.

3. Jet attachment/detachment as well as many other fluid flow and temperature properties were successfully modeled analytically by a modified integral jet model using a spreading relation for closure.

4. Successful application of the model to other flow situations (confined and unconfined, buoyant and non-buoyant, plant jets) suggests the generality of the model beyond the specific range of experiments.

5. The model can be applied to OTEC external flow fields for radial evaporator or mixed (combined evaporator and condenser) discharges above the ocean thermocline under stagnant ocean conditions. Experiments by Coxe et al (1981) show that recirculation under these conditions is less likely to occur (requires shallower submergence H) than under conditions with an ambient current, but that the percentage of recirculation, where it occurs, is greater.

6. Steps are outlined whereby the model could be extended to less restrictive discharge jet geometries and ocean stratifications. Stagnant or near stagnant ocean current conditions must still be assumed.

Bibliography

Abraham, G., "Horizontal Jets in Stagnant Fluid of Other Density,"
ASCE Journal of the Hydraulics Division, July, 1965.

Abraham, G., "Jets and Plumes Issuing into Stratified Fluid," Proceedings
International Symposium on Stratified Flows, Novosibirsk, 1972.

Abramovich, G.N., The Theory of Turbulent Jets, The M.I.T. Press, M.I.T.
Cambridge, Mass., 1963.

Adams, E.E., Fry, D., Coxe, D., Harleman, D.R.F., "Research on the
External Fluid Mechanics of Ocean Thermal Energy Conversion Plants,
Report Covering Experiments in Stagnant Water," Technical Report
No. 250, M.I.T., R.M. Parsons Laboratory, Cambridge, Mass., June, 1979.

Albertson, M.L. et al., "Diffusion of Submerged Jets," Transactions
American Society of Civil Engineers, 115, 1950, pp. 639-697.

Allender, J.H., Ditmars, J.D., Paddock, R.A., and Saunders, K.D.,
"OTEC Physical and Climatic Environmental Impacts: An Overview of
Modeling Efforts and Needs," Proceedings of the Fifth Ocean Thermal
Energy Conversion Conference, Sponsored by U.S. Department of Energy,
Miami Beach, Florida, Feb., 1978.

Becker, H.A., Hottel, H.C., and Williams, G.C., "Mixing and Flow in
Ducted Turbulent Jets," Proceedings 9th International Symposium
on Combustion, 1962, pp. 7-20.

Bourque, C., and Newman, B.G., "Reattachment of a Two-Dimensional
Incompressible Jet to an Adjacent Flat Plate, Aeronautical Quarterly,
Vol. II, 1960, pp. 201-232.

Bradbury, L.J.S. and Riley, J., "The Spread of a Turbulent Plant Jet
into a Parallel Moving Airstream," Journal of Fluid Mechanics,
Vol. 27, 1967, pp. 381-394.

Brighton, J.A., Razinsky, E., and Bowlus, D.A., "Turbulent Mixing of a
Confined Axisymmetric Jet," Proceedings of Fluidics and Internal
Flows, Pennsylvania State University, Vol. 2, 1969, pp. 57-90.

Cederwall, K., "Buoyant Slot Jets into Stagnant or Flowing Environments,"
Report No. KH-R-25, California Institute of Technology, Keck Laboratory,
Pasadena, Calif., 1971.

Corrsin, S. and Uberoi, M.S., "Investigation of Flow in an Axially Symmetric
Heat Jet of Air," National Advisory Committee for Aeronautics,
Wartime Report, W-94.

Coxe, D.H., Fry, D.J., and Adams, E.E., "Research on the External
Fluid Mechanics of Ocean Thermal Energy Conversion Plants,
Report Covering Experiments in a Current," Energy Laboratory
Report No. MIT-EL 81-049, M.I.T., Cambridge, Mass., September 1981.

Craya, A., "Recherches Theoriques sur L'Ecoulent de Couches Superposees de Fluides de Densites Differentes," LaHouille Blanche, Jan. - Feb., 1949.

Curtet, R., "Confined Jets and Recirculation Phenomena with Cold Air," Combustion and Flame; Vol. 2, 1958, pp. 383-411.

Ellison, T.H. and Turner, J.S., "Turbulent Entrainment in Stratified Flows," Journal of Fluid Mechanics, Vol. 6, 1959.

Fan, L.-N., "Turbulent Buoyant Jets into Stratified or Flowing Ambient Fluids," Report No. KH-R-15, California Institute of Technology, Keck Laboratory, Pasadena, Calif., 1967.

Förthmann, E., "Über turbulente Strahlausbreitung," Ingr. Archiv., V, 1, 1934 (English Translation, N.A.C.A., TM 789, 1936).

Fox, D.G., "Forced Plume in a Stratified Fluid," Journal of Geophysical Research, Vol. 75, No. 33, 1970.

Fry, D.J., "Effects of Oceanic Flow Patterns on the Thermal Efficiency of Ocean Thermal Energy Conversion (OTEC)," M.S. Thesis, Dept. of Civil Engineering, Carnegie-Mellon University, Pittsburgh, Pa., April, 1976.

Fuglister, F.C., Atlantic Ocean Atlas, Temperature and Salinity Profiles and Data from the International Geophysical Year of 1957-1958, the Woods Hole Oceanographic Series, Vol. 1, Woods Hole, Massachusetts, 1960.

Goertler, H., "Berechnung von Aufgaben der freien Turbulenz auf Grund eines neuen Naherungsansatzes," Z.A.M.M., 22: 244-254, 1942.

Handbook of Chemistry and Physics, C.D. Hodgman, ed., 39th Edition, Chemical Rubber Publishing Co., Cleveland, Ohio, 1958.

Heskestad, G., "Hot Wire Measurements in a Plane Turbulent Jet," Journal of Applied Mechanics, 1965, pp. 1-14.

Heskestad, G., "Hot Wire Measurements in a Radial Turbulent Jet," Journal of Applied Mechanics, 1966, pp. 417-424.

Hill, P.G., "Turbulent Jets in Ducted Streams," Journal of Fluid Mechanics, Vol. 22, 1965, pp. 161-186.

Hinze, J.D. and Van der Hegge Zijnen, B.G., "Transfer of Heat and Matter in the Turbulent Mixing Zone of an Axially Symmetrical Jet," Journal of Applied Science Research, 1A, 1948, pp. 435-445.

Hirst, E.A., "Buoyant Jets Discharged to Quiescent Stratified Ambients," Journal of Geophysical Research, Vol. 76, No. 30, 1971.

Ito, H., "Pressure Losses in Smooth Pipe Bends," Transactions of American Society of Mechanical Engineers, Series D. Journal of Basic Engineering, Vol. 82, No. 1, 1960.

Jirka, G.H., Abraham, G., and Harleman, D.R.F., "An Assessment of Techniques for Hydrothermal Prediction," Technical Report No. 203, M.I.T., R.M. Parsons Laboratory, Cambridge, Mass., July, 1975.

Jirka, G.H., Johnson, R.P., Fry, D.J., and Harleman, D.R.F., "Ocean Thermal Energy Conversion Plants: Experimental and Analytical Study of Mixing and Recirculation," Technical Report No. 231, M.I.T., R.M. Parsons Laboratory, Cambridge, Mass., Sept. 1977.

Johnson, R.P., "An Experimental and Analytical Investigation of an Ocean Thermal Energy Conversion Plant with Radial Discharge Geometry," M.S. Thesis, M.I.T., Dept. of Civil Engineering, Cambridge, Mass., May 1977.

Kirchhoff, R.H., Mangarella, P.A., McGowan, J.G., "Hydrodynamics of Gulf Stream Ocean Thermal Power Plants," University of Massachusetts, Amherst, Mass. 1975.

Kotsovinos, N.E., "A Study of the Entrainment and Turbulence in a Plane Buoyant Jet," Report No. KH-R-32, California Institute of Technology, Keck Laboratory, Pasadena, Calif., Aug., 1975.

Lavi, A., "Final Report: Solar Sea Power Project," Carnegie-Mellon University, Pittsburgh, Pa., Jan., 1975.

Liepmann, H.W. and Laufer, J., "Investigation of Free Turbulent Mixing," National Advisory Committee for Aeronautics, Technical Note 1257, 1947.

List, E.J. and Imberger, Jorg, "Turbulent Entrainment in Buoyant Jets and Plumes," ASCE Journal of the Hydraulics Division, Sept. 1973, pp. 1461-1474.

Lockheed Missiles and Space Company, Inc., "Ocean Thermal Energy Conversion - Power Plant Technical and Economic Feasibility," LMSC-D056566, Sunnyvale, Calif., Apr., 1975.

Mikhail, S. "Mixing of Coaxial Streams Inside a Closed Conduit," Journal of Mechanical Engineering Science, Vol. 2, 1960, pp. 59-68.

Morton, B.R., Taylor, G.I., Turner, J.S., "Turbulent Gravitational Convection from Maintained and Instantaneous Sources," Proceedings of the Royal Society, London, A234, 1956, pp. 1-23.

Rajaratnam, N., Turbulent Jets, 1st ed., Elsevier Scientific Publishing Company, New York, N.Y. 1976.

Reichardt, H., Gesetzmässigkeiten der Freien Turbulenz, VDI Forschung, 414, 1951.

Roberts, G.O., Piacsek, S.A., and Toomre, J., "Two Dimensional Numerical Model of the Near-Field Flow for an Ocean Thermal Power Plant. Part III. Simulation of the Lockheed Baseline Design," Naval Research Laboratory, Report No. NRL-GFD/OTEC 6-76, Dec. 1976.

Rouse, H., Yih, C., and Humphreys, H., "Gravitational Convection from a Boundary Source," Tellus, Vol. 4, pp. 200-210.

Sawyer, R.A., "The Flow due to a Two-Dimensional Jet Issuing Parallel to a Flat Plate," Journal of Fluid Mechanics, Vol. 9, 1960, pp. 543-560.

Sawyer, R.A., "Two-Dimensional Reattaching Jet Flows Including the Effects of Curvature on Entrainment," Journal of Fluid Mechanics, Vol. 17, 1963, pp. 481-498.

Schlichting, H., Boundary Layer Theory, Translated by J. Kesten, Sixth Edition, McGraw Hill Book Company, Inc., 1968.

Squire, H.B. and Trouncer, J., "Round Jets in a General Stream," Aeronautical Research Council, London, 1944.

Stolzenbach, K.D., and Harleman, D.R.F., "An Analytical and Experimental Investigation of Surface Discharges of Heated Water," Technical Report No. 135, M.I.T. R.M. Parsons Laboratory, Cambridge, Mass., Feb., 1971.

Stoy, R.L., Stenhouse, M., and Hsia, A., "Vortex Containment of Submerged Jet Discharge," ASCE Journal of the Hydraulics Division, Sept., 1973, pp. 1585-1597.

Tollmien, W., "Berechnung turbulenter Arbreitungsvargange," Z.A.M.M., 6:468-478, 1926, (English Translation, N.A.C.A. TM 1085, 1945).

TRW Systems Group, "Ocean Thermal Energy Program; Research on an Engineering Evaluation and Test Program," Contract No. NSF-C958, Redondo Beach, Calif., June, 1975.

Tuve, G.L., "Air Velocities in Ventilating Jets," Journal of Heating, Piping, and Air Conditioning, Jan., 1953, pp. 181-190.

Van der Hegge Zijnen, G.B., "Measurements of the Distribution of Heat and Matter in a Plane Turbulent Jet of Air," Journal of Applied Science Research, Vol. 7, 1957, pp. 256-292.

Vulis, L.A. and Leont'yeva, T.A., "Coflowing and Counterflowing Turbulent Jets," Izv. Akad. Nauk. Kaz. SSR, Ser. Energ., 9, 1955.

Weinstein, A.S., Osterle, J.F., and Forstall, W., "Momentum Diffusion from a Slot Jet into a Moving Secondary," Transactions of A.S.M.E., Journal of Applied Mechanics, Vol. 23, 1957, pp. 437-443.

Witze, P.O. and Dwyer, H.A., "The Turbulent Radial Jet," Journal of Fluid Mechanics, Vol. 75, June, 1976, pp. 401-417.

Wood, W.T., et al., Jet Trajectories Down Inclined Planes, Chemical Rubber Publishing Co., Pittsburgh, Pa., 1975.

Wood, I.R. and Webby, Grant, "The Effects of Boundaries Near Turbulent Plumes and Jets," Proceedings 2nd International Symposium on Stratified Flows, Norway Institute of Technology, June, 1980, pp. 128-137.

Wygnanski, I. and Fiedler, H., "Some Measurements in the Self Preserving Jet," Journal of Fluid Mechanics, Vol. 38, 1969, pp. 577-612.

Wygnanski, I. and Fiedler, H., "The Two-Dimensional Mixing Region," Journal of Fluid Mechanics, Vol. 41, 1970, pp. 327-361.

LIST OF SYMBOLS

A radial aspect ratio dimensionless number (eq. 2.9)

b mean jet boundary width

$b_{\frac{1}{2}}$ jet width where $\Delta V = \frac{1}{2} \Delta V_c$

b^* average jet width for spreading in an ambient flow (eq. 2.24)

B jet kinematic buoyancy flux (Table 3-6)

c_1 unsymmetrical entrainment constant (eq. 2.34)

c_2 jet impact constant (eq. 3.58)

c_3 jet impact constant (eq. 3.58)

c_p fluid thermal capacitance

D core width in zone of flow establishment

$f(\ )$ jet velocity profile similarity function

F densimetric Froude number (eq. 2.30)

$g(\ )$ jet temperature profile similarity function

G jet buoyant body force integral (Table 3-6)

H offset distance to boundary or plane of symmetry

I_1, I_2, J_1, J_2, K_1 integral jet profile constants (Table 2-2)

k dimensionless ratio of intake to discharge flow rates (eq. 3.2)

K molecular thermal conductivity

ℓ length of angled confining plane

ℓ_B jet buoyancy flux length scale

ℓ_H jet confinement length scale

ℓ_Q jet volume flux length scale

ℓ_r jet initial radius

L length of zone of flow establishment

$\mathbb{L}$ offset plane confinement dimensionless number (Table 2-9)

M   jet kinematic momentum flux

$\mathbb{M}$ confinement dimensionless number (eq. 2.27)

P   local pressure minus P_h

P_h hydrostatic pressure

P_d dynamic pressure

Q   jet volume flux (Table 3-6)

Q_r entrainment flow from remote boundary ambient region (eq. 3.47)

Q_i entrainment flow from impact boundary ambient region (eq. 3.47)

$\mathbb{Q}$ ambient velocity dimensionless number

r   radial coordinate

r_2 radius of jet curvature in a vertical plane

$\mathbb{R}$ initial radius dimensionless number (Table 2-9)

$\mathbb{R}_e$ jet Reynolds number (eq. 2.3)

T   temperature

u   velocity component in τ direction

U   horizontal velocity in remote boundary ambient region

v   velocity component in σ direction

V   time averaged jet axial velocity

V_e entrainment velocity

$\bar{V}$ average jet velocity for spreading in an ambient flow (eq. 2.24)

$\mathbb{V}$ external flow dimensionless number (eq. 2.23)

w   velocity component in θ direction

x   axial coordinate originating at jet port

x_r distance along confining plane to location of jet dividing stream-line

y	lateral coordinate from jet port
z	depth below free surface

Greek Letters

α	entrainment coefficient ($= V_e/\Delta V_c$)
β	vertical curvature constant ($= 1 + \tau/r_2$)
δ	length scale ratio (Table 3-1)
δ	surface boundary layer thickness (Chapter V)
ΔT	jet temperature difference above the ambient temperature
ΔV	jet velocity difference above the ambient velocity
$\Delta \rho$	jet density difference above the ambient density
ε	jet spreading rate ($db_{1/2}/dx$)
η	normalized lateral coordinate ($= y/b_{1/2}$ or $\tau/b_{1/2}$)
θ	horizontal angle in cylindrical coordinate system
κ	empirical constant for jet spreading in an ambient flow (eq. 2.25)
ν	fluid kinematic viscosity
ρ	fluid density
σ	local axial coordinate of jet
τ	local lateral coordinate of jet
ϕ	local vertical angle coordinate of jet
Φ	viscosity generated heat

Superscripts

*	circular jet value (Chapter II)
*	scale value of variable (Chapter III)
'	value for plane jet geometry

'   turbulent fluctuating component (Chapter III)

°,°°   normalized variable

Subscripts

B   value for buoyant jets

c   value at jet centerline

ent   value for entrainment flow

f   jet value at the end of its trajectory

horiz   value of horizontal component

i   value for impact boundary ambient region

ℓ local jet value

max   maximum value of variable

NB   value for nonbuoyant jets

o   value at jet discharge port

r   value for remote boundary ambient region

T   value for jet temperature profile

σ value of local axial component

τ value of local lateral component

∞ value at an infinite distance from the jet port

206

Appendix I

	Measurement	Model Prediction
T_a	15.8°C	--
ΔT_a	-1.1°C	-1.0°C
T_d	7.5°C	--
T_i	12.6°C	12.6°C

I-2

209
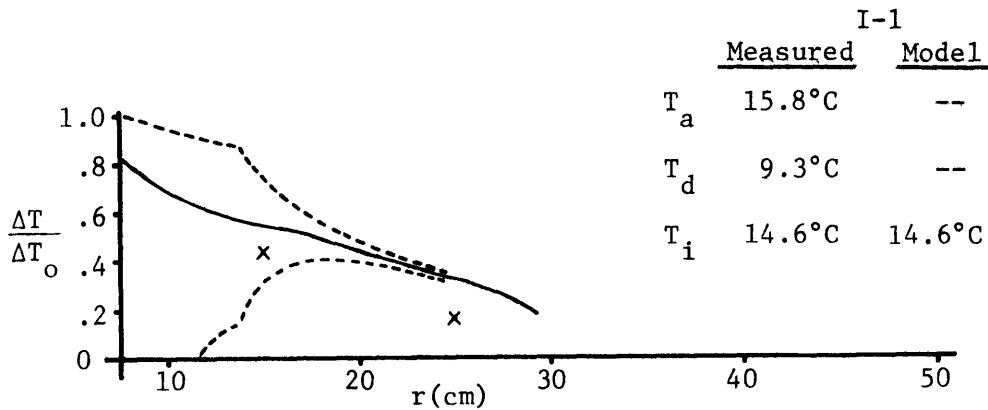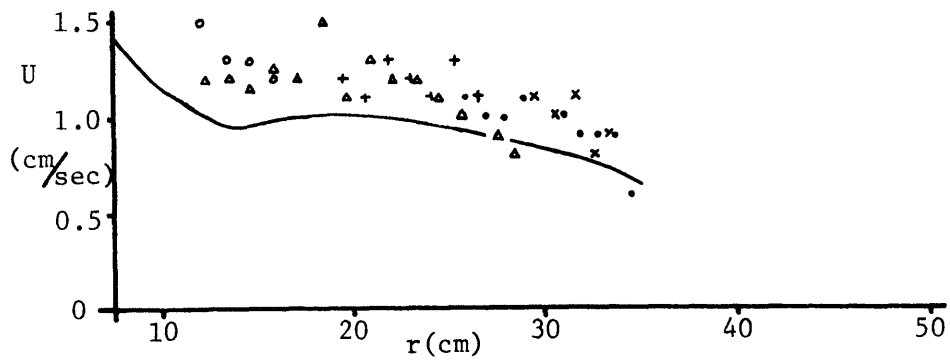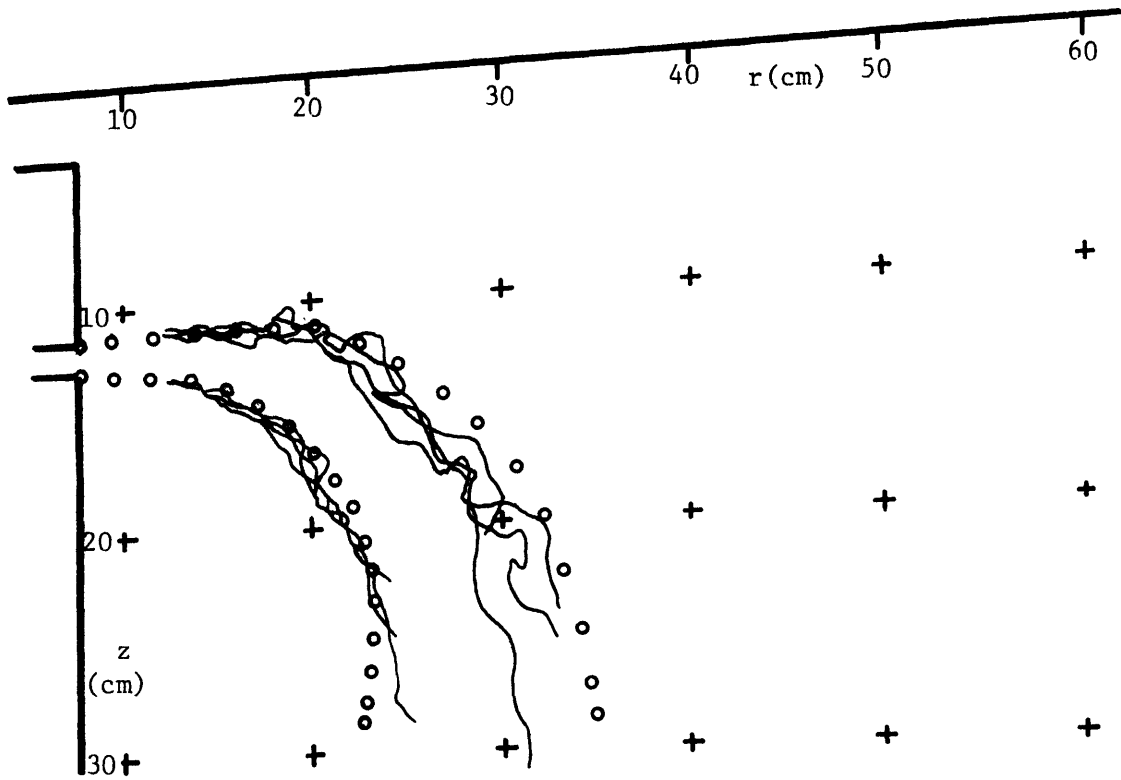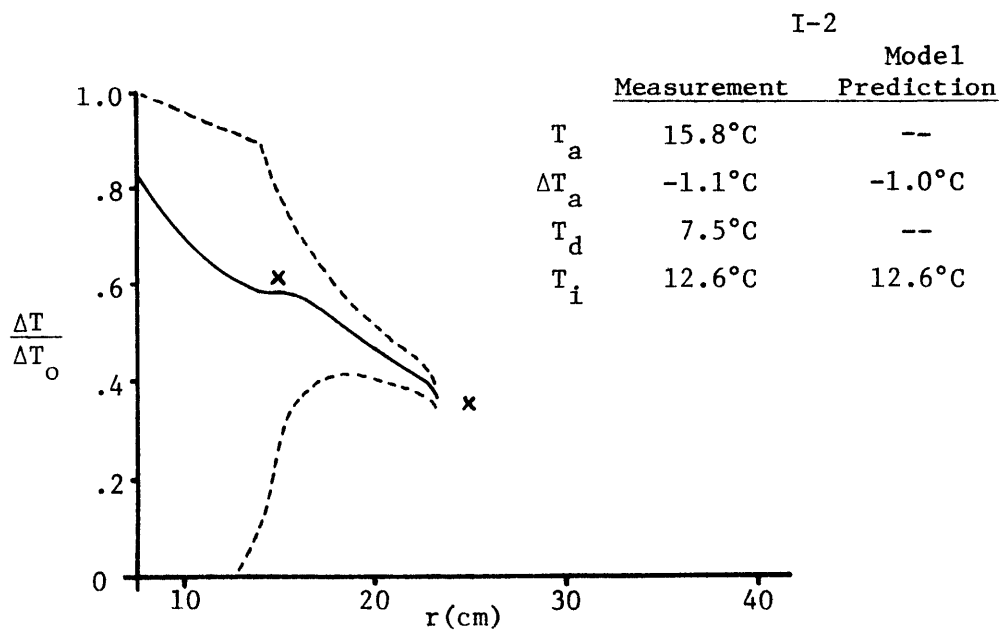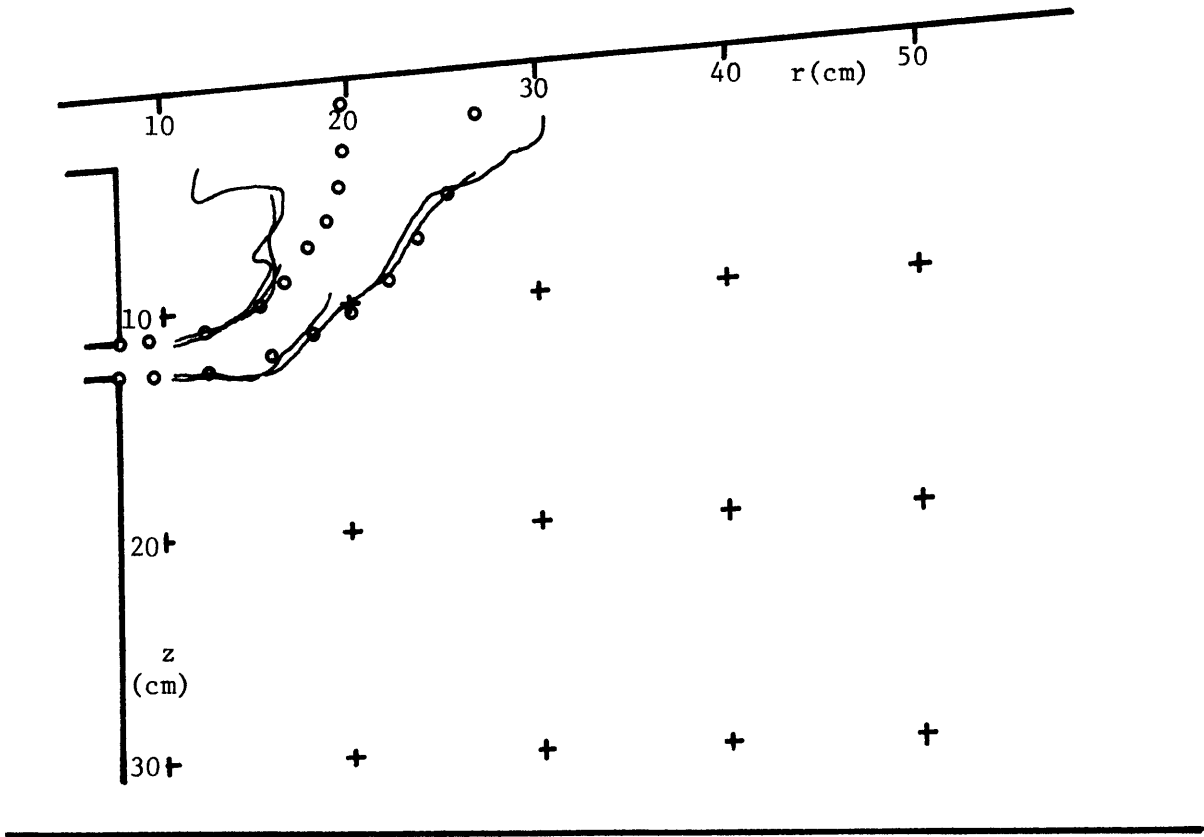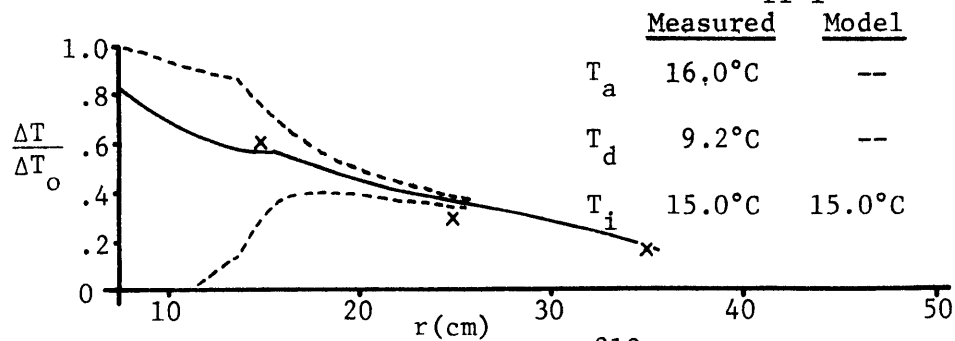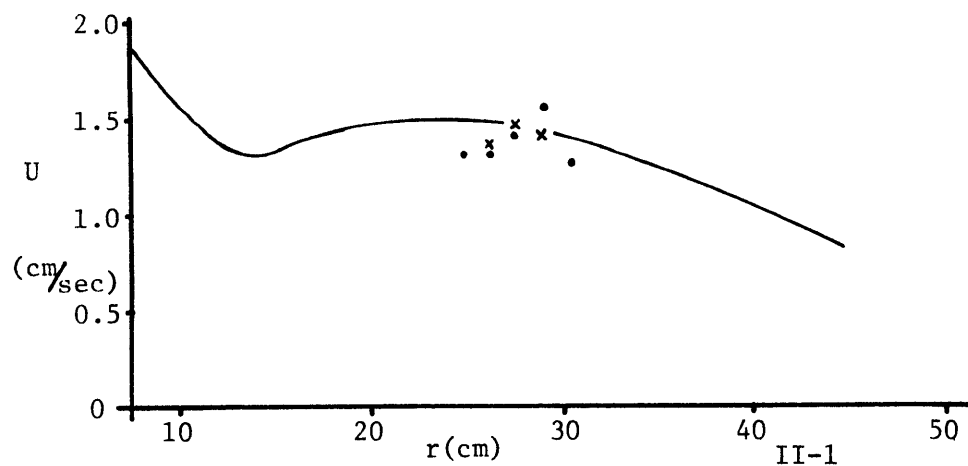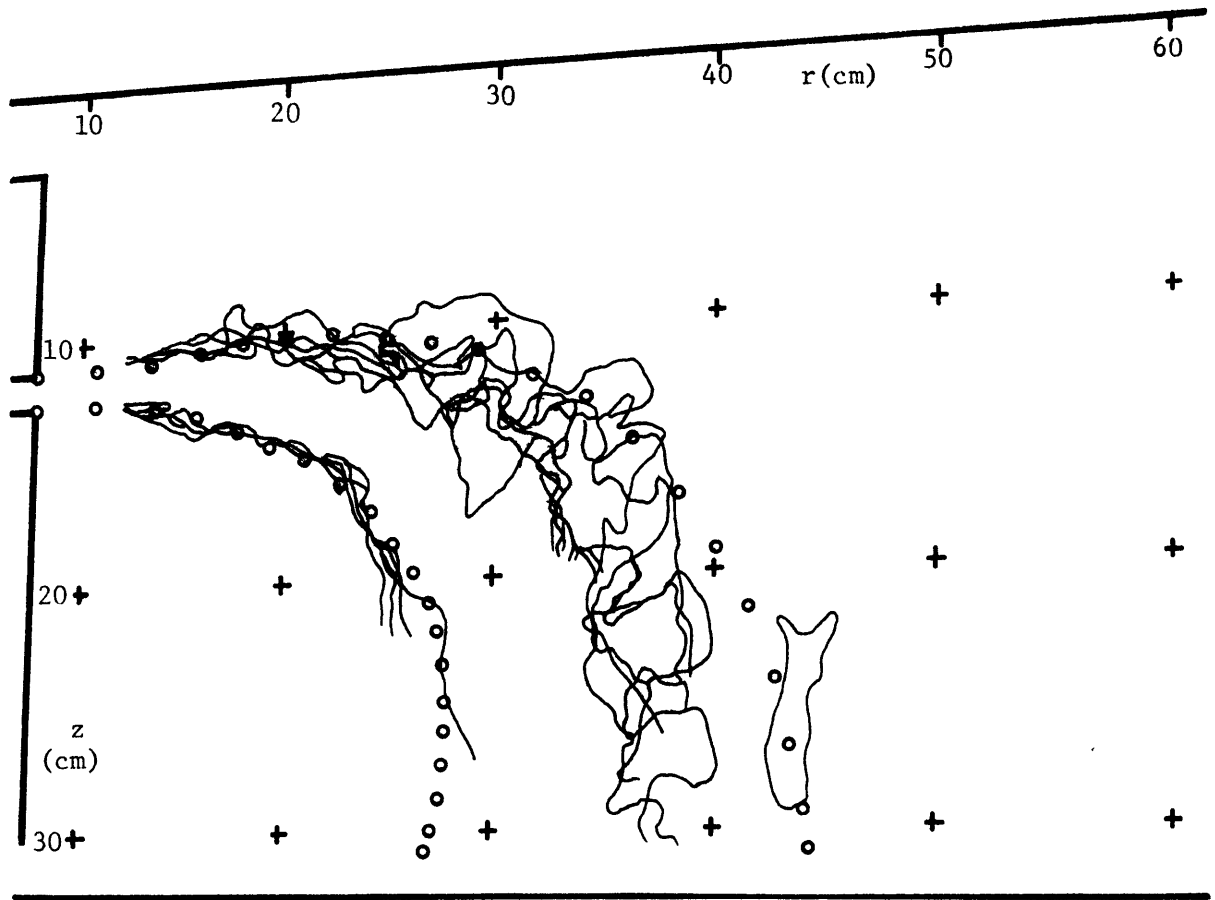
	Measured	Model
T_a	16.0°C	--
T_d	9.2°C	--
T_i	15.0°C	15.0°C

II-1

II-2
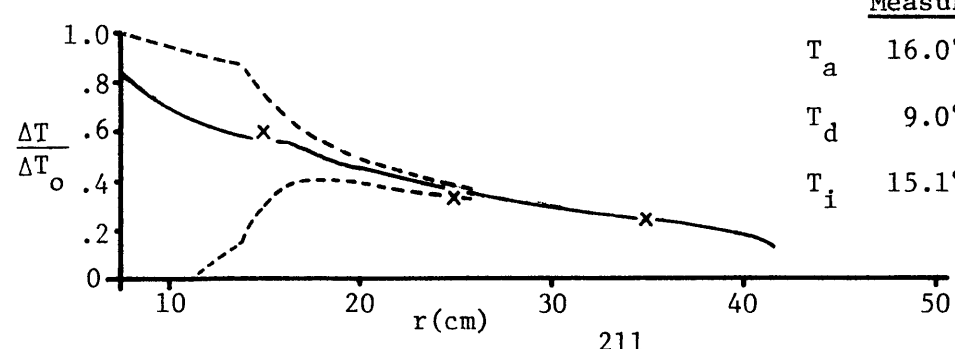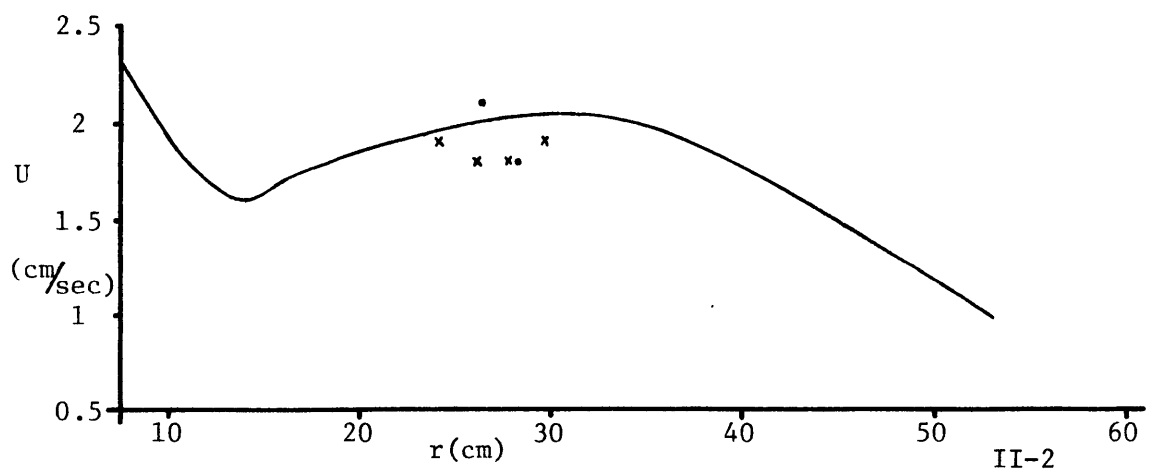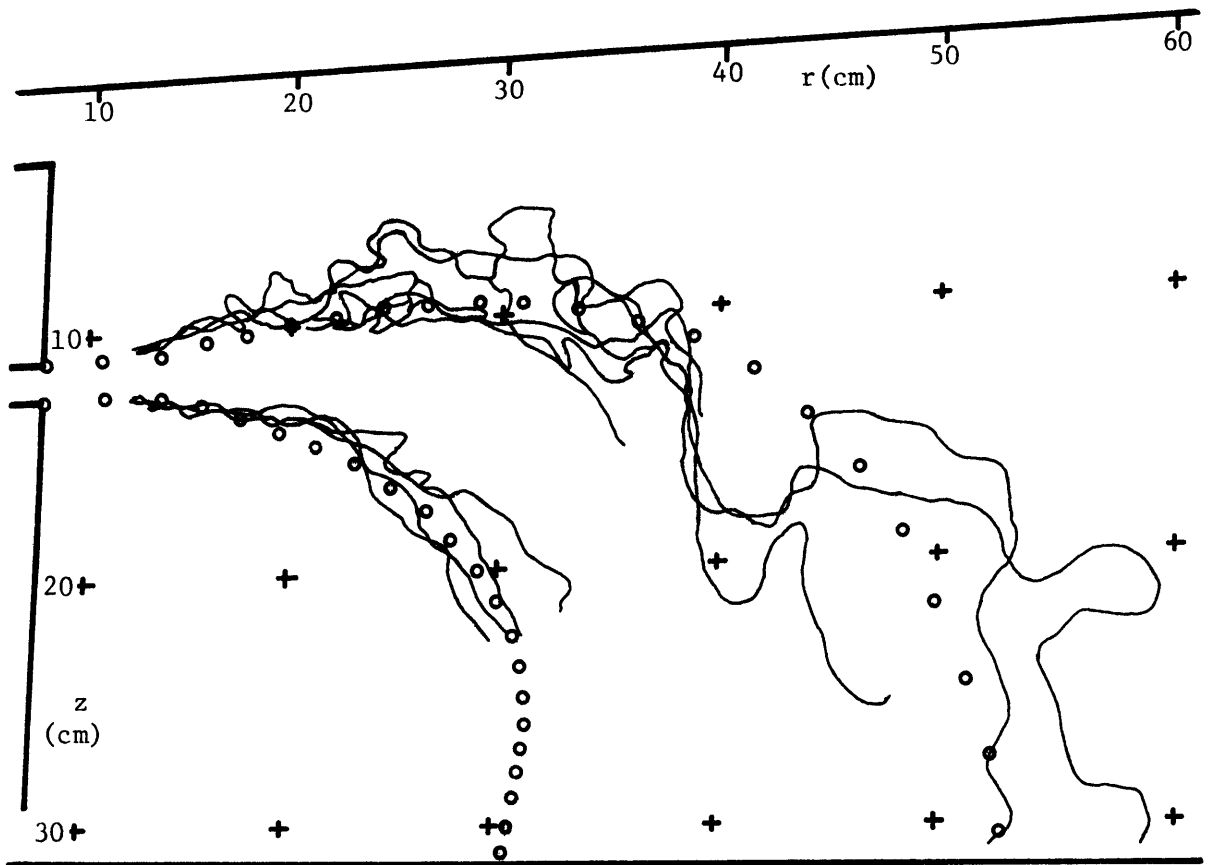
	Measured	Model
T_a	16.0°C	—
T_d	9.0°C	—
T_i	15.1°C	15.1°C

	Measurement	Model Prediction
T_a	16.0°C	--
ΔT_a	-1.4°C	-1.0
T_d	8.1°C	--
T_i	12.6°C	12.6°C

II-3

212

	Measured	Model
T_a	14.2°C	--
T_d	7,4°C	--
T_i	13.3°C	13.2°C

III-1
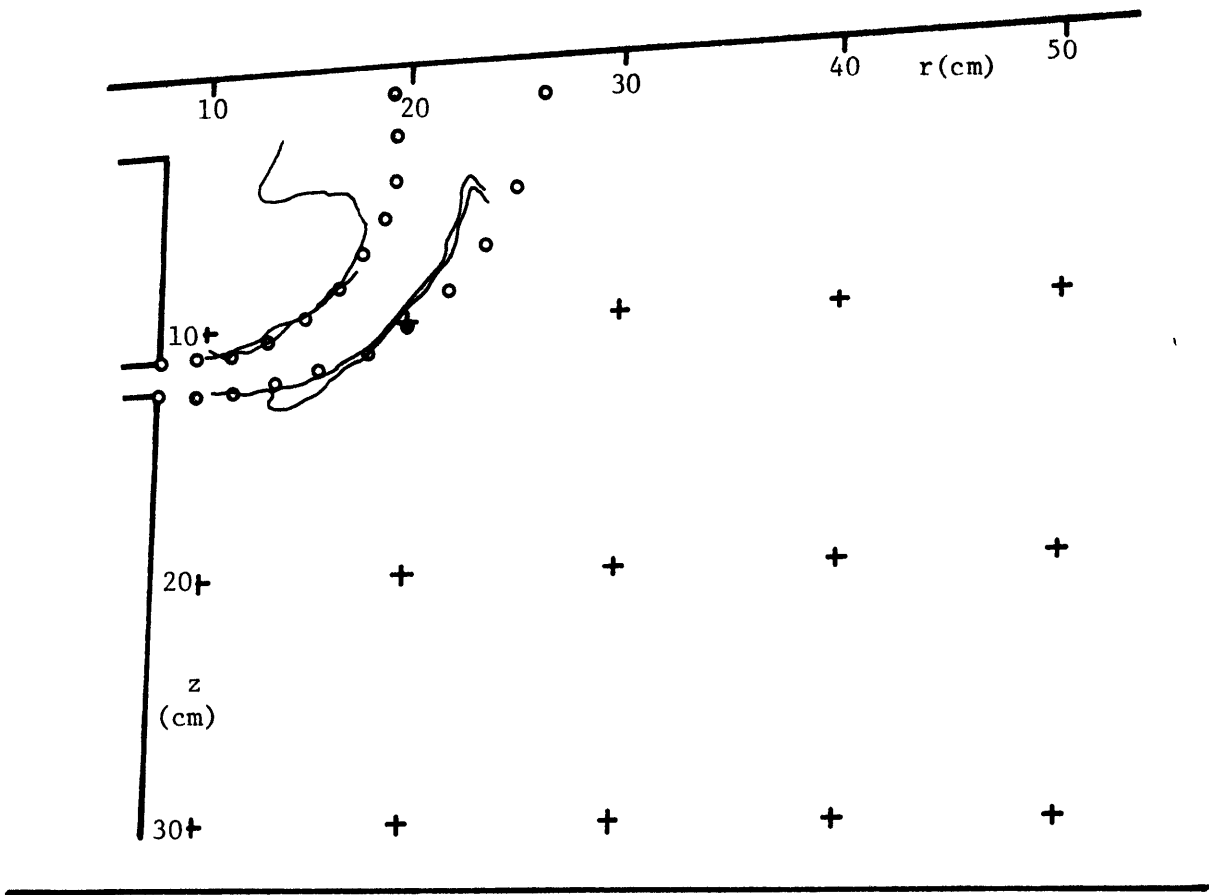
213
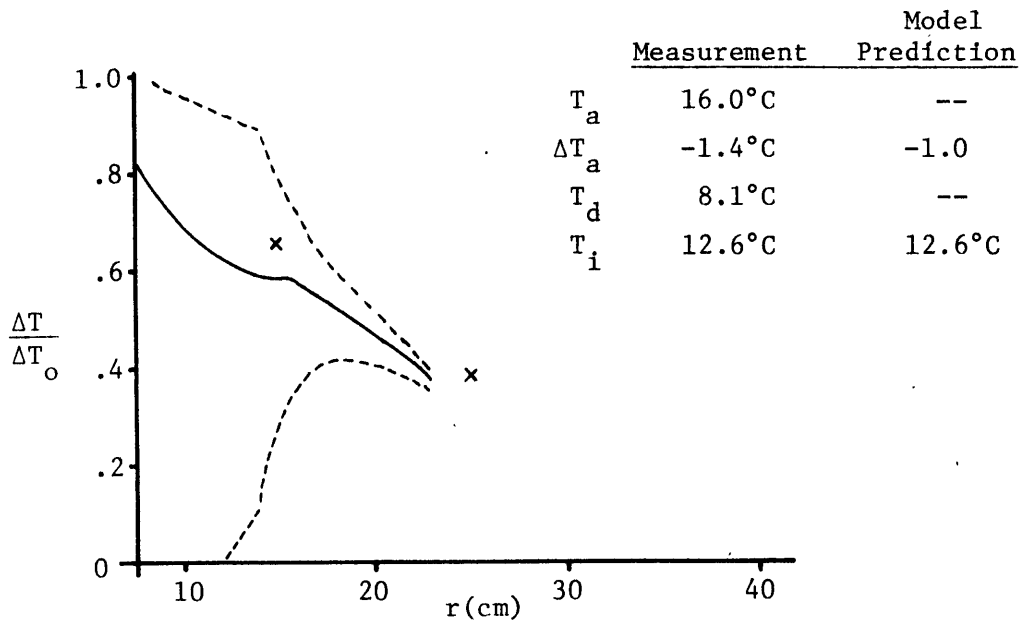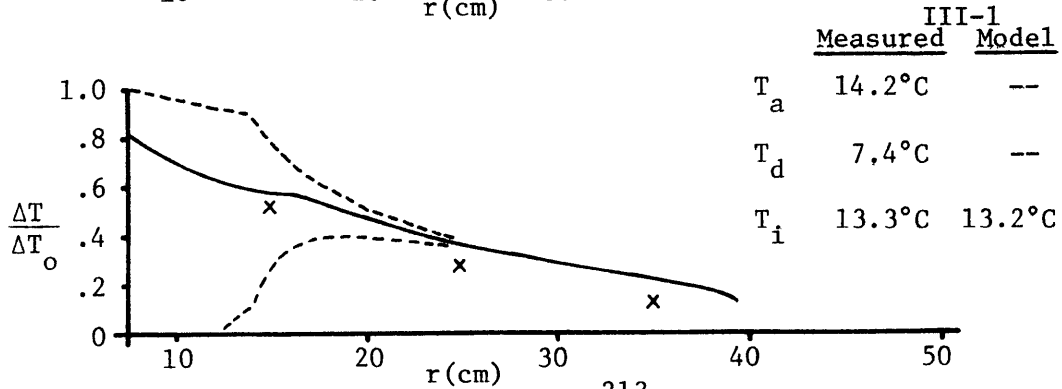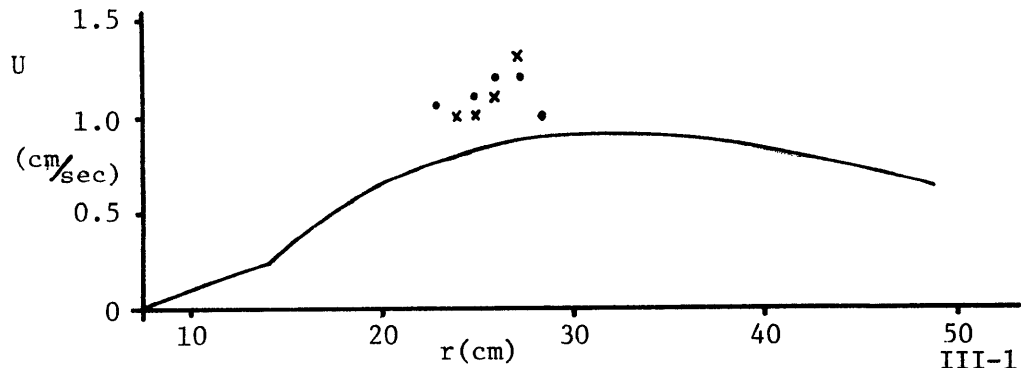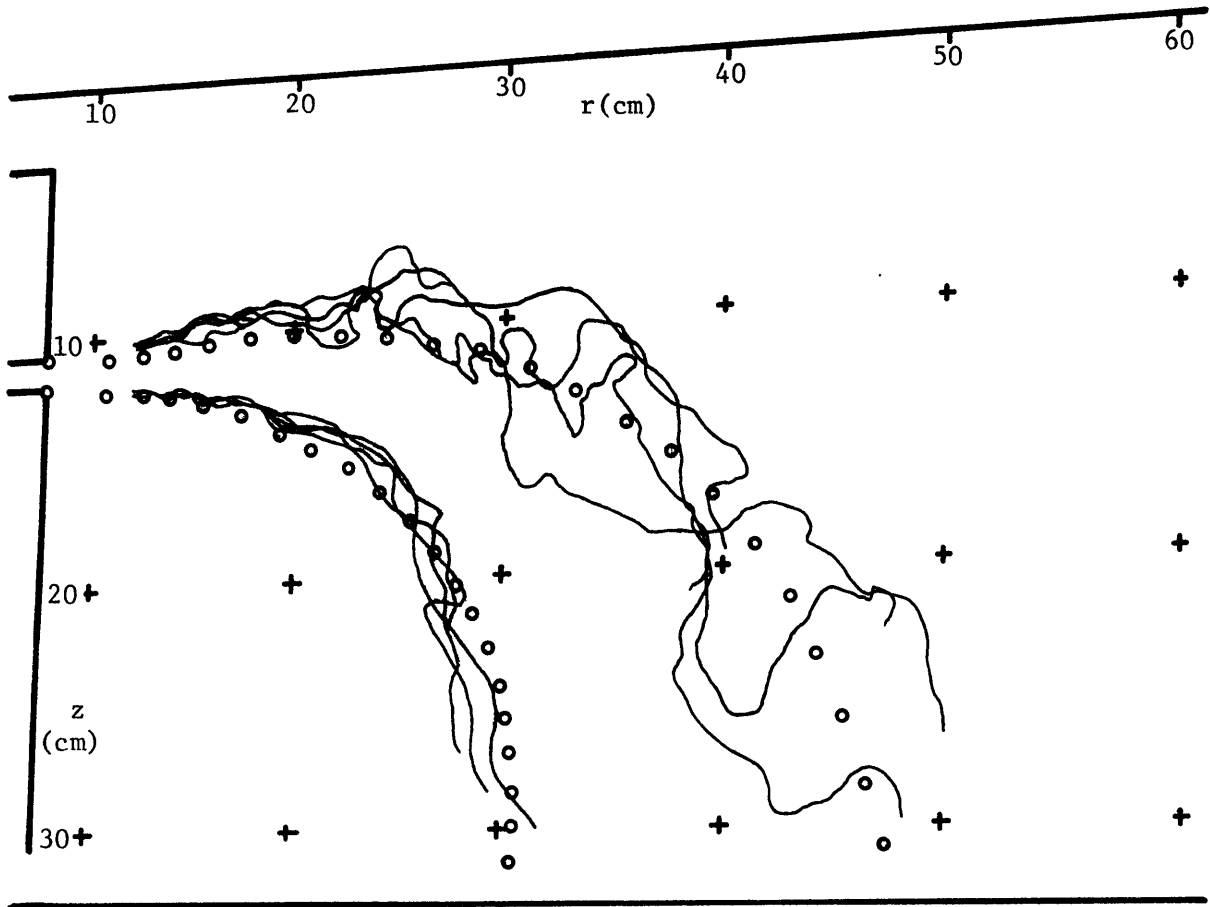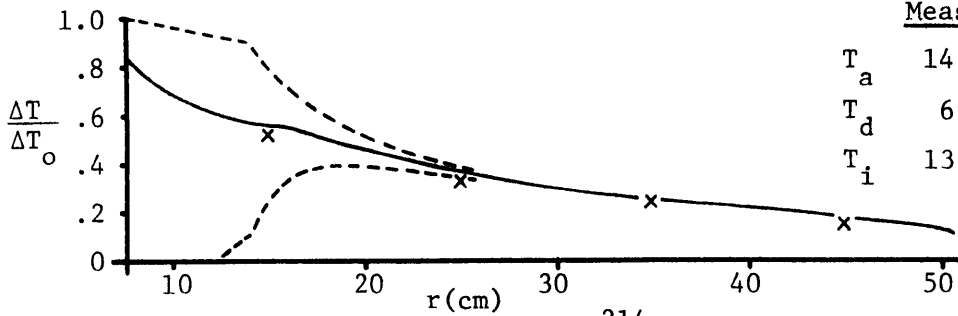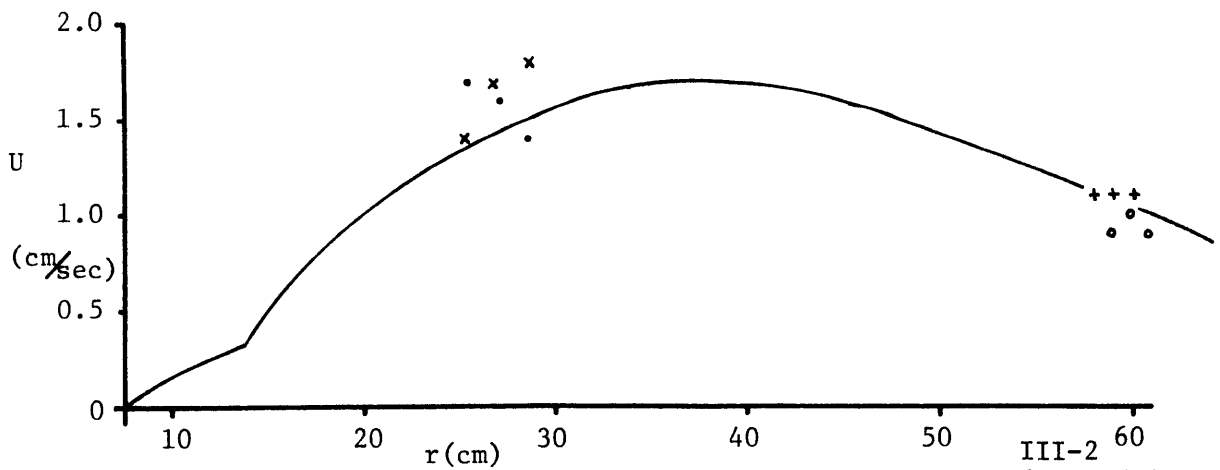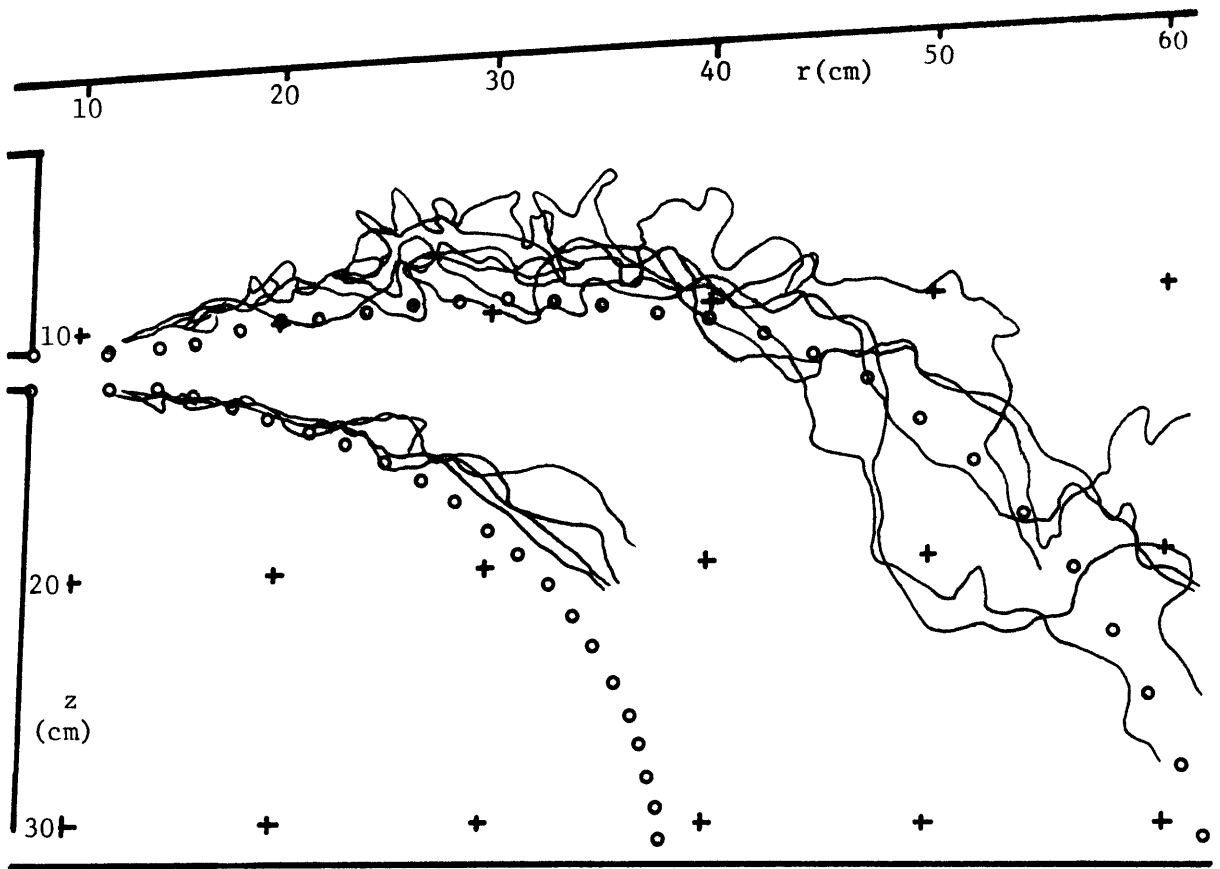
	Measured	Model
T_a	14.2°C	--
T_d	6.9°C	--
T_i	13.3°C	13.3°C

III-2

214

	Measurement	Model Prediction
T_a	14.2°C	––
ΔT_a	–0.9°C	–0.9°C
T_d	6.6°C	––
T_i	11.7°C	11.7°C

III-3

215

r(cm)

60

50

40

30

r(cm)

20

10

z
(cm)

10

20

30

U

1.5

1.0

(cm/sec)

0.5

0

10   20   30   40   50

r(cm)
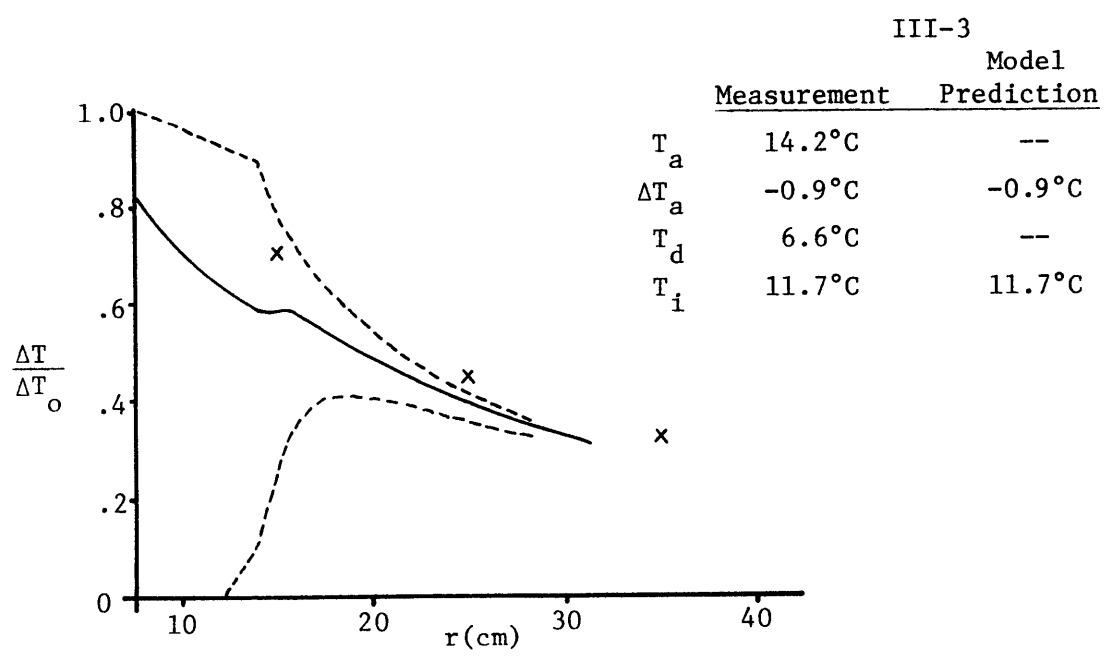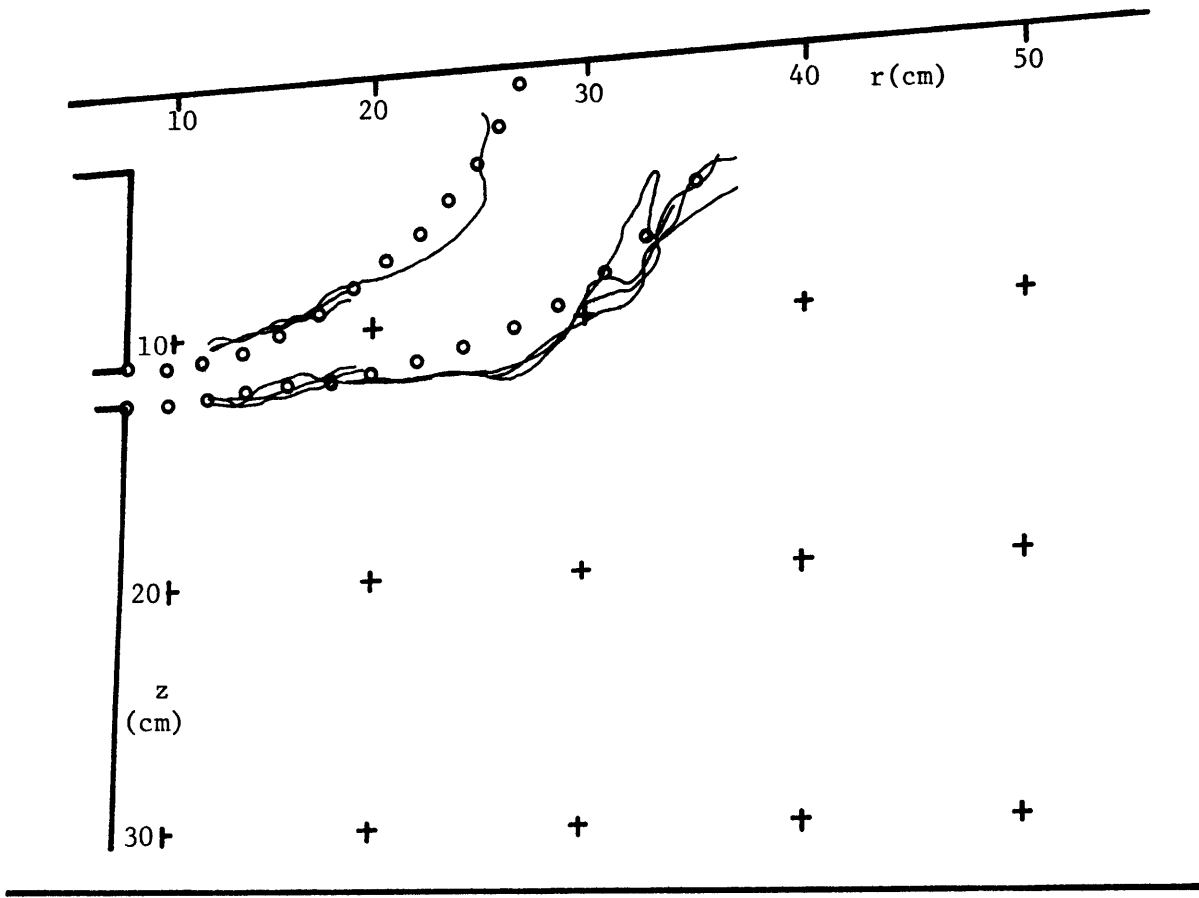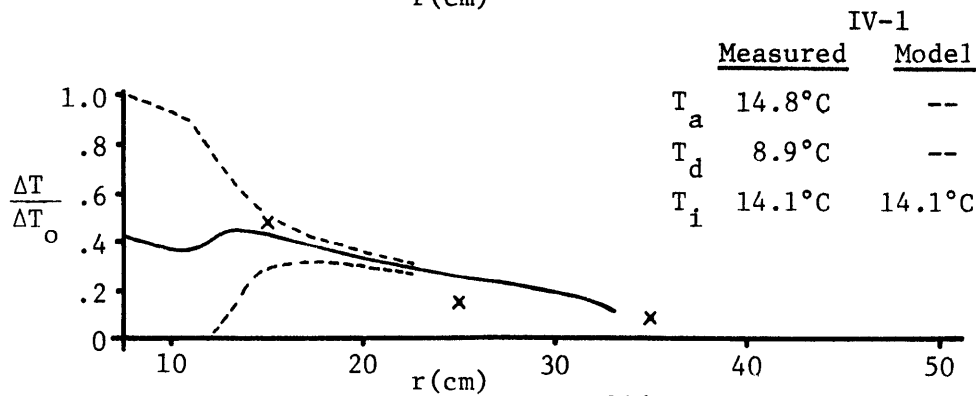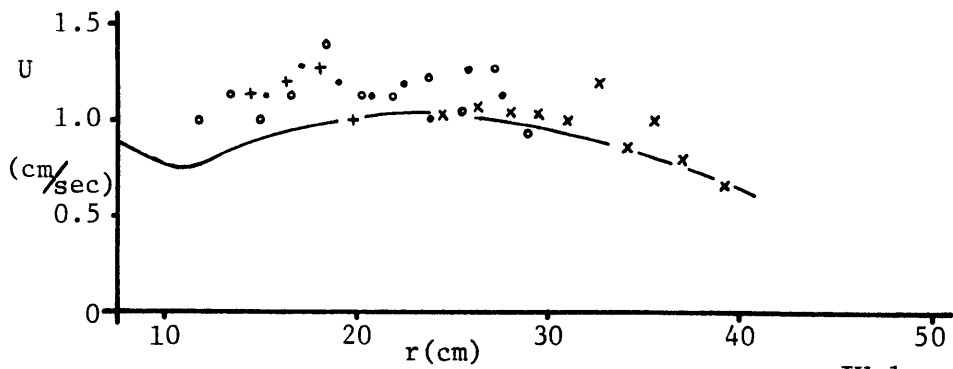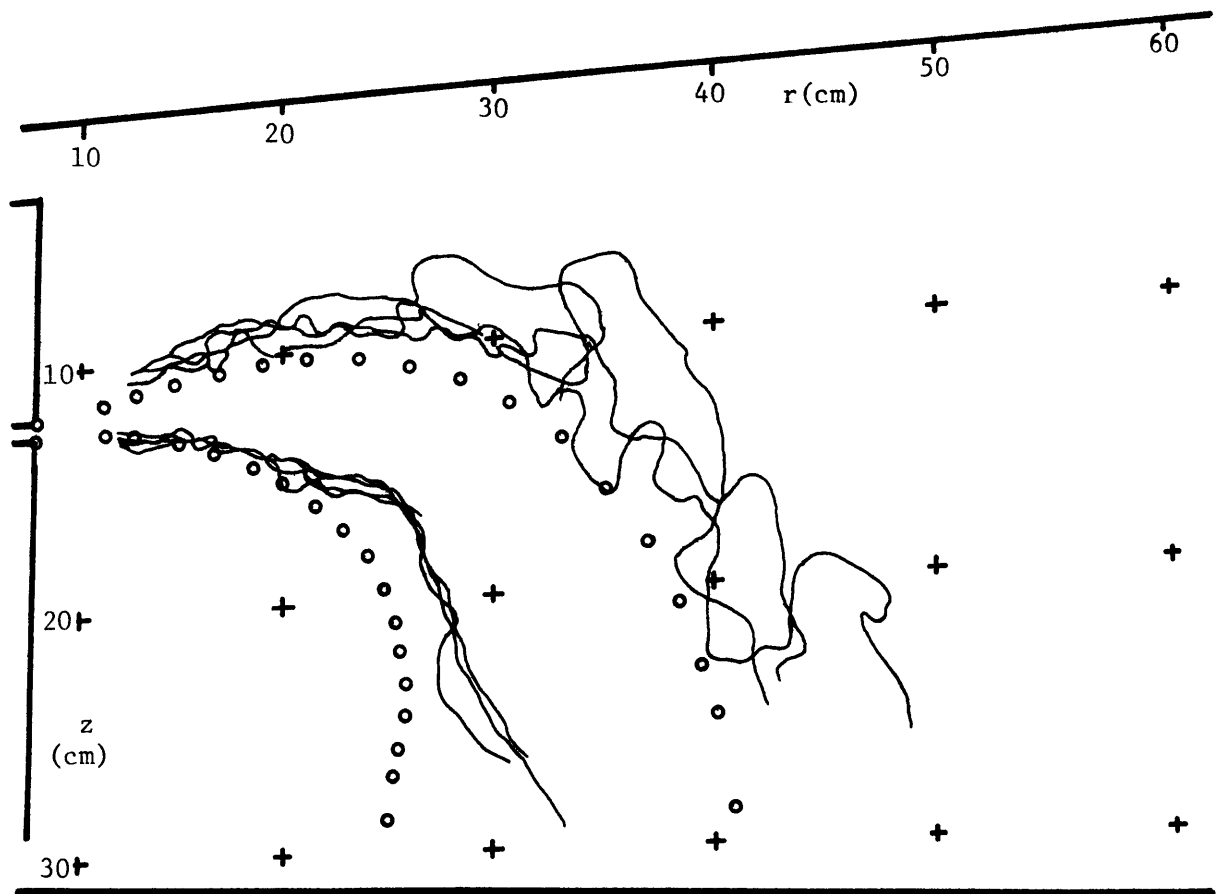
IV-1

	Measured	Model
T_a	14.8°C	--
T_d	8.9°C	--
T_i	14.1°C	14.1°C

$\dfrac{\Delta T}{\Delta T_o}$

1.0
.8
.6
.4
.2

10   20   30   40   50

r(cm)

216
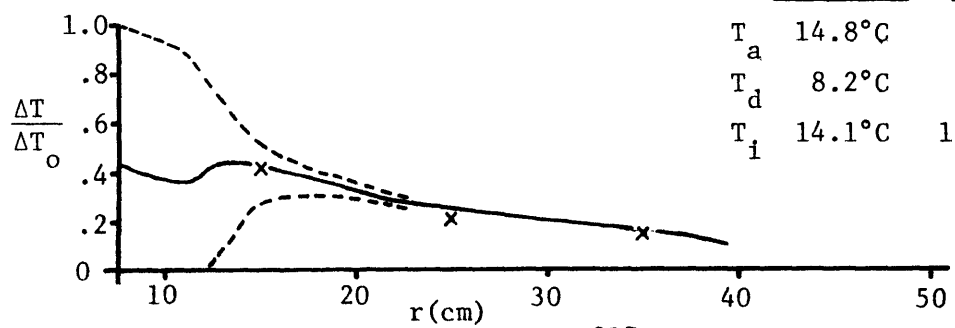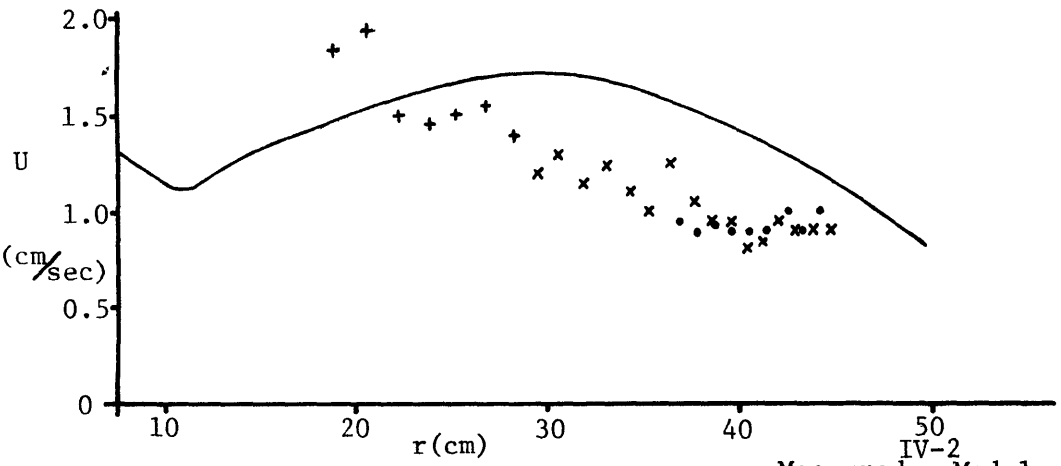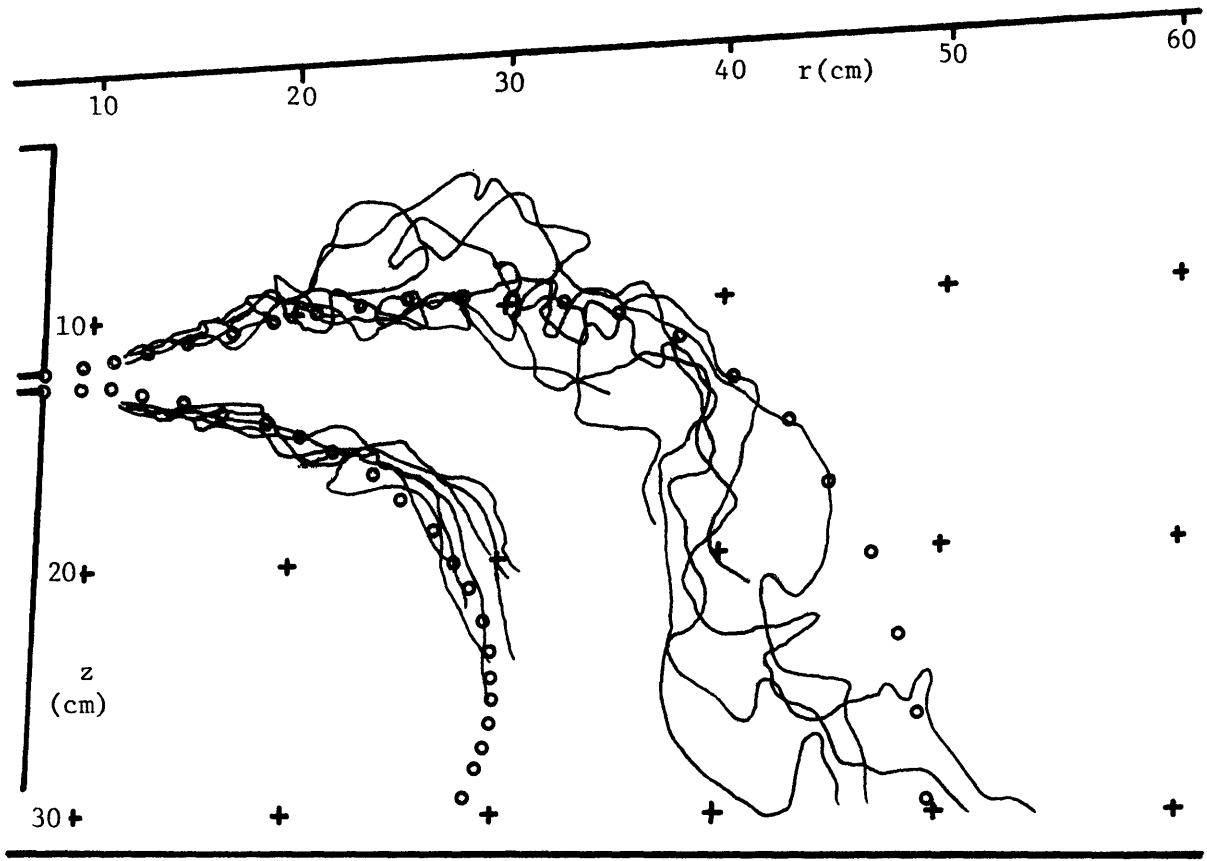
	Measured	Model
T_a	14.8°C	—
T_d	8.2°C	—
T_i	14.1°C	14.1°C

IV-2

217

IV-3

	Measurement	Model Prediction
T_a	14.8°C	--
ΔT_a	-0.5°C	-0.6°C
T_d	8.3°C	--
T_i	13.2°C	13.1°C

	Measured	Model
T_a	15.2°C	--
T_d	7.7°C	--
T_i	14.5°C	14.5°C

V-2

	Measurement	Model Prediction
T_a	15.2°C	--
ΔT_a	-0.6°C	-0.7°C
T_d	7.3°C	--
T_i	13.4°C	13.3°C

V-3

221

XIII-1

	Measured	Model
T_a	13.0°C	— —
T_d	5.3°C	—
T_i	11.6°C	11.6°C

222

	XIII-2	
	Measured	Model
T_a	13.0°C	—
T_d	5.8°C	—
T_i	11.8°C	11.9°C

XIII-3

	Measurement	Model Prediction
T_a	13.0°C	--
ΔT_a	-0.8°C	-0.7°C
T_d	5.3°C	--
T_i	10.35°C	10.30°C
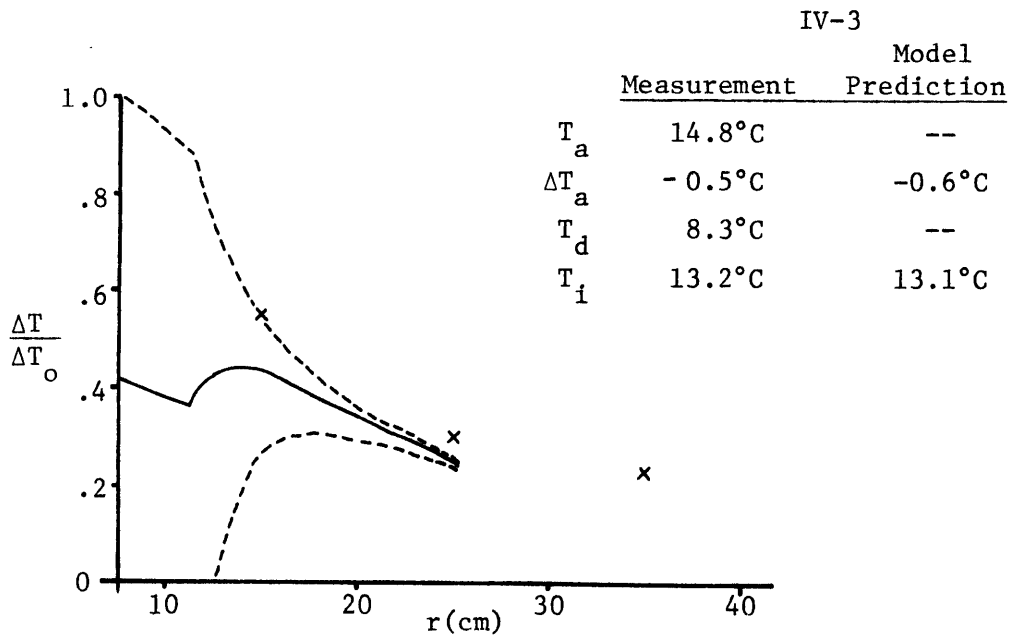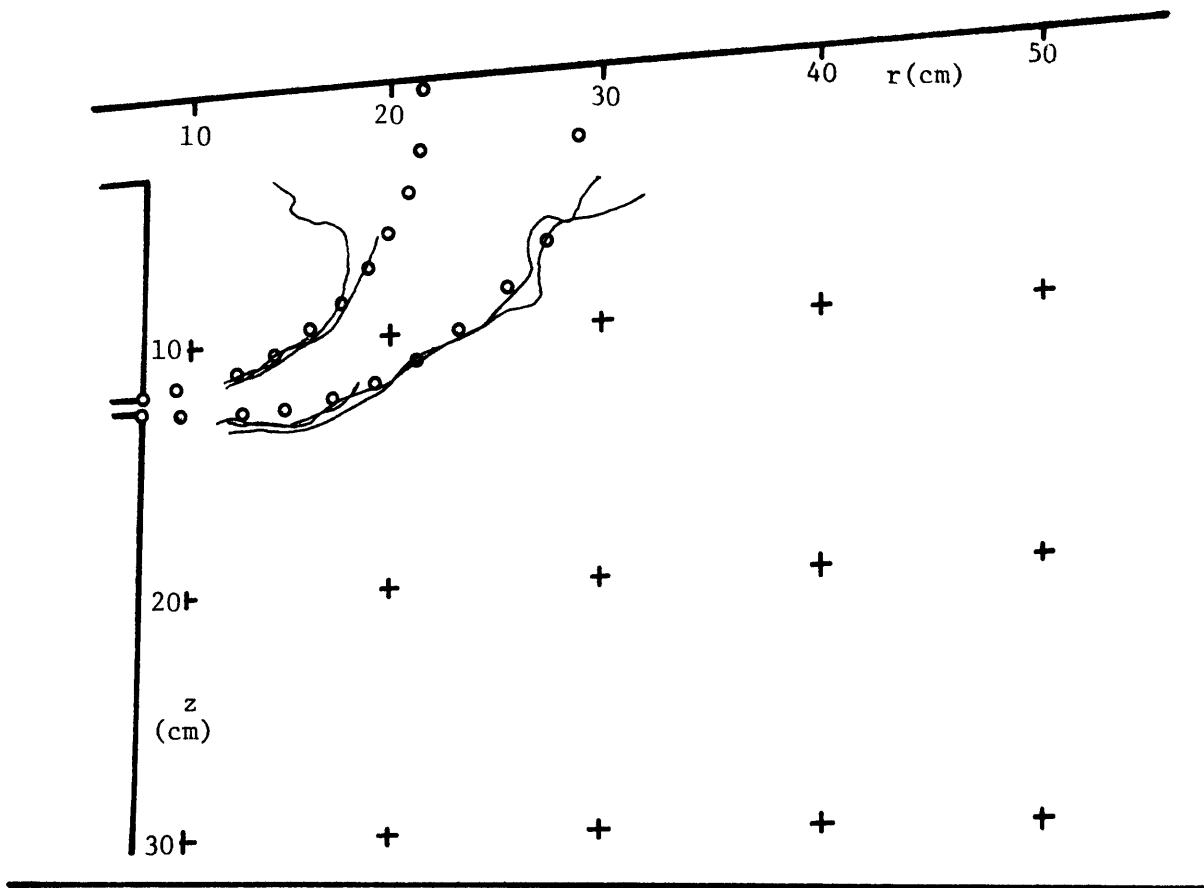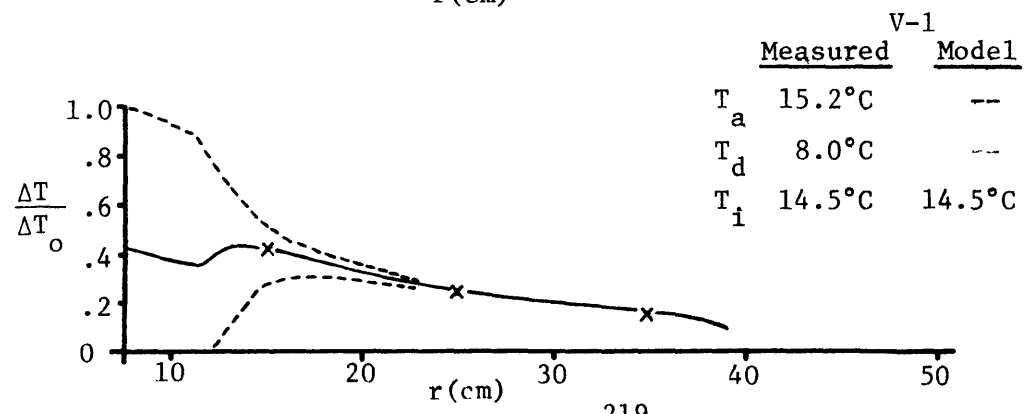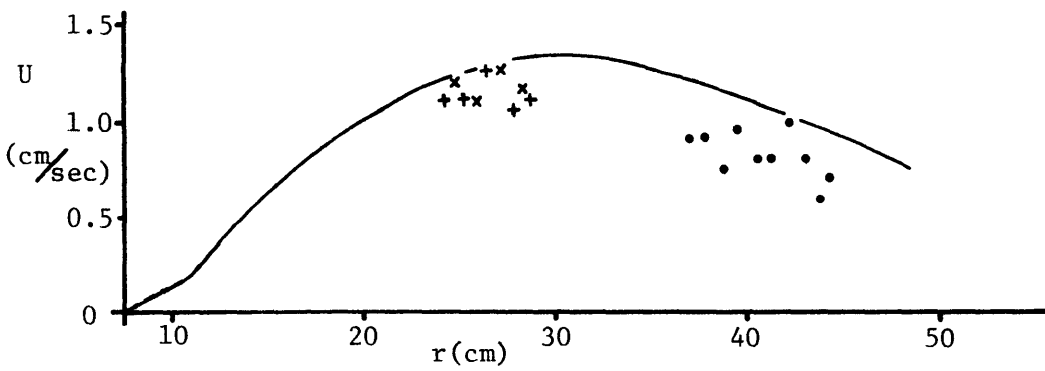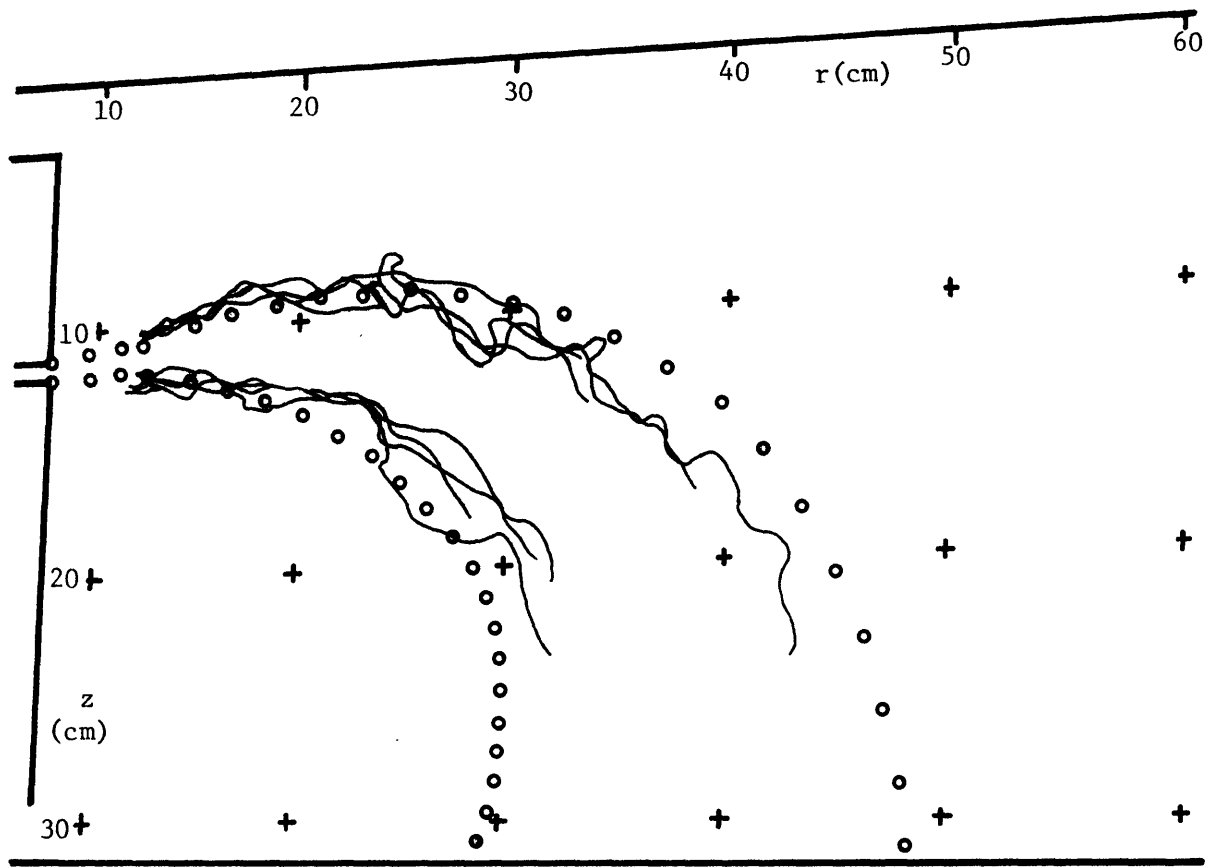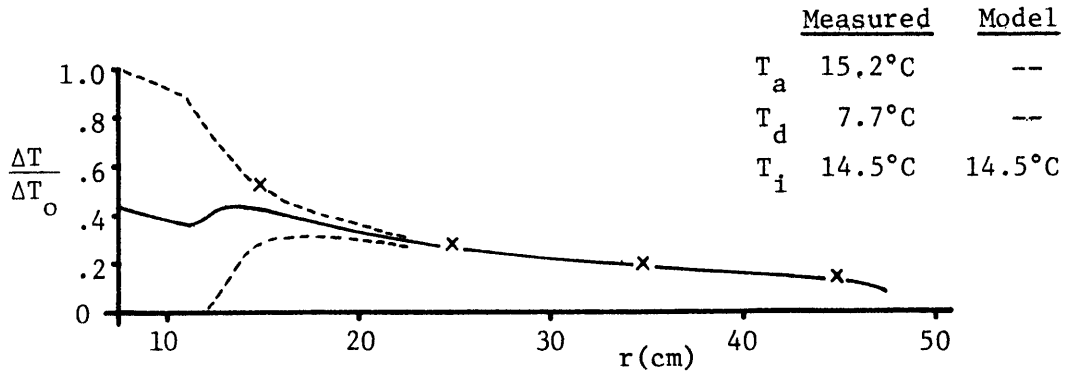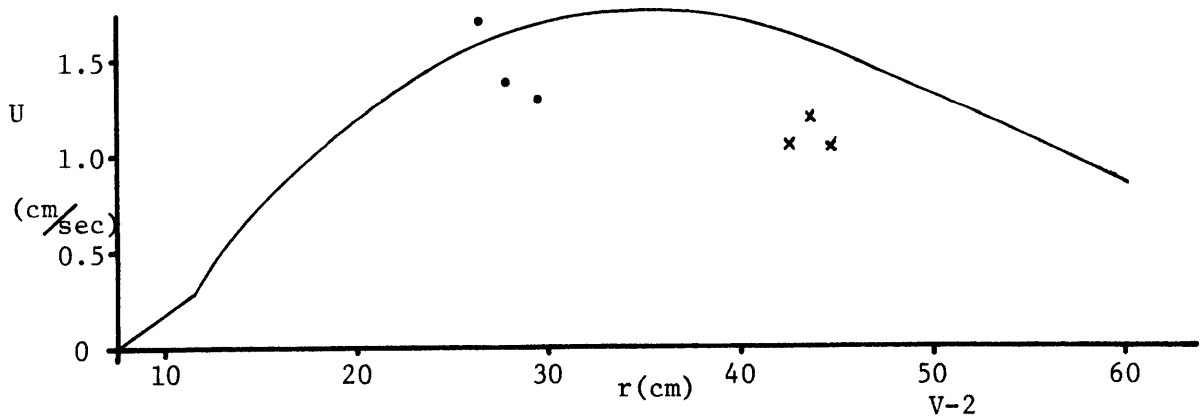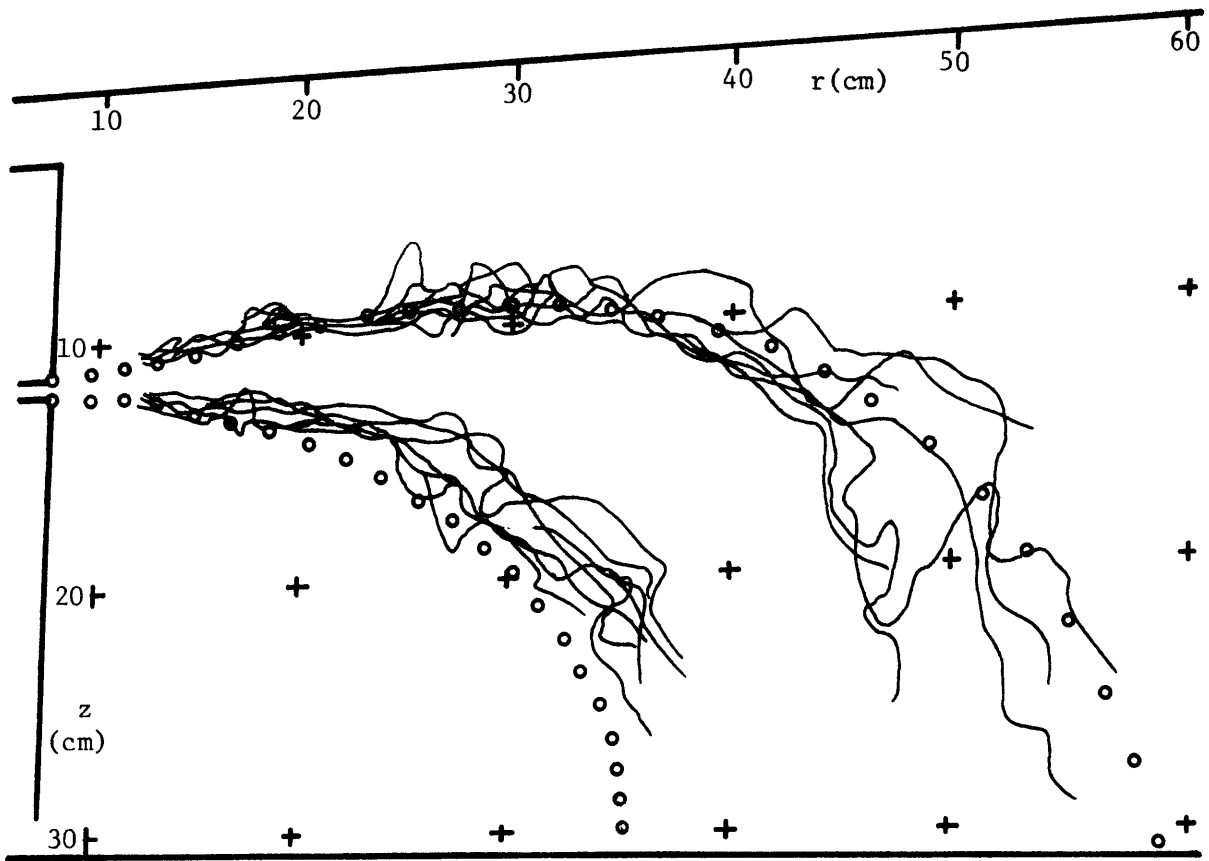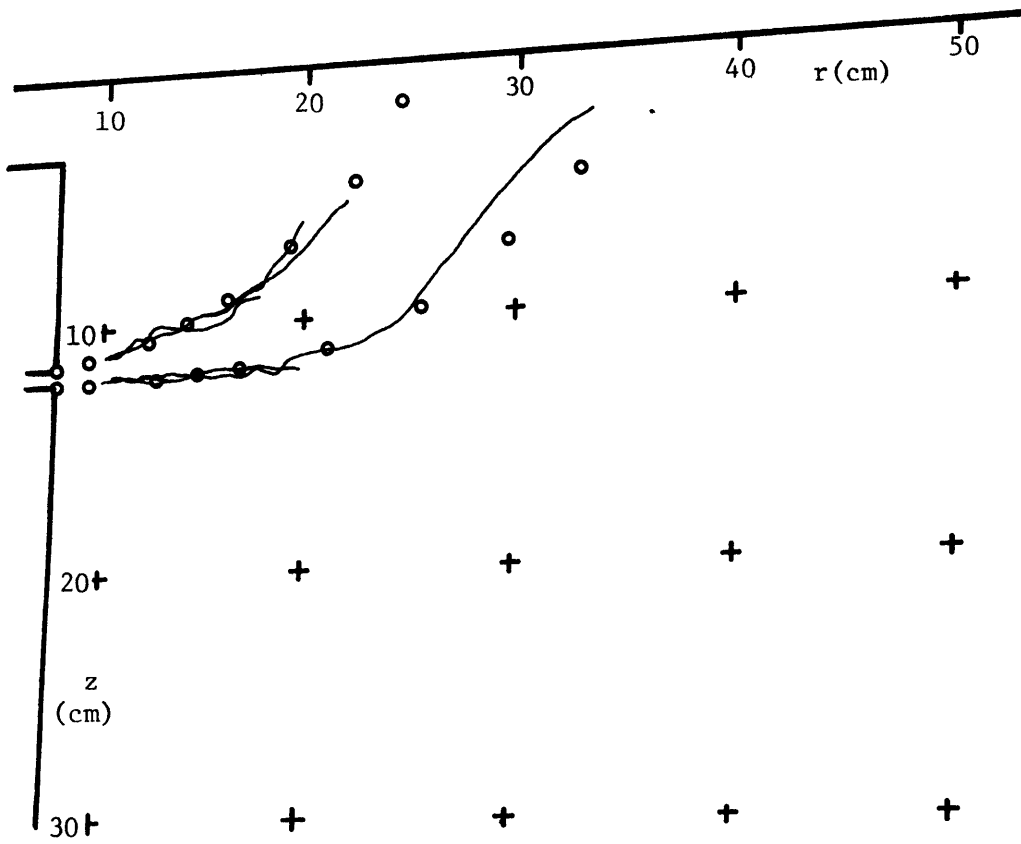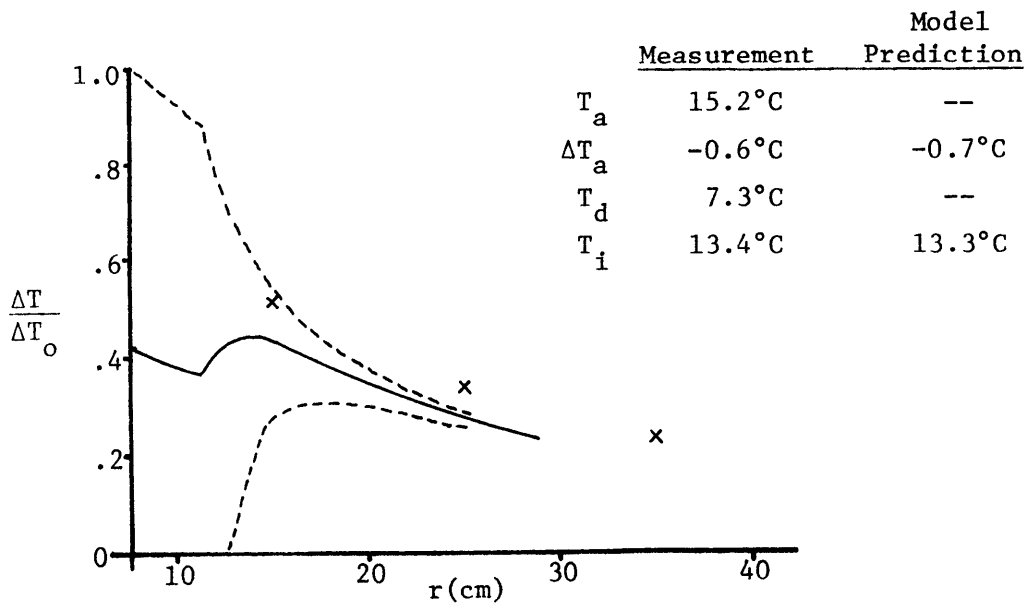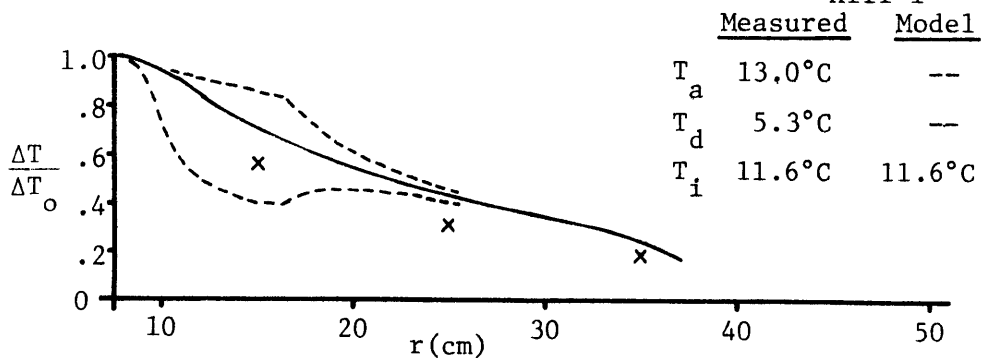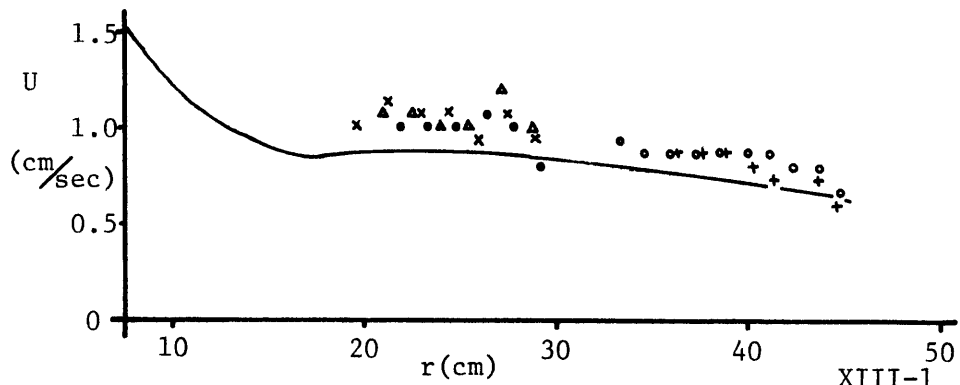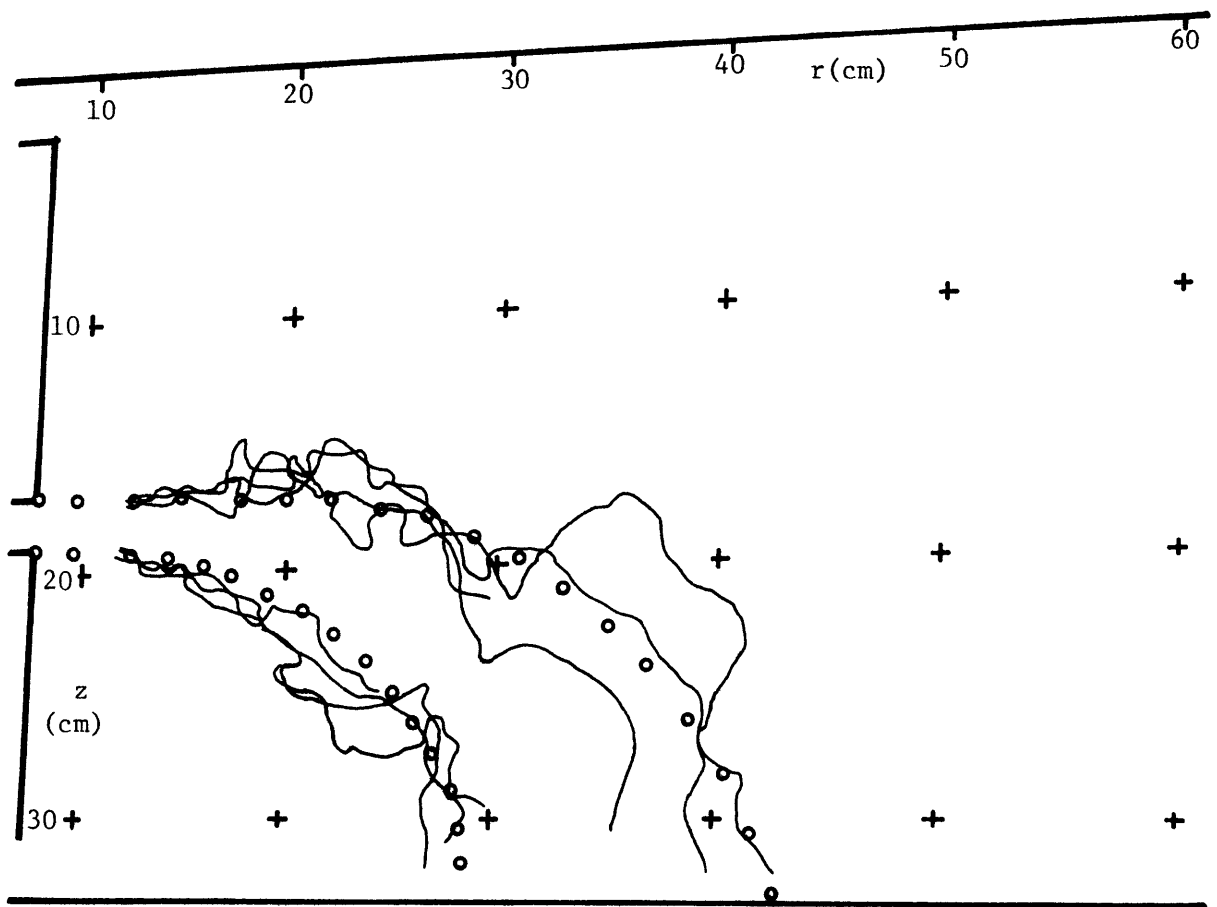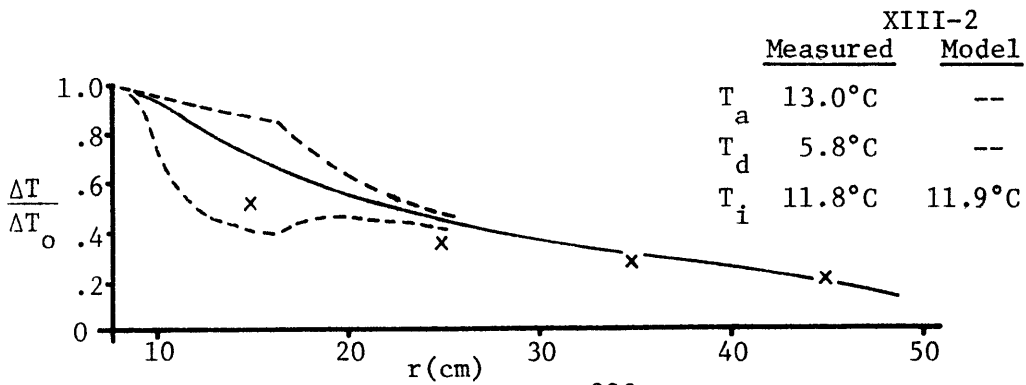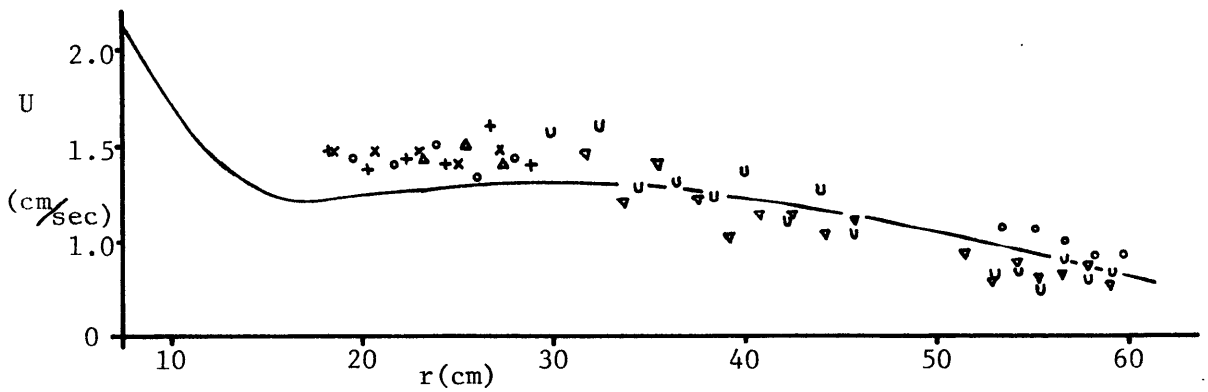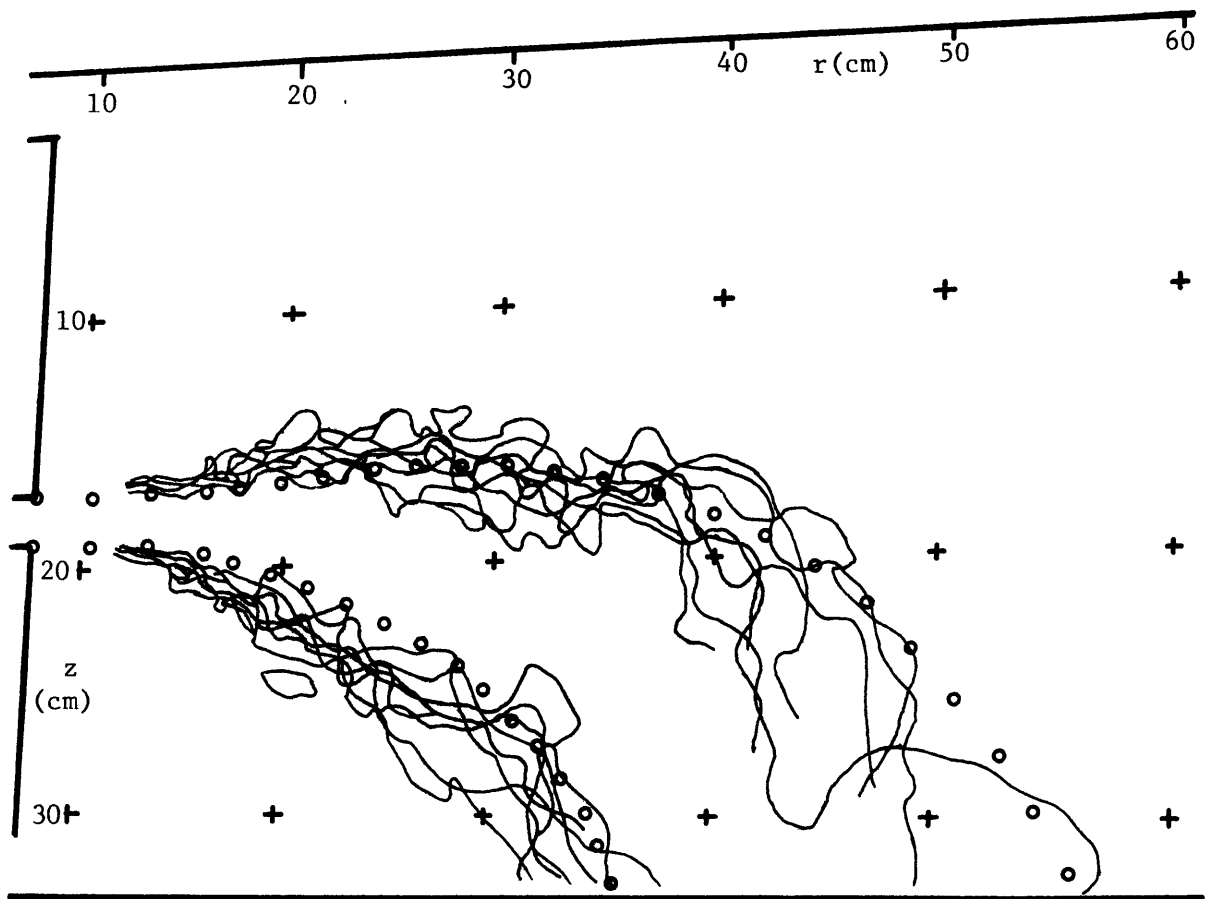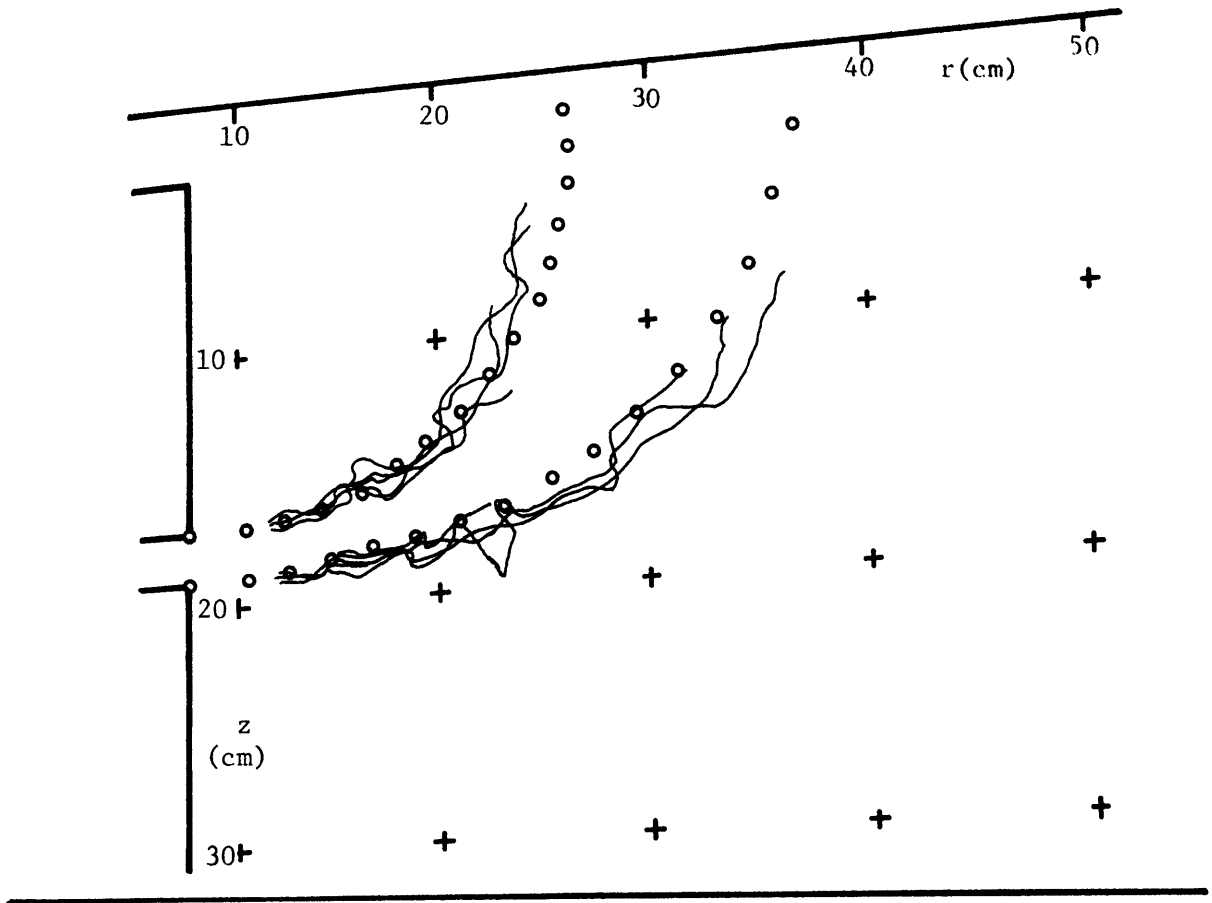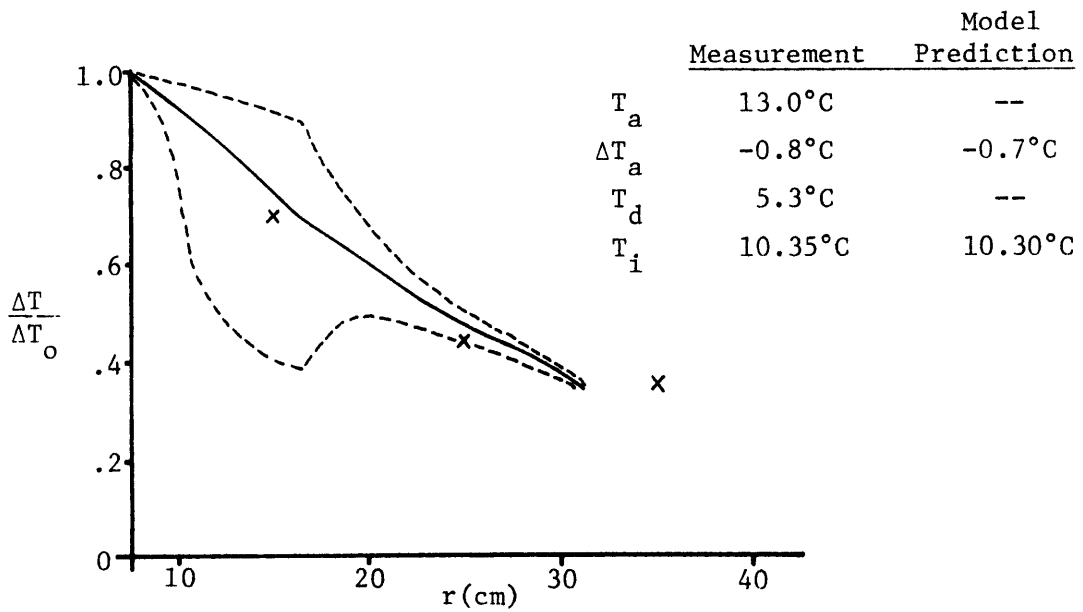
Appendix II
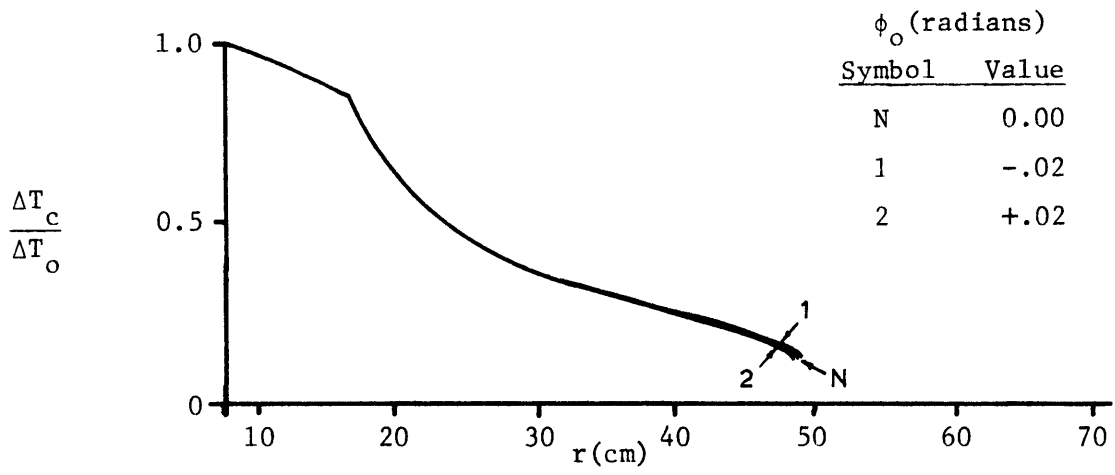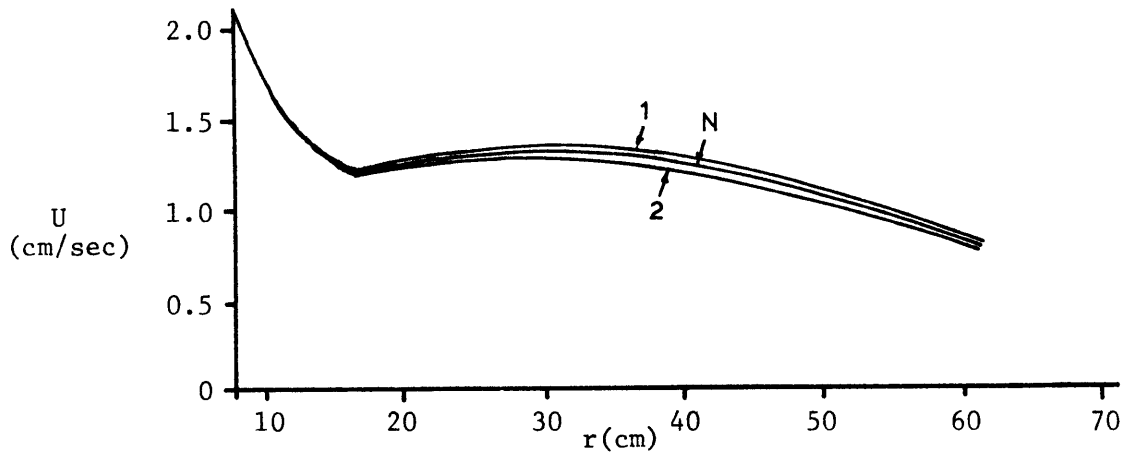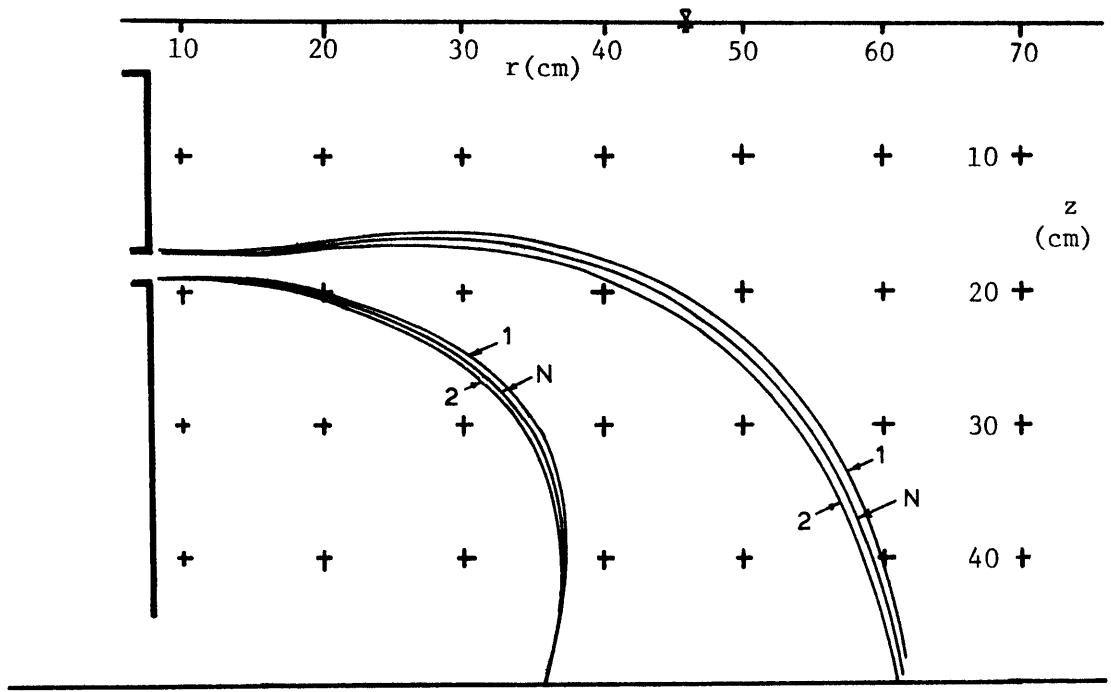
ϕ_o Sensitivity for Experiment XIII-2

226
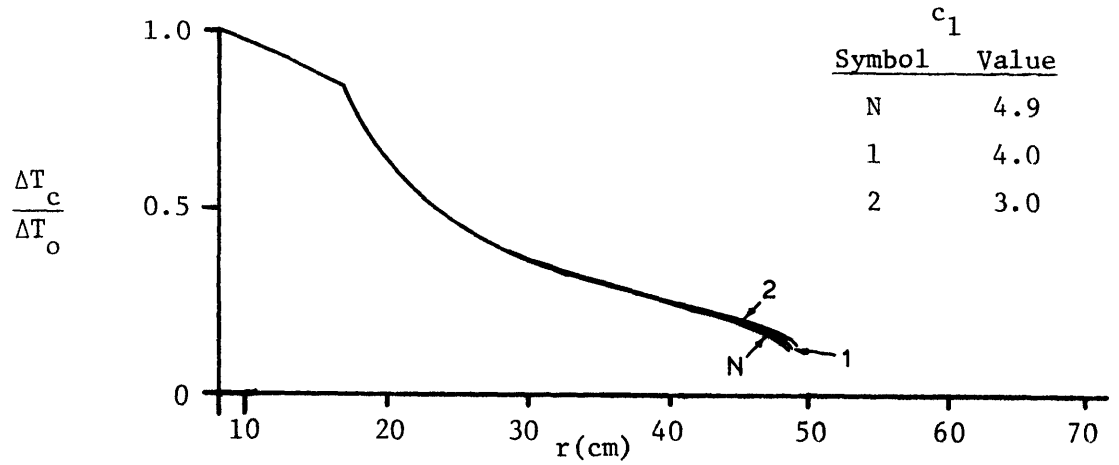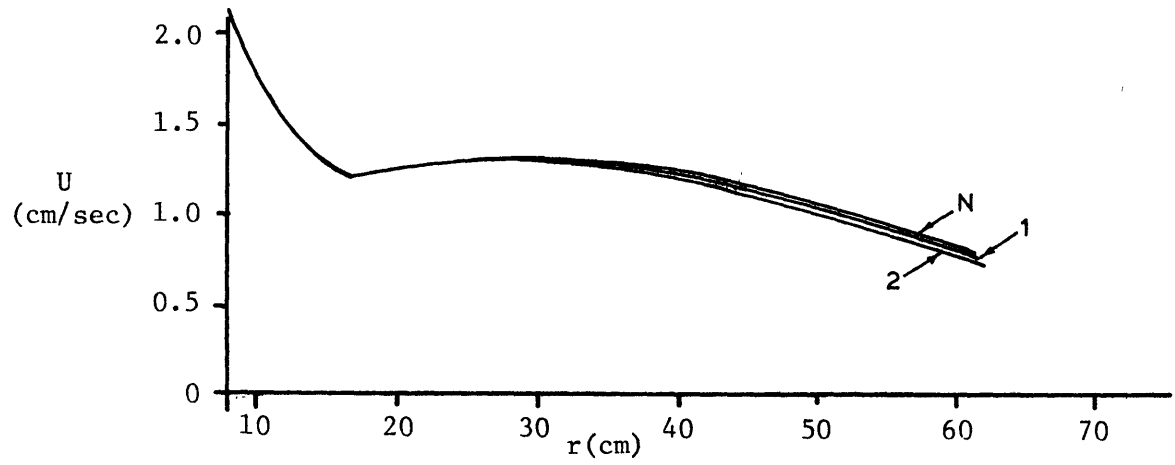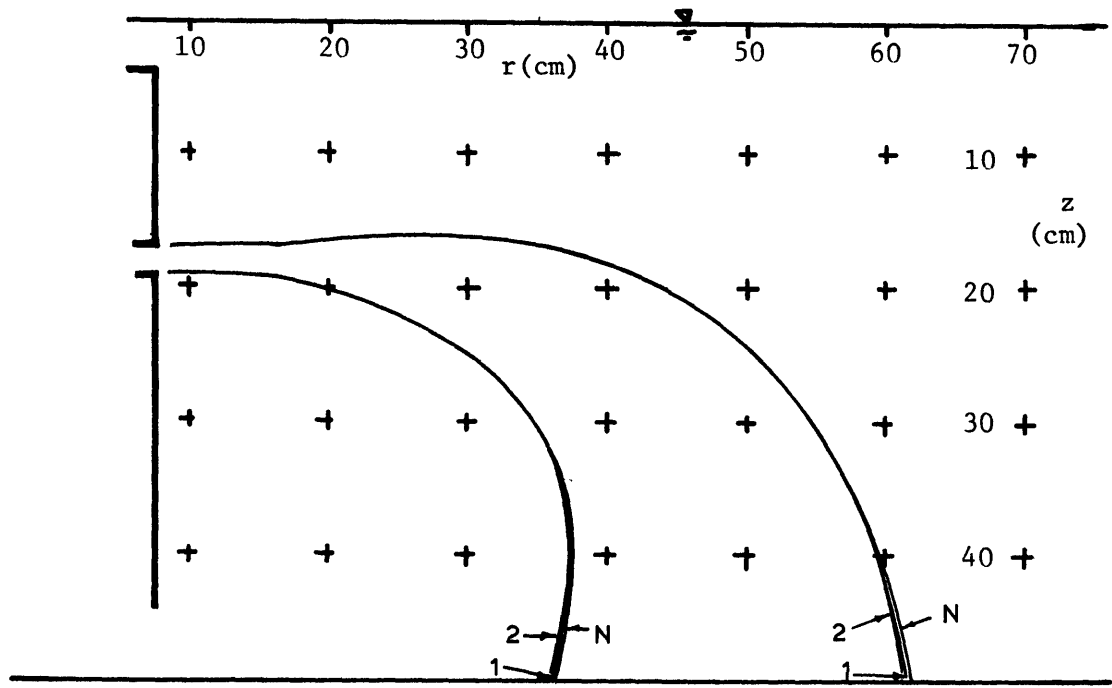
c_1

Symbol	Value
N	4.9
1	4.0
2	3.0

c_1 Sensitivity for Experiment XIII-2
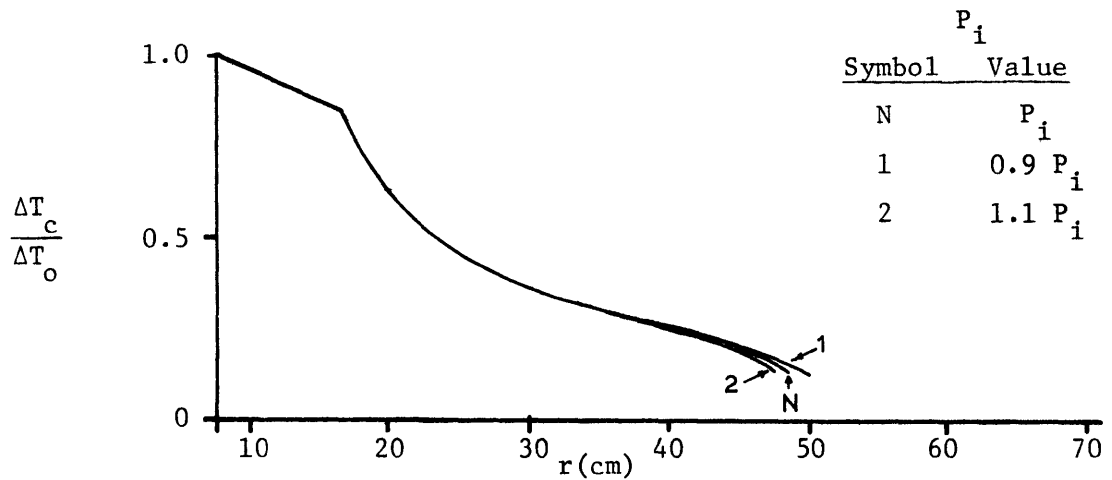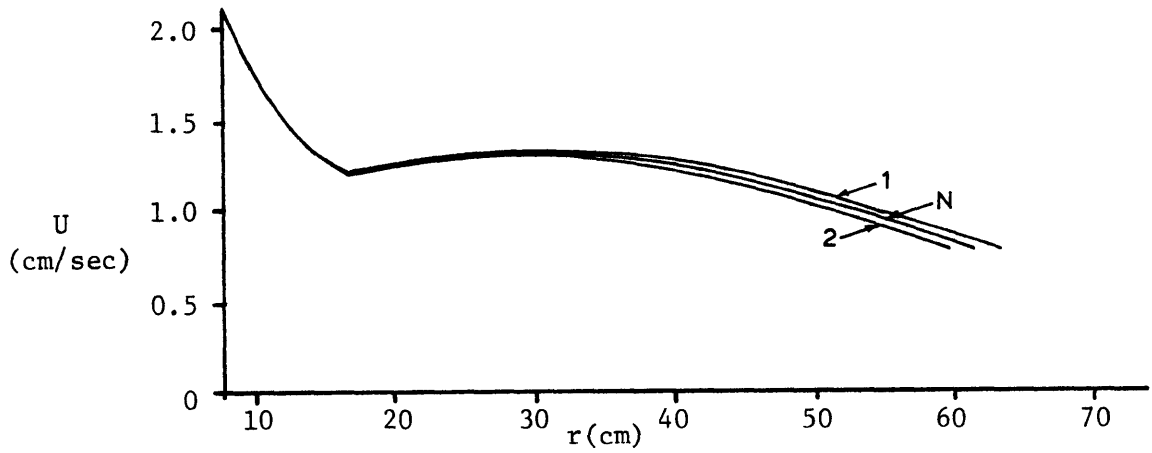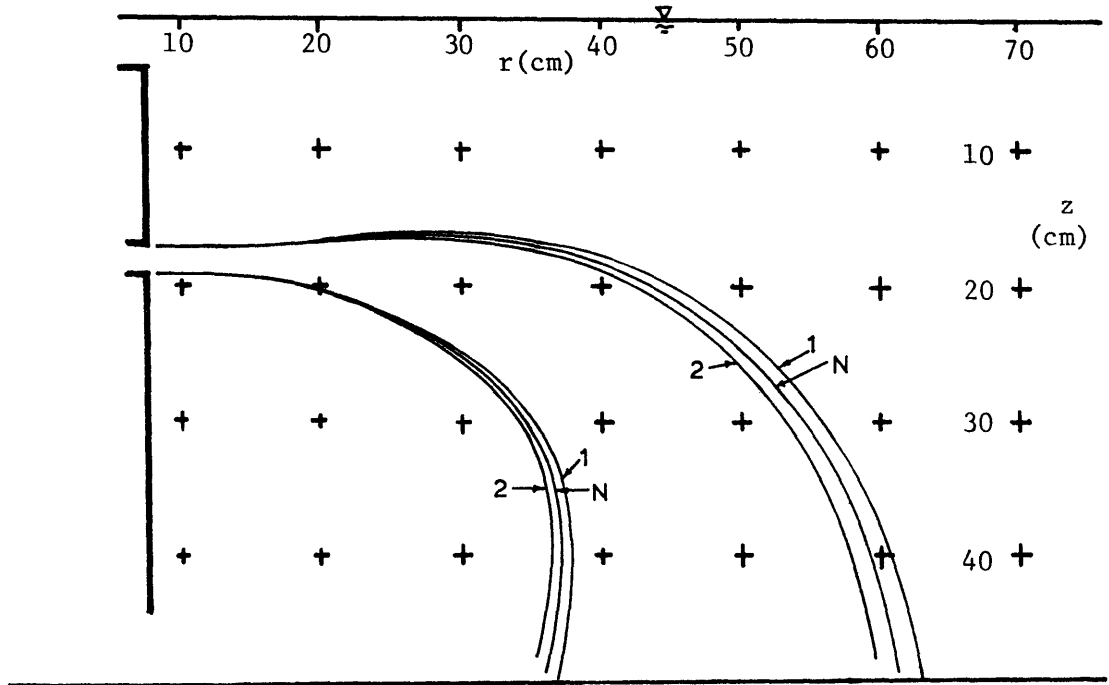
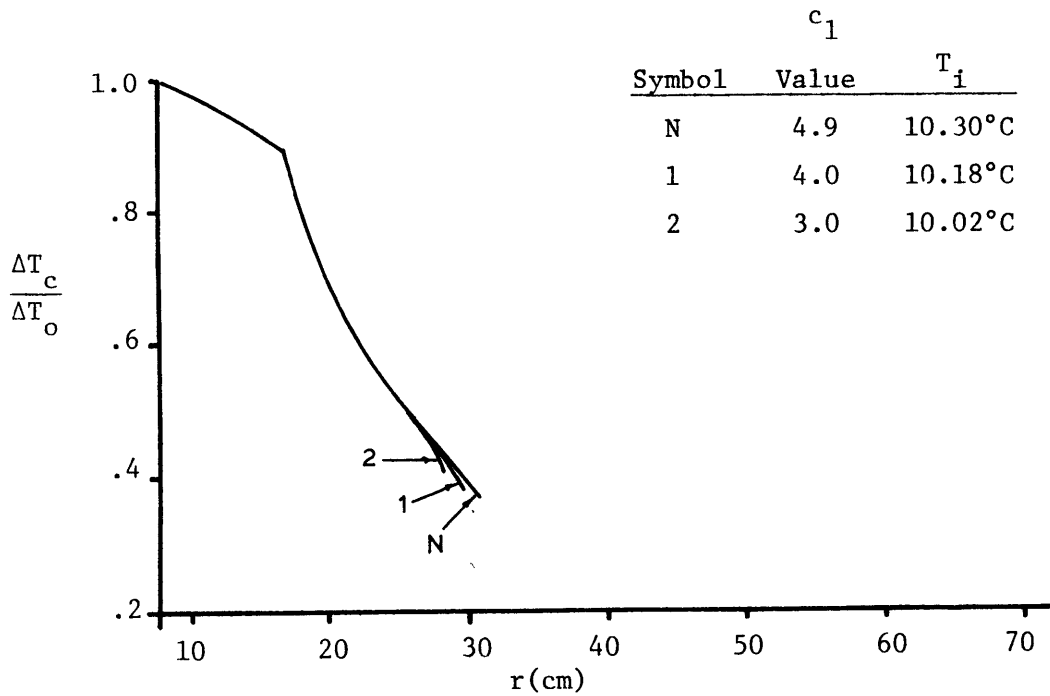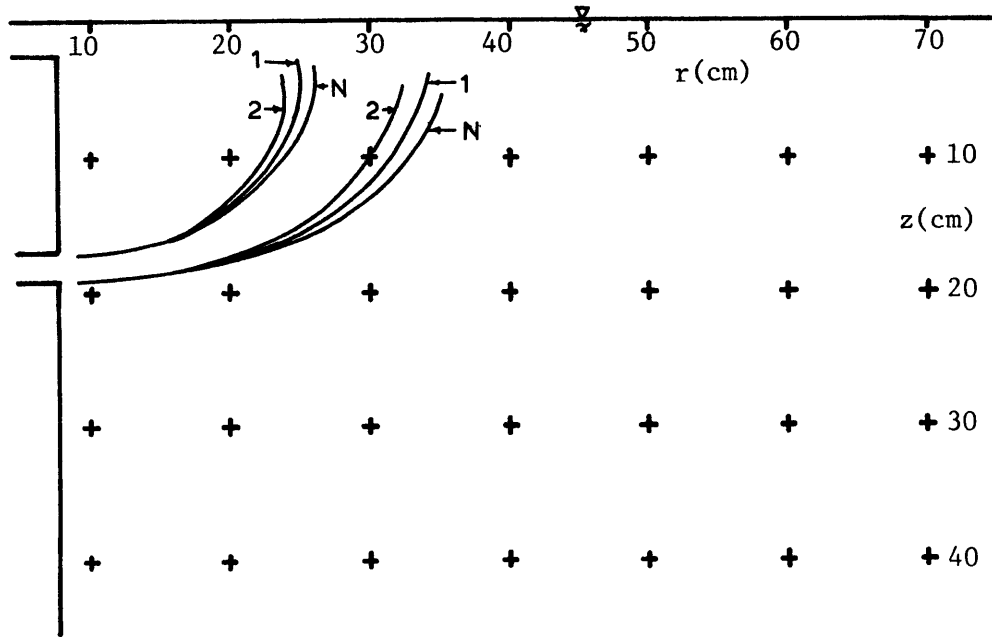|	P_i	
Symbol	Value	
N	P_i	
1	0.9 P_i	
2	1.1 P_i	

P_i Sensitivity for Experiment XIII-2
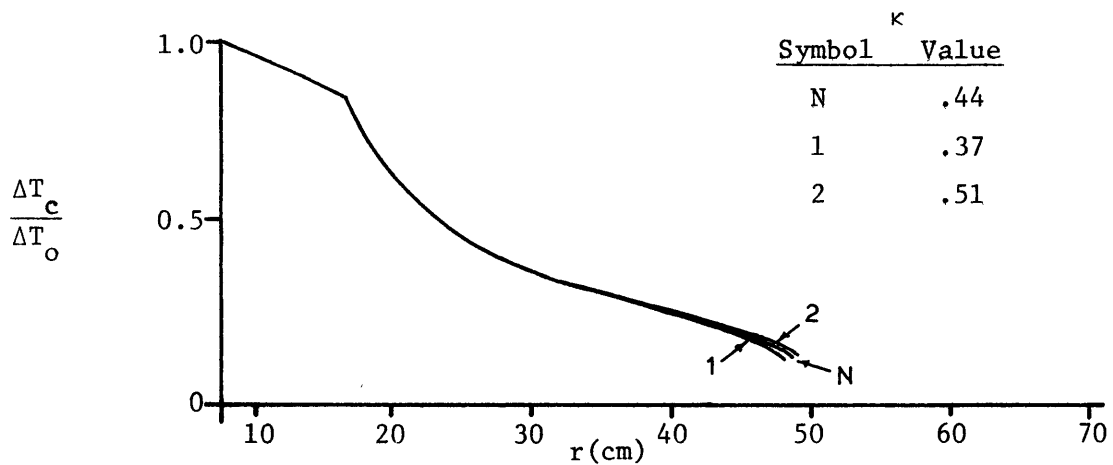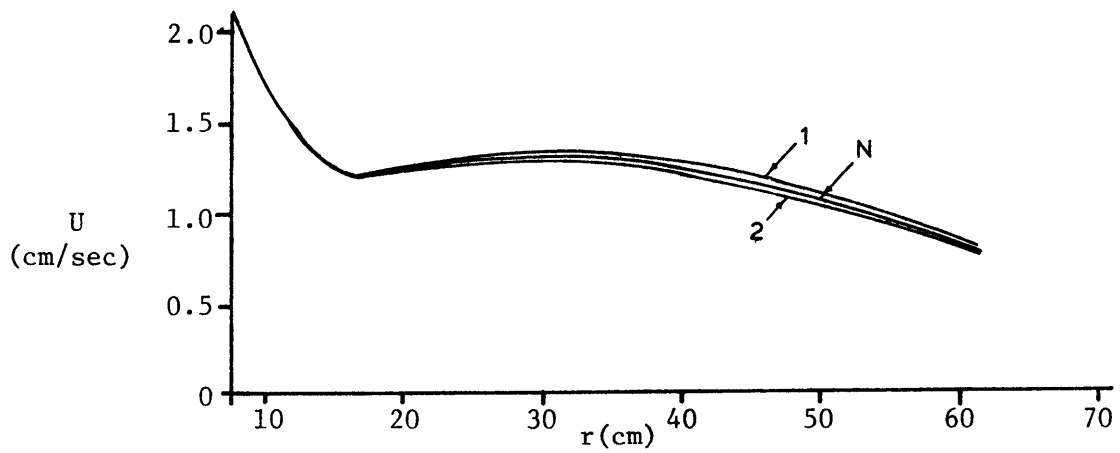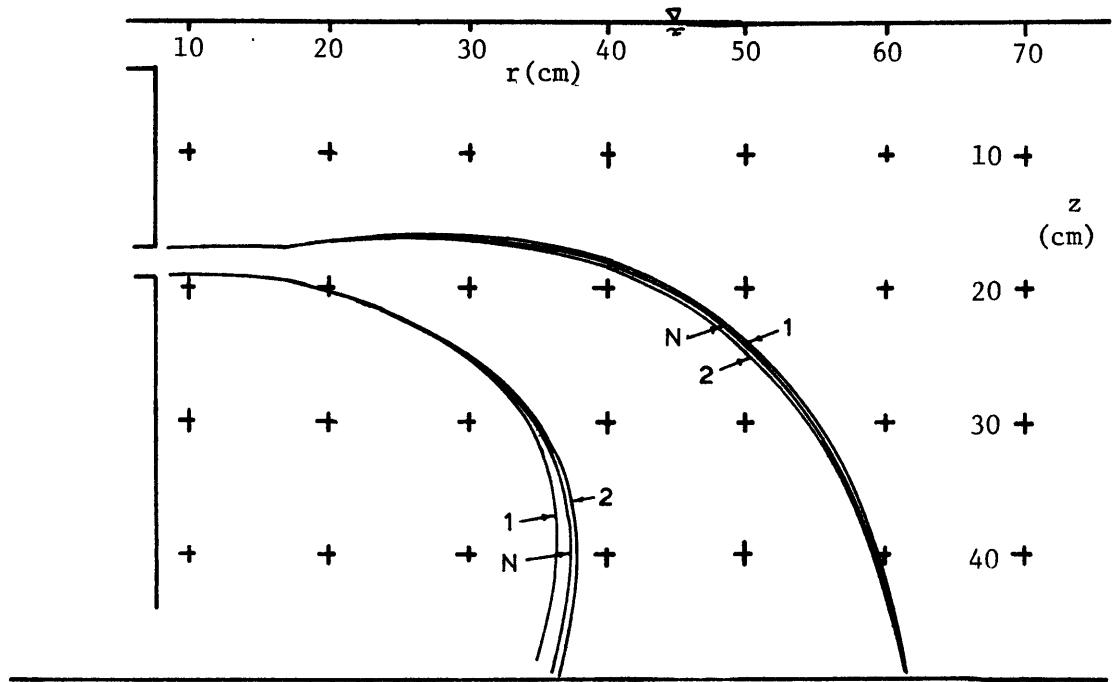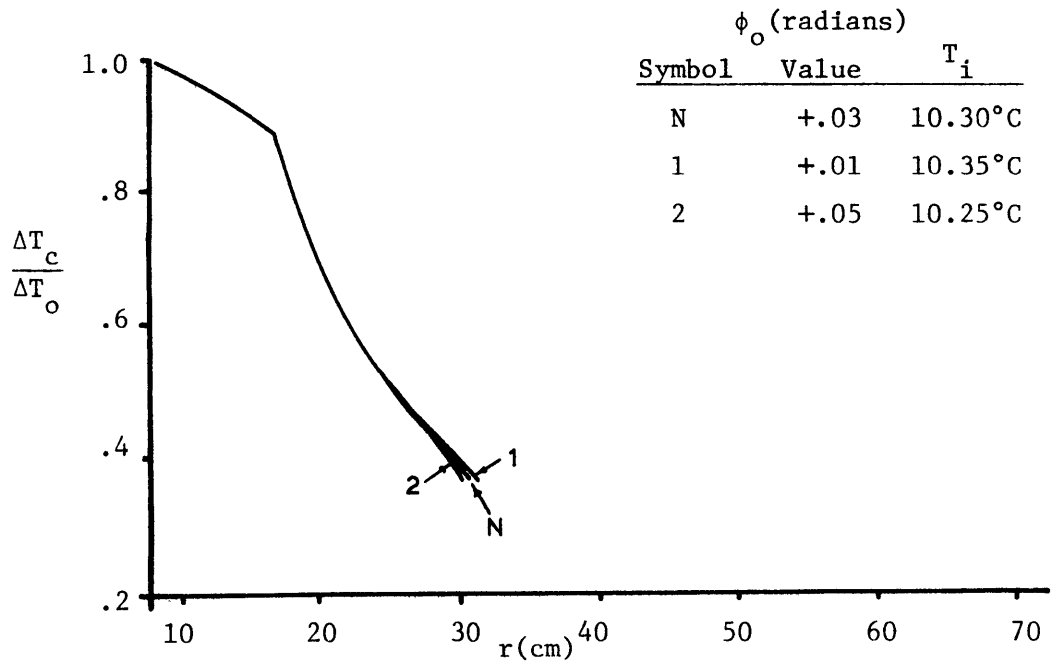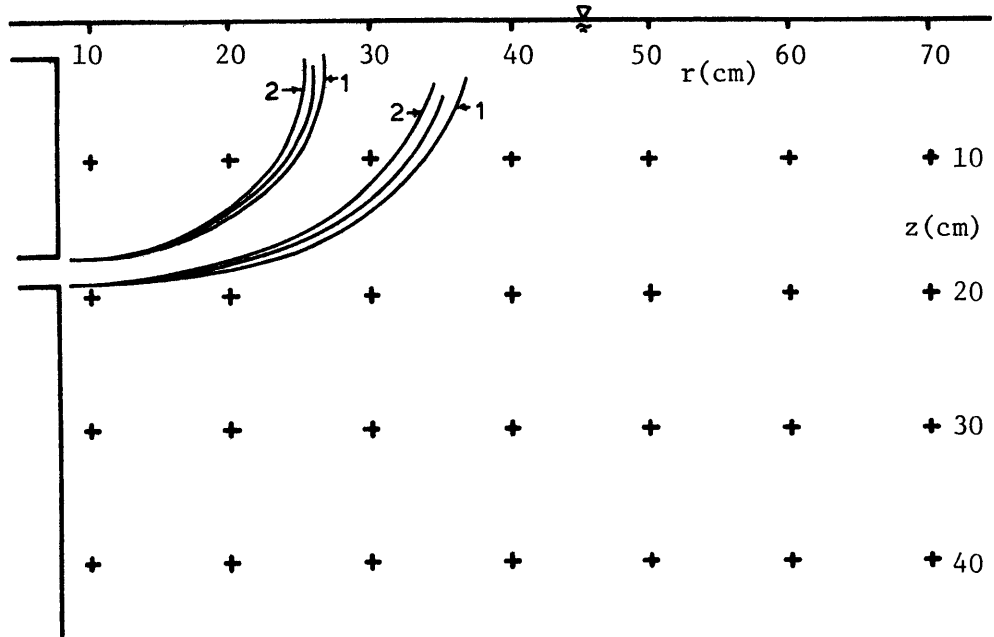
κ Sensitivity for Experiment XIII-2

Symbol	Value
N	.44
1	.37
2	.51

229

	ϕ_o (radians)	
Symbol	Value	T_i
N	+.03	10.30°C
1	+.01	10.35°C
2	+.05	10.25°C

ϕ_o Sensitivity of Experiment XIII-3

Top plot axes: r(cm) with marks 10, 20, 30, 40, 50, 60, 70; z(cm) with marks 10, 20, 30, 40. Curves labeled 1, 2, N.

Symbol	c_1 Value	T_i
N	4.9	10.30°C
1	4.0	10.18°C
2	3.0	10.02°C

Lower plot: vertical axis $\dfrac{\Delta T_c}{\Delta T_o}$ with marks 1.0, .8, .6, .4, .2; horizontal axis r(cm) with marks 10, 20, 30, 40, 50, 60, 70. Curves labeled 2, 1, N.

c_1 Sensitivity of Experiment XIII-3

231

Symbol	c_2 Value	T_i
N	.45	10.30°C
1	.30	10.38°C
2	.60	10.22°C

c_2 Sensitivity of Experiment XIII-3

	10	20	30	40	50	60	70	
	+	+	+	+	+	+	+	10
1,2,N								$z(cm)$
	+	+	+	+	+	+	+	20
	+	+	+	+	+	+	+	30
	+	+	+	+	+	+	+	40

$\dfrac{\Delta T_c}{\Delta T_o}$

1,2,N

$r(cm)$

Symbol	c_3 Value	T_i
N	.25	10.30°C
1	.15	10.19°C
2	.35	10.41°C
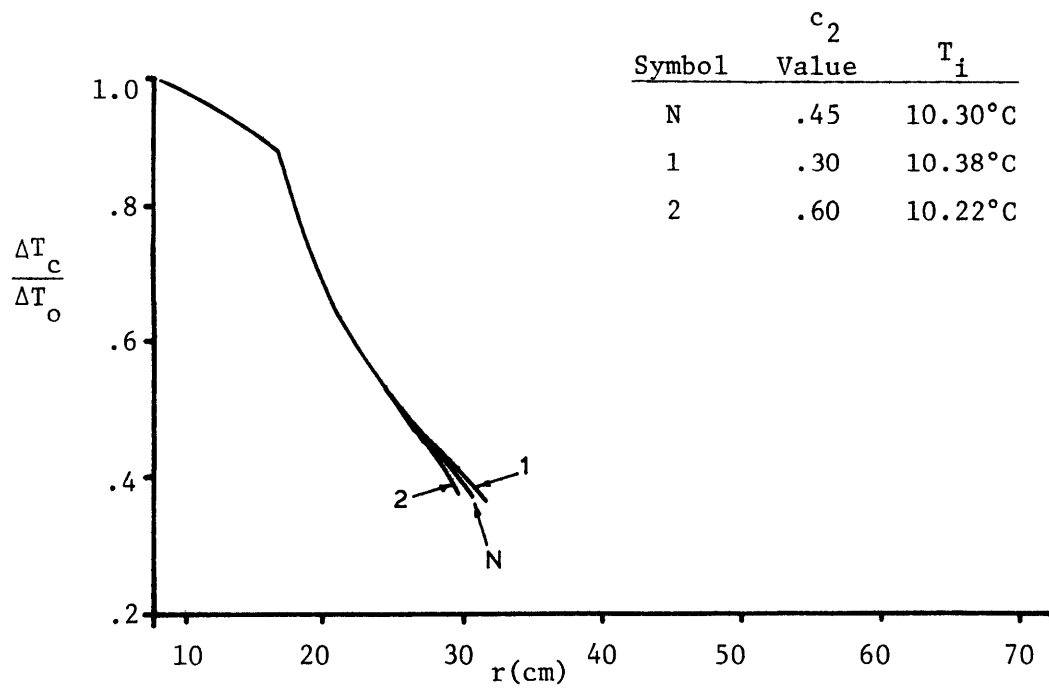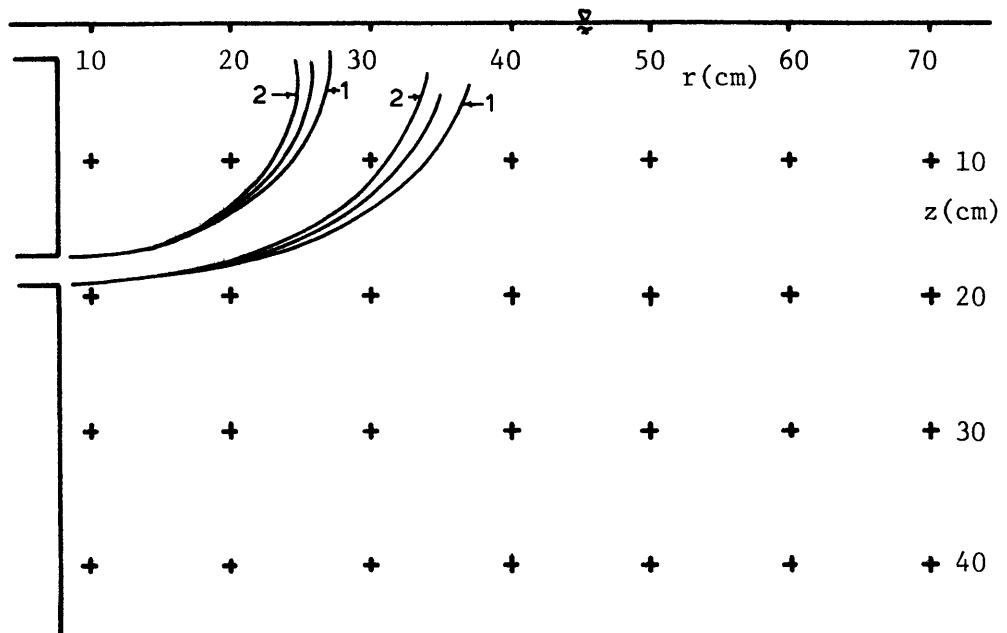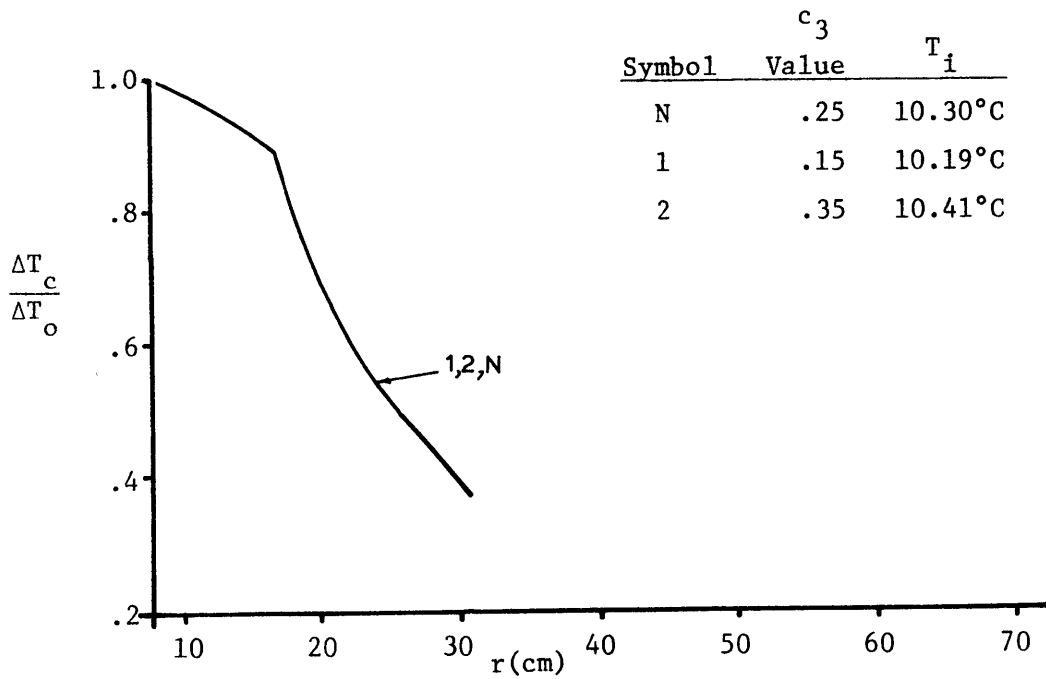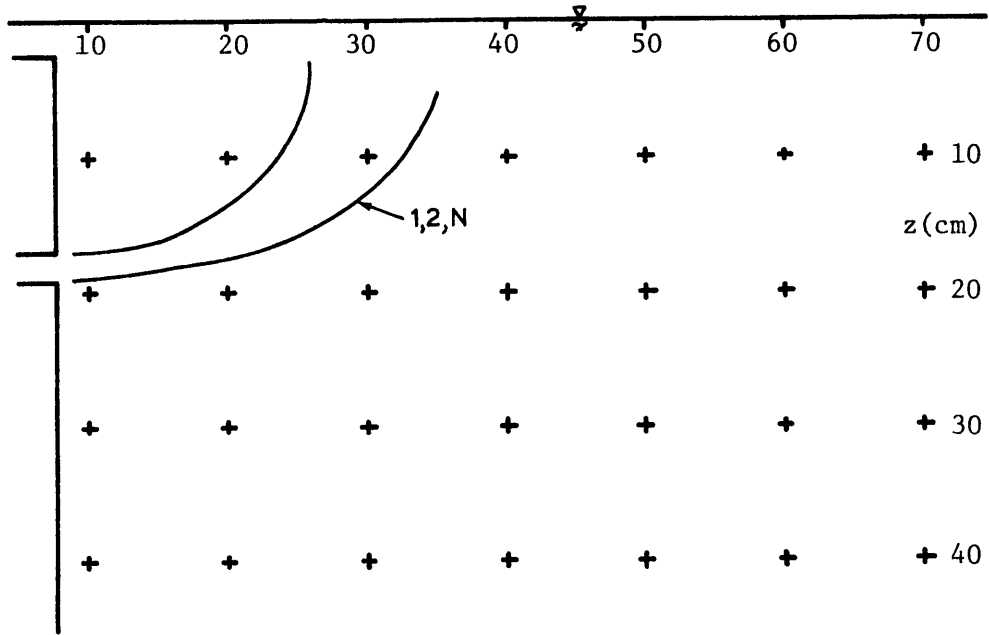
c_3 Sensitivity of Experiment XIII-3

233

Appendix III

k = 1

k = 0
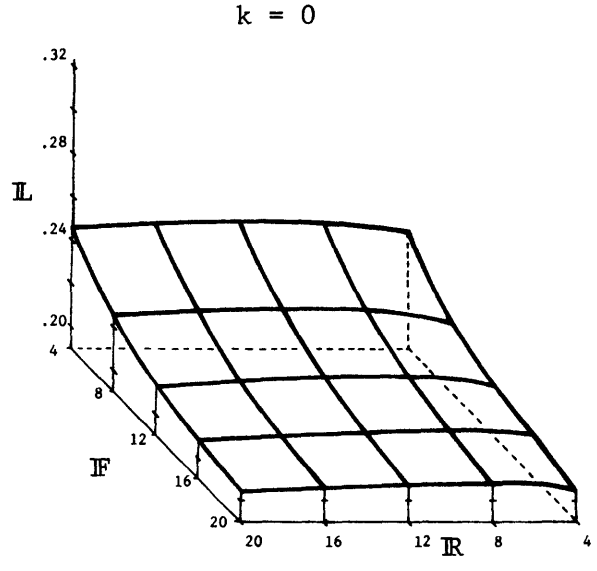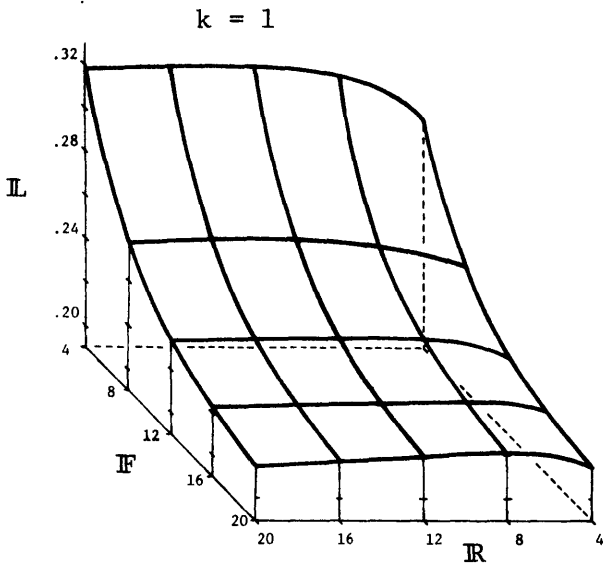
Detachment Surfaces

k = 1

k = 0
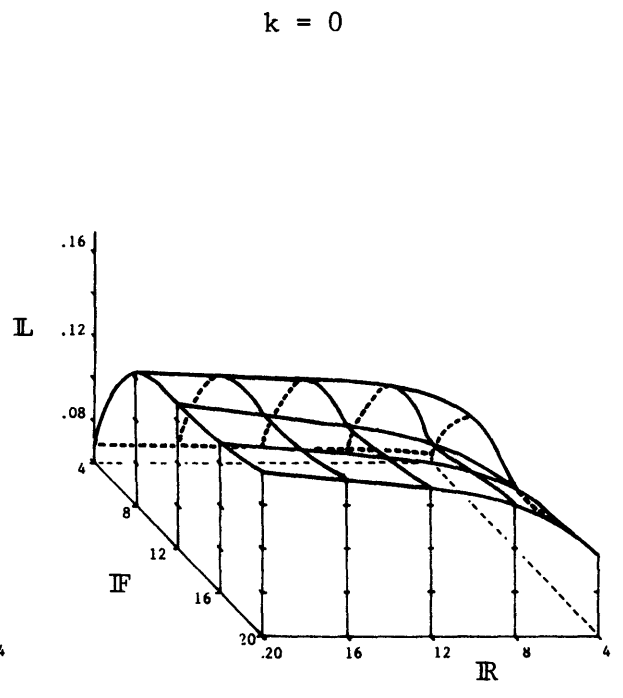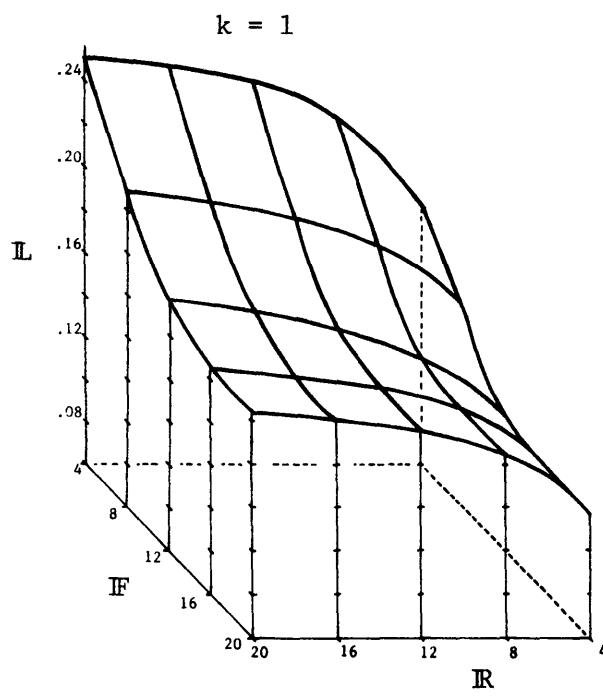
Attachment Surfaces

Three Dimensional View of Flow Regime Limits